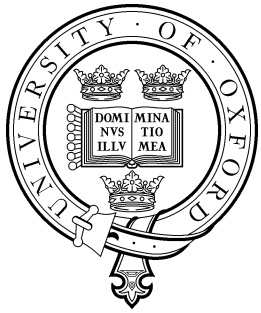
Mathematical Modelling of Dune Formation



David Cocks

Lincoln College

University of Oxford

A thesis submitted for the degree of

Doctor of Philosophy

Trinity 2005

Mathematical Modelling of Dune Formation

David Cocks

Lincoln College
University of Oxford

A thesis submitted for the degree of Doctor of Philosophy

Trinity 2005

This study is concerned with the mathematical modelling of the formation and subsequent evolution of sand dunes, both beneath rivers (fluvial) and in deserts (Aeolian). Dunes are observed in the environment in many different shapes and sizes; we begin by discussing qualitatively how and why the different forms exist.

The most important aspect of a successful model is the relationship between the bed shape and the shear stress that the flow exerts on the bed. We first discuss a simple model for this stress applied to fluvial dunes, which is able to predict dune-like structures, but does not predict the instability of a flat bed which we would hope to find. We therefore go on to look at improved models for the shear stress based on theories of turbulent flow and asymptotic methods, using assumptions of either a constant eddy viscosity or a mixing length model for turbulence. Using these forms for the shear stress, along with sediment transport laws, we obtain partial integro-differential equations for the evolution of the bed, and we study these numerically using spectral methods.

One important feature of dunes which is not taken into account by the above models is that of the slip face - a region of constant slope on the downwind side of the dune. When a slip face is present, there is a discontinuity in the slope of the bed, and hence it is clear that flow separation will occur. Previous studies have modelled separated flow by heuristically describing the boundary of the separated region with a cubic or quintic polynomial which joins smoothly to the bed at each end. We recreate this polynomial form for the wake profile and demonstrate a method for including it into an evolution system for dunes. The resulting solutions show an isolated steady-state dune which propagates downstream.

From the asymptotic framework developed earlier with a mixing length model for turbulence, we are able, using techniques of complex analysis, to model the shape of the wake region from a purely theoretical basis, rather than the heuristic one used previously. We obtain a Riemann-Hilbert problem for the wake profile, which can be solved using well-known techniques. We then use this method to calculate numerically

the wake profile corresponding to a number of dune profiles. Further, we are able to find an exact solution to the wake profile problem in the case of a sinusoidally shaped dune with a slip face.

Having found a method to calculate the shear stress exerted on the dune from the bed profile in the case of separated flow, we then use this improved estimate of the shear stress in an evolution system as before. In order to do this efficiently, we consider an alternative method for calculating the wake profile based on the spectral method used for solving the evolution system. We find that this system permits solutions describing an isolated dune with a slip face which propagates downstream without changing shape.

All of the models described above are implemented in two spatial dimensions; the wind is assumed to blow in one direction only, and the dunes are assumed to be uniform in a direction perpendicular to the wind flow. While this is adequate to explain the behaviour of transverse dunes, other dune shapes such as linear dunes, barchans, and star dunes are by nature three-dimensional, so in order to study the behaviour of such dunes, the extension of the models to three dimensions is essential. While most of the governing equations generalize easily, it is less obvious how to extend the model for separated flow, due to its reliance on complex variables. We implement some three-dimensional evolution models, and discuss the possibility of modelling three-dimensional flow separation.

For Rachel

Contents

1 Introduction **1**

1.1 Outline of thesis . . . 1

1.2 The geography of dunes . . . 2

1.2.1 Fluvial dunes . . . 3

1.2.2 Aeolian dunes . . . 4

1.2.2.1 Sand . . . 4

1.2.2.2 Features of deserts . . . 5

1.2.2.3 Types of dune . . . 6

1.2.2.4 Sand ripples . . . 10

1.2.3 The action of wind on sand particles . . . 11

1.2.4 Instability of flat sand bed . . . 11

1.2.5 Avalanching and the slipface . . . 12

1.2.6 Differences between fluvial and Aeolian sand dynamics . . . 12

1.3 Previous work . . . 13

2 Simple fluvial models **16**

2.1 Exner equation . . . 16

2.2 Sediment transport . . . 17

2.2.1 Bedload . . . 18

2.2.2 Suspended sediment . . . 19

2.3 St. Venant equations . . . 19

2.4 Non-dimensionalization . . . 21

2.5 Linear stability analysis . . . 24

2.5.1 Bedload equation . . . 24

2.5.2 Suspended sediment equation . . . 25

2.6 Constant eddy viscosity model for shear stress . . . 26

2.6.1 Asymptotic analysis of the Orr-Sommerfeld equation . . . 30

2.6.2 Linear stability analysis . . . 36

2.6.3 Stabilising term: O(1) term in expansion . . . 37
2.6.4 Stabilising term: Buoyancy-induced stress modification . . . 38
2.7 Canonical evolution equation . . . 39
2.7.1 Numerical solution . . . 40
2.7.1.1 Non-periodic solutions . . . 41
2.8 Non-saturated bedload transport . . . 50
2.9 Comparison of sediment flux functions . . . 54

3 Aeolian modelling: Mixing length model 56
3.1 The structure of the atmosphere . . . 56
3.2 Mixing length theory . . . 57
3.3 Boundary conditions . . . 59
3.4 Length scales for topography . . . 59
3.5 Asymptotic analysis . . . 60
3.5.1 $O(1)$ equations . . . 60
3.5.2 $O(\varepsilon)$ equations . . . 61
3.5.3 Inner equations . . . 63
3.5.4 Boundary layer thickness . . . 64
3.5.5 Inner solution . . . 64
3.5.6 Matching . . . 66
3.5.7 Linear stability analysis . . . 67
3.5.8 Further analysis . . . 67
3.5.9 Shear layer . . . 70
3.5.10 Linear stability analysis II . . . 77
3.5.11 Numerical analysis . . . 78
3.6 Comparison of sediment flux functions . . . 83

4 Aeolian modelling: Evolution equations 84
4.1 Non-saturated flux equation . . . 84
4.2 Polynomial separation . . . 86
4.2.1 Limitations of polynomial separation . . . 87
4.3 Comparison of sediment flux functions . . . 89
4.4 Slip face propagation . . . 90
4.5 Numerical implementation . . . 92
4.5.1 Evolution system . . . 93
4.5.2 Numerical schemes . . . 94
4.6 Results of simulation . . . 95

4.6.1 A 2d barchan dune 95
4.6.1.1 Slipface disappears 97
4.6.1.2 Slipface appears 99
4.6.2 A dune moving over an inerodible obstacle 100
4.6.3 A pair of 2d barchan dunes 102

5 Flow separation in the lee of a dune 109
5.1 Solution of Hilbert problem 115
5.2 Choice of singularities 119
5.3 Finding endpoints 122
5.4 Numerical solution 126
5.5 Further analysis for a sinusoidal bed 129

6 Evolution systems with flow separation 136
6.1 Shear stress calculation 136
6.2 Separation problem: a spectral approach 138
6.3 Implementation into evolution system 142
6.4 Numerical implementation 146
6.5 Remarks 147

7 Three-dimensional dune systems 149
7.1 Constant eddy viscosity shear stress model with uni-directional wind flow and down-slope term 149
7.2 Mixing length shear stress model with non-separated uni-directional wind flow and down-slope term 156
7.2.1 Limited sand supply 157
7.3 Improved mixing length shear stress model for three-dimensional flow 160
7.4 Three-dimensional separated wind flow 160
7.4.1 The slipface in three dimensions 160
7.4.2 Implementation of separation 165

8 Conclusions 166

A Turbulent flow modelling 169
A.1 Reynolds equations 169
A.2 Mixing length theory 171

Bibliography 172

List of Figures

1.1 Dunes in a river. The dunes migrate in the same direction as the flow. 3
1.2 Anti-dunes in a river. The bedforms are able to move in the opposite direction to the flow. 4
1.3 Sand dune in the Namibian desert, where some of the world's largest dunes are found. 6
1.4 Dunes on the surface of Mars. The wind is blowing from left to right; the darker areas are the slip faces and the lighter areas are areas with little sand. Source: NASA/JPL/MSSS [43] 7
1.5 Obstacle dunes. Left - leeward side. A dune has formed in the wake formed by the presence of the tree. Right - windward side. Dunes are building up in front of the rocks. Figures and similar ones below taken from [3]. 8
1.6 Left - barchan dunes. The tails and slip faces can be seen to point downwind. Right - transverse dunes. The ridges are very straight. . . 8
1.7 Left - barchanoid ridges. The ridges are much less straight than the transverse dunes. Eventually the variation becomes so great that the ridge breaks up, forming barchans. Right - parabolic dunes. These form due to the vegetation that can be seen on them. 8
1.8 Left - linear dunes. The direction of the ridge bisects the two directions of prevailing wind. Right - star dunes. Here the wind is coming from four different directions. 9
1.9 Sand ripples 10
1.10 Saltating sand particles. The diagram shows particles always bouncing off the surface; in fact sometimes they may not bounce but eject other particles. Figure taken from [2]. 11

2.1 Sketch of river geometry. Vertical distances are measured from an arbitrary reference level. 16

2.2 Relationship between the size of the basal shear stress $|\boldsymbol{\tau}|$ and the particle Reynolds number Re_p, from [3]. 17
2.3 Contours L_k in the definition of the generalized Airy function (2.141). 33
2.4 Contour γ used to evaluate the integral in (2.158) 35
2.5 Plot showing the relationship between $\psi_2(1)/\psi_1(1)$ and k 38
2.6 Typical random bed perturbation. Note that the vertical scale is much smaller than for the final solutions. 42
2.7 Numerical solution to evolution equation (2.197). This wave moves to the right without any change in its shape. 42
2.8 Plot of flux q and bed elevation s for the solution to (2.197). The linear relationship confirms that the wave is indeed a travelling wave. . . . 43
2.9 Numerical solution to dune equation (2.197) during growing phase. The vertical scale is the same as for Figure 2.7. 43
2.10 Flux q and bed elevation s for the solution to dune equation (2.197) during growing phase. 44
2.11 Schematic showing a desert in $x > 0$ with an ocean in $x < 0$ depositing sediment at the beach at $x = 0$. 44
2.12 Initial conditions for the sequence of solutions to (2.210) and (2.215) on $x > 0$ in the following Figures. 46
2.13 First in a sequence of solutions to (2.210) and (2.215) on $x > 0$. The dune has propagated downstream, and a depression has started to form downstream of the dune. 47
2.14 Second in a sequence of solutions to (2.210) and (2.215) on $x > 0$. The dune continues to propagate downstream, and the depression has continued to grow. 48
2.15 Third in a sequence of solutions to (2.210) and (2.215) on $x > 0$. Another dune has begun to grow downstream of the depression, and the train of dunes and depressions continue to move downstream. This pattern repeats for as long as we run the simulation. 49
2.16 A three-dimensional representation of the sequence of solutions to (2.210) and (2.215) on $x > 0$ shown in the previous Figures. 50
2.17 Numerical solution to dune equation (2.236) with $\alpha/x_0 = 0.13$. The solution shown is that obtained for large T, i. e. the steady state solution. 53
2.18 Numerical solution to dune equation (2.236) with $\alpha/x_0 = 0.13$. The solution shown is that obtained before the solution settles down to a steady state solution; there are multiple dunes which later coalesce. . 54

2.19 Comparison of three different sediment flux functions q_1, q_2, and q_3 for a Gaussian dune profile s. 55

3.1 Numerical solution to dune system (3.227)–(3.229) with $a = 1$, $b = 1.5$, and $c = 1$. 79
3.2 Plot showing bed height s against generalised flux q for the solution to the dune system (3.227)–(3.229) with $a = 1$, $b = 1.5$, and $c = 1$ shown in Figure 3.1. The multi-valued nature of the plot shows that the dune is still growing. 80
3.3 Numerical solution to modified dune system (3.227), (3.235), and (3.229) with $a = 1$, $b = 1.5$, and $c = 1$. The solution is that obtained for large t, i. e. a steady state travelling wave. 81
3.4 Plot showing bed height s against generalised flux q for the solution to the modified dune system (3.227), (3.235), and (3.229) with $a = 1$, $b = 1.5$, and $c = 1$ shown in Figure 3.3. The straight line shows that the solution is indeed a steady state travelling wave. 81
3.5 A sequence of solutions to (3.227)–(3.229) on the semi-infinite domain $[0, \infty)$. As the initial perturbation evolves, it forms a train of dunes which continues to grow for as long as we run the simulation. 82
3.6 Comparison of sediment flux functions q_1 (constant eddy viscosity) and q_2 (mixing length) for a Gaussian dune profile s. 83

4.1 Plot of q_s from (4.2) and the solution q of (4.1) when $\alpha = 1$, $a = 0$, $b = 3$, $q_1 = 2$, $q_2 = 3$, and $q_3 = 1$. 85
4.2 Polynomial flow separation with $\mu_c = 0.6$ for dune profile $s = \sin^2 x$, $x < 1.45$, and slip face with $\tan\theta = 1.5$. 88
4.3 Polynomial flow separation with $\mu_c = 0.8$ for dune profile $s = \exp[-(x-3)^2]$, $x < 3.2$, and slip face with $\tan\theta = 2$. 88
4.4 Polynomial flow separation with $\mu_c = 7$ for dune profile s from solution to evolution equation (2.197), $x < 1.83$, and slip face with $\tan\theta \approx 40$. 89
4.5 Comparison of sediment flux functions q_1 and q_2 for a Gaussian dune profile s with wake profile S. 90
4.6 Geometry for a propagating slip face 92
4.7 Series of plots of solution at regular time intervals to dune system with polynomial flow separation. The profile quickly settles down into a steady configuration. 96

4.8 Close up of the dune profile and its associated wake profile for the steady state travelling wave that the solutions in Figure 4.7 settle down to. 96
4.9 Plot of flux q against bed height s for the dune in Figure 4.8. The linear relationship confirms the existence of a steady state travelling wave. 97
4.10 Series of plots of solution at regular time intervals to dune system with polynomial flow separation and parameters adjusted so that the slipface does not persist. The slipface moves forward and disappears, and the profile settles down into a steady configuration without separation. 98
4.11 Close up of the dune profile without separation for the steady state travelling wave that the solutions in Figure 4.10 settle down to. . . . 98
4.12 Plot of flux q against bed height s for the dune in Figure 4.11. The linear relationship confirms the existence of a steady state travelling wave. 99
4.13 A sequence of solutions to the evolution system (4.28) to (4.38). We start with a profile without a slipface; this profile steepens and a slipfaces forms, before a wake region later appears and the dune approaches a steady state. 100
4.14 The first in a sequence of solutions to the system (4.28) to (4.38) in the case of an inerodible obstacle ($t = 1$). 102
4.15 The second in a sequence of solutions to the system (4.28) to (4.38) in the case of an inerodible obstacle ($t = 1.5$). 103
4.16 The third in a sequence of solutions to the system (4.28) to (4.38) in the case of an inerodible obstacle ($t = 2$). 103
4.17 The fourth in a sequence of solutions to the system (4.28) to (4.38) in the case of an inerodible obstacle ($t = 2.5$).. 104
4.18 Standard continuous solution to (4.28) for q that does not satisfy $q = 0$ at the reattachment point c_1 (signified by a blue dot). 105
4.19 Initial conditions for the simulation of the interaction of two dunes. Note that the second dune is partly inside the wake region of the first. 106
4.20 First in a sequence of solutions to (4.28) to (4.38) in the case of two interacting dunes ($t = 1$). The top of the second dune is being eroded and is causing the slipface to move downstream. 106

4.21 Second in a sequence of solutions to (4.28) to (4.38) in the case of two interacting dunes ($t = 2$). The second dune has spread out significantly due to being caught in the wake region of the first dune, and the first dune has started to move over the second dune. 107
4.22 Third in a sequence of solutions to (4.28) to (4.38) in the case of two interacting dunes ($t = 3$). The wake region of the first dune now contains both dunes, as the first dune moves over what is left of the second dune. 107
4.23 Fourth in a sequence of solutions to (4.28) to (4.38) in the case of two interacting dunes ($t = 4$). The two dunes have now become one large dune which moves downstream in a steady state configuration. . . . 108

5.1 Recirculating wake in the lee of a dune. We hope to find the shape of the dotted line. 109
5.2 A schematic layout of separated flow 110
5.3 Geometry for mixed Hilbert problem 114
5.4 Circle geometry showing derivation of γ. 123
5.5 Circle geometry showing derivation of $\alpha' - \beta'$. 124
5.6 Circle geometry showing derivation of α'. 124
5.7 Wake profile (red) calculated from the sinusoidal bed profile (blue) with a slip face between $x = 1$ and $x = 2$, and with the separation point $a = 1$. 127
5.8 A series of wake profiles (red) calculated from the sinusoidal bed profile (blue) with varying positions of the separation point a. Slip faces were not introduced as they would not affect the solutions. 128
5.9 Wake profile (red) calculated from the bed profile (blue) which was the steady state travelling wave solution to (2.197), with a separation point $a = 0.8$. No slip face was introduced in this case. 129
5.10 Wake profile (red) calculated from the Gaussian bed profile (blue) with a slip face between $x = \pi+0.2$ and $x = \pi+0.3$, and with the separation point $a = \pi + 0.2$. 130
5.11 A series of solutions (varying a) of (5.144) 133

6.1 Two flows past dunes; the first with separation, the second with a dune profile the same shape as the wake profile in the first. The two outer flows are identical. 137

6.2 Wake region (red) calculated for a sinusoidal dune profile (blue) using the spectrally-based method of Section 6.2. 143
6.3 Wake profile (red) calculated for the constant eddy viscosity solution dune profile of Chapter 2 (blue) using the spectrally-based method of Section 6.2. 143
6.4 Comparison between spectral method (green) and the method of Chapter 5 (red) for calculating wake profiles for the constant eddy viscosity profile (blue). 144
6.5 Wake profile (red) calculated for a Gaussian dune profile (blue) using the spectrally-based method of Section 6.2. 144

7.1 The first in a sequence of solutions to (7.11) with a long domain in the x-direction (c. f. Figure 2.16), most of which is not shown ($t = 0$). . . 152
7.2 The second in a sequence of solutions to (7.11). A depression has started to form downstream of the dune ($t = 1$). 152
7.3 The third in a sequence of solutions to (7.11). Another dune has started to form downstream of the depression ($t = 2$). 153
7.4 The fourth in a sequence of solutions to (7.11) ($t = 3$). The pattern of new depressions and dunes repeats for as long as we run the simulation. 153
7.5 Typical random bed perturbation used as initial conditions for the simulation shown in Figures 7.6 to 7.9. 154
7.6 First in a sequence of solutions to 7.11 growing from an initial random perturbation ($t = 1$). 154
7.7 Second in a sequence of solutions to 7.11 growing from an initial random perturbation ($t = 2$). The dunes begin to fill the periodic domain 155
7.8 Third in a sequence of solutions to 7.11 growing from an initial random perturbation ($t = 3$). The dunes begin to arrange themselves transversely to the wind direction. 155
7.9 Fourth in a sequence of solutions to 7.11 growing from an initial random perturbation ($t = 4$). The solution has become symmetric in the y-direction and is the equivalent of the two-dimensional solutions found in Chapter 2. 156
7.10 First in a sequence of solutions to (7.14) to (7.19) growing from an initial random perturbation ($t = 1$). 158
7.11 Second in a sequence of solutions to (7.14) to (7.19) growing from an initial random perturbation ($t = 2$). 158

7.12 Third in a sequence of solutions to (7.14) to (7.19) growing from an initial random perturbation ($t = 3$). 159
7.13 Fourth in a sequence of solutions to (7.14) to (7.19) growing from an initial random perturbation ($t = 4$). 159
7.14 First in a sequence of solutions growing from an initial random perturbation and using (7.28) for the three-dimensional surface shear stress ($t = 1$). 161
7.15 Second in a sequence of solutions growing from an initial random perturbation and using (7.28) for the three-dimensional surface shear stress ($t = 2$). 161
7.16 Third in a sequence of solutions growing from an initial random perturbation and using (7.28) for the three-dimensional surface shear stress ($t = 3$). 162
7.17 Fourth in a sequence of solutions growing from an initial random perturbation and using (7.28) for the three-dimensional surface shear stress ($t = 4$). 162
7.18 A barchan dune with a slipface showing the slipface region D, the brink curve C_1, and the base curve C_2. 163

Chapter 1

Introduction

Dunes are found wherever a fluid interacts with an erodible bed beneath it, whether this is in the familiar context of sand in a desert blown by the force of the wind, the silt on the bed of a river being eroded by the water flowing over it, or drifts formed by the action of wind on powdery snow. The ubiquity of these repetitive, wave-like features suggests that there is an inherent instability making it impossible for a horizontal bed to stay horizontal, and that there is an underlying reason, predictable by analytic study of the processes involved, that causes such features to form in a wide variety of circumstances, and on a number of different scales.

The interaction between a fluid and an erodible substrate beneath it is a complex one. The flow of water in a river and the flow of wind in the atmosphere are always turbulent, making analytical study difficult. Similarly the behaviour of granular flow is complex and only partially understood. These two mechanisms in turn affect each other, since the fluid exerts a force on the substrate, causing it to be eroded, and thereby changing its shape, whereas the shape of the bed in turn influences the characteristics of the flow of the fluid over it. It is the understanding of this feedback mechanism that is the goal of any study of dune formation, and it is for these reasons that previous studies have been only partially successful in predicting the formation, evolution, and migration of dunes in a general framework.

1.1 Outline of thesis

We now describe the structure of this thesis. We begin by describing qualitatively some geographical aspects of dunes, deserts, and sand that we will later use to derive quantitative models for the behaviour of dunes. We describe various types of dunes and conditions under which they occur, we describe features of dunes as well as processes that they are involved in, and we discuss physically the differences between

desert and river dunes. We then conclude this Chapter by reviewing some of the existing work that has been undertaken on this subject.

The remainder of the thesis is then concerned with the derivation, solution, and discussion of deterministic models for the formation and subsequent evolution of dunes. In Chapter 2 we consider and extend existing dune evolution systems derived using theories from river flow. We solve these systems using numerical methods, and are able to obtain solutions that exhibit many properties of dunes. We find that the key aspect of these systems is the description of the shear stress exerted by the fluid upon the substrate, and we explore how the form of this shear stress affects the behaviour of our solutions.

In Chapter 3 we consider an alternative method of calculating the surface shear stress, the derivation being based on theories of wind flow rather than the theories of river flow used in Chapter 2. We consider the effect that a small perturbation to the lower boundary (corresponding to a dune) has to the logarithmic velocity profile of the flow of wind over a horizontal boundary.

At this point the theory assumes that there is no flow separation occurring (i. e. that there are no wake regions present) in any part of the flow. Since flow separation is a ubiquitous process in the turbulent flow of air over an uneven boundary, we go on in Chapter 4 to consider an existing, heuristic, method of modelling the phenomenon of flow separation. We then incorporate this model into the evolution system obtained in Chapter 3 and simulate a number of different dune evolution configurations.

Having explored the use of this existing flow separation model, in Chapter 5 we derive a new method for modelling separated flow based on the theory of Chapter 3 and using techniques of complex analysis. We explore the results of this method for some known dune shapes and compare it to the method of Chapter 4. Then in Chapter 6 we incorporate the new method into our existing evolution systems.

Finally in Chapter 7 we consider the extension of the methods of previous Chapters, which are all based on two-dimensional flow, into three dimensions. We implement some of these methods, and discuss the implications of others. We conclude this thesis in Chapter 8 by discussing possibilities for future work.

1.2 The geography of dunes

In this Section we consider various geographical properties of dunes that will be useful to us when later considering models of their behaviour. A wide variety of dune shapes can be seen in deserts (see Section 1.2.2.3), the occurrence of different types depending

on various conditions such as sand supply, particle size, wind direction, vegetation, etc. Dunes occurring under rivers show less variety in their form. This is because the flow of water in a river is much simpler than the flow of wind in a desert – the flow is restricted to the channel of the river, and while the flow is not truly two-dimensional, the downstream flow is much larger in magnitude than the cross-stream component.

In both cases, dunes form because of the action of the fluid upon the substrate. The stress force associated with the shear flow acts on the particles, causing them either to be entrained into the flow (and subsequently be deposited elsewhere) or to move along the surface. The shear stress thus changes the profile of the underlying surface, but the shear stress itself depends on the bed profile, so there is a feedback mechanism between the two. There are, therefore, two basic mechanisms to be explored in this study: firstly, the relationship between the bed profile and the shear stress of the fluid over this profile, and secondly, the relationship between the shear stress and the transport of sediment.

1.2.1 Fluvial dunes

A number of different bed features are found beneath rivers and, generally speaking, the type of feature depends on the flow rate of the water above it. At very slow flow speeds, the bed is a simple plane surface. As speeds increase, small ripples appear, to be replaced by dunes, with both larger amplitude and larger wavelength (Figure 1.1). Dunes move slowly in the direction of flow, and have a shallow upstream slope with a steep downstream slope. Typically disturbances to the free surface of the water are out of phase with the dunes.

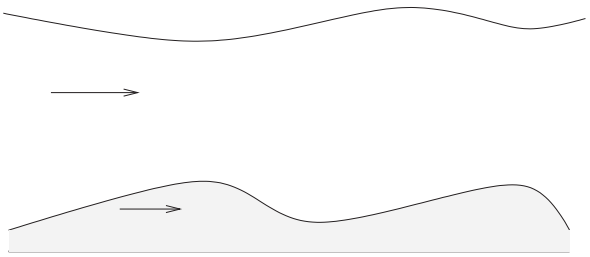


Figure 1.1: Dunes in a river. The dunes migrate in the same direction as the flow.

Increasing the flow rate further causes the dunes to flatten out, giving a plane bed once again. After this, *anti-dunes* form. Anti-dunes are unlike dunes in that they are much more symmetric, can move both up- or downstream (usually up), and are typically in phase with the free surface disturbances (Figure 1.2). At very high flow rates, one can also observe time dependence, where anti-dunes form, grow, destroy

themselves, and then reform. In comparison, dunes normally migrate downstream with no change in size or shape.

We consider ways to model such fluvial dunes in Chapter 2.

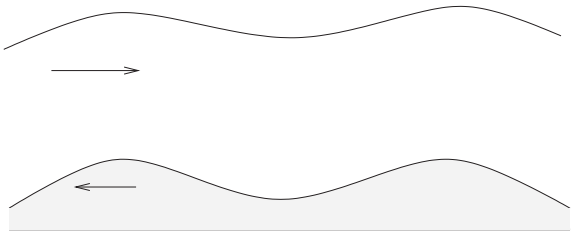


Figure 1.2: Anti-dunes in a river. The bedforms are able to move in the opposite direction to the flow.

1.2.2 Aeolian dunes

Aeolian dunes are dunes formed by the action of wind on desert sand, the name coming from the mythical god of the winds, Æolus. Aeolian dunes show a massive variety of forms, which arise both from the nature of the sand of which they consist, and from the patterns of air movement which cause them to exist.

1.2.2.1 Sand

> [...] instead of finding chaos and disorder, the observer never fails to be amazed at a simplicity of form, an exactitude of repetition and a geometric order unknown in nature on a scale larger than that of crystalline structure. In places vast accumulations of sand weighing millions of tons move inexorably, in regular formation, over the surface of the country, growing, retaining their shape, even breeding, in a manner which, by its grotesque imitation of life, is vaguely disturbing to an imaginative mind. [8]

Sand is defined by Bagnold [8] as being any particle with a diameter of between 0.02 mm and 1 mm. Obviously particles in general are not spherical so that a unique diameter does not exist; instead we consider a typical diameter of the particle, for example the mean of the diameter in a number of different directions. The motivation for this definition comes from the behaviour of particles under the action of wind. The smallest sand particles are those which are not carried away by the wind and scattered as dust, i. e. they are sufficiently large that when picked up by the wind, they return to the ground in a reasonable amount of time. The biggest sand particles

are those which are so large that they only just move, either from the force of the wind blowing over them, or because of the impact of other particles on them.

The particles which fall into this range are hence the only particles which, under the influence of wind, exhibit self-accumulation. These particles use the energy of the wind to collect together and form heaps, commonly called dunes, which can retain their identity, move from place to place, pile up, elongate, and combine with other dunes, always forming regular patterns. Some of the many ways in which this happens are explored later in this section.

The above definition does not specify the material from which particles of sand are made. Therefore any sort of rock can be classified as being sand provided it is the right size, similarly for particles of plastic, metals, etc. The ice crystals of snow also fall into this size range and are therefore defined as sand.

It turns out that the only characteristic of sand particles which has a significant effect on the dynamics is the particle size. Other factors such as the material or the weight of the particle have much smaller effects on, for example, the formation of ripples and dunes. For example, two particles made of the same material, one twice as heavy as the other, will only differ in grain diameter by a factor of $\sqrt[3]{2} \approx 1.26$. For this reason, drifting snow behaves in a very similar way to desert sand dunes.

However, despite the very broad definition of sand given above, the common perception of sand is much more specific, namely particles of quartz silica. The reason for this is that for most materials, particles which are classified as sand are unstable; they do not remain in this form for very long. Particles of rocks other than quartz tend to get smaller due to collisions with each other under the action of wind and water. Similarly snowflakes soon turn into either ice, water, or vapour. Quartz, on the other hand, is much longer-lasting, as it resists the action of chemicals, is not soluble in water, and is not generally susceptible to abrasion or fracture. In other words, quartz sand particles are stable; they tend to remain in essentially the same form for substantial periods of time.

1.2.2.2 Features of deserts

The common view of deserts is of landscapes dominated by sand dunes, but in fact only between one third and one quarter of the world's deserts are covered by Aeolian sand [26]. In particular, sand dunes only make up 1% of the surface area of the American deserts. Despite this, deserts are the only place in the world where large seas of sand, called *dune fields* or *ergs*, are found, which form very beautiful, repetitious



Figure 1.3: Sand dune in the Namibian desert, where some of the world's largest dunes are found.

and regular landforms (Figure 1.3). Large ergs occur in Arabia and the Sahara, and they have also been observed on Mars (Figure 1.4).

1.2.2.3 Types of dune

The following is a brief overview of some common types of dune found in deserts.

1. **Obstacle dunes:** These are dunes formed by the interference of an obstacle with the wind flow. Such obstacles may be vegetation or small hills. The dunes may form on either the windward or leeward side of the obstacle. See Figure 1.5.

2. **Barchan dunes:** This type of dune occurs when the wind blows from a single dominant direction and the sand supply is limited. The dune is crescent-shaped, with the tails pointing downwind. A slip face (see Section 1.2.5) occurs on the dune. See Figure 1.6.

3. **Transverse dunes:** These occur under the same wind conditions as for barchan dunes, but when there is an abundant supply of sand. They consist of parallel rows of essentially straight dunes, again with a slip face on the down-wind side. See Figure 1.6. In between these two sorts of dune are **barchanoid ridges**,

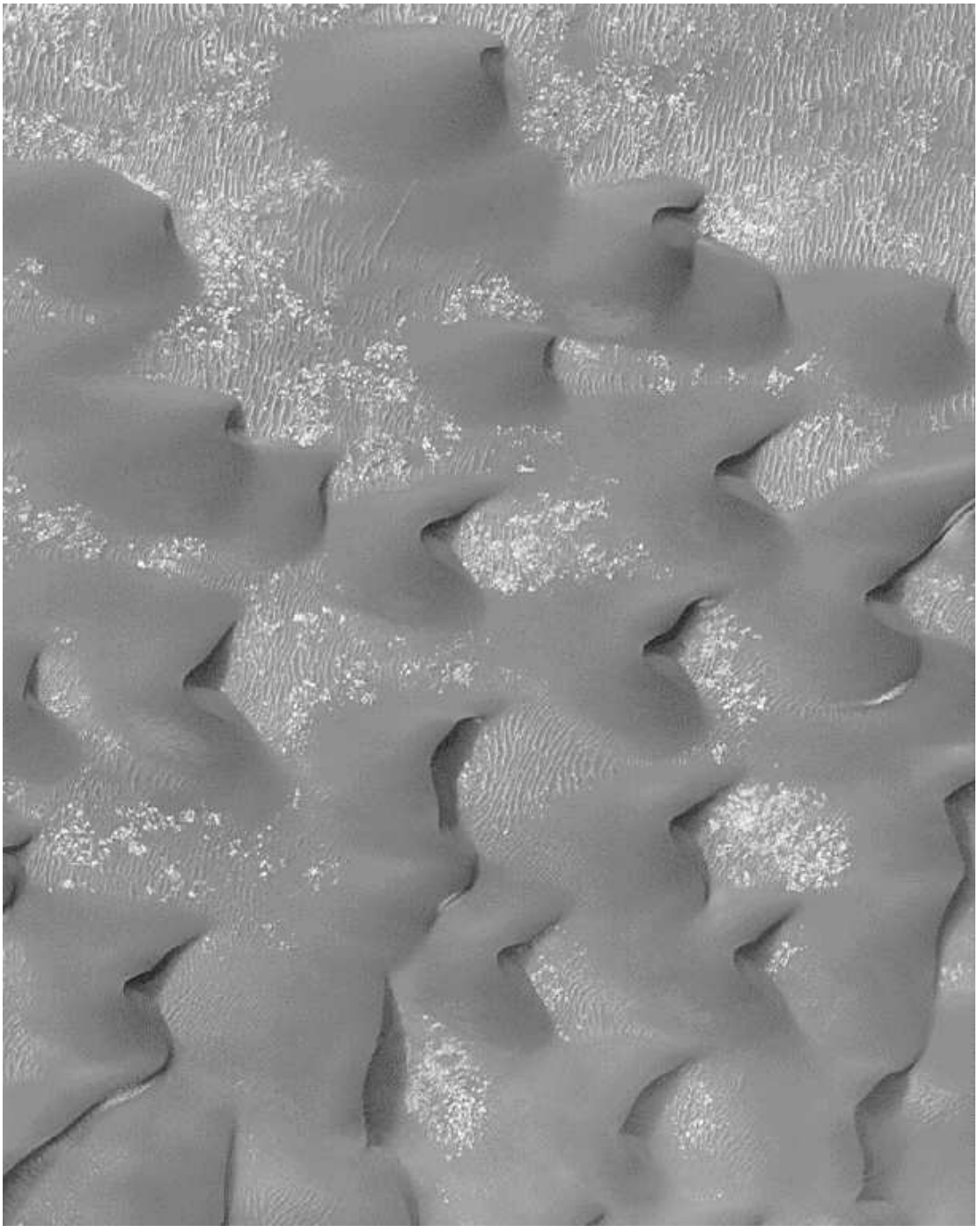


Figure 1.4: Dunes on the surface of Mars. The wind is blowing from left to right; the darker areas are the slip faces and the lighter areas are areas with little sand. Source: NASA/JPL/MSSS [43]

parallel rows of barchan-like ridges. See Figure 1.7. Transverse dunes have an inherent instability [8], therefore barchanoid ridges are more likely to be seen.

4. **Parabolic dunes:** Dunes with a parabolic shape, with the tails pointing upwind, can occur when there is a limited cover of vegetation or some moisture in the sand. They tend to occur in clusters. See Figure 1.7.

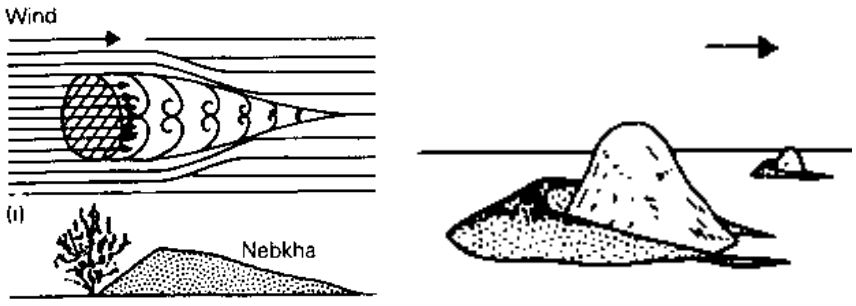


Figure 1.5: Obstacle dunes. Left - leeward side. A dune has formed in the wake formed by the presence of the tree. Right - windward side. Dunes are building up in front of the rocks. Figures and similar ones below taken from [3].

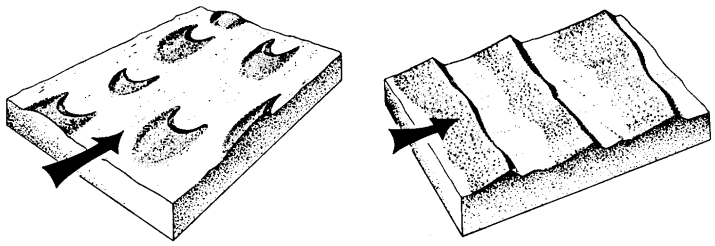


Figure 1.6: Left - barchan dunes. The tails and slip faces can be seen to point downwind. Right - transverse dunes. The ridges are very straight.

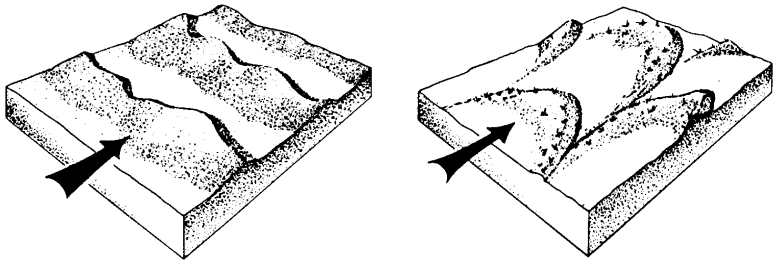


Figure 1.7: Left - barchanoid ridges. The ridges are much less straight than the transverse dunes. Eventually the variation becomes so great that the ridge breaks up, forming barchans. Right - parabolic dunes. These form due to the vegetation that can be seen on them.

5. **Linear dunes:** These are straightish ridges, with slip faces on both sides, that run approximately parallel to the wind. They tend occur in areas where this is a seasonal change in wind direction. They are also known as *seifs*. See Figure 1.8.

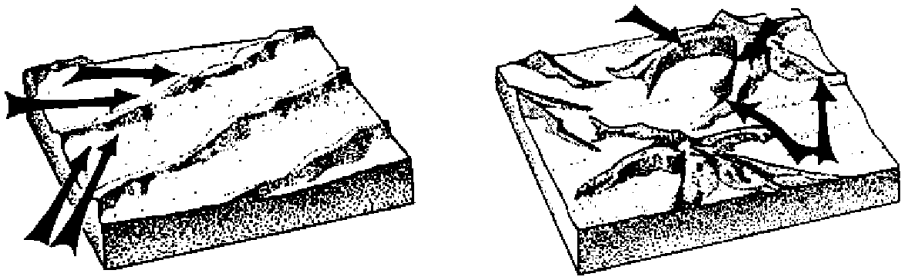


Figure 1.8: Left - linear dunes. The direction of the ridge bisects the two directions of prevailing wind. Right - star dunes. Here the wind is coming from four different directions.

6. **Star dunes:** Wind coming from many different directions causes star dunes, or *rhourds*, which have arms extending radially from a central peak, typically up to 150m high and 1 to 2km across. See Figure 1.8

Different types of sand dune are able to evolve into other types. For example, barchans may become deformed into seifs, and parabolic dunes can be elongated into two longitudinal dunes.

The types of dune listed above can be categorized [67] into three main types:

1. **Migrating dunes:** These advance without changing their shape or size. Examples are transverse and barchan dunes.

2. **Elongating dunes:** These do not advance, but change their shape by getting longer. The best examples are linear dunes.

3. **Accumulating dunes:** These do not advance or change shape, but increase in size by the accumulation of sand. Star dunes fall into this category.

The main factor which determines the category of a dune is the variability in wind direction. Migrating dunes occur when the wind always blows in approximately the same direction. Elongating dunes generally occur when the wind direction is bimodal, and the directions differ by between 70° and 90°. Accumulating dunes are found when the direction is bi- or multi-modal, and the two main modes are approximately in opposite directions.



Figure 1.9: Sand ripples

1.2.2.4 Sand ripples

Sand ripples are features of the sand on a much smaller scale than dunes (see Figure 1.9). They typically have wavelengths of a few centimetres, and form transverse to the direction of flow. As well as being found on desert dunes, they are commonly seen on coastal beaches, in regions intermittently covered by tidal water.

The feature that distinguishes a ripple from a dune, other than size, is the variation of particle size with height in the dune or ripple [8]. On a ripple the coarsest particles are found at the crests, with the finest particles in the troughs. For dunes, the reverse is the case.

1.2.3 The action of wind on sand particles

When wind blows over sand at a low velocity, the sand does not move. The particles of sand on the bed are prevented from moving by other particles, i. e. the particles keep themselves in place. Hence a minimum threshold force is required to act upon them to overcome this and to make them move. This threshold velocity depends on such things as grain size and the slope of the bed, but typically for sand it is around 20 km h^{-1}. When this velocity is exceeded, grains start to roll along the bed, and after a short distance this becomes a bounding and jumping action called *saltation* (Figure 1.10). The saltating grains are the smallest of those particles defined in section 1.2.2, and the force of these particles causes the larger particles to move along by *surface creep* or *reptation*. Smaller grains (those falling outside our definition of sand above) may be carried high up into the air in suspension.

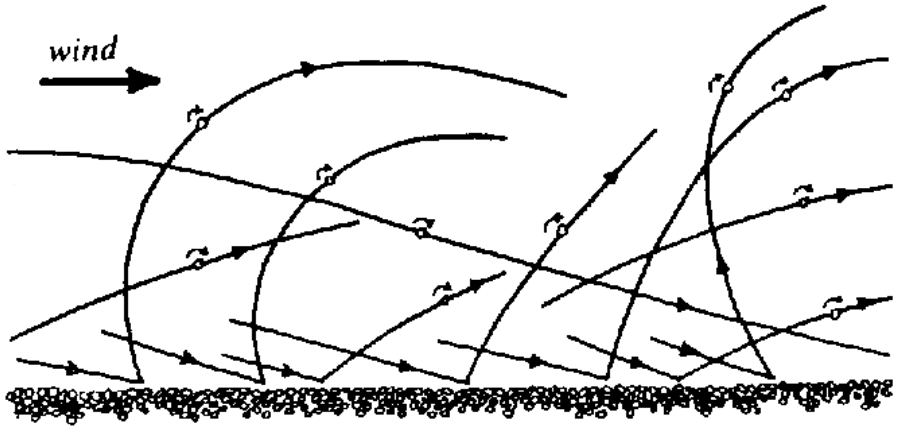


Figure 1.10: Saltating sand particles. The diagram shows particles always bouncing off the surface; in fact sometimes they may not bounce but eject other particles. Figure taken from [2].

As a sand particle leaves the surface it is part of, its upward path is generally a very steep curve. Once it is away from the ground, its path becomes much more shallow on the way down. It has been found experimentally [8] that falling sand particles return to the ground at an angle of between 10° and 16°, depending on grain size, maximum height reached, and the wind speed.

1.2.4 Instability of flat sand bed

In order for dunes and ripples to form, it is necessary that a flat bed of sand is unstable, i. e. that small disturbances to the bed will grow. This instability can be

explained qualitatively in the following way: We may consider (in the notation used in later Chapters) the immobile sand height by s, and the mobile sand transport rate (in units of m^2s^{-1}) by q. At a given point on the dune, at a given point in time, if q is spatially increasing, then some sand must be being eroded and hence the sand height s must be decreasing temporally. Conversely, if q is decreasing in space then s must be increasing in time. Therefore if the gradient of q is negative at the highest point of a disturbance to a flat bed, then that maximum will increase and the disturbance will grow; the flat bed will be unstable.

1.2.5 Avalanching and the slipface

It is an easily-observed fact that avalanches will occur on a pile of sand if the slope is too steep. Experiments have shown [8] that this critical slope is around 30° to 34°.

More precisely, the process is as follows: as sand builds up, the slope increases to a critical slope of around 34°. When this critical slope is attained, an avalanche occurs, and sand moves rapidly down the slope. This gives rise to a slip face with an angle of 30° to 32°, and the process then repeats. The slipface is a very important, and commonly found, feature of a dune. Of the various dune types listed above, all incorporate a slipface in some way.

Due to the discontinuity in slope associated with the brink of a slipface, it is common to find a *recirculating* or *wake region* downstream of the brink. Within this region little sand is eroded due to the slower fluid velocities. Hence the slipface, and its associated wake region, act as a trap for sand; when sand is deposited on or below the slipface, it remains there until the dune has moved over it. This is in contrast to other parts of the dune, where deposited sand is immediately susceptible to erosion. A dune with a slipface is thus much more likely to pervade and not get dispersed by fluid than one without a slipface.

1.2.6 Differences between fluvial and Aeolian sand dynamics

Typical densities of air and water are 1.22 kg m^{-3} and 10^3 kg m^{-3} respectively. The density of the quartz grains that make up the sand is typically 2.65×10^3 kg m^{-3}, so that the sand is only 2.65 times denser than water, but over 2000 times denser than air. This difference in densities has a large effect on the mechanics of sand movement. In the Aeolian case, when grains of sand that have been picked up by the wind (this occurs when the wind speed reaches some threshold value, as described above) return to the sand surface, they strike other grains and either bounce back up themselves or

cause other grains to bounce up. In either case, the grains reach heights of hundreds or even thousands of grain diameters above the sand surface. These grains then return to the surface and again either bounce or eject other grains. Thus the motion of sand grains is maintained without the need for further grains to be entrained by the wind. The presence of saltated grains in the air causes a drag effect which slows the wind speed locally (because of the loss of momentum from the wind to the sand grains), and in general this maintained saltation occurs with wind speed less than the threshold value.

In a fluvial context, because of the much greater density of water, the impact momentum of a descending grain is insufficient to raise surface grains by more than a fraction of a grain diameter. The grains that are raised by the flow of water only rise themselves to a height of a few grain diameters. Hence saltation in water is not maintained by grain impact as it is in air; it occurs only because of the shear stress effect of the flow. Also, due to the higher density of water, the loss of momentum to saltated grains is less pronounced, i. e. the speed of the water flow is not affected as much by the presence of sand grains.

The drag effect of saltated grains on wind speed means that the sand flux q is predominantly affected by the wind speed and the size of the grains. The effect of surface features has a much smaller effect on q. In water, however, the drag effect is much less pronounced, so that the sand flux q depends primarily on the shape of the bed.

1.3 Previous work

There is a large literature on the modelling of dune formation. A qualitative study of both fluvial and aeolian bedforms was undertaken in the first part of the twentieth century by Cornish [18]. He claims that dunes arise from variations in wind speed, with sand being periodically picked up and dropped depending on the rate of motion above it. He also recognises the importance of the downstream wake region in dune formation (see Chapter 5). Cornish defines the term *kumatology* as the "study of the surface waves of the atmosphere, hydrosphere, and lithosphere." He also predicted [17] mathematical studies of dunes:

> Such data [on wind velocity], if combined with my plan of treating sand-dunes as waves, would, I think, render the tactics of blown sand susceptible of mathematical treatment.

An example of the earliest work on fluvial bed dynamics is related by Leliavsky [41]: A French scientist, Sainjon, derived in 1871 an empirical relation between the rate of movement of the bed of the Loire (c) and the velocity of the water on the surface (v). This was $c = A(v^2 - B)$ ms^{-1}, with constant values $A = 1.3 \times 10^{-4}$ m^{-1}s and $B = 0.11$ m^{2}s^{-2}.

The seminal work (for wind-blown dunes at least) is by Brigadier Ralph Bagnold [8], a British military scientist who in the 1930s spent time in the Sahara studying dunes and put forward many (empirical) theories and models for sand dynamics. Some of his theories have subsequently been disproved, for example his hypothesis that the wavelength of sand ripples depends on saltation length, in [4], but many are still in use today.

In the 1920s Exner [21] (see also [41]) derived the equation that now bears his name (2.2) for the evolution of the bed height in terms of the bedload.

In the 1960s many researchers started to work in this area. Benjamin [14] studied the flow over a sinusoidal surface at high Reynolds number for stable laminar shear flow, and found relationships between the bed profile and the shear stress at the boundary.

Kennedy [38] introduced the idea of using a potential-based model for the flow, and also used the artificial phase-lag discussed in Chapter 2. Raudkivi [52] derived an expression for this phase lag based on a simple model for the shear stress. Reynolds [53] followed similar lines of investigation to Kennedy, and extended the theory to three dimensions. A detailed review of the theories at this time is given in the book by Allen [2].

Engelund [20] and Smith [63] took alternative approaches to the potential model used by Kennedy, both assuming a constant eddy viscosity. Engelund used the vorticity transport equation for two-dimensional flow, $\dot{\omega} = \varepsilon \nabla^2 \omega$, where ε is the eddy viscosity and ω is the vorticity. Smith used the Reynolds equations with constant eddy viscosity and considered small perturbations to the uniform steady flow. Both approaches lead to an Orr-Sommerfeld type equation for the disturbances to the flow. These ideas were then combined with the potential flow model of Kennedy and Reynolds by Fowler [23, 24]. This theory is summarised in Chapter 2.

In recent years there has been an increase in interest in the modelling of Aeolian bedforms, being part of the more general area of granular flow, in which there is a large amount of research being carried out. Work in the related area of the flow of air over a small hill has been carried out by Hunt and others [11, 12, 35, 36, 65, 69]. Much of this work is discussed in Chapter 3. The work also overlaps significantly with

the theory of wind-generated waves on water. One of the first numerical simulations of dune evolution was performed by Wipperman and Gross [70], who successfully modelled the evolution of a barchan.

A large amount of work has been done on the formation and evolution of Aeolian dunes, using the theory by Hunt mentioned above, by Herrmann and his co-workers [27, 29, 30, 39, 54–56]. The work is reviewed and extended by Andreotti and others in [6] and [7]. This approach, and particularly that in [39], is discussed in Chapter 4.

Other approaches to dune formation not considered in this work include stochastic modelling (e. g. by Vandewalle and Galam, [68]), and discrete computer simulation, one example being the work by Miao [45]. Experimental work has also been done to verify the theory, for example by Zou et al [72] and by Lancaster et al [40].

While we will not consider coastal dunes in this thesis, mathematical studies have been done of them, for example the paper by Bauer and Davidson-Arnott [10].

Sand ripples have been the subject of much research (see the review by Anderson [4] and recent work by Prigozhin [51] and by Hoyle and others [33, 34]). Approaches used have included both stochastic cellular automata models, considering the motion of individual particles, as well as continuum models of varying complexity. Numerical simulations of each type have successfully produced ripple-like structures. Bagnold [8] hypothesised that the structure of ripples is related to the paths taken by the sand particles, e. g. that the wavelength of the ripple depends on the typical saltation length of a sand particle. Subsequent research (e. g. [4]), however, has concluded that saltation has only an indirect effect on the ripples, and that reptation flux, the flux of sand particles rolling along the surface, is the key influence. In the models for dunes presented in this thesis, the paths of particles between erosion and deposition are not considered, so we would not expect to be able to predict ripples that are not scaled-down dunes, which is in fact the case.

Chapter 2

Simple fluvial models and linear stability analysis

The earliest work on dune formation was done in the fluvial context, as a natural progression from the study of river flow. In this Chapter we present some basic fluvial models and explore their ability to predict the instability of a flat bed.

2.1 Exner equation

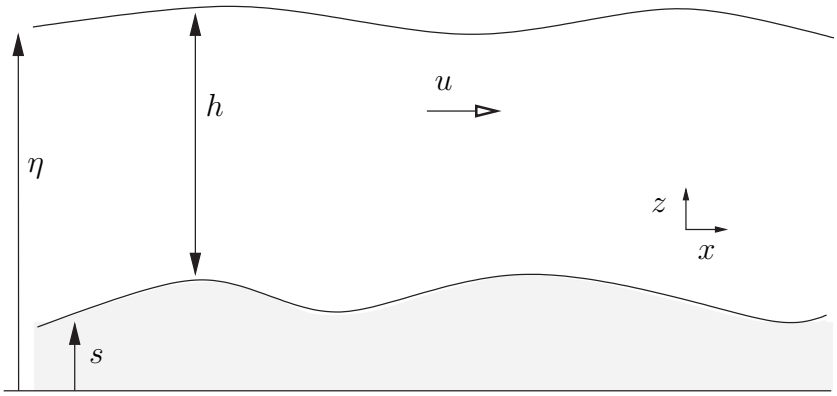


Figure 2.1: Sketch of river geometry. Vertical distances are measured from an arbitrary reference level.

The geometry of a river is shown in Figure 2.1. The free surface of the river is at $z = \eta(x, y, t)$ and the bed (also a free surface) is at $z = s(x, y, t)$. Hence the depth of the river is

$$h = \eta - s. \tag{2.1}$$

The most basic equation describing the interaction between the flow and the erodible substrate beneath it was first obtained by Exner [21] in the 1920s, and today

bears his name. It is based on the principle of conservation of mass for the substrate, and may be written

$$(1-n)\frac{\partial s}{\partial t} + \nabla \cdot \boldsymbol{q} = f_S, \tag{2.2}$$

where s (m) is the height of the bed relative to some reference height, n is the (dimensionless) porosity of the substrate, $\boldsymbol{q}$ ($\mathrm{m^2 s^{-1}}$) is the bedload transport rate, and f_S is a source function corresponding to the exchange of sediment between the fluid and the bed. Also the differential operator ∇ is taken to be two-dimensional, $\nabla = \left(\frac{\partial}{\partial x}, \frac{\partial}{\partial y}\right)$, as it is for the rest of this chapter.

2.2 Sediment transport

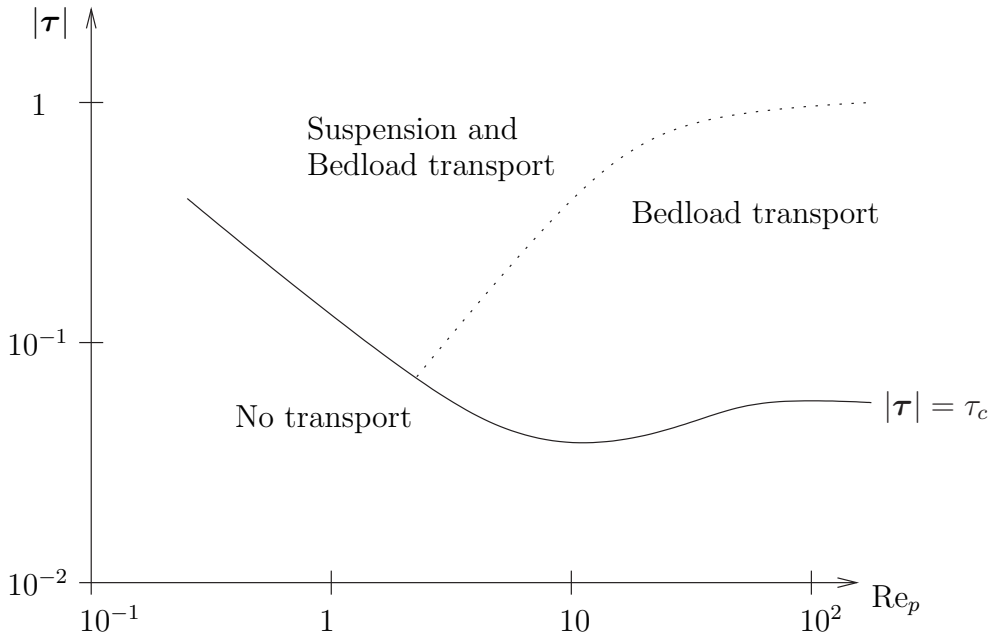


Figure 2.2: Relationship between the size of the basal shear stress $|\boldsymbol{\tau}|$ and the particle Reynolds number Re_p, from [3].

Sediment may be transported in two different ways: as bedload, rolling along the bed, as well as being carried in suspension in the fluid. Allen [3] gives a graphical representation (Figure 2.2) of the relationship between the size of the basal shear stress (here non-dimensionalized by scaling with $\Delta\rho g D_s$, where $\Delta\rho$ (kg $\mathrm{m^{-3}}$) is the density difference between the fluid and the sediment, g (m $\mathrm{s^{-2}}$) is acceleration due to gravity, and D_s (m) is a typical grain diameter) and the particle Reynolds number $\mathrm{Re}_p = u_* D_s/\nu$ ($u_* = \sqrt{|\boldsymbol{\tau}|/\rho_w}$ is the friction velocity and ν is the kinematic viscosity). The solid line indicates the boundary between transport and no transport; hence there

is a critical shear stress τ_c below which no transport occurs. The dotted line indicates the edge of the region where suspended sediment is present. Since Re_p depends on $|\boldsymbol{\tau}|$, we notice that the critical basal shear stress τ_c depends on $|\boldsymbol{\tau}|$ (and hence the curve $|\boldsymbol{\tau}| = \tau_c$ in Figure 2.2 is not straight). However, for $\mathrm{Re}_p \gtrsim 10$, which is the flow regime that we are interested in, this dependence is a weak one and τ_c is approximately constant, typically about 0.05.

2.2.1 Bedload

The bedload transport rate $\boldsymbol{q}$ is generally regarded to be a function of the basal shear stress $\boldsymbol{\tau}$; typically it has been obtained empirically, the most popular example being the *Meyer-Peter & Müller law* [44],

$$\boldsymbol{q} = C_{MPM}\widehat{\boldsymbol{\tau}}(|\boldsymbol{\tau}| - \tau_c)_+^{\frac{3}{2}}, \tag{2.3}$$

where τ_c is the critical value of the shear stress for transport mentioned above, (now dimensional) and $\widehat{\boldsymbol{\tau}}$ is a unit vector in the direction of $\boldsymbol{\tau}$. By introducing the effective shear stress

$$\boldsymbol{\tau}_e = \widehat{\boldsymbol{\tau}}(|\boldsymbol{\tau}| - \tau_c)_+, \tag{2.4}$$

we may write this as

$$\boldsymbol{q} = C_{MPM}\boldsymbol{\tau}_e\sqrt{|\boldsymbol{\tau}_e|}. \tag{2.5}$$

Other forms for the bedload transport rate include those proposed by Lettau and Lettau [42]

$$\boldsymbol{q} = C_L\boldsymbol{\tau}(\sqrt{|\boldsymbol{\tau}|} - \sqrt{\tau_c})_+, \tag{2.6}$$

and by Sørensen [64],

$$\boldsymbol{q} = C_S\widehat{\boldsymbol{\tau}}\sqrt{|\boldsymbol{\tau}|}(\sqrt{|\boldsymbol{\tau}|} + a\sqrt{\tau_c} + b)(\sqrt{|\boldsymbol{\tau}|} - \sqrt{\tau_c})_+, \tag{2.7}$$

for some constants a and b. Each of the three bedload laws (2.5), (2.6), and (2.7) are equivalent for $|\boldsymbol{\tau}| \gg \tau_c$, when

$$\boldsymbol{q} \sim \boldsymbol{\tau}\sqrt{|\boldsymbol{\tau}|}. \tag{2.8}$$

In addition, these laws all assume that there is a limitless supply of sediment available to be eroded; in reality there is typically a finite amount of sediment, with inerodible bedrock beneath it. Once the bedrock is reached, there will be no bedload and the laws above will cease to apply.

Recently Andreotti [5] studied bedload from a theoretical basis, but was able only to obtain $\boldsymbol{q} \sim \boldsymbol{\tau}$.

2.2.2 Suspended sediment

An equation for the conservation of mass of suspended sediment with depth-averaged concentration c may be written

$$\frac{\partial(hc)}{\partial t} + \nabla \cdot (hc\boldsymbol{u}) = -\rho_s f_S, \tag{2.9}$$

where $\boldsymbol{u}$ is the depth-averaged velocity vector $\boldsymbol{u} = (u, v)$, and f_S is as in (2.2), and may be expressed as the difference between erosion and deposition. The erosion rate v_E is generally taken to be a function of the flow velocity $\boldsymbol{u}$, while the deposition rate v_D is also proportional to the concentration c. We therefore write

$$\begin{aligned} f_S &= v_D - v_E \\ &= v_s \left(\frac{1}{\rho_s} c D(\boldsymbol{u}) - E(\boldsymbol{u}) \right) \end{aligned} \tag{2.10}$$

for some choice of functions D and E, and where v_s (m s^{-1}) is the settling velocity,

$$v_s = \frac{\Delta \rho g D_s^2}{18 \rho_w \nu} \tag{2.11}$$

(ν is the kinematic viscosity of water).

Typical choices for D and E include [23]

$$D = \frac{R}{1 - e^{-R}}, \qquad R = \frac{v_s}{\varepsilon_T |\boldsymbol{u}|}, \tag{2.12}$$

and the van Rijn relationship

$$E \propto |\boldsymbol{q}| \mathrm{Re}_p^{1/5}, \tag{2.13}$$

where $\varepsilon_T = 4\kappa\sqrt{f}/15$, $\kappa \approx 0.4$ is the von Kármán constant, and $f \approx 0.05$ is a friction factor.

2.3 St. Venant equations

We currently have five equations (2.1), (2.2), (2.5), (2.9), and (2.10) for unknowns h, η, s, $\boldsymbol{q}$, $\boldsymbol{\tau}$, c, f, and $\boldsymbol{u}$. We therefore require three further equations to describe the motion of the fluid. These are the St. Venant equations of river flow, which may be derived in the following way. The Navier-Stokes equations for this system in the case of two-dimensional flow are

$$u_x + w_z = 0, \tag{2.14}$$

$$\rho_w (u_t + u u_x + w u_z) = -p_x + \rho_w g S + \mu (u_{xx} + u_{zz}), \tag{2.15}$$

$$\rho_w (w_t + u w_x + w w_z) = -p_z + \rho_w g \sqrt{1 - S^2} + \mu (w_{xx} + w_{zz}), \tag{2.16}$$

where S is the mean slope of the bed, and μ is the viscosity.

The boundary conditions are the kinematic conditions at the two free surfaces,

$$\frac{\mathrm{d}}{\mathrm{d}t}(z-\eta)=0, \quad z=\eta, \tag{2.17}$$

and

$$\frac{\mathrm{d}}{\mathrm{d}t}(z-s)=0, \quad z=s, \tag{2.18}$$

which lead to

$$w=\eta_t+u\eta_x, \quad z=\eta, \tag{2.19}$$

and

$$w=s_t+us_x, \quad z=s, \tag{2.20}$$

along with conditions of no stress and constant pressure at the upper free surface,

$$u_z=0 \quad \text{and} \quad p=\text{constant}, \quad z=\eta. \tag{2.21}$$

Integrating in the z-direction transforms (2.14) into

$$\int_s^\eta u_x \,\mathrm{d}z+[w]_s^\eta=0, \tag{2.22}$$

and then using the boundary conditions this becomes

$$h_t+(h\overline{u})_x=0, \tag{2.23}$$

where

$$\overline{u}:=\frac{1}{h}\int_s^\eta u \,\mathrm{d}z \tag{2.24}$$

is the depth-averaged velocity.

We may similarly integrate (2.15), which quickly leads to

$$(h\overline{u})_t+\frac{\partial}{\partial x}(h\overline{u^2})=gh(S-\eta_x)-\frac{\tau}{\rho_w}. \tag{2.25}$$

Here we have assumed a hydrostatic pressure profile

$$p=\rho_w g(\eta-z), \tag{2.26}$$

which may be obtained from (2.16) and (2.21) when $\boldsymbol{u}\equiv 0$ and S is small. Then, using (2.23), (2.25) may be simplified into

$$\overline{u}_t+\overline{u}\overline{u}_x=g(S-\eta_x)-\frac{\tau}{\rho_w h}, \tag{2.27}$$

provided that we make the assumption that

$$\frac{1}{h}\int_s^\eta u^2\,\mathrm{d}z = \left(\frac{1}{h}\int_s^\eta u\,\mathrm{d}z\right)^2, \tag{2.28}$$

i. e. that $\overline{u}^2 = \overline{u^2}$. We must also specify the shear stress τ; we take this for now to be the classical law for the turbulent shear stress due to Chézy

$$\tau = f\rho_w\overline{u}^2 \tag{2.29}$$

for a friction factor f (as in (2.13)).

2.4 Non-dimensionalization

We now have, in two dimensions, the system of equations

$$\begin{aligned}
h &= \eta - s, && (2.30)\\
(1-n)s_t + q_x &= v_s\left(\frac{1}{\rho_s}cD(u) - E(u)\right), && (2.31)\\
(hc)_t + (hcu)_x &= -\rho_s v_s\left(\frac{1}{\rho_s}cD(u) - E(u)\right), && (2.32)\\
h_t + (hu)_x &= 0, && (2.33)\\
u_t + uu_x &= gS - \frac{\tau}{\rho_w h} - g\eta_x, && (2.34)\\
q &= C_{MPM}\tau_e^{\frac{3}{2}}, && (2.35)\\
\tau_e &= (\tau - \tau_c)_+, && (2.36)\\
\tau &= f\rho_w u^2, && (2.37)
\end{aligned}$$

which we now wish to non-dimensionalize. Here we have replaced $\overline{u}$ with u for notational simplicity. We scale the system with a vertical length scale h_0 for h, s, and η, a horizontal length scale x_0 for x, a velocity scale u_0 for u, a time scale t_0, and a concentration scale c_0. We also require a bedload scale q_0, a stress scale τ_0, an erosional scale E_0, and a depositional scale D_0, all of which we take to be the sizes of the functions that define them (e. g. $\tau_0 = f\rho_w u_0^2$). On nondimensionalizing the effective shear stress τ_e we assume that $\tau_c \approx 0$ so that $\tau \approx \tau_e$. We choose the remaining scales in the following way: we first assume a constant incoming flux of fluid Q_0 so that

$$Q_0 = h_0 u_0. \tag{2.38}$$

Next we balance terms on the left of the Exner equation by taking

$$(1-n)\frac{h_0}{t_0} = \frac{q_0}{x_0}, \tag{2.39}$$

and we balance gravity and friction terms in the momentum equation by taking

$$gS = \frac{\tau_0}{\rho_w h_0}. \tag{2.40}$$

We assume that erosion and deposition are of comparable importance, so that

$$E_0 = \frac{c_0 D_0}{\rho_s}, \tag{2.41}$$

and finally we balance terms in the suspended sediment equation by choosing

$$\frac{h_0 c_0 u_0}{x_0} = \rho_s v_s E_0. \tag{2.42}$$

The non-dimensionalized system is therefore

$$\begin{aligned}
h &= \eta - s, && (2.43)\\
s_t + q_x &= \gamma(cD - E), && (2.44)\\
h\left(\varepsilon c_t + u c_x\right) &= -(cD - E), && (2.45)\\
\varepsilon h_t + (hu)_x &= 0, && (2.46)\\
\mathrm{Fr}^2\left(\varepsilon u_t + u u_x\right) &= \delta\left(S - \frac{\tau}{h}\right) - \eta_x, && (2.47)\\
q &= \tau^{\frac{3}{2}}, && (2.48)\\
\tau &= u^2. && (2.49)
\end{aligned}$$

We have four parameters δ, Fr, ε, and γ, which are given by

$$\begin{aligned}
\delta &= \frac{x_0 S}{h_0}, && (2.50)\\
\mathrm{Fr} &= \frac{u_0}{\sqrt{g h_0}}, && (2.51)\\
\varepsilon &= \frac{q_0}{(1-n)Q_0}, && (2.52)\\
\gamma &= \frac{Q_0 c_0}{\rho_s q_0 E_0}. && (2.53)
\end{aligned}$$

Hence δ is related to the bed slope, which typically is small, Fr is the standard Froude number, typically $O(1)$, ε reflects the ratio of bedload flux to fluid flux, typically small, and γ reflects the ratio of suspended sediment flux to bedload flux, which may be large, small, or $O(1)$. We now take the limit $\varepsilon, \delta \to 0$, which in particular turns (2.46) into

$$(hu)_x = 0. \tag{2.54}$$

and hence integrating this leads to

$$\begin{aligned} h &= \eta - s, && (2.55)\\ s_t + q_x &= \gamma(cD - E), && (2.56)\\ c_x &= -(cD - E), && (2.57)\\ hu &= 1, && (2.58)\\ \frac{\mathrm{Fr}^2 u^2}{2} + \eta &= \frac{\mathrm{Fr}^2}{2} + 1, && (2.59)\\ q &= u^3. && (2.60) \end{aligned}$$

We may use the first, fourth, fifth, and sixth of these equations to write u, q, η, and h, and therefore E and D, as functions of s, since

$$s = s(q) = \frac{1}{2}\mathrm{Fr}^2(1 - q^{2/3}) + 1 - \frac{1}{q^{1/3}}, \tag{2.61}$$

so that we are left with two equations for s and c,

$$s_t + q'(s)s_x = \gamma(cd(s) - e(s)) = -\gamma c_x, \tag{2.62}$$

where $d(s) = D(u(s))$ and $e(s) = E(u(s))$. When γ is small (bedload dominates), we may take the limit $\gamma \to 0$ to obtain

$$s_t + q'(s)s_x = 0 \tag{2.63}$$

which is a hyperbolic first order equation for s, the properties of which will be explored below. When γ is large (suspended sediment dominates), we may take the limit $\gamma \to \infty$ to obtain

$$c_x + cd(s) = e(s), \tag{2.64}$$

which given s may be solved for c, but we have lost information about s. Instead we consider a shorter time-scale, with $T = \gamma t$, so that we obtain

$$s_T = cd(s) - e(s) = -c_x. \tag{2.65}$$

Again we will consider properties of this system below. We may simplify the system by eliminating c; using

$$c = \frac{s_T + e}{d}, \tag{2.66}$$

we may write

$$\frac{\partial s}{\partial T} + \frac{\partial}{\partial x}\left(\frac{\frac{\partial s}{\partial T} + e}{d}\right) = 0 \tag{2.67}$$

which is a hyperbolic second-order pde for s.

2.5 Linear stability analysis

We note that solutions to (2.63), which applies when $\gamma \ll 1$, have wave speed $q'(s) = 1/s'(q)$, so that if $s'(q) > 0$ then bed forms will propagate downstream. In addition, solutions will evolve to form downstream-facing shocks if $q''(s) = -s''(q)/s'(q)^2$ is positive anywhere, and upstream-facing shocks if it is negative.

Near the basic state $u = 1$,

$$s'(q) \approx \frac{1 - \mathrm{Fr}^2}{3}, \tag{2.68}$$

and

$$q''(s) \approx \frac{4 - 9\mathrm{Fr}^2}{(1 - \mathrm{Fr}^2)^2}. \tag{2.69}$$

Hence for $0 < \mathrm{Fr} < 2/3$ (tranquil flow), bedforms move downstream and form downstream-facing shocks; for $2/3 < \mathrm{Fr} < 1$, downstream-moving bedforms form upstream-facing shocks; finally for $\mathrm{Fr} > 1$ (rapid flow), bedforms propagate upstream and form upstream-facing shocks. These three situations correspond reasonably well with the qualitative descriptions of dunes and anti-dunes in Chapter 1; here $\mathrm{Fr} < 2/3$ would be dunes and $\mathrm{Fr} > 2/3$ would be anti-dunes.

We have described how solutions to (2.63) evolve, but we have not yet explained how such bedforms may form in the first place. We now explore the stability of the uniform steady state $s = 0$ for both the bedload equation (2.63) and the suspended sediment equation (2.65), and we hope to be able to find instabilities for each that will explain the formation of bedforms.

2.5.1 Bedload equation

Assuming s is small, we may linearize (2.63) to obtain

$$s_t + q'(0)s_x = 0. \tag{2.70}$$

Substituting a solution $s = s_0 e^{\sigma t + ikx}$ then leads to

$$\sigma + ikq'(0) = 0, \tag{2.71}$$

so that the growth rate is $\mathrm{Re}\,\sigma = 0$. Hence a flat bed is neutrally stable; there is no instability explained by this model.

This lack of an instability is due to the fact that the shear stress τ is a function of s. Hence the stress is the same both up- and downstream of a disturbance, so that no net deposition occurs. With a uni-directional flow over a disturbance, one would

expect the stress to be greater on the upstream side, which causes a net deposition on the downstream side, therefore enabling the disturbance to grow.

Kennedy [38] introduced the idea of the stress leading the bed, so that instead of taking $\tau = \tau(s(x,t))$, we instead take

$$\tau = \tau(s(x+\delta, t)), \tag{2.72}$$

for some lead distance δ (which is of course unrelated to the δ of (2.50)). This will have the effect of making the stress greater on the upstream side of a disturbance than on the downstream side, and so we expect that this will produce an instability.

Two physical explanations for this lead are presented by Reynolds [53]. The lead is indeed present [14], although this simplistic way of modelling it is rather artificial.

The linearized equation (2.70) becomes

$$s_t(x,t) + q'(0)s_x(x+\delta, t) = 0 \tag{2.73}$$

when this lead is introduced, so that

$$\sigma + ikq'(0)e^{ik\delta} = 0, \tag{2.74}$$

and the growth rate is now

$$\operatorname{Re}\sigma = kq'(0)\sin k\delta. \tag{2.75}$$

We have from (2.61)

$$q'(0) = \frac{1}{s'(1)} = \frac{3}{1-\mathrm{Fr}^2}. \tag{2.76}$$

Hence for tranquil flow, $\mathrm{Fr} < 1$, we require $\sin k\delta < 0$ for an instability, and for rapid flow we require $\sin k\delta > 0$ for an instability. Therefore for any $\delta \neq 0$, we will obtain an instability for some non-empty set of wavenumbers k. For large k, $\operatorname{Re}\sigma \sim \pm k$, so that arbitrarily short wavelength disturbances are able to grow at an arbitrarily large rate; this suggests that the model is ill-posed, so we must find a more sophisticated method of modelling the shear stress.

2.5.2 Suspended sediment equation

A steady state of equation (2.65) is $s \equiv 0$, $c \equiv 1$, since $d(0) = D(1) = 1$ and $e(0) = E(1) = 1$. We now consider disturbances to this steady state, and write $s = S$, $c = 1 + C$, where we assume $S, C \ll 1$. Equation (2.65) thus becomes

$$S_t = C + Sd'(0) - Se'(0) = -C_x \tag{2.77}$$

upon linearization, and then seeking wave solutions $S = S^* e^{\sigma t + ikx}$, $C = C^* S$ leads to

$$\sigma = C^* + d'(0) - e'(0) = -ikC^*. \tag{2.78}$$

Eliminating C^* then leads to an expression for the growth rate

$$\mathrm{Re}\,\sigma = -\frac{k^2(e'(0) - d'(0))}{1 + k^2} \tag{2.79}$$

which is positive (indicating instability) provided

$$e'(0) - d'(0) < 0, \tag{2.80}$$

or equivalently

$$u'(0)\,(E'(1) - D'(1)) < 0. \tag{2.81}$$

Since

$$u'(0) = \frac{1}{s'(1)} = \frac{1}{1 - \mathrm{Fr}^2} \tag{2.82}$$

and we assume $E'(u) > 0 > D'(u)$ in general, we therefore have an instability for $\mathrm{Fr} > 1$ (rapid flow). We may also find the wave speed; this is

$$-\frac{\mathrm{Im}\,\sigma}{k} = \frac{e'(0) - d'(0)}{1 + k^2}, \tag{2.83}$$

so that these unstable disturbances propagate upstream, and stable disturbances propagate downstream as they decay. Again, however, we have $\mathrm{Re}\,\sigma \to d'(0) - e'(0) > 0$ as $k \to \infty$, so that any arbitrarily small disturbance will grow.

2.6 Constant eddy viscosity model for shear stress

We have so far predicted an instability in the suspended sediment equation (2.65) which gives rise to upstream-moving anti-dunes; we have also found an instability in the bedload model which can give rise to dunes or anti-dunes, but this was based on a rather artificial model for the shear stress which also had an undesirable short-wavelength instability. We now seek a modification to the bedload model which we hope will predict an instability.

We consider the turbulent flow of the river and assume that we may model the Reynolds stresses with a constant kinematic eddy viscosity ν_T (see Appendix A). The Reynolds equations (for a one-dimensional river) are therefore

$$u_t + uu_x + wu_z = -\frac{1}{\rho_w}\frac{\partial p}{\partial x} + \nu_T \nabla^2 u + gS, \tag{2.84}$$

$$w_t + uw_x + ww_z = -\frac{1}{\rho_w}\frac{\partial p}{\partial z} + \nu_T \nabla^2 w - g\sqrt{1 - S^2}, \tag{2.85}$$

$$u_x + w_z = 0. \tag{2.86}$$

In the uniform steady state, where $\frac{\partial}{\partial t} = \frac{\partial}{\partial x} = w = 0$ and $\eta = h_0$, we see that

$$p = \rho_w g\sqrt{1 - S^2}(h_0 - z), \tag{2.87}$$

and

$$u_{zz} = \frac{gS}{\nu_T}, \tag{2.88}$$

so that

$$u = \frac{gSz}{2\nu_T}\left(2h_0 - z\right). \tag{2.89}$$

Taking the depth average of u therefore shows that if we assume a constant eddy viscosity for all flows (not just the steady state), it must be given by

$$\nu_T = \frac{gSh_0^2}{3\overline{u}}, \tag{2.90}$$

where

$$\overline{u} = \frac{1}{h_0}\int_0^{h_0} u\,\mathrm{d}z. \tag{2.91}$$

This is consistent with the previous model for the basal stress $\tau = \rho_w \nu_T u_z|_{z=0}$ in the uniform state provided

$$\nu_T = \frac{f\overline{u}h_0}{3}; \tag{2.92}$$

hence we take the previous two equations to specify the vertical length scale h_0 for our subsequent non-dimensionalization in terms of $\overline{u}$; this relationship turns out to be

$$gSh_0 = f\overline{u}^2 \tag{2.93}$$

which is identical to what we have used before. We also take $u_0 = \overline{u}$, so that the non-dimensionalized equations are

$$u_t + uu_x + wu_z = -p_x + \frac{1}{\mathrm{Re}_T}\nabla^2 u + \frac{S}{\mathrm{Fr}^2}, \tag{2.94}$$

$$w_t + uw_x + ww_z = -p_z + \frac{1}{\mathrm{Re}_T}\nabla^2 w - \frac{\sqrt{1 - S^2}}{\mathrm{Fr}^2}, \tag{2.95}$$

$$u_x + w_z = 0, \tag{2.96}$$

where the Froude number Fr has its usual definition, and the turbulent Reynolds number Re_T is defined by

$$\mathrm{Re}_T = \frac{u_0 h_0}{\nu_T}. \tag{2.97}$$

After cross-differentiating to eliminate p, we obtain

$$u_{zt} + uu_{xz} + wu_{zz} - w_{xt} - uw_{xx} - ww_{xz} = \frac{1}{\mathrm{Re}_T}\nabla^2\left(u_z - w_x\right). \tag{2.98}$$

The velocity profile in the uniform steady state (2.89) becomes

$$u = U(z) = \frac{3z}{2}(2 - z)\,. \tag{2.99}$$

We now consider the effect of disturbances to the bed; these will perturb the flow, and will be propagated along the bed by the flow. We assume that the timescale over which such disturbances move is much longer than the timescale for the flow (as in (2.47) where the time derivative was multiplied by a small coefficient ε). We may therefore consider flow over an immobile bed, and look for steady solutions to (2.98). We write

$$(u, w) = (U(z) + \psi_z, -\psi_x), \tag{2.100}$$

where $\psi \ll 1$, and linearize (2.98) to obtain

$$U(z)\nabla^2\psi_x - U''(z)\psi_x = \frac{1}{\mathrm{Re}_T}\nabla^4\psi, \tag{2.101}$$

which is the Orr-Sommerfeld equation for ψ.

We now describe the boundary conditions for ψ. At $z = \eta$, we have a zero pressure condition, which may be linearised to obtain

$$p|_{z=1} \approx (1 - \eta)p_z|_{z=1}\,, \tag{2.102}$$

and since

$$p_z|_{z=1} = -\frac{1}{\mathrm{Fr}^2} + O(\psi), \tag{2.103}$$

we may write this as

$$\eta \approx 1 + \mathrm{Fr}^2 p\big|_{z=1}\,. \tag{2.104}$$

We are interested in placid flow (since we have already used suspended sediment to predict an instability in rapid flow), so we may approximate this further by taking $\mathrm{Fr} \ll 1$, and hence $\eta \approx 1$. Now $z = 1$ is a streamline, so that $\psi =$ constant, and we may take this constant to be zero. A second condition at the upper surface is one of no stress, i. e.

$$0 = u_z|_{z=\eta} = U'(1) + \psi_{zz}|_{z=1}\,, \tag{2.105}$$

but $U'(1) = 3(1 - z)|_{z=1} = 0$, so that the condition is $\psi_{zz} = 0$ at $z = 1$.

At the lower surface, $z = s$, we have a no-slip condition

$$0 = u|_{z=s} = u|_{z=0} + su_z|_{z=0} + \cdots \tag{2.106}$$

which is

$$\psi_z|_{z=0} + sU'(0) \approx 0 \tag{2.107}$$

to highest order. Finally we have the condition that the volume flux with the perturbed bed must be equal to the volume flux in the uniform case, i. e. that

$$\int_0^1 U(z)\,\mathrm{d}z = \int_s^\eta U(z) + \psi_z\,\mathrm{d}z. \tag{2.108}$$

Using $\eta = 1$ and $\psi|_{z=1} = 0$, this may be written

$$\int_0^s U\,\mathrm{d}z + \psi|_{z=s} = 0, \tag{2.109}$$

which when linearized becomes

$$\psi|_{z=0} = 0 \tag{2.110}$$

to highest order, since $U(0) = 0$.

We therefore have a fourth-order pde (2.101) for ψ with boundary conditions

$$\psi|_{z=0} = \psi|_{z=1} = \psi_{zz}|_{z=1} = 0, \quad \psi_z|_{z=0} = -sU'(0). \tag{2.111}$$

If we are able to find a solution ψ to this equation, the (dimensional) basal shear stress τ will be given by

$$\begin{aligned} \tau &= \mu_T \left.\frac{\partial u}{\partial z}\right|_{z=s} \\ &= \frac{\rho_w \nu_T u_0}{h_0}\left(U'(s) + \psi_{zz}|_{z=s}\right). \end{aligned} \tag{2.112}$$

The eddy viscosity is

$$\nu_T = \frac{f u_0 h_0}{3}, \tag{2.113}$$

and we know that

$$\overline{u}h = \text{ constant } = u_0 h_0. \tag{2.114}$$

Hence

$$\tau = \frac{\rho_w f \overline{u}^2}{3}\left(U'(0) + sU''(0) + \psi_{zz}|_{z=0} + \cdots\right). \tag{2.115}$$

While we are unable to solve (2.101) with (2.111) exactly, we may exploit the fact that Re_T is large (since $\mathrm{Re}_T = 3/f$ and we have previously taken f to be in the range 0.1 to 0.01) and perform an asymptotic analysis to obtain an analytic approximation for $\psi_{zz}|_{z=0}$.

We first eliminate the dependence on x by taking the Fourier transform of (2.101); here we denote the Fourier transform of ψ to be

$$\widehat{\psi}(z,k) = \int_{-\infty}^{\infty} \psi(x,z) e^{-ikx}\,\mathrm{d}x. \tag{2.116}$$

We also rescale with

$$\widehat{\psi} = -\widehat{s}U'(0)\widehat{\Psi} \tag{2.117}$$

in order to simplify the boundary conditions. (2.101) therefore becomes the canonical problem

$$ik\left[U\left(-k^2\widehat{\Psi}+\widehat{\Psi}''\right)-U''\widehat{\Psi}\right] = \frac{1}{\mathrm{Re}_T}\left(k^4\widehat{\Psi}-2k^2\widehat{\Psi}''+\widehat{\Psi}^{(4)}\right) \tag{2.118}$$

with boundary conditions

$$\widehat{\Psi}(0,k) = \widehat{\Psi}(1,k) = \widehat{\Psi}''(1,k) = 0, \quad \widehat{\Psi}'(0,k) = 1. \tag{2.119}$$

In order to find τ, we require $\psi_{zz}|_{z=0}$; this may be obtained from $\widehat{\Psi}$ using

$$\begin{aligned}
\psi_{zz}|_{z=0} &= -\frac{U'(0)}{2\pi}\int_{-\infty}^{\infty}\widehat{s}\widehat{\Psi}''(0,k)e^{ikx}\,\mathrm{d}k & (2.120)\\
&= -\frac{U'(0)}{2\pi}\int_{-\infty}^{\infty}\widehat{s'}\frac{\widehat{\Psi}''(0,k)}{ik}e^{ikx}\,\mathrm{d}k & (2.121)\\
&= \int_{-\infty}^{\infty}s'(\xi)K(x-\xi)\,\mathrm{d}\xi, & (2.122)
\end{aligned}$$

using $\widehat{s'} = ik\widehat{s}$ and the convolution theorem, where the convolution kernel $K(x)$ satisfies

$$\widehat{K}(k) = -\frac{U'(0)}{2\pi}\frac{\widehat{\Psi''(0,k)}}{ik}. \tag{2.123}$$

Hence we may write

$$\tau = f\rho_w u_0^2\left(1-s+\int_{-\infty}^{\infty}K(x-\xi)s'(\xi)\,\mathrm{d}\xi\right). \tag{2.124}$$

2.6.1 Asymptotic analysis of the Orr-Sommerfeld equation

We perform an asymptotic analysis of the ODE (2.118), with boundary conditions (2.119), for a fixed k, in the limit $\mathrm{Re}_T \to \infty$. This is done in detail in the appendix of [19]; we reproduce the key details here for later reference.

The outer solution may be expanded in powers of Re_T^{-1},

$$\widehat{\Psi} \sim \mathrm{Re}_T^{-m}\left(\Psi_0 + \mathrm{Re}_T^{-1}\Psi_1 + O\left(\mathrm{Re}_T^{-2}\right)\right), \tag{2.125}$$

where m will be chosen to ensure $\Psi_0 = O(1)$.

The equation for Ψ_0 is then

$$U\left(\Psi_0''-k^2\Psi_0\right)-U''\Psi_0 = 0, \tag{2.126}$$

the inviscid Rayleigh equation. We note that $\Psi_0(1) = 0$ if and only if $\Psi_0''(1) = 0$, and since this is a singular perturbation problem we do not expect to be able to satisfy the boundary conditions at $z = 0$. Hence we will have one unknown quantity in Ψ which will be obtained by matching with the inner solution.

Solutions to (2.126) may be written in terms of Frobenius series; two linearly independent solutions are

$$\psi_1(z) = \sum_{n=0}^{\infty} a_n z^n \tag{2.127}$$

and

$$\psi_2(z) = \sum_{n=0}^{\infty} b_n z^n - \psi_1(z) \log z, \tag{2.128}$$

where the coefficients a_n, b_n are given by the recurrence relations

$$a_n = \frac{1}{n(n-1)} \left(\frac{1}{2} n(n-3) a_{n-1} + k^2 a_{n-2} - \frac{1}{2} k^2 a_{n-3} \right), \tag{2.129}$$

$$\begin{aligned} b_n = \frac{1}{n(n-1)} \Bigg(& \frac{1}{2} n(n-3) b_{n-1} + k^2 b_{n-2} - \frac{1}{2} k^2 b_{n-3} \\ & + \frac{1}{2}(2n-3) a_{n-1} - (2n-1) a_n \Bigg), \end{aligned} \tag{2.130}$$

for $n \geqslant 3$, with

$$a_0 = 0, \quad a_1 = 1, \quad a_2 = -\frac{1}{2}, \quad b_0 = 1, \quad b_1 = 0, \quad b_2 = \frac{k^2}{2} - 1. \tag{2.131}$$

We may take a combination of these two series in order to satisfy the boundary condition $\Psi_0(1) = 0$, e. g.

$$\Psi_0(z) = \beta \left(\psi_2(z) - \frac{\psi_2(1)}{\psi_1(1)} \psi_1(z) \right); \tag{2.132}$$

in particular we note that $\psi_1(1) = \sum_{n=0}^{\infty} a_n$ and $\psi_2(1) = \sum_{n=0}^{\infty} b_n$.

As $z \to 0$, $\Psi \sim \beta \mathrm{Re}_T^{-m} \neq 0$; we therefore introduce a boundary layer of thickness ε (to be chosen), and rescale with

$$z = \varepsilon Z. \tag{2.133}$$

Equation (2.118) then becomes

$$ik \left[U(\varepsilon Z) \left(-k^2 \widehat{\Psi} + \frac{1}{\varepsilon^2} \widehat{\Psi}'' \right) - U''(\varepsilon Z) \widehat{\Psi} \right] = \frac{1}{\mathrm{Re}_T} \left(k^4 \widehat{\Psi} - \frac{2k^2}{\varepsilon^2} \widehat{\Psi}'' + \frac{1}{\varepsilon^4} \widehat{\Psi}^{(4)} \right), \tag{2.134}$$

and so in order to retain the two terms with the highest derivatives, we choose ε to satisfy

$$\frac{ikU'(0)}{\varepsilon} = \frac{1}{\varepsilon^4 \mathrm{Re}_T}, \tag{2.135}$$

or equivalently

$$\varepsilon = (ikU'(0)\mathrm{Re}_T)^{-\frac{1}{3}}. \tag{2.136}$$

The inner equation thus becomes

$$\widehat{\Psi}^{(4)} - Z\widehat{\Psi}'' + \varepsilon\left(\frac{Z^2}{2}\widehat{\Psi}'' - \widehat{\Psi}\right) = O(\varepsilon^2), \tag{2.137}$$

so that the first two terms of the inner expansion

$$\widehat{\Psi} \sim \mathrm{Re}_T^{-m}\left(\Phi_0 + \varepsilon\Phi_1 + \cdots\right) \tag{2.138}$$

satisfy

$$\Phi_0^{(4)} - Z\Phi_0'' = 0, \tag{2.139}$$

$$\Phi_1^{(4)} - Z\Phi_1'' = \Phi_0 - \frac{Z^2}{2}\Phi_0''. \tag{2.140}$$

These are fourth order ODEs; we have two boundary conditions, and hence we will require two matching conditions from the outer solution.

Solutions to (2.139) may be written [19] in terms of generalized Airy functions defined as

$$A_p^{(k)}(Z) = \frac{1}{2\pi i}\int_{L_k} t^{-p}e^{Zt-\frac{1}{3}t^3}\,\mathrm{d}t, \tag{2.141}$$

where the contours L_k are as shown in Figure 2.3. In particular, since by differentiation

$$\frac{\mathrm{d}}{\mathrm{d}Z}A_p^{(k)}(Z) = A_{p-1}^{(k)}(Z), \tag{2.142}$$

and by integration by parts

$$ZA_p^{(k)}(Z) = A_{p-2}^{(k)}(Z) - pA_{p+1}^{(k)}(Z), \tag{2.143}$$

we see that

$$\frac{\mathrm{d}^4}{\mathrm{d}Z^4}A_p^{(k)}(Z) - Z\frac{\mathrm{d}^2}{\mathrm{d}Z^2}A_p^{(k)}(Z) = (p-2)A_{p-1}^{(k)}(Z), \tag{2.144}$$

so that choosing $p = 2$ implies that $A_2^{(k)}(Z)$ solves (2.139) for $k = 0, 1, 2, 3$. These four solutions are not however independent; by deformation of the contours in Figure 2.3 it is clear that

$$\sum_{k=0}^{3} A_p^{(k)}(Z) = 0. \tag{2.145}$$

We note also that by Cauchy's integral formula [50], $A_2^{(0)} = Z$. We therefore have three linearly independent solutions to (2.139), e. g. $A_2^{(1)}(Z)$, $A_2^{(3)}(Z)$, and $A_2^{(0)}(Z) = Z$; a

fourth may be found by noticing that a constant function is also a solution. We may therefore write

$$\Phi_0 = \alpha_0 + \alpha_1 Z + \alpha_2 A_2^{(1)}(Z) + \alpha_3 A_2^{(3)}(Z). \tag{2.146}$$

In order to match between the outer and inner solutions, we must have

$$\lim_{Z\to 0} \Psi_0 = \lim_{\varepsilon Z\to\infty} \Phi_0, \tag{2.147}$$

i. e.

$$\beta \sim \alpha_0 + \alpha_1 Z + \alpha_2 A_2^{(1)}(Z) + \alpha_3 A_2^{(3)}(Z) \tag{2.148}$$

as $Z \to \infty e^{\pi i/6}$. The asymptotic behaviour of the functions $A_p^{(k)}(Z)$ are given in [19], in particular we see that $A_2^{(1)}(Z) \to 0$ and $A_2^{(3)}(Z) \sim e^Z$ as $Z \to \infty e^{\pi i/6}$. Hence matching the two solutions gives us

$$\alpha_0 = \beta, \quad \alpha_1 = 0, \quad \text{and} \quad \alpha_3 = 0. \tag{2.149}$$

The remaining two constants, β and α_2, may be obtained from the boundary conditions

$$\widehat{\Psi}(0) = 0, \quad \frac{\mathrm{d}\widehat{\Psi}}{\mathrm{d}z} = \frac{1}{\varepsilon}\frac{\mathrm{d}\widehat{\Psi}}{\mathrm{d}Z} = 1 \tag{2.150}$$

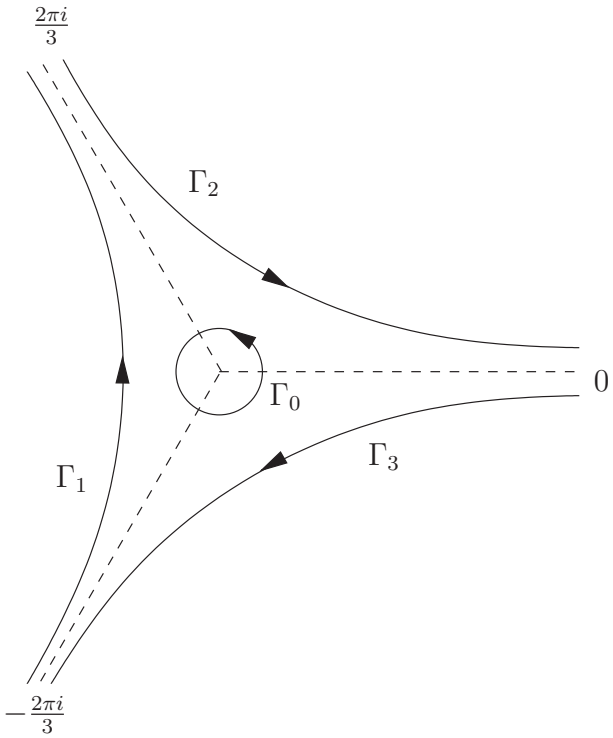


Figure 2.3: Contours L_k in the definition of the generalized Airy function (2.141).

which require

$$\alpha_2 = -\frac{\beta}{A_2^{(1)}(0)} \tag{2.151}$$

and

$$\beta = -\frac{\varepsilon A_2^{(1)}(0)\mathrm{Re}_T^m}{A_1^{(1)}(0)}. \tag{2.152}$$

Hence the inner solution is

$$\widehat{\Psi} \sim \frac{\varepsilon}{A_1^{(1)}(0)}\left(A_2^{(1)}(Z) - A_2^{(1)}(0)\right) + O(\varepsilon^2), \tag{2.153}$$

and the outer solution is

$$\widehat{\Psi} \sim -\frac{\varepsilon A_2^{(1)}(0)}{A_1^{(1)}(0)}\left(\psi_2(z) - \frac{\psi_2(1)}{\psi_1(1)}\psi_1(z)\right) + O(\varepsilon^2). \tag{2.154}$$

We have not mentioned the value of the exponent $-m$ of Re_t pre-multiplying our expansions since it cancelled when finding β. Since β was implicitly assumed to be $O(1)$, it follows that $m = \frac{1}{3}$.

We may now differentiate the inner solution to obtain

$$\begin{aligned}\left.\frac{\mathrm{d}^2\widehat{\Psi}}{\mathrm{d}z^2}\right|_{z=0} = \frac{1}{\varepsilon^2}\left.\frac{\mathrm{d}^2\widehat{\Psi}}{\mathrm{d}Z^2}\right|_{Z=0} &\sim \frac{A_0^{(1)}(0)}{\varepsilon A_0^{(0)}(0)} + O(1) \\ &= -3^{4/3}\mathrm{Re}_T^{1/3}\,(ik)^{1/3}\,\mathrm{Ai}(0).\end{aligned} \tag{2.155}$$

Hence the convolution kernel in (2.123) is given by

$$K(x) = \frac{3^{2/3}\mathrm{Re}_T^{1/3}}{\Gamma(2/3)2\pi}\int_{-\infty}^{\infty}(ik)^{-2/3}\,e^{ikx}\,\mathrm{d}k, \tag{2.156}$$

where we take $(ik)^{-2/3}$ to be $|k|^{-2/3}e^{\mp\pi i/3}$ for $k \gtrless 0$. We may simplify this integral by first splitting the integral into two, then changing the sign of k in one to obtain a single integral from 0 to ∞:

$$\begin{aligned}K^*(x) := \int_{-\infty}^{\infty}(ik)^{-2/3}e^{ikx}\,\mathrm{d}k &= \left(\int_{-\infty}^{0} + \int_0^{\infty}\right)(ik)^{-2/3}e^{ikx}\,\mathrm{d}k \\ &= \int_0^{\infty}(-ik)^{-2/3}e^{-ikx} + (ik)^{-2/3}e^{ikx}\,\mathrm{d}k \\ &= 2\,\mathrm{Re}\int_0^{\infty}(ik)^{-2/3}e^{ikx}\,\mathrm{d}k.\end{aligned} \tag{2.157}$$

We now make the substitution $z = kx$ to obtain

$$K^*(x) = 2\,\mathrm{sgn}\,x\;\mathrm{Re}\left\{x^{-1/3}\int_0^{\infty}(iz)^{-2/3}e^{iz}\,\mathrm{d}z\right\}. \tag{2.158}$$

We may evaluate this integral by integrating over the contour γ shown in Figure 2.4. The integrand is holomorphic inside γ, and by Jordan's inequality [50] the integrals over the two arcs vanish as $\delta \to 0$ and $R \to \infty$. Hence (with $z = iy$ on the imaginary axis, and using the definition of the gamma function)

$$\begin{aligned} K^*(x) &= 2\operatorname{sgn} x \operatorname{Re}\left\{ x^{-1/3} \int_0^\infty i(-z)^{-2/3} e^{-z}\, \mathrm{d}z \right\} \\ &= 2\operatorname{sgn} x \Gamma\left(\frac{1}{3}\right) \operatorname{Re}\left\{ i(-1)^{-2/3} x^{-1/3} \right\}. \end{aligned} \tag{2.159}$$

If $x < 0$, $(-1)^{-2/3}x^{-1/3} = -(-x)^{-1/3}$, so that the real part is zero. Hence $K = 0$ for $x < 0$, and for $x > 0$,

$$K(x) = \mu x^{-1/3}, \tag{2.160}$$

where

$$\mu = \frac{3^{2/3}\mathrm{Re}_T^{1/3}}{\Gamma(2/3)^2} \tag{2.161}$$

and we have used $\Gamma(2/3)\Gamma(1/3) = 2\pi/\sqrt{3}$.

Hence the basal shear stress is

$$\tau = f\rho_w u_0^2 \left(1 - s + \frac{3^{2/3}\mathrm{Re}_T^{1/3}}{\Gamma(2/3)^2} \int_{-\infty}^{x} \frac{s'(\xi)}{(x-\xi)^{1/3}}\, \mathrm{d}\xi \right), \tag{2.162}$$

and therefore τ at a certain point depends on the slope of the bed at all points upstream of that point; we draw an analogy here with the previous model for τ when it depended on the nature of the bed at a single point a finite distance upstream.

We note at this point that τ is proportional to u_0^2, u_0 being a velocity scale coming from the average velocity in the unperturbed state. However, since we were aiming to obtain an improvement on our previous model for τ which was $\tau = f\rho_w \overline{u}^2$, we would like to have τ being proportional to the variable $\overline{u}^2$ rather than the constant u_0^2. It is clear that increasing $\overline{u}$ will cause τ to increase; hence we modify the form of the

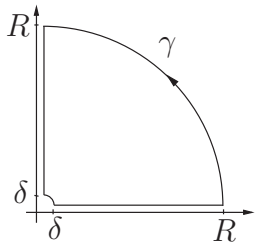


Figure 2.4: Contour γ used to evaluate the integral in (2.158)

shear stress to include a dependence on $\overline{u}$. We may do this by writing $u_0 = \overline{u}(1-s)$, substituting into (2.162), and linearizing in s, so that the shear stress may be written

$$\tau = f\rho_w \overline{u}^2 \left(1 - 2s + \frac{3^{2/3}\mathrm{Re}_T^{1/3}}{\Gamma(2/3)^2} \int_{-\infty}^{x} \frac{s'(\xi)}{(x-\xi)^{1/3}}\,\mathrm{d}\xi\right). \tag{2.163}$$

2.6.2 Linear stability analysis

We return to equations (2.55) to (2.60), which with our new model for τ and with $\gamma \to 0$ (no suspension) and $\mathrm{Fr} \to 0$ (tranquil flow) become

$$\begin{aligned} h &= 1 - s, && (2.164)\\ s_t + q_x &= 0, && (2.165)\\ hu &= 1, && (2.166)\\ q &= \tau^{3/2}, && (2.167)\\ \tau &= u^2\left(1 - s + K * s_x\right). && (2.168) \end{aligned}$$

Here the $\overline{u}$ in our definition of τ in (2.163) has become u to match the notation of (2.55) to (2.60). We may simplify these equations to obtain

$$\begin{aligned} s_t + q'(\tau)\tau_x &= 0, && (2.169)\\ q(\tau) &= \tau^{3/2}, && (2.170)\\ \tau &= \frac{1}{1-s} + \frac{1}{(1-s)^2} K * s_x, && (2.171) \end{aligned}$$

which when linearized for small s become

$$s_t + q'(1)\left(s_x + K * s_{xx}\right) = O(s^2). \tag{2.172}$$

Substituting $s = s_0 e^{\sigma t + ikx}$ then gives

$$\sigma + q'(1)\left(ik - k^2\widehat{K}\right) = 0, \tag{2.173}$$

since

$$K * \left(s_0 e^{\sigma t + ikx}\right) = s_0 e^{\sigma t + ikx} \int_{-\infty}^{\infty} K(\xi) e^{-ik\xi}\,\mathrm{d}\xi = s_0 e^{\sigma t + ikx}\widehat{K}, \tag{2.174}$$

and therefore the growth rate is

$$\mathrm{Re}\,\sigma = q'(1)k^2\,\mathrm{Re}\,\widehat{K}. \tag{2.175}$$

We have already seen what $\widehat{K}$ is from our calculation above; it is given by

$$\widehat{K}(k) = \frac{(ik)^{-2/3}}{\Gamma(2/3)}, \tag{2.176}$$

so that

$$\operatorname{Re}\widehat{K} = \frac{\cos\frac{\pi}{3}k^{-2/3}}{\Gamma(2/3)}, \tag{2.177}$$

and

$$\operatorname{Re}\sigma = \frac{q'(1)}{2\Gamma(2/3)}k^{4/3} > 0, \tag{2.178}$$

so that we have successfully predicted an instability. The wave speed is

$$-\frac{\operatorname{Im}\sigma}{k} = q'(1)\left(1 + \frac{\sqrt{3}}{2\Gamma(2/3)}k^{1/3}\right) > 0, \tag{2.179}$$

so that these waves propagate downstream, as we have seen before.

As before, however, the growth rate is unbounded for large wavenumber (since $\operatorname{Re}\sigma \sim k^{4/3}$). Hence this model still has the undesirable property of showing signs of being ill-posed. We now consider two possible ways of overcoming this difficulty.

2.6.3 Stabilising term: O(1) term in expansion

In our asymptotic expansion of $\widehat{\Psi}''(0)$, we took the leading order term which was of order $\varepsilon^{-1} = (3ik\mathrm{Re}_T)^{1/3}$. It was this which contributed a factor of $k^{1/3}$ to the expression for $\operatorname{Re}\sigma$; the remaining factor of k came from the x-derivative in the Exner equation. If we were to take the next term in the expansion, we may expect this to contribute a term proportional to k in $\operatorname{Re}\sigma$, since the second term in $\widehat{\Psi}''(0)$ is of order ε^0. However, if the coefficient of ε^0 in the expansion is calculated, it turns out that one of its terms depends on k, while the rest do not. This dependence on k comes from the fact that the solutions (2.127) and (2.128) to the outer equation depend on k.

The $O(1)$ term in the expansion of $\widehat{\Psi}''(0)$ may be written as

$$a + b\frac{\psi_2(1)}{\psi_1(1)}, \tag{2.180}$$

where we are not concerned with the value of a (since it will contribute a term proportional to k in $\operatorname{Re}\sigma$, which will neither affect the stability nor eliminate the large wavenumber instability), and

$$b = -\frac{A_2^{(1)}(0)A_0^{(1)}(0)}{A_1^{(1)}(0)^2} < 0. \tag{2.181}$$

Numerical investigation suggests that

$$\frac{\psi_2(1)}{\psi_1(1)} \sim k \tag{2.182}$$

as $k \to \infty$; this is shown in Figure 2.5. Hence we obtain an additional term in $\operatorname{Re}\sigma$

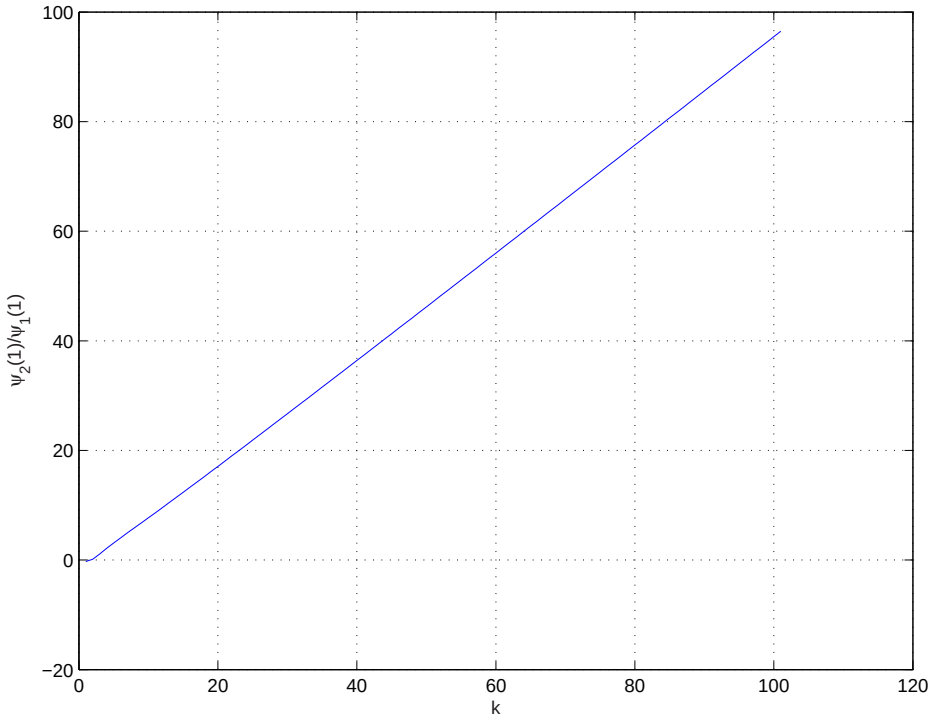


Figure 2.5: Plot showing the relationship between $\psi_2(1)/\psi_1(1)$ and k

which is proportional to k^2, and with a negative coefficient, i. e.

$$\operatorname{Re}\sigma = \alpha k^{4/3} - \beta_1 k^2, \tag{2.183}$$

with $\alpha, \beta_1 > 0$. Therefore for small k, $\operatorname{Re}\sigma > 0$ so that we still have an instability, but as $k \to \infty$, $\operatorname{Re}\sigma \sim -\beta_1 k^2 < 0$; this extra term has stabilized the model for short wavelength disturbances.

2.6.4 Stabilising term: Buoyancy-induced stress modification

An alternative way to obtain this stabilising term is to consider the effect of gravity on the sediment particles, which is ignored by the Meyer-Peter & Müller law.

A particle of diameter D_s has a force exerted on it by the flow of approximately τD_s^2. If the particle is on a slope s_x, there is a downstream force due to gravity of

$-\Delta\rho g D_s^3 s_x$. Hence in dimensionless terms, the net force per unit area causing the particle to move is

$$\tau' = \tau - \frac{\Delta\rho D_s}{\rho h_0 S} s_x = \tau - \beta_2 s_x. \tag{2.184}$$

The growth rate thus becomes

$$\mathrm{Re}\,\sigma = \frac{q'(1)}{2\Gamma(2/3)} k^{4/3} - \beta_2 k^2; \tag{2.185}$$

the effect of gravity is a diffusive one which again stabilises the model for short wavelength disturbances, while preserving the instability for small k. Using typical values $\Delta\rho = 10^4 \mathrm{kg\ m^{-3}}$, $D_s = 10^{-4}\mathrm{m}$, $\rho_w = 10^3 \mathrm{kg\ m^{-3}}$, $h_0 = 1\mathrm{m}$, and $S = 0.01$, leads to a value for β_2 of 1, and so we may safely assume it is $O(1)$.

2.7 Canonical evolution equation

If we assume that the non-dimensionalized bed height s varies with amplitude $s_0 \ll 1$ over a length scale $L \gg 1$, with

$$s_0 \sim \frac{\mu}{L} \sim \frac{\beta}{L}, \tag{2.186}$$

where $\mu = q'(1)/2\Gamma(2/3)$ is the coefficient of the integral term in the shear stress τ, and β may be β_1 or β_2 as we wish, then the shear stress may be written as

$$\tau = 1 + s + s^2 + \mu \int_0^\infty s_x(x-\xi,t)\xi^{-1/3}\,\mathrm{d}\xi - \beta s_x + O(s_0^3). \tag{2.187}$$

Using also

$$\begin{aligned} q(\tau) &= q(1) + q'(1)(\tau-1) + \frac{q''(1)}{2}(\tau-1)^2 + O([\tau-1]^3) \\ &= q(1) + q'(1)\left(s + s^2 + \mu\int_0^\infty s_x(x-\xi,t)\xi^{-1/3}\,\mathrm{d}\xi - \beta s_x\right) + \frac{q''(1)}{2}s^2 \\ &\quad + O(s_0^3), \end{aligned} \tag{2.188}$$

we may write the evolution equation as

$$\frac{\partial s}{\partial t} + \frac{\partial}{\partial x}\left[q'(1)\left(s + s^2 + \mu\int_0^\infty \frac{\partial s}{\partial x}(x-\xi,t)\xi^{-1/3}\,\mathrm{d}\xi - \beta\frac{\partial s}{\partial x}\right) + \frac{q''(1)}{2}s^2\right] = O(s_0^3). \tag{2.189}$$

By making the scalings

$$X = (x - q'(1)t)\left(\frac{\mu}{\beta}\right)^{\frac{3}{2}}, \tag{2.190}$$

$$T = \frac{\mu^3 t}{\beta^2}, \tag{2.191}$$

$$S = (2q'(1) + q''(1))\sqrt{\frac{\beta}{\mu^3}}s, \tag{2.192}$$

where typical values of the coefficients are

$$q'(1)\left(\frac{\mu}{\beta}\right)^{\frac{3}{2}} \approx 0.62, \tag{2.193}$$

$$\frac{\mu^3}{\beta^2} \approx 0.17, \tag{2.194}$$

and

$$(2q'(1) + q''(1))\sqrt{\frac{\beta}{\mu^3}} \approx 9.1; \tag{2.195}$$

we are then able to eliminate all of these coefficients to obtain the canonical evolution equation

$$\frac{\partial S}{\partial T} + S\frac{\partial S}{\partial X} = \frac{\partial^2 S}{\partial X^2} - \int_0^\infty \frac{\partial^2 S}{\partial X^2}(X - \xi, t)\,\xi^{-\frac{1}{3}}\,\mathrm{d}\xi. \tag{2.196}$$

The terms on the left-hand side of this equation are the same as those found in Burger's equation; these terms will have the effect of convecting waves to the right and forming shocks. The first term on the right-hand side is a diffusive one, stabilising short-wavelength disturbances and smoothing out shocks. The integral term is a destabilising one, and ensures the instability of the steady state $S \equiv$ constant.

2.7.1 Numerical solution

The form of (2.196) makes it particularly suitable for solution by a Fourier spectral method, because the integral term is a Fourier convolution. If we write (2.196) as

$$s_t + ss_x + K * s_{xx} - s_{xx} = 0, \tag{2.197}$$

with

$$K(x) = \begin{cases} x^{-\frac{1}{3}}, & x > 0, \\ 0, & x \leqslant 0, \end{cases} \tag{2.198}$$

then taking the Fourier transform, we obtain

$$\frac{\mathrm{d}}{\mathrm{d}t}\mathcal{F}(s) + \frac{ik}{2}\mathcal{F}(s^2) + k^2\left(1 - \mathcal{F}(K)\right)\mathcal{F}(s) = 0. \tag{2.199}$$

We have already calculated the form of $\mathcal{F}(K)$; it is

$$\mathcal{F}(K) \propto (ik)^{-\frac{2}{3}}. \tag{2.200}$$

Writing

$$s^2 = \left[\mathcal{F}^{-1}\left(\mathcal{F}(s)\right)\right]^2 \tag{2.201}$$

(as in [66]), we have an ODE for $\mathcal{F}(s)$ which may be solved numerically, e. g. using a forward Euler scheme.

Implementing this reveals a steady-state travelling dune which grows from a small random perturbation in the bed (a typical perturbation is shown in Figure 2.6), and the solution is shown in Figure 2.7, which also shows a plot of bed elevation s and generalized flux $q = \frac{1}{2}s^2 + K * s_x - s_x$. As can be seen, q is proportional to s, which suggests that the solution obtained is indeed a steady state travelling wave, since substituting

$$s = s(x - ct) \tag{2.202}$$

into

$$s_t + q_x = 0 \tag{2.203}$$

implies that

$$q'(s) = c. \tag{2.204}$$

The wave speed c may thus be obtained by finding the slope of the straight line obtained by plotting $q = \frac{1}{2}s^2 + K * s_x - s_x$ against s.

Figure 2.9 is the same plot as Figure 2.7, but shows the dune as it is growing. Here q is not proportional to s (and is multi-valued), confirming that a steady-state travelling wave has not yet been attained. q is greater on the upstream side of the dune than on the downstream side (at a fixed height), which means that sediment is being deposited on the dune, i. e. the dune is growing.

2.7.1.1 Non-periodic solutions

The spectral method used above for the numerical solution of (2.196) uses a finite spatial domain $-L/2 < x < L/2$ as an approximation to the infinite domain $-\infty < x < \infty$. We found above that any initial perturbation led to a solution which filled this finite domain. Clearly this is not an appropriate approximation to a solution on the full infinite domain. We may instead treat it as the solution of (2.196) on a finite domain, along with the periodic boundary conditions enforced by the use of the spectral method. The solution obtained must therefore be thought of as an infinite train of dunes, where the wavelength is arbitrary.

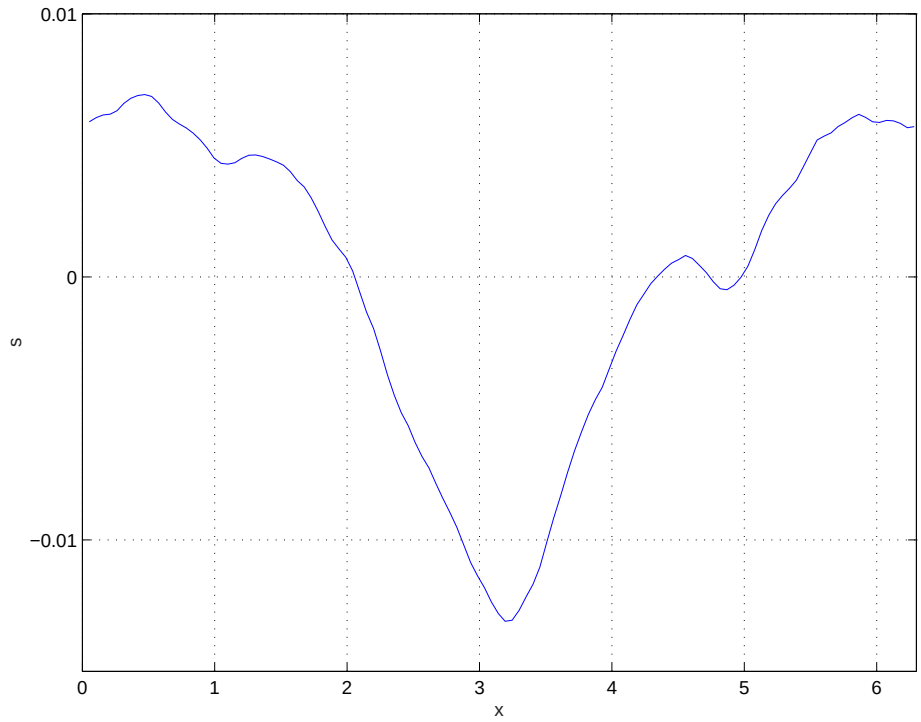


Figure 2.6: Typical random bed perturbation. Note that the vertical scale is much smaller than for the final solutions.

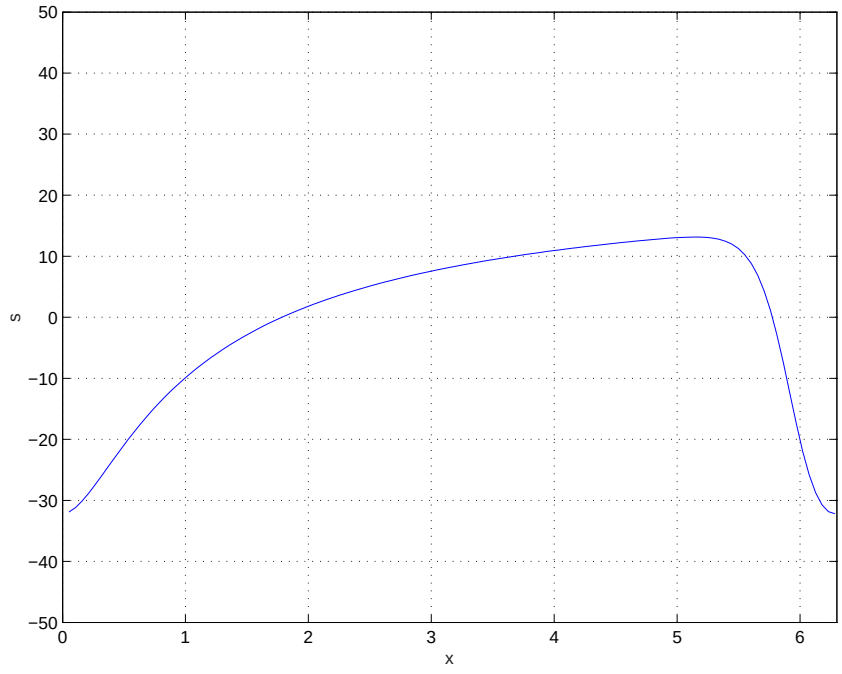


Figure 2.7: Numerical solution to evolution equation (2.197). This wave moves to the right without any change in its shape.

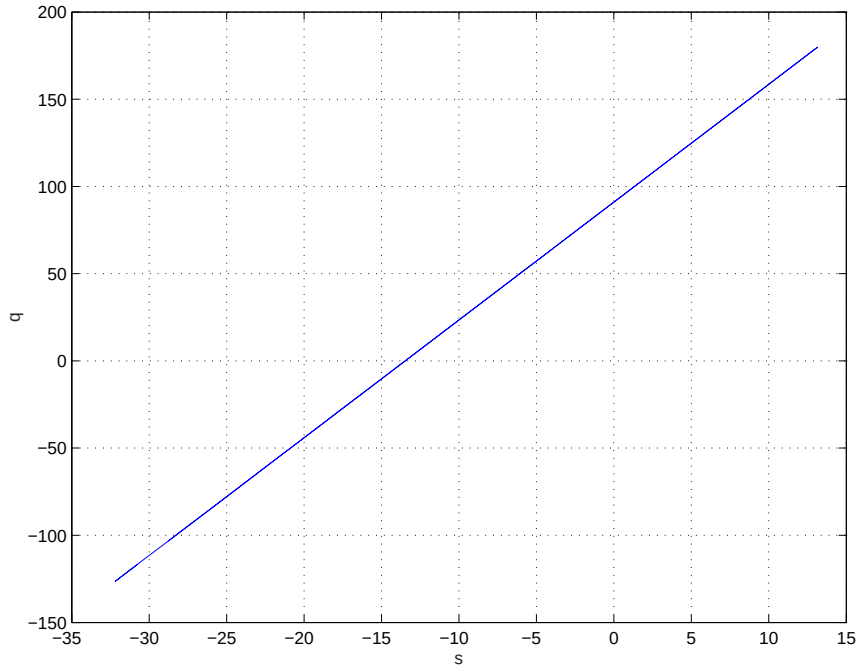


Figure 2.8: Plot of flux q and bed elevation s for the solution to (2.197). The linear relationship confirms that the wave is indeed a travelling wave.

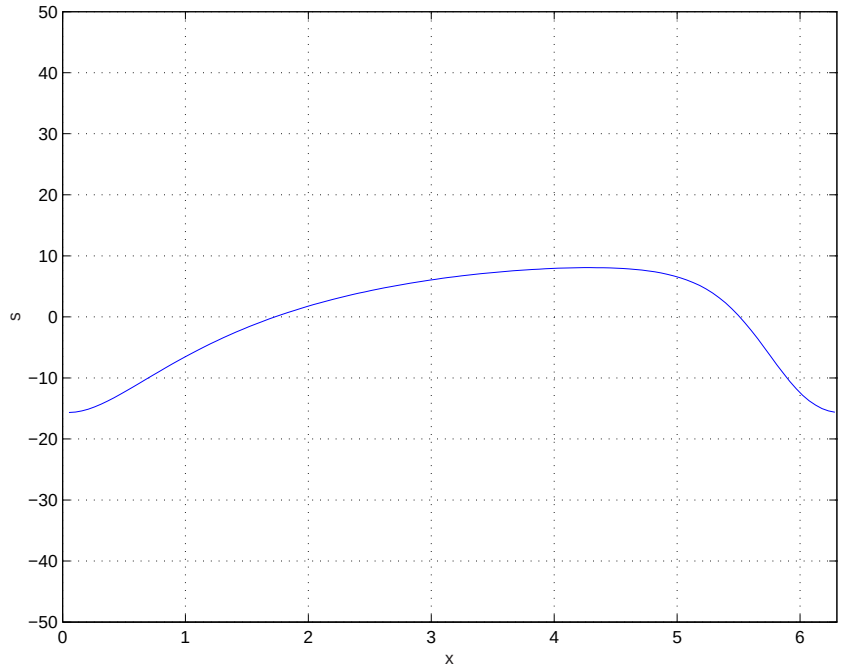


Figure 2.9: Numerical solution to dune equation (2.197) during growing phase. The vertical scale is the same as for Figure 2.7.

An alternative way of considering solutions to (2.196) is to look for solutions on the interval $[0, \infty)$, with a certain prescribed flux at $x = 0$. This could be thought of as a simplified model of a desert (e. g. the Sahara) in $x > 0$, with an ocean (the Atlantic) in $x < 0$, where sediment is deposited from the water at the beach at $x = 0$ and blown into the desert by the prevailing wind (see Figure 2.11).

Since

$$q = \frac{1}{2}s^2 + K * s_x - s_x, \tag{2.205}$$

a constant bed height $s = s_0$ will lead to a constant sediment flux $q = q_0 = \frac{1}{2}s_0^2$. Specifying a flux $q = q_0$ at the boundary $x = 0$ and solving (2.196) in $x > 0$ is therefore equivalent to using the full domain $-\infty < x < \infty$ and taking $s \equiv s_0$ in

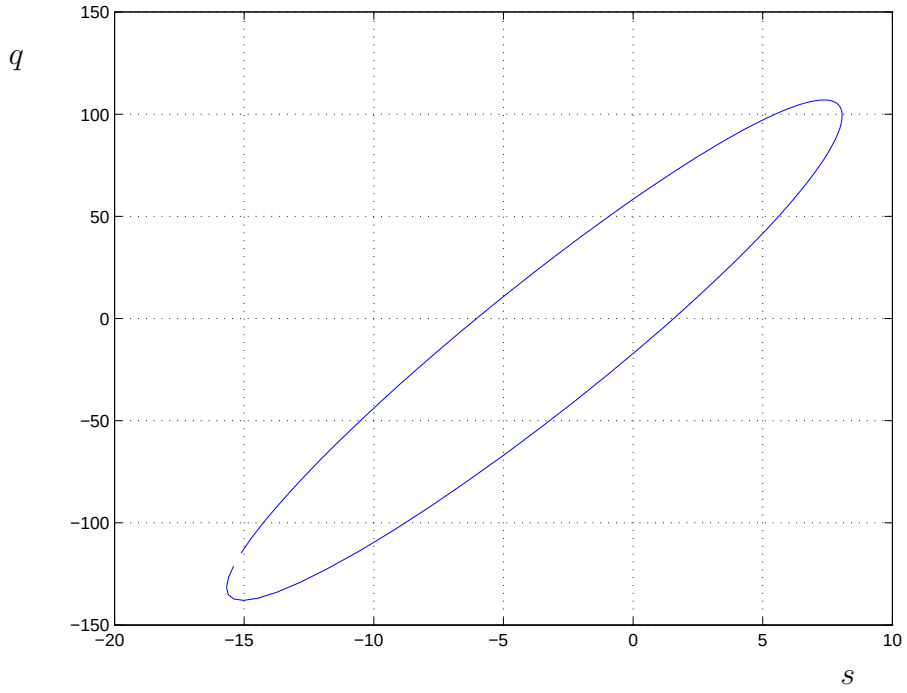


Figure 2.10: Flux q and bed elevation s for the solution to dune equation (2.197) during growing phase.

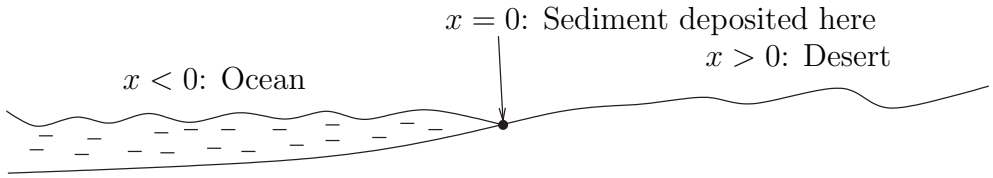


Figure 2.11: Schematic showing a desert in $x > 0$ with an ocean in $x < 0$ depositing sediment at the beach at $x = 0$.

$x < 0$. This motivates us to write

$$s(x,t) = s_0 + S(x,t)H(x), \tag{2.206}$$
$$q(x,t) = q_0 + Q(x,t)H(x), \tag{2.207}$$

where $H(x)$ is the Heaviside function

$$H(x) = \begin{cases} 1, & x > 0, \\ 0, & x < 0, \end{cases} \tag{2.208}$$

and we have the boundary conditions

$$S(0,t) = Q(0,t) = 0. \tag{2.209}$$

Substitution into the Exner equation yields

$$\left(S_t(x,t) + Q_x(x,t)\right) H(x) + Q(x,t)\delta(x) = 0, \tag{2.210}$$

where we have used the fact that the derivative of the Heaviside function is the Dirac delta function $\delta(x)$.

Taking the Fourier cosine transform then leads to

$$\int_0^\infty (S_t + Q_x) \cos kx \, \mathrm{d}x = 0, \tag{2.211}$$

where the δ term has disappeared since $Q(0,t) = 0$. Finally we use the fact that

$$\int_0^\infty f(x) \cos kx \, \mathrm{d}x = \frac{1}{2} \int_{-\infty}^\infty f_e(x) e^{-ikx} \, \mathrm{d}x, \tag{2.212}$$

where f_e is the even extension of f, to obtain

$$\frac{\mathrm{d}}{\mathrm{d}t} \widehat{S_e} + ik\widehat{Q_e} = 0, \tag{2.213}$$

so that S_e and Q_e, the even extensions of S and Q, satisfy the same equation in Fourier space as did our previous functions s and q in the case of the full spatial domain.

The second equation for S and Q is

$$\begin{aligned} q_0 + Q &= \frac{1}{2}s^2 + K * s_x - s_x \\ &= \frac{1}{2}(s_0 + S)^2 + \int_{-\infty}^x \frac{\delta(\xi)S(\xi,t) + H(\xi)S_x(\xi,t)}{(x-\xi)^{\frac{1}{3}}} \, \mathrm{d}\xi \\ &\quad -(\delta(x)S + H(x)S_x), \end{aligned} \tag{2.214}$$

and for $x > 0$ this becomes

$$Q = s_0 S + \frac{1}{2}S^2 + \int_0^x \frac{S_x(\xi, t)}{(x-\xi)^{\frac{1}{3}}}\,\mathrm{d}\xi - S_x, \tag{2.215}$$

so that after a Fourier cosine transform it is

$$\widehat{Q_e} = s_0 \widehat{S_e} + \frac{1}{2}\widehat{S_e^2} + ik\widehat{K}\,\widehat{S_e} - ik\widehat{S_e}. \tag{2.216}$$

Hence we have a similar equation for Q in terms of S as for q and s but this time with a parameter s_0.

The equations (2.210) and (2.215) may then be solved numerically using the same spectral method as before; we may simply ignore the solution obtained in $x < 0$. We use a large domain length L (approximating ∞), and start with a small perturbation near and to the right of $x = 0$. A sequence of solutions is shown in Figures 2.12 to 2.15 and in Figure 2.16.

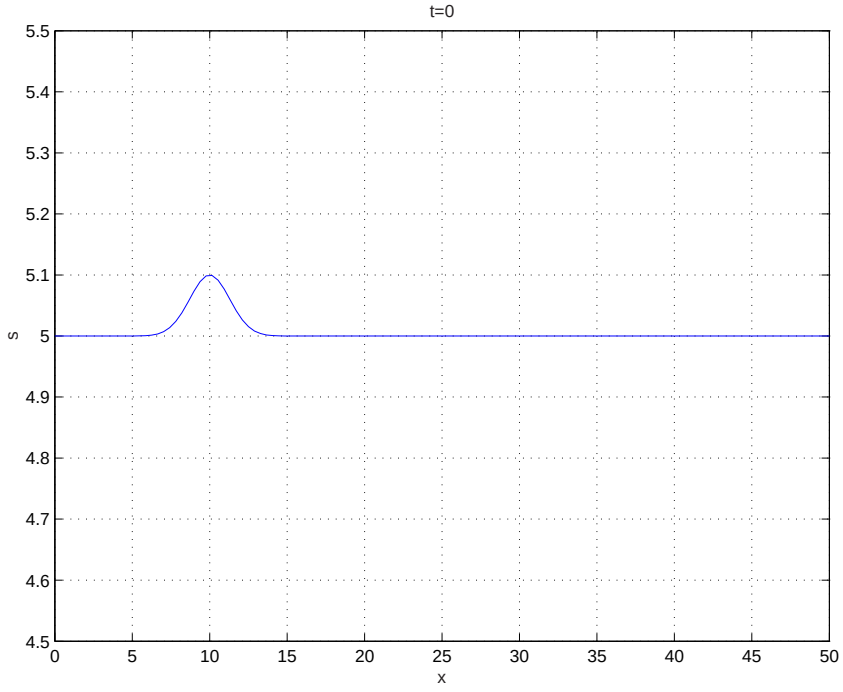


Figure 2.12: Initial conditions for the sequence of solutions to (2.210) and (2.215) on $x > 0$ in the following Figures.

We observe that the perturbation grows initially as a dune, before a depression grows downwind of the dune. A new dune then grows downwind of the depression, and this sequence repeats itself as the group of dunes moves downstream, for as long as the simulation runs.

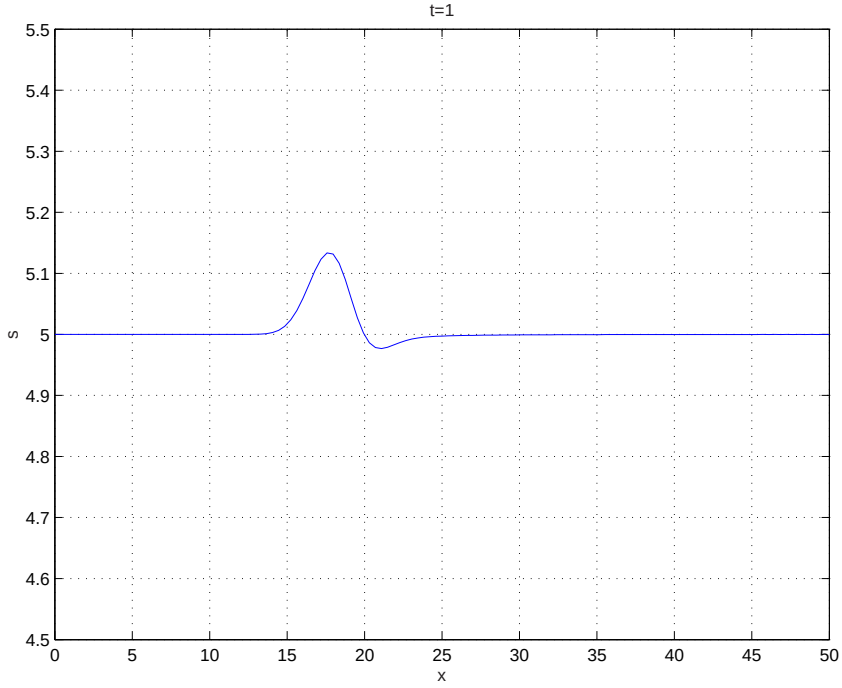


Figure 2.13: First in a sequence of solutions to (2.210) and (2.215) on $x > 0$. The dune has propagated downstream, and a depression has started to form downstream of the dune.

The results of the above simulation suggest that there is no travelling wave solution in this case. We now show that this is indeed true. Suppose that we have a travelling wave dune occupying $a < x < b$ at time t, with $s = s_0$ outside this interval. Then by integrating the Exner equation between points $x_1 < a$ and $x_2 > b$ we have

$$\frac{\mathrm{d}}{\mathrm{d}t}\int_{x_1}^{x_2} s\,\mathrm{d}x = q|_{x_1} - q|_{x_2}\,. \tag{2.217}$$

Since the dune is a travelling wave dune, the left hand side of this equation must be zero, and hence

$$q|_{x=x_1} = q|_{x=x_2}\,, \tag{2.218}$$

i. e. the flux upstream of the dune must equal the flux downstream of the dune, since no sediment has been deposited on or eroded from the dune. However, due to the form of

$$q = \frac{1}{2}s^2 + K * s_x - s_x, \tag{2.219}$$

the fact that $q(x_1, t) = q(x_2, t)$ implies that

$$\int_{-\infty}^{x_2} \frac{s_x(\xi, t)}{(x_2 - \xi)^{\frac{1}{3}}}\,\mathrm{d}\xi = 0 \tag{2.220}$$

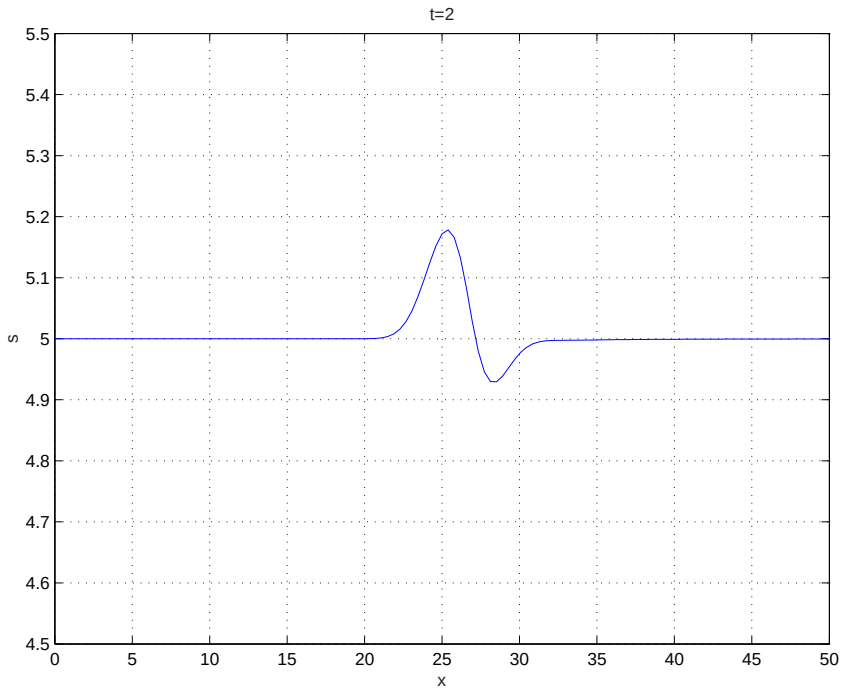


Figure 2.14: Second in a sequence of solutions to (2.210) and (2.215) on $x > 0$. The dune continues to propagate downstream, and the depression has continued to grow.

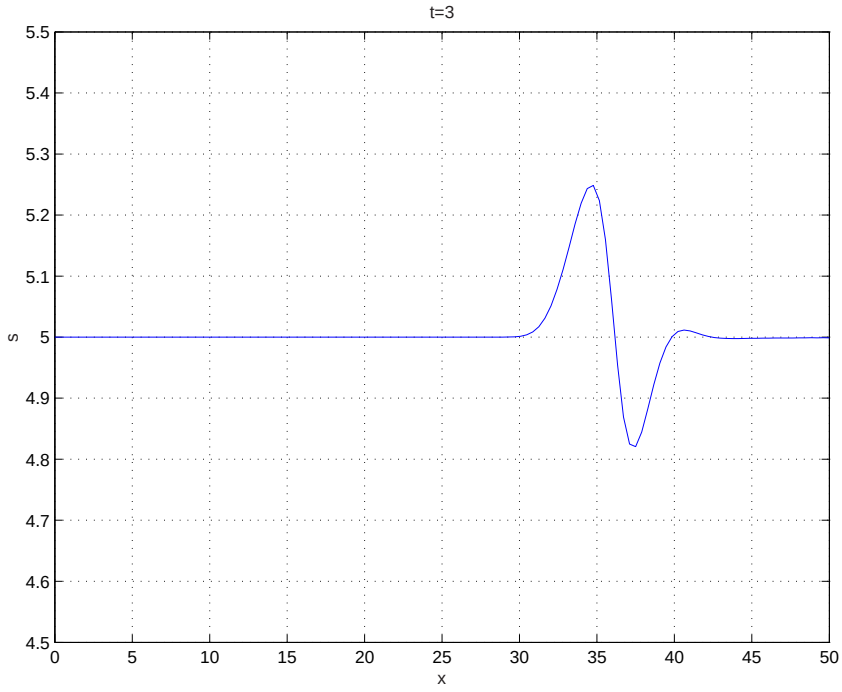


Figure 2.15: Third in a sequence of solutions to (2.210) and (2.215) on $x > 0$. Another dune has begun to grow downstream of the depression, and the train of dunes and depressions continue to move downstream. This pattern repeats for as long as we run the simulation.

for all $x_2 > b$, which is impossible unless $s_x \equiv 0$. Hence the only two possibilities for a travelling wave are the trivial solution of a horizontal bed, or a dune which is not confined to a certain interval $a < x < b$ so that our above argument does not apply. This second case is the one that the periodic travelling wave solutions found above are covered by.

2.8 Non-saturated bedload transport

Each of the three bedload transport laws (2.5), (2.6), and (2.7) above assume that the bedload flux $\boldsymbol{q}$ is always saturated. This assumption relies on there being a plentiful supply of erodible sediment, which is not necessarily always the case, for example at the windward end of an isolated barchan dune, where the flux will have zero saturation regardless of the shear stress, since no sediment will have been entrained.

Sauermann and his colleagues [55] derived a phenomenological model for non-saturated bedload transport by considering the motion of individual particles and obtaining a continuum relation; in the notation of the model above, the equation

$$\boldsymbol{q} = \boldsymbol{q}(\boldsymbol{\tau}) \tag{2.221}$$

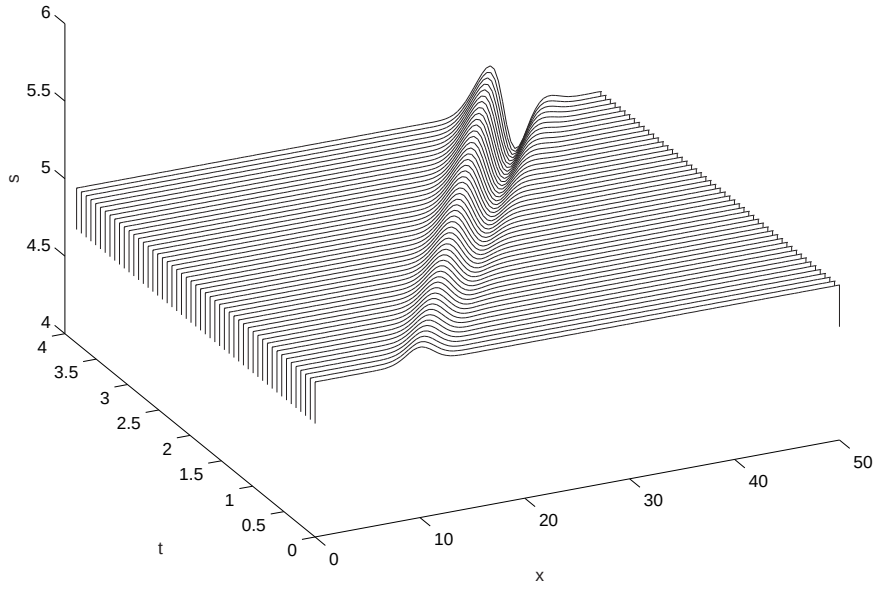


Figure 2.16: A three-dimensional representation of the sequence of solutions to (2.210) and (2.215) on $x > 0$ shown in the previous Figures.

is replaced by three equations,

$$q_s = q_s(\boldsymbol{\tau}), \tag{2.222}$$

$$\boldsymbol{q} = q\widehat{\boldsymbol{\tau}}, \tag{2.223}$$

and

$$\widehat{\boldsymbol{\tau}} \cdot \nabla q = \frac{1}{l_s}\left(q_s - q\right), \tag{2.224}$$

where $\widehat{\boldsymbol{\tau}}$ is a unit vector in the direction of $\boldsymbol{\tau}$. Hence q_s is the saturated flux which was used previously, and $\boldsymbol{q}$ is now the actual flux which has an amplitude that varies between zero and the amplitude of the saturated flux. The *saturation length* is l_s (m), and is a typical length scale over which the flux becomes saturated. According to Sauermann, l_s is weakly dependent on the shear velocity u_*, and is approximately 0.1m.

We may follow through our previous calculations using this new flux relation. After non-dimensionalizing, equation (2.224) becomes

$$\alpha\widehat{\boldsymbol{\tau}} \cdot \nabla q = q_s - q, \tag{2.225}$$

where

$$\alpha = \frac{l_s}{x_0} \tag{2.226}$$

is typically small. In the limit $\alpha \to 0$, we return to our previous model.

We now consider the effect that this modified flux relation has on the linear stability studied above.

The steady state of the simplest model (2.63) was found to be neutrally stable. After incorporating (the one-dimensional version of) equation (2.225) into this model, we find the growth rate to be

$$\operatorname{Re}\sigma = -\frac{3\alpha k^2}{1+\alpha^2 k^2} < 0, \tag{2.227}$$

so that the steady state is now stable.

The introduction of a phase difference δ into the shear stress (2.72) gave us an instability in this model. We now find that the growth rate is

$$\operatorname{Re}\sigma = -\frac{3k\left(\alpha k\cos\delta - \sin\delta\right)}{1+\alpha^2 k^2}, \tag{2.228}$$

so that again an instability is possible for certain values of δ, and again we may have $\operatorname{Re}\sigma > 0$ as $k \to \infty$; the introduction of non-saturated flux has not affected how well the model works.

With the model (2.163) for τ based on the asymptotic analysis of the Orr-Sommerfeld equation, we find that the growth rate for non-zero α is

$$\mathrm{Re}\,\sigma = -\frac{3k^2}{2(1+\alpha^2k^2)}\left(\alpha - \frac{k^{-\frac{2}{3}}}{2\Gamma(\frac{2}{3})} + \frac{\alpha\sqrt{3}k^{\frac{1}{3}}}{2\Gamma(\frac{2}{3})}\right) \tag{2.229}$$

which is positive for small k and negative for large k; hence we have successfully predicted an instability, whilst also avoiding having an unbounded growth rate at large wavenumber, without needing to introduce the stabilising terms in Sections 2.6.3 or 2.6.4.

We may also attempt to derive a canonical equation in the same manner as (2.196). We note that for q and q_s close to 1 we may linearize (2.225) to obtain

$$\alpha q_x = q_s - q = \tau^{\frac{3}{2}} - q, \tag{2.230}$$

so that

$$\alpha q_{xx} + q_x = \frac{3}{2}\tau^{\frac{1}{2}}\tau_x. \tag{2.231}$$

We may then use the Exner equation (2.2) to eliminate q, since

$$q_x = -s_t \tag{2.232}$$

and

$$q_{xx} = -s_{xt}, \tag{2.233}$$

so that

$$s_t + \frac{3}{2}\tau^{\frac{1}{2}}\tau_x + \alpha s_{xt} = 0, \tag{2.234}$$

and this is the same equation as (2.169) but with an extra term involving s_{xt}.

Assuming that we have the same scales as in (2.186), we may linearize in the same way to obtain the analogue of (2.189) which is

$$\frac{\partial s}{\partial t} + \frac{\partial}{\partial x}\left[q'(1)\left(s + s^2 + \mu\int_0^\infty \frac{\partial s}{\partial x}(x-\xi,t)\xi^{-1/3}\,\mathrm{d}\xi\right) + \frac{q''(1)}{2}s^2\right] + \alpha\frac{\partial^2 s}{\partial x\partial t} = O(s_0^3). \tag{2.235}$$

Again we may scale the variables in a suitable way to eliminate parameters; however this time we may not eliminate them all, and the best we can do is to write our evolution equation as

$$\frac{\partial S}{\partial T} + S\frac{\partial S}{\partial X} = \frac{\partial^2 S}{\partial X^2} - \int_0^\infty \frac{\partial^2 S}{\partial X^2}(X-\xi,t)\,\xi^{-\frac{1}{3}}\,\mathrm{d}\xi + \frac{\alpha}{x_0}\frac{\partial^2 S}{\partial X\partial T} \tag{2.236}$$

which we would expect to have similar properties to (2.196), especially as we would expect $\alpha/x_0 \ll 1$. However, the presence of the parameter α/x_0 does of course introduce a distinct length scale, in contrast to (2.196).

We may solve (2.236) in a very similar way to how we solved (2.196). Following (2.198) we may take the Fourier transform of (2.236) to obtain

$$\frac{\mathrm{d}}{\mathrm{d}T}\mathcal{F}(S) + \frac{ik}{2}\mathcal{F}(S^2) - k^2(1+\mathcal{F}(K))\mathcal{F}(S) - \frac{\alpha}{x_0}ik\frac{\mathrm{d}}{\mathrm{d}T}\mathcal{F}(S) = 0, \tag{2.237}$$

and this may be rearranged to give

$$\frac{\mathrm{d}}{\mathrm{d}T}\mathcal{F}(S) = \frac{x_0}{ik\alpha - x_0}\left(\frac{ik}{2}\mathcal{F}(S^2) - k^2(1+\mathcal{F}(K))\mathcal{F}(S)\right) \tag{2.238}$$

which is again an ODE for S. Again this equation leads to a steady-state travelling wave solution which we show in Figure 2.17. The main qualitative difference between the solutions of (2.196) and the solutions of (2.236) are that the solutions of the latter equation tend to show multiple dunes which persist for some time before coalescing into one large steady-state dune (see Figure 2.18). This effect becomes less marked if the horizontal length scale is increased, i. e. as the parameter α/x_0 approaches zero.

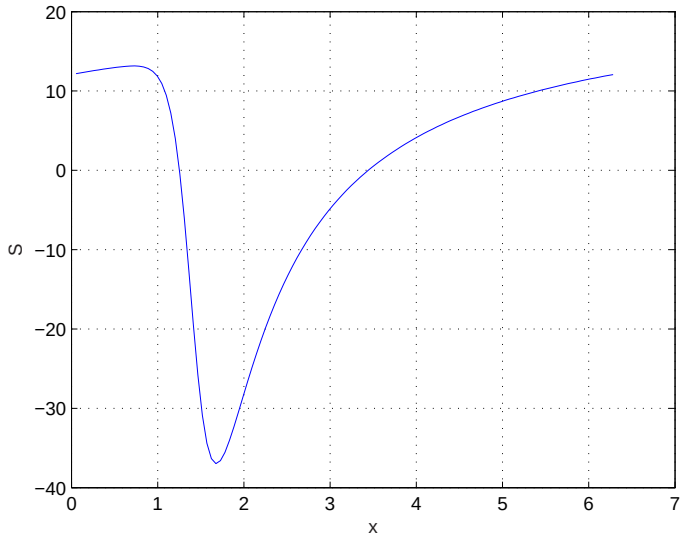


Figure 2.17: Numerical solution to dune equation (2.236) with $\alpha/x_0 = 0.13$. The solution shown is that obtained for large T, i. e. the steady state solution.

2.9 Comparison of sediment flux functions

We finish this Chapter by comparing qualitatively the sediment flux function q obtained from each of the three variants of this Chapter's model. In Figure 2.19 we plot a Gaussian dune profile s and three corresponding sediment fluxes q_1, q_2, and q_3, which are defined as follows. The first, q_1 is the most simple form obtained from (2.55), (2.58), and (2.60), which is (in non-dimensional form)

$$q_1 = \frac{1}{(1-s)^3}. \tag{2.239}$$

The second, q_2, is obtained from (2.170) and (2.171) with (2.184), so that

$$q_2 = \left\{1 + \frac{1}{2}s^2 + K * \frac{\partial s}{\partial x} - \frac{\partial s}{\partial x}\right\}^{\frac{3}{2}}. \tag{2.240}$$

The third, q_3, is the solution to the system with non-saturated flux, i. e. it is given by

$$\frac{\partial q_3}{\partial x} = \left\{1 + \frac{1}{2}s^2 + K * \frac{\partial s}{\partial x}\right\}^{\frac{3}{2}} - q_3. \tag{2.241}$$

We may see that each of the three profiles for the sediment flux is qualitatively different. The simplest, q_1, reaches its maximum at the brink of the dune, and this is a sign of the neutral stability that we found earlier. The other two, q_2 and q_3, have

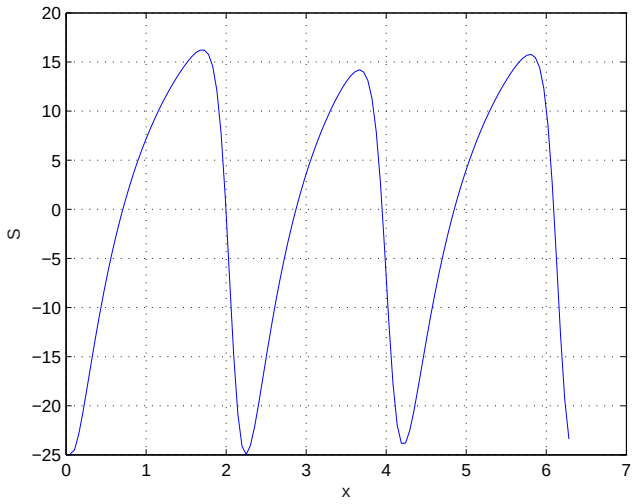


Figure 2.18: Numerical solution to dune equation (2.236) with $\alpha/x_0 = 0.13$. The solution shown is that obtained before the solution settles down to a steady state solution; there are multiple dunes which later coalesce.

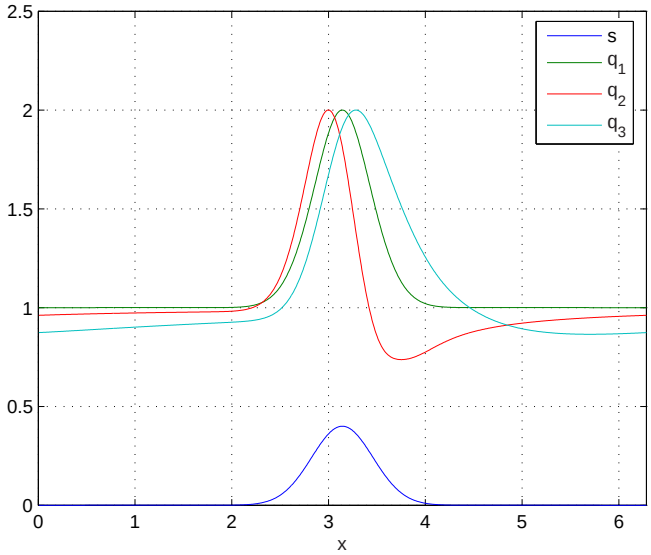


Figure 2.19: Comparison of three different sediment flux functions q_1, q_2, and q_3 for a Gaussian dune profile s.

peaks that are either side of the brink, and this shift provides the instablity that we required. Finally, q_2 has a large dip downstream of the dune that q_1 and q_3 do not have.

Chapter 3

Aeolian modelling: Mixing length model

The theory outlined in Chapter 2 was formulated within the context of river flow, in particular the geometry of the problem, the boundary conditions used, and the choice of a constant eddy viscosity model for the turbulent flow. At some level, we would expect the results obtained to have some relevance in the context of wind flow interacting with erodible sediment, i. e. sand in a desert.

However, the flow predicted is rather different to that observed in the field and in laboratory experiments; the assumption of a constant eddy viscosity is a poor approximation, the basic flow profile is not as simple as the $U(z)$ in (2.99) of the previous Chapter, and of course it would not be appropriate to impose boundary conditions at the top of the atmosphere, since the large vertical length scale would not be compatible with the shorter horizontal scales under consideration, particularly as we considered two-dimensional flow.

In this Chapter therefore, we consider more general models for turbulent flow over topography in which the eddy viscosity is allowed to vary spatially. We then go on to compare our results with those of the previous Chapter.

3.1 The structure of the atmosphere

Houghton [32] describes the structure of the flow of air in the atmosphere. Above the planetary boundary layer, approximately the lowest kilometre of the atmosphere, the flow is approximately inviscid and is driven by a combination of the Coriolis effect from the Earth's rotation and thermal effects.

In the planetary boundary layer, viscous effects become important (since the velocity must decrease to zero at the Earth's surface in order to satisfy a no-slip condition).

Within this boundary layer there is a layer above the surface which is a few tens of metres thick in which the shear stress is approximately constant. Hence under an assumption of mixing-length theory for turbulence (see Appendix A), which is appropriate due to the vicinity of a wall (the Earth's surface), we obtain a logarithmic profile for the mean velocity u:

$$u = \frac{u_*}{\kappa} \log \frac{z}{z_0}, \tag{3.1}$$

where u_* is the *shear velocity* (see Appendix A), $\kappa \approx 0.4$ is the *von Kármán constant*, z is the height above the surface, and z_0 is a *roughness length*. This layer is called the *constant flux layer*.

3.2 Mixing length theory

We may therefore consider the flow in the constant flux layer only, assuming that we know the depth d of this layer. Then the logarithmic profile in the undisturbed case is given by (3.1), so that the velocity U_d at the top of this layer is

$$U_d = \frac{u_*}{\kappa} \log \frac{d}{z_0}. \tag{3.2}$$

Hence if we know U_d, we may use (3.2) to find the shear velocity

$$u_* = \frac{\kappa U_d}{\log \frac{d}{z_0}}, \tag{3.3}$$

so that we may write the logarithmic profile for u in terms of U_d rather than u_*; it is

$$u = U_d \left(1 + \frac{\log z/d}{\log d/z_0}\right). \tag{3.4}$$

We are interested in perturbations to the basic flow

$$\boldsymbol{u} = (u, w) = \left(U_d \left(1 + \frac{\log z/d}{\log d/z_0}\right), 0\right) \tag{3.5}$$

induced by perturbations to the horizontal surface $z = 0$.

This problem has been studied in much detail by Hunt and his co-workers [11, 12, 35, 36, 69] as well as by others [13, 25, 28, 59, 60, 65, 71], through use of matched asymptotic expansions in a number of different layers above the surface. This work was done with a number of different applications in mind, such as meteorology, civil engineering, as well as dune modelling. Since our objective is simply to predict the

shear stress at the surface, we present here our understanding of the theory with this particular goal in mind.

We define a parameter ε as the ratio of the shear velocity u_* to the velocity at the top of the constant flux layer U_d. Then

$$\varepsilon = \frac{u_*}{U_d} = \kappa \left(\log \frac{d}{z_0} \right)^{-1}, \tag{3.6}$$

and for typical values $d = 100\text{m}$, $z_0 = 10^{-4}\text{m}$, $\kappa = 0.4$, we obtain $\varepsilon \approx 0.03 \ll 1$, so it is reasonable to perform an asymptotic analysis in the small parameter ε.

We now non-dimensionalize the system in the following way, with capitals denoting non-dimensional perturbation variables:

$$\begin{aligned}
x &= dX, && (3.7)\\
z &= dZ, && (3.8)\\
u &= U_d(1 + \varepsilon U), && (3.9)\\
w &= \varepsilon U_d W, && (3.10)\\
p &= \varepsilon \rho U_d^2 P, && (3.11)\\
\tau_{11} &= \varepsilon^2 \rho U_d^2 T_1, && (3.12)\\
\tau_{13} &= \varepsilon^2 \rho U_d^2 T_3, && (3.13)\\
\mu_T &= \varepsilon \rho d U_d M. && (3.14)
\end{aligned}$$

The Reynolds equations (see Appendix A) thus become

$$\begin{aligned}
U_X + W_Z &= 0, && (3.15)\\
U_X + P_X &= \varepsilon(T_{1,X} + T_{3,Z} - UU_X - WU_Z), && (3.16)\\
W_X + P_Z &= \varepsilon(T_{3,X} - T_{1,Z} - UW_X - WW_Z), && (3.17)\\
T_1 &= 2MU_X, && (3.18)\\
T_3 &= M(U_Z + W_X). && (3.19)
\end{aligned}$$

The eddy viscosity is given by

$$M = \kappa^2 (Z - S)^2 U_Z, \tag{3.20}$$

since we are considering flow above the topography $Z = S(X)$, where we must assume that this topography has a small slope, so that mixing-length theory (for flow past a horizontal wall) is still appropriate.

3.3 Boundary conditions

We now consider boundary conditions for the system of equations (3.15) to (3.20). The condition at the lower surface is a no-slip condition, as we are considering viscous flow. Before rescaling, this condition was $\mathbf{u} = (0, 0)$ at $z = z_0 + s$, because of the definition of the roughness length. This condition therefore becomes

$$\boldsymbol{U} = (-\varepsilon^{-1}, 0) \text{ on } Z = S + Z_0, \tag{3.21}$$

where $Z_0 := z_0/d = e^{-\kappa/\varepsilon}$.

Outside the constant flux layer, where $Z \gg 1$, it is natural to suppose that the flow is uniform in the horizontal direction, so that $U \sim V(Z)$ as $Z \to \infty$. In the case where $S \equiv 0$, V will have a logarithmic profile related to (3.1), but a perturbation in S will change V. Nonetheless, the form of V depends on T_3 and M only, which can be seen by taking $U = V(Z)$, $W = 0$ in (3.19). Hence we may take a boundary condition at $Z \to \infty$ to be a prescribed value of T_3, from which V will follow. In the unperturbed case, the pressure vanishes at infinity; thus we take this as a boundary condition also.

Our boundary conditions are therefore

$$U = -\frac{1}{\varepsilon}, \quad W = 0 \quad \text{at} \quad Z = S + Z_0, \tag{3.22}$$

$$T_3 \to 1, \quad W \to 0, \quad P \to 0 \quad \text{as} \quad Z \to \infty. \tag{3.23}$$

3.4 Length scales for topography

In the current framework, we have the same scaling for horizontal and for vertical distances. While this is reasonable for the flow of air in the atmospheric boundary layer, it does not necessarily apply to a topography consisting of dunes, which are in general much longer than they are high. The length scale $d \sim 100$m is a reasonable horizontal scale for a dune, but a shorter scale is required for the height. While we could introduce a new scale H for this height, it is reasonable to avoid doing this, since we would expect dunes to evolve to a length scale already present in the system. We are therefore justified in taking the distinguished limit $H = \varepsilon d$, so that the dimensionless surface topography is given by $Z = \varepsilon\Sigma(X)$, with $\Sigma = O(1)$.

3.5 Asymptotic analysis

By expanding the functions U, W, P, T_1, and T_3 in powers of the small parameter ε, we hope to obtain some insight into the solutions of (3.15) to (3.19). We write

$$U = U^0 + \varepsilon U^1 + \cdots , \tag{3.24}$$

with similar expressions for the other functions.

3.5.1 $O(1)$ equations

The lowest order equations are obtained by setting $\varepsilon = 0$ and are given by

$$\begin{aligned} U^0_X + W^0_Z &= 0, & (3.25)\\ U^0_X + P^0_X &= 0, & (3.26)\\ W^0_X + P^0_Z &= 0, & (3.27) \end{aligned}$$

from which T^0_1 and T^0_3 follow. Integrating (3.26) then gives

$$U^0 + P^0 = V(Z), \tag{3.28}$$

using the boundary conditions $U \sim V(Z)$, $P \to 0$ as $Z \to \infty$.

Eliminating U^0 from these equations, we obtain

$$P^0_X = W^0_Z \tag{3.29}$$

and

$$P^0_Z = -W^0_X, \tag{3.30}$$

which are the Cauchy-Riemann equations for P^0 and W^0. Hence $P^0 + iW^0$ is an analytic function of $X + iZ$, and therefore P^0 and W^0 both satisfy Laplace's equation in $Z > \varepsilon\Sigma$.

The boundary condition for W at the surface may be linearized onto $Z = 0$ since

$$W(X, Z_0 + \varepsilon\Sigma) = W^0(X, 0) + O(\varepsilon). \tag{3.31}$$

Therefore the boundary condition for W^0 is

$$W^0(X, 0) = 0. \tag{3.32}$$

However, the unique solution to

$$\nabla^2 W^0 = 0, \quad Z > 0; \quad W^0 = 0, \quad Z = 0; W^0 \to 0, Z \to \infty \tag{3.33}$$

is $W^0 \equiv 0$ which contradicts our scaling of W (when we assumed $W^0 = O(1)$). This therefore suggests the presence of a boundary layer, which is to be expected since this is a singular perturbation problem, with the highest derivative in the system (3.15)–(3.19) having a coefficient involving ε.

Assuming that W on the boundary is in fact

$$W^0(X, 0) = f(X), \tag{3.34}$$

where the form of f will come from matching with the solution inside the boundary layer, we may write the solution of

$$\nabla^2 W^0 = 0, \quad Z > 0; \quad W^0 = f(X), \quad Z = 0; W^0 \to 0, Z \to \infty \tag{3.35}$$

as [47]

$$W^0 = \frac{Z}{\pi} \int_{-\infty}^{\infty} \frac{f(\xi)}{(X-\xi)^2 + Z^2} \, \mathrm{d}\xi, \tag{3.36}$$

from which it follows (using (3.29) and (3.30)) that

$$P^0 = -\frac{1}{\pi} \int_{-\infty}^{\infty} \frac{(X-\xi) f(\xi)}{(X-\xi)^2 + Z^2} \, \mathrm{d}\xi. \tag{3.37}$$

The surface pressure $P^0(X, \varepsilon\Sigma)$ is therefore given to leading order by

$$P^0(X, 0) = \frac{1}{\pi} \fint_{-\infty}^{\infty} \frac{f(\xi)}{\xi - X} \, \mathrm{d}\xi =: \mathcal{H}(f), \tag{3.38}$$

the Hilbert transform of $f(X)$; we note further that

$$P^0(X, \varepsilon\Sigma) = P^0(X, 0) + O(\varepsilon^2). \tag{3.39}$$

We are left with

$$U^0 + P^0 = V(Z), \tag{3.40}$$

but we have no information about V; we must therefore consider equations at the next order in ε.

3.5.2 $O(\varepsilon)$ equations

On dividing the system (3.15)–(3.19) by ε, using (3.25)–(3.27), then setting $\varepsilon = 0$, we obtain equations at the next order in ε for U, W, P, T_1, and T_3 which may be

written

$$\begin{aligned} U_X^1 + W_Z^1 &= 0, && (3.41)\\ U_X^1 + P_X^1 &= T_{1,X}^0 + T_{3,Z}^0 - U^0 U_X^0 - W^0 U_Z^0, && (3.42)\\ W_X^1 + P_Z^1 &= T_{3,X}^0 - T_{1,Z}^0 - U^0 W_X^0 - W^0 W_Z^0, && (3.43)\\ T_1^0 &= 2\kappa^2 Z^2 U_X^0 U_Z^0, && (3.44)\\ T_3^0 &= \kappa^2 Z^2 U_Z^0 (U_Z^0 + W_X^0). && (3.45) \end{aligned}$$

Then (3.42) may be written as

$$(U^1 + P^1)_X = T_{3,Z}^0 + \left(T_1^0 - \frac{1}{2}(U^0)^2 - \frac{1}{2}(W^0)^2 + \Psi^0 V' \right)_X, \tag{3.46}$$

where the stream function Ψ satisfies

$$\Psi_X = -W. \tag{3.47}$$

We expect behaviour of the solutions as $X \to \pm\infty$ to be unaffected by the topography; therefore integrating (3.46) between $-\infty$ and ∞ leads to

$$\frac{\mathrm{d}}{\mathrm{d}Z} \int_{-\infty}^{\infty} T_3^0 \, \mathrm{d}X = 0, \tag{3.48}$$

or equivalently

$$\frac{\mathrm{d}}{\mathrm{d}Z} \overline{T_3^0} = 0, \tag{3.49}$$

where the overbar denotes the mean value in the X-direction. Hence, using the boundary condition at $Z \to \infty$, $\overline{T_3^0} \equiv 1$, and then using (3.45),

$$\overline{\kappa^2 Z^2 ((V')^2 + 2(W_X^0)^2 + 3V' W_X^0)} = 1, \tag{3.50}$$

so that

$$(V')^2 = \frac{1}{\kappa^2 Z^2} - 2\overline{(W_X^0)^2}, \tag{3.51}$$

from which we may obtain the previously unknown flow profile at infinity, $V(Z)$. The non-zero term $-2\overline{(W_X^0)^2}$ corresponds to the effect that the topography has on this profile. Near $Z = 0$,

$$(V')^2 \approx \frac{1}{\kappa^2 Z^2}, \tag{3.52}$$

so that

$$V \sim \frac{1}{\kappa} \log Z, \tag{3.53}$$

which is the logarithmic profile seen before.

We now have lowest-order approximations U^0, W^0, P^0, T_1^0, and T_3^0 which satisfy the boundary conditions at $Z \to \infty$. As mentioned above, however, these will not in general satisfy the boundary conditions at $Z = Z_0 + \varepsilon\Sigma$, due to the presence of a boundary layer. We now rescale equations (3.15)–(3.19) in order to consider the behaviour inside this boundary layer.

3.5.3 Inner equations

We assume the presence of a boundary layer of thickness δ (to be determined), and hence we rescale the vertical coordinate Z so that it is of order unity in the boundary layer. We note that $U = O(\varepsilon^{-1})$ in the boundary layer, due to the boundary condition for U at the surface, and replace U with

$$u = U + \frac{1}{\varepsilon}. \tag{3.54}$$

We then write

$$Z = \delta\zeta + \varepsilon\Sigma(X), \tag{3.55}$$

and under this change of variables from Z to ζ, equation (3.15) becomes

$$u_X + \frac{1}{\delta}(W - \varepsilon\Sigma' u)_\zeta = 0; \tag{3.56}$$

in order to retain a conservation of mass equation with both terms balanced, we choose to rescale W by writing

$$w = \frac{1}{\delta}(W - \varepsilon\Sigma' u), \tag{3.57}$$

so that (3.15) is

$$u_X + w_\zeta = 0. \tag{3.58}$$

The eddy viscosity becomes

$$M = \delta\kappa^2\zeta^2 u_\zeta; \tag{3.59}$$

to balance this relationship we rescale with

$$M = \delta m. \tag{3.60}$$

The stresses are then given by

$$T_1 = 2m(\delta u_X - \varepsilon\Sigma' u_\zeta) \tag{3.61}$$

and

$$T_3 = m(1-\varepsilon^2\Sigma'^2)u_\zeta + \delta m\left(\delta w_X - \varepsilon[w_\zeta - \Sigma' u_X - \Sigma'' u]\right). \tag{3.62}$$

There is no need to rescale T_3 as there is already a consistent balance in the expression for it; we will have to rescale T_1 with a factor of δ or ε, whichever is larger.

The remaining two momentum equations become

$$\varepsilon\left(T_{3,\zeta} + \Sigma' P_\zeta\right) - \varepsilon^2\Sigma' T_{1,\zeta} = \delta\left(u_X + P_X + \varepsilon(wu_\zeta + uu_X - T_{1,X})\right) \tag{3.63}$$

and

$$P_\zeta + \varepsilon T_{1,\zeta} + \varepsilon^2\Sigma' T_{3,\zeta} = \varepsilon\delta\left(T_{3,X} - \varepsilon u(\Sigma' u)_X - \varepsilon\Sigma'(uw)_\zeta\right) + \varepsilon\delta^2\left(-uw_X - ww_\zeta + \varepsilon\Sigma' uw_\zeta\right). \tag{3.64}$$

3.5.4 Boundary layer thickness

We have not said anything yet about the size of δ; we note that if $\delta \ll \varepsilon^3$ then our equations may be greatly simplified by taking the limit $\delta \to 0$. To justify this, we consider the boundary conditions that must be applied in the boundary layer. These are (in the scaled variables)

$$u = w = 0 \quad \text{on} \quad \zeta = \frac{Z_0}{\delta}, \tag{3.65}$$

and so it is natural to choose

$$\delta = Z_0 = \frac{z_0}{d} = e^{-\kappa/\varepsilon}, \tag{3.66}$$

which does indeed satisfy $\delta \ll \varepsilon^3$ as $\varepsilon \to 0$ (and of course satisfies $\delta \ll \varepsilon^n$ as $\varepsilon \to 0$ for any n).

3.5.5 Inner solution

We may therefore ignore any term in equations (3.58) and (3.61) to (3.64) involving δ, giving our system as

$$\begin{aligned}
u_X + w_\zeta &= 0, && (3.67)\\
T_{3,\zeta} + \Sigma' P_\zeta - \varepsilon^2\Sigma' t_{1,\zeta} &= O(\delta/\varepsilon), && (3.68)\\
P_\zeta + \varepsilon^2(t_{1,\zeta} + \Sigma' T_{3,\zeta}) &= O(\delta), && (3.69)\\
t_1 + 2\kappa^2\Sigma'\zeta^2 u_\zeta^2 &= O(\delta/\varepsilon), && (3.70)\\
T_3 - \kappa^2\zeta^2(1-\varepsilon^2\Sigma'^2)u_\zeta^2 &= O(\delta), && (3.71)
\end{aligned}$$

where we have scaled

$$T_1 = \varepsilon t_1 \tag{3.72}$$

as mentioned above.

From (3.68) and (3.69) we see that

$$T_{3,\zeta} = O(\varepsilon^2), \tag{3.73}$$

so that T_3 is approximately constant in the ζ-direction, and equal to its value at the surface $\zeta = 0$, which we write as $T_b(X) := T_3|_{\zeta=0}$. Hence

$$T_3 = T_b + O(\varepsilon^2). \tag{3.74}$$

In addition (3.71) says that

$$T_3 = \kappa^2 \zeta^2 u_\zeta^2 + O(\varepsilon^2), \tag{3.75}$$

and so, on equating (3.74) and (3.75), we obtain an equation for u which is

$$T_b = \kappa^2 \zeta^2 u_\zeta^2 + O(\varepsilon^2), \tag{3.76}$$

leading to

$$u = \frac{\sqrt{T_b}}{\kappa} \log \zeta + O(\varepsilon^2) \tag{3.77}$$

after using the boundary conditions $u = w = 0$ on $\zeta = 1$. Reverting to the outer variables U, X, and Z, this expression becomes

$$U = \frac{\sqrt{T_b} - 1}{\varepsilon} + \frac{\sqrt{T_b}}{\kappa} \log (Z - \varepsilon\Sigma) + O(\varepsilon^2); \tag{3.78}$$

this must match with the outer solution obtained above as $Z \to \varepsilon\Sigma$.

We may now also find w using (3.67) and our knowledge of u; we obtain

$$w = -\frac{1}{\kappa} (\zeta \log \zeta - \zeta + 1) \frac{\mathrm{d}}{\mathrm{d}X} \sqrt{T_b} \tag{3.79}$$

which in terms of W and Z is

$$W = \Sigma'(1 + \varepsilon U) - \frac{1}{\kappa} \left\{ (Z - \varepsilon\Sigma) \left(\log (Z - \varepsilon\Sigma) - 1 + \frac{\kappa}{\varepsilon} \right) + Z_0 \right\} \frac{\mathrm{d}}{\mathrm{d}X} \sqrt{T_b}. \tag{3.80}$$

As $Z \to \varepsilon\Sigma$,

$$W \sim \Sigma'(1 + \varepsilon U) + O(\delta) \sim \Sigma' \sqrt{T_b} + O(\varepsilon). \tag{3.81}$$

3.5.6 Matching

The leading order outer solution for W was assumed to satisfy

$$W^0(X,0) = f(X), \tag{3.82}$$

where the boundary condition had been linearized onto $Z = 0$. Using

$$W(X,\varepsilon\Sigma) = W(X,0) + O(\varepsilon) = f(X) + O(\varepsilon) \tag{3.83}$$

and writing

$$T_b = 1 + \varepsilon T_b^1 + \cdots, \tag{3.84}$$

the matching as $Z \to \varepsilon\Sigma$ fixes

$$f(X) = \Sigma'(X). \tag{3.85}$$

The leading order outer solution for U is

$$U^0 = V - P^0. \tag{3.86}$$

Using

$$P^0(X,\varepsilon\Sigma) = P^0(X,0) + (Z - \varepsilon\Sigma) + O((Z-\varepsilon\Sigma)^2), \tag{3.87}$$

we see that

$$U \sim \frac{1}{\kappa}\log Z - \mathcal{H}(\Sigma') + (Z-\varepsilon\Sigma)\Sigma'' + O(\varepsilon^2) \tag{3.88}$$

as $Z \to \varepsilon\Sigma$, since

$$P_Z^0(X,\varepsilon\Sigma) = -W_X^0(X,\varepsilon\Sigma) = -\Sigma''. \tag{3.89}$$

The inner solution satisfies

$$U = \frac{(1+\varepsilon T_b^1 + \cdots)^{1/2} - 1}{\varepsilon} + \frac{(1+\varepsilon T_b^1 + \cdots)^{1/2}}{\kappa}\log(Z-\varepsilon\Sigma) + O(\varepsilon^2) \tag{3.90}$$

$$= \frac{1}{2}T_b^1 + \frac{1}{\kappa}\log Z + \varepsilon\left(T_b^2 + \frac{T_b^1}{\kappa}\log Z - \frac{\Sigma}{\kappa Z}\right) + O(\varepsilon^2), \tag{3.91}$$

so that matching at $O(1)$ with the outer solution requires

$$T_b^1 = -2\mathcal{H}(\Sigma'). \tag{3.92}$$

We have therefore found the surface shear stress, which is the quantity that we are ultimately interested in, to first-order accuracy in ε; it is

$$T_b = 1 - 2\varepsilon\mathcal{H}(\Sigma') + O(\varepsilon^2). \tag{3.93}$$

3.5.7 Linear stability analysis

We may now assess the ability of this shear stress model to predict the formation of dunes. The Exner equation in our scaled variables is

$$\varepsilon\frac{\partial\Sigma}{\partial t}+\frac{\partial q}{\partial X}=0, \tag{3.94}$$

where $q=q(T_b)$. Thus

$$\varepsilon\Sigma_t+q'(T_b)\left(-2\varepsilon\mathcal{H}(\Sigma')\right)_X=O(\varepsilon^2), \tag{3.95}$$

so that, expanding q' in a Taylor series, the linearized Exner equation is

$$\Sigma_t-2q'(1)\mathcal{H}(\Sigma'')=0. \tag{3.96}$$

Substituting

$$\Sigma=e^{\sigma t+ikX}, \tag{3.97}$$

we obtain

$$\sigma+2k^2q'(1)e^{-ikX}\mathcal{H}(e^{ikX})=0, \tag{3.98}$$

and then

$$e^{-ikX}\mathcal{H}(e^{ikX})=\frac{1}{\pi}\fint_{-\infty}^{\infty}\frac{e^{ik(\xi-X)}}{\xi-X}\,\mathrm{d}\xi=\frac{1}{\pi}\fint_{-\infty}^{\infty}\frac{\exp[ik\eta]}{\eta}\,\mathrm{d}\eta=i\,\mathrm{sgn}\,k \tag{3.99}$$

leads to

$$\sigma=-2ik|k|q'(1), \tag{3.100}$$

so that $\mathrm{Re}\,\sigma=0$, meaning that a flat bed is neutrally stable. We must therefore find the $O(\varepsilon^2)$ term in T_b to be able to predict an instability.

3.5.8 Further analysis

We now continue the analysis in order to find U^1. Using (3.30), (3.40), (3.45), and (3.51), we find

$$T_3^0=1+\kappa^2Z^2(3V'W^0+2\Phi)_X, \tag{3.101}$$

where Φ satisfies

$$\Phi_X=(W_X^0)^2-\overline{(W_X^0)^2}. \tag{3.102}$$

Hence (3.46) may be integrated in X to give

$$U^1=-P^1+\kappa^2(3Z^2V'W^0+2Z^2\Phi)_Z+T_1^0-\frac{1}{2}(U^0)^2-\frac{1}{2}(W^0)^2+\Psi^0V'+V_1(Z), \tag{3.103}$$

where $U^1 \sim V_1$ as $Z \to \infty$, and V_1 may be determined at next order in ε.

As $Z \to 0$,

$$\begin{aligned} P^1 &\to P_0^1, && (3.104)\\ W^0 &\to \Sigma', && (3.105)\\ V' &\sim \frac{1}{\kappa Z}, && (3.106)\\ \Phi &= \int_{-\infty}^{X} (W_X^0)^2 - \overline{(W_X^0)^2}\,\mathrm{d}X = O(1), && (3.107)\\ T_1^0 &\to 0, && (3.108)\\ U^0 &\sim \frac{1}{\kappa}\log Z - \mathcal{H}(\Sigma'), && (3.109) \end{aligned}$$

so that

$$U^1 \sim -P_0^1 + 3\kappa\Sigma' - \frac{1}{2}\left(\frac{1}{\kappa}\log Z - \mathcal{H}(\Sigma')\right)^2 - \frac{1}{2}(\Sigma')^2 + \frac{1}{\kappa Z}\Psi^0 + V_1(Z). \quad (3.110)$$

The stream function Ψ satisfies

$$\Psi_X = -W; \quad (3.111)$$

hence the Fourier transform of the leading order term in its expansion satisfies

$$\widehat{\Psi^0} = \frac{i}{k}\widehat{W^0} = \frac{i}{k}e^{-|k|Z}\widehat{\Sigma'} \quad (3.112)$$

and we therefore look for a function $g(X, Z)$ such that

$$\widehat{g}(k, Z) = \frac{i}{k}e^{-|k|Z}. \quad (3.113)$$

Then

$$\begin{aligned} g(X,Z) &= \frac{1}{2\pi}\int_{-\infty}^{\infty}\frac{i}{k}e^{-|k|Z-ikX}\,\mathrm{d}k && (3.114)\\ &= \frac{1}{\pi}\,\mathrm{Im}\int_0^{\infty}\frac{1}{k}e^{k(-Z+iX)}\,\mathrm{d}k. && (3.115) \end{aligned}$$

This may be found by considering a complex integral of the form

$$I = \int_\gamma \frac{e^{rz}}{z}\,\mathrm{d}z, \quad (3.116)$$

where r is the modulus of $-Z + iX$, i. e. $-Z + iX = re^{i\theta}$, and γ is the wedge-shaped contour with line segments along the negative real axis and along the line $x = se^{i\theta}$,

$s \in \mathbb{R}$, indented at the origin. Standard techniques of contour integration (see [50]) lead to

$$\int_0^\infty \frac{1}{k} e^{k(-Z+iX)}\,\mathrm{d}k = \int_0^\infty \frac{e^{-r\rho}}{\rho}\,\mathrm{d}\rho + i(\theta-\pi). \tag{3.117}$$

Hence

$$g(X,Z) = \frac{1}{\pi}(\theta-\pi) = -\frac{1}{\pi}\tan^{-1}\frac{X}{Z}, \tag{3.118}$$

and therefore

$$\Psi^0 = -\frac{1}{\pi}\int_{-\infty}^{\infty} \tan^{-1}\frac{X-\xi}{Z}\Sigma'(\xi)\,\mathrm{d}\xi \tag{3.119}$$

$$= -\frac{1}{\pi}\int_{-\infty}^{\infty} \frac{Z\Sigma(\xi)}{Z^2+(X-\xi)^2}\,\mathrm{d}\xi, \tag{3.120}$$

provided

$$\lim_{X\to\infty}\Sigma = \lim_{X\to-\infty}\Sigma. \tag{3.121}$$

As $Z \to 0$,

$$\Psi^0 \sim \Psi^0\big|_{Z=0} + Z\,\Psi^0_Z\big|_{Z=0} + O(Z^2). \tag{3.122}$$

We have

$$\Psi^0\big|_{Z=0} = -\Sigma \tag{3.123}$$

and

$$\Psi^0_Z\big|_{Z=0} = -\frac{1}{\pi}\int_{-\infty}^{\infty}\frac{\Sigma(\xi)}{(X-\xi)^2}\,\mathrm{d}\xi = -\mathcal{H}(\Sigma') \tag{3.124}$$

(after integrating by parts). Hence

$$\Psi^0 \sim -\Sigma - Z\mathcal{H}(\Sigma') + O(Z^2) \tag{3.125}$$

as $Z \to 0$, and therefore

$$U^1 \sim -P_0^1 + 3\kappa\Sigma' - \frac{1}{2}\left(\frac{1}{\kappa}\log Z - \mathcal{H}(\Sigma')\right)^2 - \frac{1}{2}(\Sigma')^2 - \frac{\Sigma}{\kappa Z} - \frac{1}{\kappa}\mathcal{H}(\Sigma') + V_1. \tag{3.126}$$

The behaviour of the outer solution as $Z \to 0$, correct to $O(\varepsilon^2)$, is

$$U \sim U^0 + \varepsilon U^1 + O(\varepsilon^2) \tag{3.127}$$

$$\sim -\mathcal{H}(\Sigma') + \frac{1}{\kappa}\log Z + +\varepsilon\left(-\Sigma\Sigma'' - P_0^1 - \frac{1}{2}(\Sigma')^2 + 3\kappa\Sigma'\right.$$
$$\left. -\frac{1}{2}\left(\frac{1}{\kappa}\log Z - \mathcal{H}(\Sigma')\right)^2 - \frac{\Sigma}{\kappa Z} - \frac{1}{\kappa}\mathcal{H}(\Sigma') + V_1\right) + O(\varepsilon^2) \tag{3.128}$$

while the inner solution satisfies

$$U \sim -\mathcal{H}(\Sigma') + \frac{1}{\kappa}\log Z + \varepsilon\left(T_b^2 - \frac{\mathcal{H}(\Sigma')}{\kappa}\log Z - \frac{\Sigma}{\kappa Z}\right) + O(\varepsilon^2). \tag{3.129}$$

The constant terms at $O(\varepsilon)$ may be matched by a choice of T_b^2, and the ε/Z terms automatically match, but the $\varepsilon \log Z$ terms have opposite signs and we are unable to match the two expansions. We are therefore forced to consider a third, intermediate, shear layer.

3.5.9 Shear layer

The shear layer occurs between the inner region, where $Z = O(e^{-\kappa/\varepsilon})$, and the outer region, where $Z = O(1)$. A distinguished limit exists when $Z = O(\varepsilon)$, so we write

$$Z = \varepsilon(\Sigma + z) \tag{3.130}$$

for the new vertical co-ordinate z. We write also

$$W = \Sigma'(1 + \varepsilon U) + \varepsilon w, \tag{3.131}$$

and

$$T_1 = \varepsilon t_1, \tag{3.132}$$

and thus equations (3.15) to (3.19) become

$$\begin{aligned}
U_X + w_z &= 0, && (3.133)\\
U_X + P_X - \Sigma' P_z &= T_{3,z} - \varepsilon(UU_X + wU_z) + O(\varepsilon^2), && (3.134)\\
P_z + \varepsilon\Sigma'' &= O(\varepsilon^2), && (3.135)\\
t_1 &= 2\kappa^2 z^2 (U_X - \Sigma' U_z) U_z, && (3.136)\\
T_3 &= \kappa^2 z^2 U_z (U_z + \varepsilon\Sigma'') + O(\varepsilon^2). && (3.137)
\end{aligned}$$

At $z = 0$, corresponding to the surface $Z = \varepsilon\Sigma$, we know

$$P = P_0 + \varepsilon P_{10} \tag{3.138}$$

(where $P_0 = \mathcal{H}(\Sigma')$) and $w = 0$. Hence (3.135) leads to

$$P = \mathcal{H}(\Sigma') + \varepsilon(P_{10} - z\Sigma'') + O(\varepsilon^2), \tag{3.139}$$

and using (3.133) and (3.134) we have

$$w_z = -U_X = P_X - \Sigma' P_z - T_{3,z} + \varepsilon(UU_X + wU_z) + O(\varepsilon^2) \tag{3.140}$$

so that

$$w = zP_0' - T_3 + T_b + O(\varepsilon), \tag{3.141}$$

using the conditions $w = 0$ and $T_3 = T_b$ on $z = 0$. This may also be written

$$w = zP_0' + 1 - \kappa^2 z^2 U_z^2 + O(\varepsilon). \tag{3.142}$$

Finally we may write (3.134) as an equation for U,

$$\begin{aligned} U_X &= -P_0' - \varepsilon(P_{10}' - z\Sigma''') - \varepsilon\Sigma'\Sigma'' + \frac{\partial}{\partial z}\left(\kappa^2 z^2 U_z(U_z + \varepsilon\Sigma'')\right) \\ &\quad -\varepsilon\left(UU_X + U_z\left(P_0' z + 1 - \kappa^2 z^2 U_z^2\right)\right) + O(\varepsilon^2), \end{aligned} \tag{3.143}$$

which may be simplified by writing

$$U = -P_0 + \frac{1}{\kappa}\log\varepsilon z + \varepsilon u, \tag{3.144}$$

becoming

$$u_X + P_{10}' - z\Sigma''' + \Sigma'\Sigma'' + P_0'\left(P_0 - \frac{1}{\kappa}\log\varepsilon z + \frac{1}{\kappa}\right) - \kappa\left(2zu_z + z\Sigma''\right)_z = O(\varepsilon). \tag{3.145}$$

The solution u to this equation must match with the solution in the inner $O(e^{-\kappa/\varepsilon})$ region as $z \to 0$, and with the outer $O(1)$ region as $z \to \infty$. These conditions, obtained from (3.128) and (3.129), may be written as

$$u \sim z\Sigma'' - P_{10} - \frac{1}{2}(\Sigma')^2 + 3\kappa\Sigma' - \frac{1}{2}\left(\frac{1}{\kappa}\log\varepsilon z - P_0\right)^2 - \frac{P_0}{\kappa} + V_1 \tag{3.146}$$

as $z \to \infty$ and

$$u \sim \frac{1}{2}\left(T_b^2 - (P_0)^2\right) - \frac{P_0}{\kappa}\log\varepsilon z \tag{3.147}$$

as $z \to 0$. Here T_b^2 is to be determined.

Equation (3.145) is

$$\frac{\partial u}{\partial X} = 2\kappa\left(zu_z\right)_z + \frac{\partial}{\partial X}\left(z\Sigma'' - P_{10} - \frac{1}{2}(\Sigma')^2 - \frac{1}{2}(P_0)^2 + \frac{P_0}{\kappa}\log\varepsilon z - \frac{P_0}{\kappa} + \kappa\Sigma'\right) + O(\varepsilon) \tag{3.148}$$

or

$$u_X = 2\kappa(zu_z)_z + f_X, \tag{3.149}$$

so that if Γ satisfies

$$\Gamma_X = 2\kappa(z\Gamma_z)_z \tag{3.150}$$

then writing

$$u = \Gamma + f + g \tag{3.151}$$

leads to

$$g_X = 2\kappa\left(z(f+g)_z\right)_z = 2\kappa\left(z\Sigma'' + zg_z\right)_z \tag{3.152}$$

which is satisfied by the particular integral

$$g = 2\kappa\Sigma'. \tag{3.153}$$

Boundary conditions are therefore given (using (3.146) and (3.147)) by

$$\Gamma \sim V_1 - \frac{1}{2\kappa^2}\log^2 \varepsilon z \tag{3.154}$$

as $z \to \infty$, and

$$\begin{aligned} \Gamma &\sim \frac{1}{2}T_b^2 - \frac{2P_0}{\kappa}\log \varepsilon z + P_{10} + \frac{1}{2}(\Sigma')^2 + \frac{P_0}{\kappa} - 3\kappa\Sigma' && (3.155)\\ &=: \Lambda(X) - \frac{2P_0}{\kappa}\log \varepsilon z && (3.156) \end{aligned}$$

as $z \to 0$. Having found Γ,

$$u = \Gamma + z\Sigma'' - P_{10} - \frac{1}{2}(\Sigma')^2 - \frac{1}{2}(P_0)^2 + \frac{P_0}{\kappa}\log \varepsilon z - \frac{P_0}{\kappa} + 3\kappa\Sigma' + O(\varepsilon). \tag{3.157}$$

The Fourier transform $\widehat{\Gamma}(k, z)$ of Γ satisfies

$$z\widehat{\Gamma}'' + \widehat{\Gamma}' - \frac{ik}{2\kappa}\widehat{\Gamma} = 0, \tag{3.158}$$

which has the general solution

$$\widehat{\Gamma}(k, z) = A(k)I_0\left(\sqrt{\frac{2ik}{\kappa}}\sqrt{z}\right) + B(k)K_0\left(\sqrt{\frac{2ik}{\kappa}}\sqrt{z}\right), \tag{3.159}$$

where I_0 and K_0 are modified Bessel functions of order zero.

As $z \to 0$, $I_0(z) \to 1$ and $K_0(z) \sim -\left(\gamma + \log\frac{z}{2}\right)$, where γ is the Euler-Mascheroni constant. As $z \to \infty$, $I_0(z) \sim z^{-1/2}e^z$ and $K_0(z) \to 0$. Hence we must have $A(k) = 0$ to ensure that $\widehat{\Gamma}$ is not exponentially large as $k \to \pm\infty$ and is therefore invertible; this however means that as $z \to \infty$, $\widehat{\Gamma}(k, z) \to 0$ and so $\Gamma(X, z) \to 0$. It therefore must be the case that

$$V_1 \sim \frac{1}{2\kappa^2}\log^2 \varepsilon z \tag{3.160}$$

as $z \to \infty$ in order for a solution to exist. As $z \to 0$,

$$\widehat{\Gamma} \sim -B(k)\left(\gamma + \log\sqrt{\frac{ikz}{2\kappa}}\right) \tag{3.161}$$

which must match with the boundary condition (3.156) which in Fourier space is

$$\widehat{\Gamma} \sim \widehat{\Lambda}(k) - \frac{2\widehat{P_0}}{\kappa}\log z \tag{3.162}$$

as $z \to 0$ and hence we see straight away that

$$B(k) = \frac{4\widehat{P_0}}{\kappa} \tag{3.163}$$

by matching terms in $\log z$. Matching constant terms leads to

$$\widehat{\Lambda} = -\frac{4\widehat{P_0}}{\kappa}\left(\gamma + \frac{1}{2}\log\frac{ik}{2\kappa}\right), \tag{3.164}$$

and this allows us to find the unknown term T_b^2 in the expansion of the basal shear stress. We rearrange this as

$$\widehat{\Lambda} + \frac{4\widehat{P_0}}{\kappa}\left(\gamma - \frac{1}{2}\log 2\kappa\right) = -\frac{2}{\kappa}\widehat{P_0}\log ik, \tag{3.165}$$

so that it remains only to find the inverse Fourier transform of the right-hand side of this equation. We have

$$\widehat{P_0} = \widehat{\mathcal{H}(\Sigma')} = i\,\mathrm{sgn}\,k\widehat{\Sigma}', \tag{3.166}$$

and

$$\begin{aligned}\mathrm{sgn}\,k\log ik &= \mathrm{sgn}\,k\left(\log|k| + \frac{\pi}{2}i\,\mathrm{sgn}\,k\right)\\ &= \mathrm{sgn}\,k\log|k| + \frac{\pi i}{2},\end{aligned} \tag{3.167}$$

and therefore

$$\widehat{\Lambda} + \frac{4}{\kappa}\left(\gamma - \frac{1}{2}\log 2\kappa\right)\widehat{P_0} - \frac{\pi}{\kappa}\widehat{\Sigma}' = -\frac{2}{\kappa}\widehat{\Sigma}' i\,\mathrm{sgn}\,k\log|k|. \tag{3.168}$$

The inverse transform $h(X)$ of $i\,\mathrm{sgn}\,k\log|k|$ satisfies

$$h(X) = \frac{1}{2\pi}\int_{-\infty}^{\infty} e^{ikX} i\,\mathrm{sgn}\,k\log|k|\,\mathrm{d}k \tag{3.169}$$

which may be expressed after some manipulation as

$$h(X) = -\frac{1}{\pi}\,\mathrm{Im}\int_0^{\infty} e^{ikX}\log k\,\mathrm{d}k. \tag{3.170}$$

Integrating $e^{iX\zeta}\log\zeta$ over a right-angled wedge-shaped contour in the positive quadrant of the complex ζ-plane with an indent at the origin, we find

$$\int_0^{\infty} e^{ikX}\log k\,\mathrm{d}k = -\frac{1}{X}\left(\frac{\pi}{2} + i\left(\gamma + \log|X|\right)\right), \tag{3.171}$$

so that

$$h(X) = \frac{1}{\pi X}\left(\gamma + \log|X|\right). \tag{3.172}$$

Inverting (3.168) (using the convolution theorem $\widehat{f*g} = \widehat{f}\widehat{g}$), we obtain

$$\Lambda + \frac{2}{\kappa}\left(2\gamma - \log 2\kappa\right) P_0 - \frac{\pi}{\kappa}\Sigma' = -\frac{2}{\pi\kappa}\int_{-\infty}^{\infty} \frac{1}{\xi}\left(\gamma + \log|\xi|\right)\Sigma'(X-\xi)\,\mathrm{d}\xi \tag{3.173}$$

which leads to

$$T_b^2 = 2\left(\frac{\pi}{\kappa} + 3\kappa\right)\Sigma' - \frac{4}{\kappa}\left(2\gamma - \log 2\kappa\varepsilon + \frac{1}{2}\right)P_0 - 2P_{10} - (\Sigma')^2 - \frac{4}{\kappa}h * \Sigma'. \tag{3.174}$$

It now remains only to find an expression for P_{10}, where

$$P|_{Z=\varepsilon\Sigma} = P_0 + \varepsilon P_{10} + O(\varepsilon^2). \tag{3.175}$$

As $Z \to \infty$, we have

$$W^1 \sim (\Sigma U^0)_X = \big(\Sigma(U_0 - P^0)\big)_X = \Sigma' U_0 - (\Sigma P_0)_X \tag{3.176}$$

so that

$$\widetilde{W}^1 := W^1 - \Sigma' U_0 \sim -(\Sigma P_0)_X. \tag{3.177}$$

We then use (3.41) to (3.43) to obtain

$$P_X^1 - \widetilde{W}_Z^1 = R_1, \tag{3.178}$$

$$\widetilde{W}_X^1 + P_Z^1 = R_2, \tag{3.179}$$

where

$$R_1 := T_{1,X}^0 + T_{3,Z}^0 - U^0 U_X^0 - W^0 U_Z^0 + \Sigma' U_0' \tag{3.180}$$

and

$$R_2 := T_{3,X}^0 + T_{1,Z}^0 - U^0 W_X^0 - W^0 W_Z^0 - \Sigma'' U_0, \tag{3.181}$$

so that eliminating $\widetilde{W}^1$,

$$\nabla^2 P^1 = \nabla \cdot \boldsymbol{R} \quad \text{in} \quad Z > 0, \tag{3.182}$$

where

$$\boldsymbol{R} = (R_1, R_2). \tag{3.183}$$

For a suitable Green's function $G(X, Z, \xi, \zeta)$ (which we find below) we may write

$$\nabla \cdot \big(G(\nabla P^1 - \boldsymbol{R}) - P^1 \nabla G\big) = -\boldsymbol{R} \cdot \nabla G - P^1 \nabla^2 G, \tag{3.184}$$

then integrating over all X and $Z > 0$ and using Green's Theorem,

$$\int_{-\infty}^{\infty} \left[P^1 G_Z - G(P_Z^1 - R_2)\right]\big|_{Z=0}\,\mathrm{d}X = -\int_{-\infty}^{\infty}\int_0^{\infty} \boldsymbol{R}\cdot\nabla G\,\mathrm{d}Z\,\mathrm{d}X - P^1(\xi,\eta) \tag{3.185}$$

which may be simplified to

$$P^1(\xi,\eta) = -\int_{-\infty}^{\infty}\int_0^{\infty} \boldsymbol{R}\cdot\nabla G\,\mathrm{d}Z\,\mathrm{d}X + \int_{-\infty}^{\infty} (\Sigma P_0)_X\, G_X|_{Z=0}\,\mathrm{d}X. \tag{3.186}$$

G must satisfy

$$G_{XX} + G_{ZZ} = \delta\left(|(X,Z)-(\xi,\zeta)|\right), \quad Z>0 \tag{3.187}$$

and

$$G_Z = 0, \quad Z = 0, \tag{3.188}$$

and ∇G must be bounded at ∞ for the integrals in (3.186) to exist. Hence we have

$$G(X,Z,\xi,\zeta) = \frac{1}{2\pi}\left(\log r_1 + \log r_2\right), \tag{3.189}$$

where

$$r_1 = |(X,Z)-(\xi,\zeta)|, \tag{3.190}$$

$$r_2 = |(X,-Z)-(\xi,\zeta)|. \tag{3.191}$$

Then

$$G_X = \frac{X-\xi}{2\pi}\left(\frac{1}{r_1^2}+\frac{1}{r_2^2}\right) \tag{3.192}$$

and

$$G_Z = \frac{1}{2\pi}\left(\frac{Z-\zeta}{r_1^2}+\frac{Z+\zeta}{r_2^2}\right). \tag{3.193}$$

Hence

$$P_{10} = P^1(\xi,0) = -\frac{1}{\pi}\int_{-\infty}^{\infty}\int_0^{\infty}\frac{(X-\xi)R_1+ZR_2}{(X-\xi)^2+Z^2}\,\mathrm{d}Z\,\mathrm{d}X - \frac{1}{\pi}\int_{-\infty}^{\infty}\frac{(\Sigma P_0)_X}{X-\xi}\,\mathrm{d}X \tag{3.194}$$

which may be written in the form

$$P_{10}(X) = \frac{1}{\pi}\int_0^{\infty} a*R_1 - b*R_2\,\mathrm{d}Z - \mathcal{H}\left((\Sigma P_0)_X\right), \tag{3.195}$$

where

$$a(X,Z) = \frac{X}{X^2+Z^2}, \quad b(X,Z) = \frac{Z}{X^2+Z^2}, \tag{3.196}$$

and the convolution is done in the X variable, i. e.

$$(a*R_1)(X,Z) = \int_{-\infty}^{\infty} a(X-\xi,Z)R_1(\xi,Z)\,\mathrm{d}\xi. \tag{3.197}$$

Taking the Fourier transform,

$$\widehat{P_{10}} = \frac{1}{\pi}\int_0^\infty \widehat{a}\widehat{R_1} - \widehat{b}\widehat{R_2}\,\mathrm{d}Z + |k|\widehat{\Sigma P_0}. \tag{3.198}$$

$\widehat{a}$ and $\widehat{b}$ may be found by noting that $a - ib = z^{-1}$, where $z = X + iZ$, and integrating z^{-1} and $\overline{z}^{-1}$ over suitable semi-circular contours to obtain

$$(\widehat{a}, \widehat{b}) = \pi e^{-|k|Z}(-i\,\mathrm{sgn}\,k, 1). \tag{3.199}$$

Thus

$$\widehat{P_{10}} = -\int_0^\infty \left(i\,\mathrm{sgn}\,k\widehat{R_1} + \widehat{R_2}\right) e^{-|k|Z}\,\mathrm{d}Z + |k|\widehat{\Sigma P_0}. \tag{3.200}$$

We have also

$$\widehat{R_1} = ik\widehat{T_1^0} + \widehat{T_{3,Z}^0} - \widehat{U^0U_X^0} - \widehat{W^0U_Z^0} + ikU_0'\widehat{\Sigma}, \tag{3.201}$$

$$\widehat{R_2} = ik\widehat{T_3^0} - \widehat{T_{1,Z}^0} - \widehat{U^0W_Z^0} - \widehat{W^0W_Z^0} + k^2U_0\widehat{\Sigma}. \tag{3.202}$$

We now consider small perturbations to the uniform profile $\Sigma \equiv 0$, and thus ignore terms that are quadratic in the perturbation variables Σ and W^0. We obtain

$$\widehat{R_1} \approx ik\widehat{T_1^0} + \widehat{T_{3,Z}^0} + U_0'(ik\widehat{\Sigma} - \widehat{W^0}) + U_0\widehat{W_Z^0}, \tag{3.203}$$

$$\widehat{R_2} \approx ik\widehat{T_3^0} - \widehat{T_{1,Z}^0} - ikU_0\widehat{W^0} + k^2U_0\widehat{\Sigma}, \tag{3.204}$$

with

$$\widehat{T_1^0} \approx -2ik\kappa Z\widehat{P^0}, \tag{3.205}$$

$$\widehat{T_3^0} \approx 3ik\kappa Z\widehat{W^0}. \tag{3.206}$$

From (3.36), (3.37), and (3.196), we may write

$$W^0 = \frac{1}{\pi}b * \Sigma', \tag{3.207}$$

so that

$$\widehat{W^0} = ik\widehat{\Sigma}e^{-|k|Z}, \tag{3.208}$$

and similarly

$$P^0 = -\frac{1}{\pi}a * \Sigma', \tag{3.209}$$

so that

$$\widehat{P^0} = -|k|\widehat{\Sigma}e^{-|k|Z}. \tag{3.210}$$

Combining (3.208) and (3.210) with (3.203), (3.204), and (3.198) therefore leads to

$$\widehat{P_{10}} \approx -\widehat{\Sigma} \int_0^\infty \left(k^2(1+2e^{-|k|Z})U_0 - |k|(1-e^{-|k|Z})U_0' - 5ik|k|\kappa e^{-|k|Z}\right) e^{-|k|Z}\,\mathrm{d}Z \tag{3.211}$$

which may be simplified using

$$\gamma = -\int_0^\infty e^{-t}\log t\,\mathrm{d}t \tag{3.212}$$

to

$$\widehat{P_{10}} \approx \widehat{\Sigma}\left(\frac{2|k|}{\kappa}(\gamma + \log 2|k|) + \frac{5ik\kappa}{2}\right). \tag{3.213}$$

Then inverting the Fourier transform,

$$P_{10} \approx \frac{5\kappa}{2}\Sigma' - \frac{2}{\kappa}(\gamma+\log 2)\mathcal{H}(\Sigma') - \frac{2}{\kappa}h * \Sigma', \tag{3.214}$$

where h is as defined in (3.172).

Therefore

$$T_b^2 \approx \left(\frac{2\pi}{\kappa} + \kappa\right)\Sigma' - \frac{4}{\kappa}\left(\gamma - \log 4\varepsilon\kappa + \frac{1}{2}\right)\mathcal{H}(\Sigma') \tag{3.215}$$

and

$$T_b = 1 - 2\varepsilon\mathcal{H}(\Sigma') + \varepsilon^2\left(-\alpha\mathcal{H}(\Sigma') + \beta\Sigma'\right) + O(\varepsilon^3), \tag{3.216}$$

where

$$\alpha = \frac{4}{\kappa}\left(\gamma - \log 4\varepsilon\kappa + \frac{1}{2}\right) \tag{3.217}$$

and

$$\beta = \frac{2\pi}{\kappa} + \kappa. \tag{3.218}$$

3.5.10 Linear stability analysis II

We now have

$$(T_b)_X = -2\varepsilon\mathcal{H}(\Sigma'') + \varepsilon^2(-\alpha\mathcal{H}(\Sigma'') + \beta\Sigma'') + O(\varepsilon^3) \tag{3.219}$$

so that (3.96) becomes

$$\Sigma_t - 2q'(1)\mathcal{H}(\Sigma'') + \varepsilon(\beta\Sigma'' - \alpha\mathcal{H}(\Sigma''))q'(1) = 0 \tag{3.220}$$

and the usual perturbation formulation leads to

$$\sigma = -ik|k|q'(1)(2+\varepsilon\alpha) + \varepsilon\beta q'(1)k^2. \tag{3.221}$$

The growth rate is

$$\mathrm{Re}\,\sigma = \varepsilon\beta q'(1)k^2 > 0, \tag{3.222}$$

and we have successfully predicted an instability, though one which has an unbounded growth rate for short wavelength disturbances. The wave speed is

$$c = -\frac{\mathrm{Im}\,\sigma}{k} = q'(1)|k|(2+\varepsilon\alpha) \tag{3.223}$$

so that disturbances are propagated downstream.

The expression

$$T_b = 1 - \varepsilon(2+\varepsilon\alpha)\mathcal{H}(\Sigma') + \varepsilon^2\beta\Sigma' + O(\varepsilon^3) \tag{3.224}$$

is consistent with that used by Kroy et al [39], which is

$$T_b = 1 - A\mathcal{H}(\Sigma') + B\Sigma' \tag{3.225}$$

for positive constants A and B.

In order to get around the problem of unbounded growth rate at large wavenumber, it does not make sense to introduce a buoyancy term as in Section 2.6.4. This is because this term acted as a diffusive term, while the term that produces the instability in the current model is a backward diffusive term, and so introducing buoyancy will serve only to reduce, or remove completely, this destabilising effect.

Considering a non-saturated flux relation as was done in Section 2.8, we obtain

$$\mathrm{Re}\,\sigma = \frac{q_s'(1)(\varepsilon\beta k^2 - (2+\varepsilon\alpha)\mu|k|k^2)}{1+\mu^2k^2} \tag{3.226}$$

which is positive for small k and negative for large k, which is the behaviour we desire; again the flux relation has a stabilising effect at large wavenumber.

3.5.11 Numerical analysis

We now demonstrate briefly the numerical solution of a system including the shear stress form derived in this Chapter, along with the non-saturated flux equation. We may write our system as

$$\begin{aligned} s_t + q_x &= 0, && (3.227)\\ Q &= -a\mathcal{H}(s_x) + bs_x, && (3.228)\\ cq_x &= Q - q && (3.229) \end{aligned}$$

for positive constants a, b, and c, and in Fourier space these become

$$\frac{\mathrm{d}}{\mathrm{d}t}\widehat{s} + ik\widehat{q} = 0, \tag{3.230}$$

$$\widehat{Q} = a|k|\widehat{s} + bik\widehat{s}, \tag{3.231}$$

$$cik\widehat{q} = \widehat{Q} - \widehat{q}, \tag{3.232}$$

which may be combined into the single ODE for $\widehat{s}$

$$\frac{\mathrm{d}}{\mathrm{d}t}\widehat{s} = -\frac{ik}{1+ikc}\left(a|k| + ikb\right)\widehat{s}, \tag{3.233}$$

and this may be solved directly to obtain

$$\widehat{s} = \widehat{s_0}\exp\left[-\frac{ik}{1+ikc}\left(a|k| + bik\right)t\right]. \tag{3.234}$$

It is therefore straightforward to find solutions using only Fourier transforms. We find that the solution settles down from a random initial perturbation to a single dune-like profile, filling the whole domain as before, but with no limit to the dune's amplitude. An example is shown in Figure 3.1, and Figure 3.2 shows a plot of bed height s against generalised flux q — the multivalued relationship between s and q confirms that the dune is still growing.

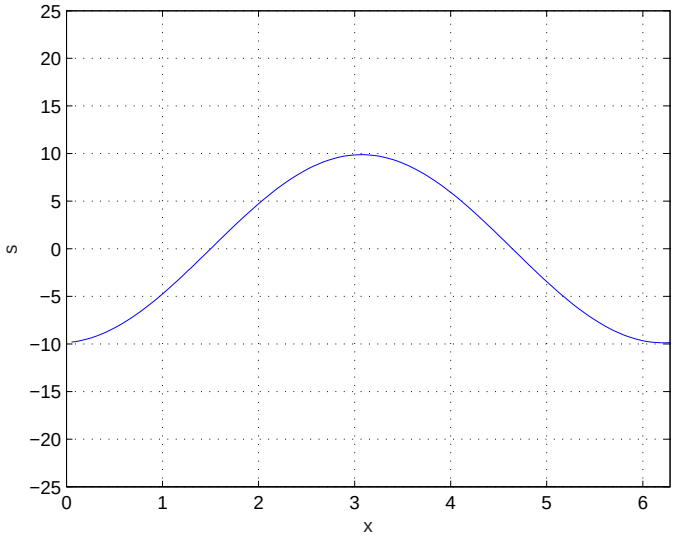


Figure 3.1: Numerical solution to dune system (3.227)–(3.229) with $a = 1$, $b = 1.5$, and $c = 1$.

We may modify this equation by referring back to (2.196). The ss_x term in this model came from the $\frac{1}{1-s}$ term earlier in the derivation; this was a result of the upper fluid boundary being rigid. If we artificially introduce this term into the expression for Q in our current system, i. e.

$$Q = -a\mathcal{H}(s_x) + bs_x + \frac{1}{2}s^2, \tag{3.235}$$

we note that it has the effect of limiting the amplitude of the solution, so that a steady-state travelling wave solution is obtained (see Figures 3.3 and 3.4).

We would also hope to be able to carry out a similar analysis to that in Section 2.7.1.1, where we solved the dune system of Chapter 2 on a semi-infinite domain. We may write

$$s(x,t) = \widetilde{S}(x,t)H(x), \tag{3.236}$$
$$q(x,t) = \widetilde{q}(x,t)H(x), \tag{3.237}$$
$$Q(x,t) = \widetilde{Q}(x,t)H(x), \tag{3.238}$$

and after substituting these into (3.227)–(3.229), applying the Fourier cosine transform, and writing these in terms of the Fourier transform of the even extensions, we

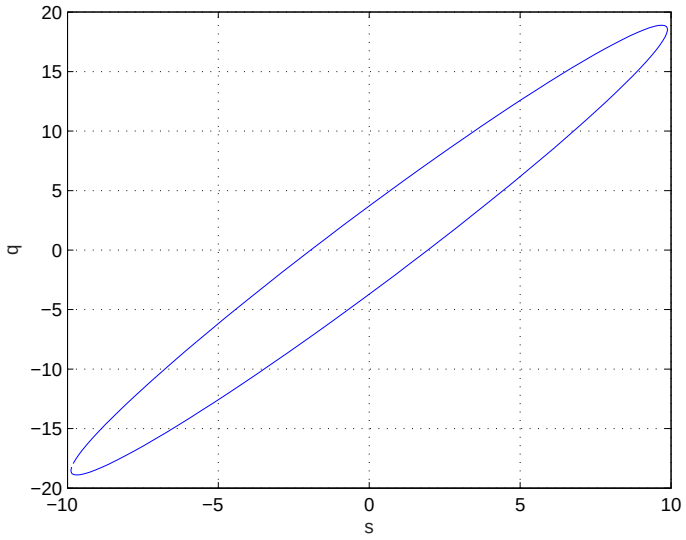


Figure 3.2: Plot showing bed height s against generalised flux q for the solution to the dune system (3.227)–(3.229) with $a = 1$, $b = 1.5$, and $c = 1$ shown in Figure 3.1. The multi-valued nature of the plot shows that the dune is still growing.

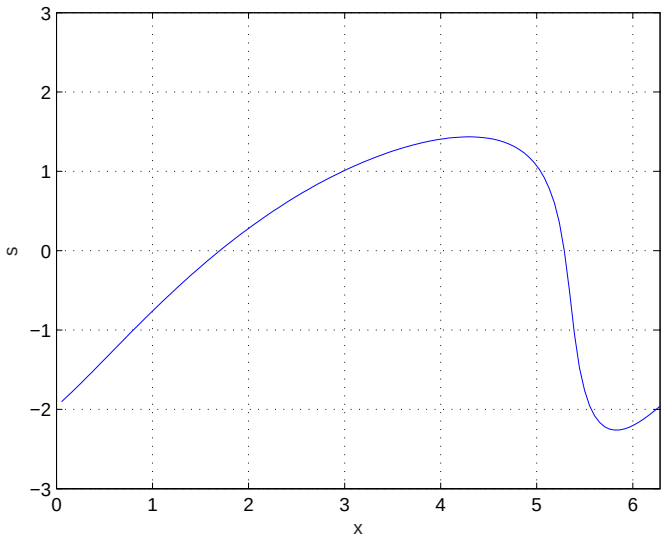


Figure 3.3: Numerical solution to modified dune system (3.227), (3.235), and (3.229) with $a = 1$, $b = 1.5$, and $c = 1$. The solution is that obtained for large t, i. e. a steady state travelling wave.

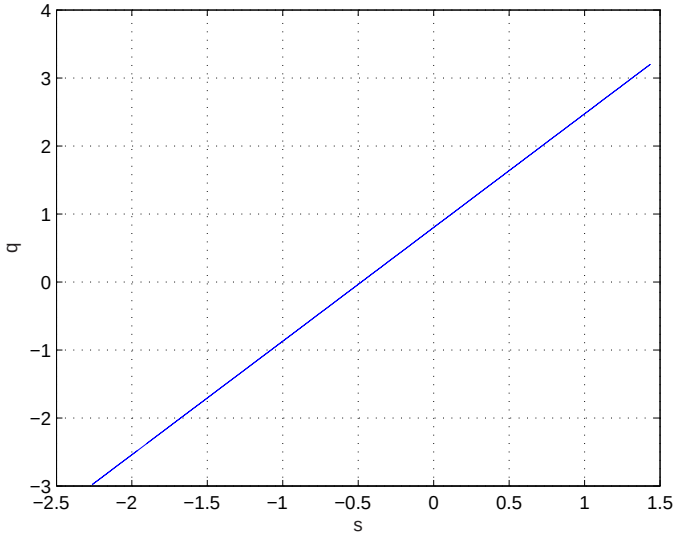


Figure 3.4: Plot showing bed height s against generalised flux q for the solution to the modified dune system (3.227), (3.235), and (3.229) with $a = 1$, $b = 1.5$, and $c = 1$ shown in Figure 3.3. The straight line shows that the solution is indeed a steady state travelling wave.

obtain (dropping tildas)

$$\frac{\mathrm{d}}{\mathrm{d}t}\widehat{s_e} + ik\widehat{q_e} = 0, \tag{3.239}$$

$$\widehat{Q_e} = (a|k| + bik)\,\widehat{s_e}, \tag{3.240}$$

$$cik\widehat{q_e} = \widehat{Q_e} - \widehat{q_e}, \tag{3.241}$$

so that again we may look for solutions to (3.227)–(3.229) that are non-zero on $[0, \infty)$ only. We show a sequence of resulting solutions in Figure 3.5, and we note that the solutions obtained are very similar to those obtained in Section 2.7.1.1. The biggest difference in this case is that upstream of the propagating dune, the bed is very slow to return to being horizontal. This is in contrast to the previous results when the dune train moved downstream leaving behind a flat bed.

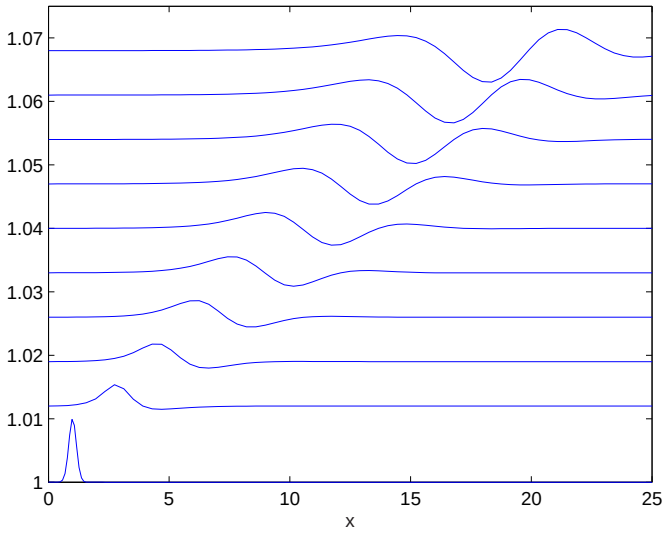


Figure 3.5: A sequence of solutions to (3.227)–(3.229) on the semi-infinite domain $[0, \infty)$. As the initial perturbation evolves, it forms a train of dunes which continues to grow for as long as we run the simulation.

As in Section 2.7.1.1, we do not observe a steady-state travelling wave when solving the dune system on a semi-infinite domain. However, our argument of Chapter 2 proving that this was impossible does not apply here, due to the fact that the integral term (i. e. the Hilbert transform) depends on the bed slope in both directions rather than just one.

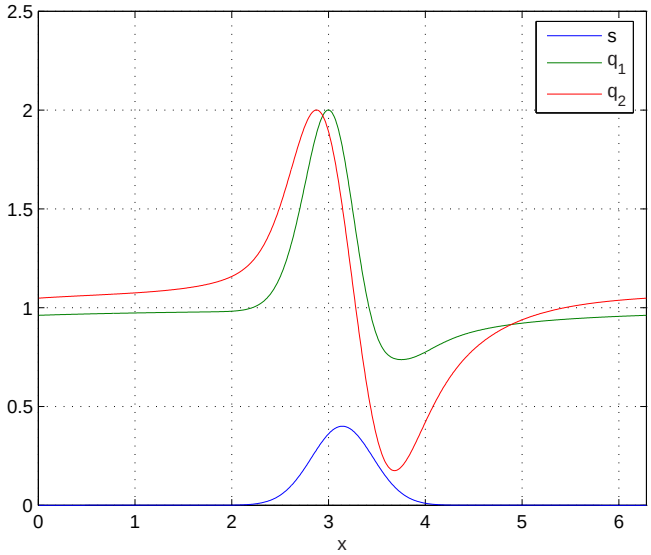


Figure 3.6: Comparison of sediment flux functions q_1 (constant eddy viscosity) and q_2 (mixing length) for a Gaussian dune profile s.

3.6 Comparison of sediment flux functions

We may again compare qualitatively the sediment flux function obtained in this Chapter with that of the previous Chapter. Figure 3.6 shows a Gaussian dune profile along with its associated sediment flux profiles q_1 and q_2, where q_1 is derived from the constant eddy viscosity theory of Chapter 2,

$$q_1 = \left\{ 1 + \frac{1}{2}s^2 + K * \frac{\partial s}{\partial x} - \frac{\partial s}{\partial x} \right\}^{\frac{3}{2}}, \tag{3.242}$$

and q_2 is the mixing length based sediment flux of this Chapter, being the solution to

$$\frac{\partial q_2}{\partial x} = \left\{ 1 - \mathcal{H}\left(\frac{\partial s}{\partial x}\right) + \frac{\partial s}{\partial x} \right\}^{\frac{3}{2}} - q_2. \tag{3.243}$$

We note that both profiles show the same basic qualitative shape, with the maximum sediment flux in both cases being attained a short distance upstream of the brink of the dune, this confirming that both models provide an instability.

In the next Chapter we go on to consider the mechanism of flow separation which we expect to stabilize the model, as well as providing the model with a natural length scale which it currently lacks.

Chapter 4

Aeolian modelling: Evolution equations

In this Chapter, we present a numerical simulation of an evolution system for dunes, based primarily on the mixing length model for wind flow presented in the previous Chapter. We describe a number of aspects of implementing the simulation, before presenting the results of the simulation.

4.1 Non-saturated flux equation

As has been seen in the previous Chapter, the non-saturated flux equation

$$\alpha q_x = q_s - q \tag{4.1}$$

due to Sauermann et al [55] (here in its linearized form) has the effect of ensuring a bounded growth rate for perturbations with large wavenumbers, when used with a mixing length model for shear stress and a Meyer-Peter Müller type law for the saturated flux. Therefore when implementing such a model numerically, we would expect this stabilising effect to lead to well-behaved solutions, since small departures from the solution caused by numerical errors will not grow.

An added benefit is the fact that even if the saturated flux q_s has jump discontinuities, there will still exist a solution q which is continuous — the effect of (4.1) is to smooth out these discontinuities by means of the *relaxation length* α^{-1}, which is a typical length over which the flux becomes saturated. When simulating the evolution of a dune with flow separation included, the shear stress τ, and therefore q_s, will be zero within the separated region, with no guarantee that they will be continuous at the extremes of this region. Using (4.1) will therefore ensure that the flux q is contin-

uous, thus avoiding numerical problems associated with discontinuous functions and their derivatives.

For example, we may illustrate this 'smoothing out' of discontinuities by solving (4.1) exactly in the case when q_s is piecewise constant. Suppose we have

$$q_s = \begin{cases} q_1, & x \in (-\infty, a), \\ q_2, & x \in [a, b], \\ q_3, & x \in (b, \infty); \end{cases} \tag{4.2}$$

the solution to (4.1) in each of the three intervals of the real line may be written

$$q = A_i e^{-x/\alpha} + q_s, \tag{4.3}$$

where the constant A_i is different in each interval. These constants may be found by requiring q to be continuous at $x = a$ and $x = b$ and bounded as $x \to \infty$. The solution is thus

$$q = \begin{cases} q_1, & x \in (-\infty, a), \\ q_2 + (q_1 - q_2)e^{a/\alpha}e^{-x/\alpha}, & x \in [a, b], \\ q_3 + \left[(q_1 - q_2)e^{a/\alpha} + (q_2 - q_3)e^{b/\alpha}\right] e^{-x/\alpha}, & x \in (b, \infty), \end{cases} \tag{4.4}$$

and we plot q_s and q in Figure 4.1.

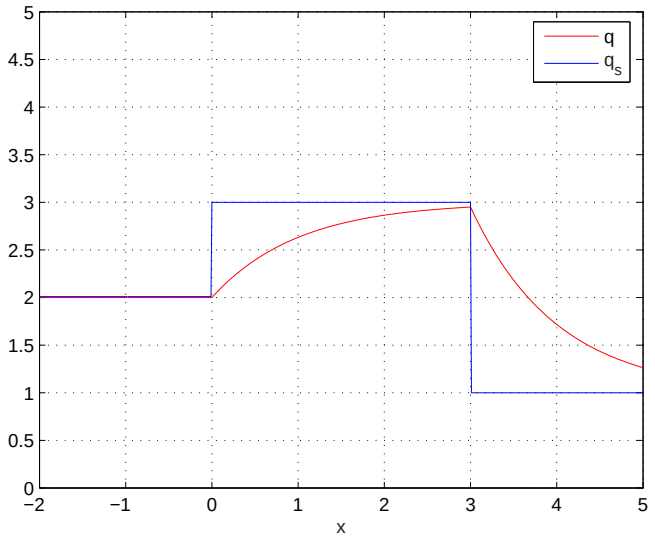


Figure 4.1: Plot of q_s from (4.2) and the solution q of (4.1) when $\alpha = 1$, $a = 0$, $b = 3$, $q_1 = 2$, $q_2 = 3$, and $q_3 = 1$.

4.2 Polynomial separation

In this Section we follow the example of Kroy et al [39] in describing the upper limit of the separated region in the lee of a dune using a polynomial function. Kroy et al suggest the use of a cubic polynomial in [39] but go into no further detail; here we attempt to recreate those details.

A cubic function has four degrees of freedom; we may specify four arbitrary constants. The most natural conditions to specify are that the wake profile joins smoothly to the bed profile at both endpoints. If the bed profile is

$$y = s(x), \tag{4.5}$$

the wake profile is

$$y = S(x) = A_0 + A_1(x-a) + A_2(x-a)^2 + A_3(x-a)^3, \tag{4.6}$$

and the endpoints are $x = a$ and $x = b$, then these conditions are

$$s(a) = S(a), \quad s'(a) = S'(a), \quad s(b) = S(b), \quad \text{and} \quad s'(b) = S'(b), \tag{4.7}$$

which lead to

$$\begin{aligned} A_0 &= s(a), \quad A_1 = s'(a), & (4.8)\\ s(b) &= s(a) + s'(a)(b-a) + A_2(b-a)^2 + A_3(b-a)^3, & (4.9)\\ s'(b) &= s'(a) + 2A_2(b-a) + 3A_3(b-a)^2, & (4.10) \end{aligned}$$

and the last two of these expressions may be solved to give A_2 and A_3 in terms of a, b, and $s(x)$, and hence the wake profile is known.

At this point, however, we have said nothing about the values of a and b, the positions of the separation and reattachment points respectively. Andreotti [7] suggests a condition which states that the slope of the wake profile should not exceed some critical value μ_c (which is certainly no larger than the the slope of the slip face). Assuming that the maximum slope is attained at a point $x_m \in (a, b)$, we have

$$S''(x_m) = 0, \tag{4.11}$$

so that

$$2A_2 + 6A_3(x_m - a) = 0, \tag{4.12}$$

and

$$x_m = a - \frac{A_2}{3A_3}. \tag{4.13}$$

Assuming further that the maximum slope attained is equal to the critical slope μ_c, we have

$$S'(x_m) = -\mu_c. \tag{4.14}$$

This may be written in full as

$$\begin{aligned} &[(b-a)(2s'(a)+s'(b)) - 3(s(b)-s(a))]^2 \\ &\quad = \; 3(b-a)(s'(a)+\mu_c)\left[(b-a)(s'(a)+s'(b)) - 2(s(b)-s(a))\right], \end{aligned} \tag{4.15}$$

which is an algebraic relation between a and b. Provided we know what μ_c is, we are therefore left with one free parameter which we may take to be a, the separation point. In the presence of a slip face, it is clear that a will coincide with the brink of the slip face, where there is a slope discontinuity which will induce flow separation.

In the absence of such a slope discontinuity, it is less clear where the separation point will be. It may be the case that the bed profile is sufficiently smooth and the aspect ratio of the dune sufficiently small that the mean flow will remain attached everywhere on the dune, but it is also true that separation may certainly occur over smooth profiles.

Due to the implicit form of (4.15), it is unclear when solving for b whether there is a unique solution, or even whether there is a solution at all. In the case of no solution, we are forced to assume that there is no flow separation present; in the case of multiple solutions, we simply take the smallest value of b as the solution, and we assume this is the most physical solution.

Figures 4.2 to 4.4 show the calculated polynomial wake profiles (in red) for certain bed profiles (in blue).

4.2.1 Limitations of polynomial separation

We now discuss some of the limitations of the polynomial method for modelling flow separation that we have described above. Firstly, as was noted in the previous Section, there is no guarantee of a unique solution to the problem, or that a solution exists at all. Non-existence of a solution is less of a difficulty, since we may interpret this physically as an indication of the flow not separating. Non-uniqueness, however, is more problematic to explain physically, and we are forced to make an *ad hoc* decision about which solution to choose.

Related to the disadvantage of non-uniqueness is the fact that the wake profile depends only on the bed elevation and slope at two points, the separation point and the reattachment point. This is in contrast to both the shear stress and the

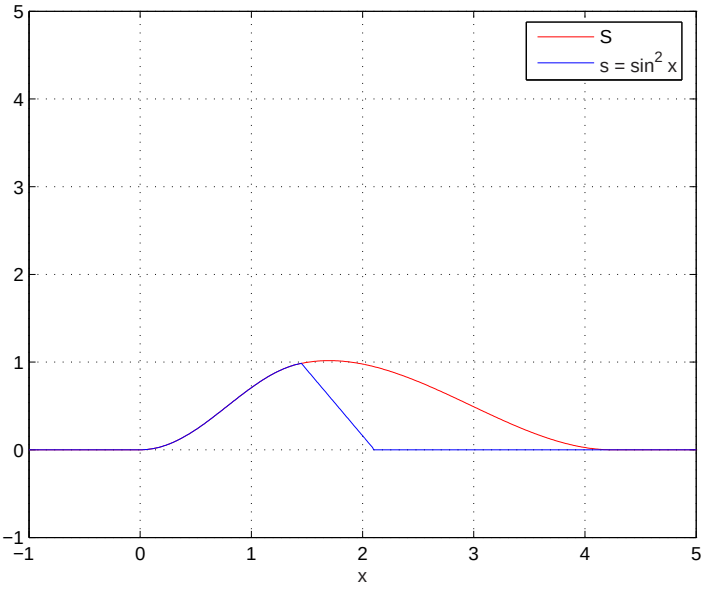


Figure 4.2: Polynomial flow separation with $\mu_c = 0.6$ for dune profile $s = \sin^2 x$, $x < 1.45$, and slip face with $\tan\theta = 1.5$.

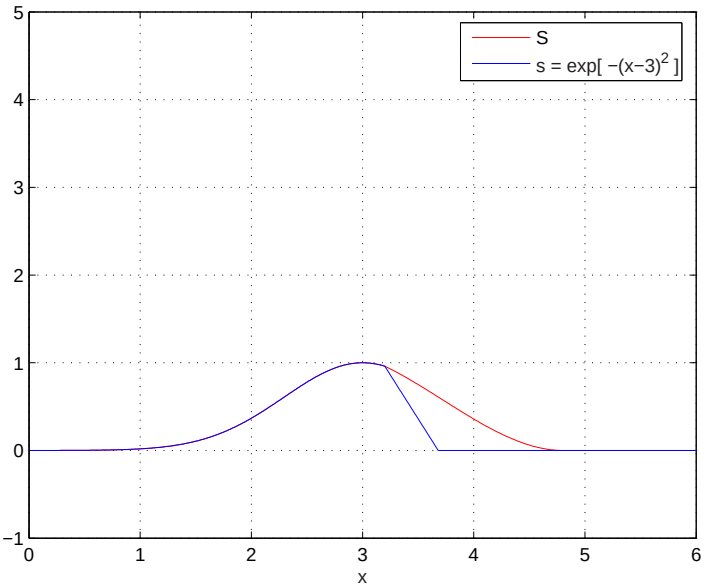


Figure 4.3: Polynomial flow separation with $\mu_c = 0.8$ for dune profile $s = \exp[-(x - 3)^2]$, $x < 3.2$, and slip face with $\tan\theta = 2$.

whole wind profile which depend on the bed slope at all points through the Hilbert transform, because the flow is described by an elliptic system (see (3.29) and (3.30)). Therefore we would also expect the shape of the wake region to be dependent on the bed at all points. The solution to the polynomial separation problem is thus ill-posed; we may change the solution substantially by making small adjustments to the bed profile in the neighbourhood of only two points.

Our final misgiving about the polynomial method regards the heuristic nature of the model. While the interpolation of a cubic polynomial works reasonably well in many cases, there is no guarantee that it will for an arbitrary dune, and there is no theory-based reason why a cubic polynomial should be a good approximation to the wake profile. In the next Chapter we attempt to approximate the wake profile using a model with a more theoretical basis, but for the rest of this Chapter we stick with this method and explore its use in an evolution system.

4.3 Comparison of sediment flux functions

In Figure 4.5 we show two different sediment flux profiles q_1 and q_2 calculated from a Gaussian dune with a slipface s. Both q_1 and q_2 are calculated using the mixing length model of Chapter 3, along with a non-saturated flux equation. The difference

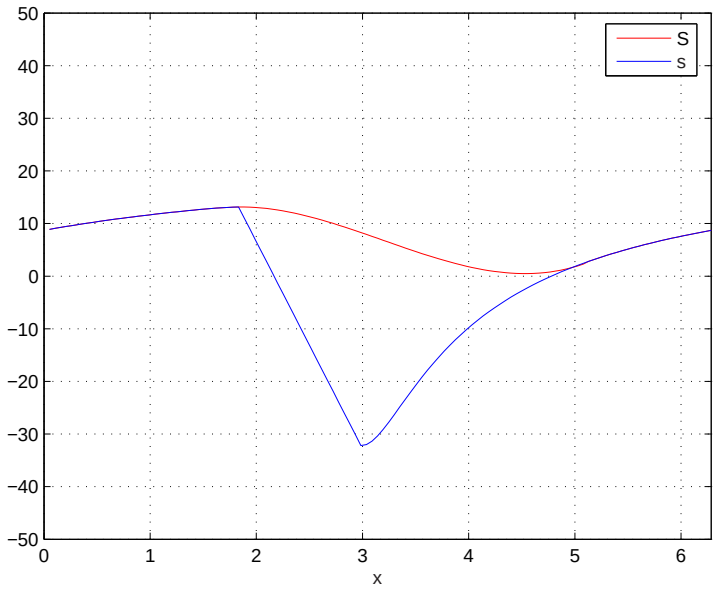


Figure 4.4: Polynomial flow separation with $\mu_c = 7$ for dune profile s from solution to evolution equation (2.197), $x < 1.83$, and slip face with $\tan\theta \approx 40$.

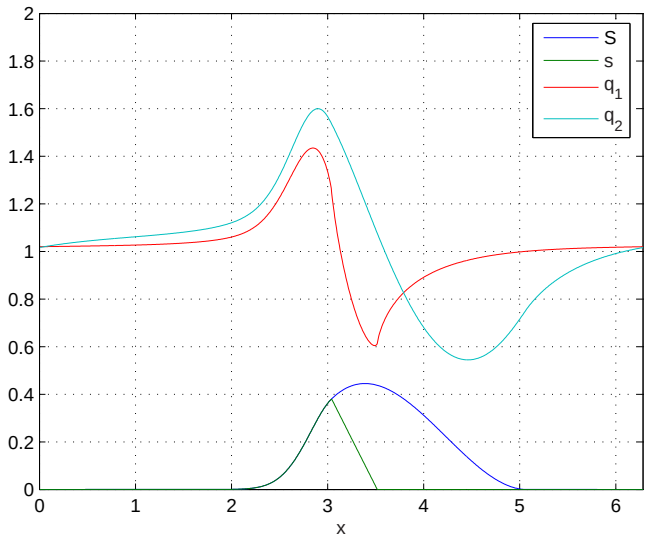


Figure 4.5: Comparison of sediment flux functions q_1 and q_2 for a Gaussian dune profile s with wake profile S.

is that we calculate q_1 as if the flow is not separated, while we calculate q_2 using the wake profile S derived above. Hence we solve

$$\frac{\partial q_1}{\partial x} = \left\{1 - \mathcal{H}\left(\frac{\partial s}{\partial x}\right) + \frac{\partial s}{\partial x}\right\}^{\frac{3}{2}} - q_1 \tag{4.16}$$

and

$$\frac{\partial q_2}{\partial x} = \left\{1 - \mathcal{H}\left(\frac{\partial S}{\partial x}\right) + \frac{\partial S}{\partial x}\right\}^{\frac{3}{2}} - q_2 \tag{4.17}$$

At first glance the two sediment flux profiles appear to be substantially different; however we are only interested in the behaviour on the upwind side of the separation point (which is coincident with the brink of the slipface). Downwind of this point we do not need q since we assume that all sediment is absorbed by the slipface (see below). In the non-separated region, the two profiles are qualitatively similar, but we note that q_1 underestimates the sediment flux on the upwind side of the dune compared to the separated flow version q_2.

4.4 Slip face propagation

It is well-known that sandpiles have an *angle of repose*, around 35°, which is the steepest angle that may be achieved on the surface of a stationary sandpile. It is also well-known that sand dunes frequently have a *slip face* on their downwind sides, a slip

face being a region of the surface which is at the angle of repose. When modelling the evolution of a dune or dunes, it is important to understand the mechanics of the slip face. Mobile sediment reaching the brink of the face will be deposited onto it, since within the region of flow separation (where the slip face is), the shear stress τ is zero and hence the sediment flux q rapidly decreases. Sediment being deposited will lead to a steepening of the surface past the angle of repose, and avalanching will occur. While it is possible to model the details of this avalanching behaviour, for example using the system of equations due to Bouchaud, Cates, Ravi Prakash, and Edwards [15], known as the BCRE equations, we choose to assume that the avalanching occurs on a much shorter time scale than the forward motion of the slip face. We assume further that the avalanches have the effect of distributing the sediment over the entire slip face, so that the slip face propagates forwards, retaining a constant slope — the angle of repose.

By considering the value of q at the brink of the slip face, we may infer the speed at which the slip face is moving. If the brink has position

$$(x, y) = (a(t), s(a(t), t)), \tag{4.18}$$

then by conservation of mass we have

$$q(a(t), t) = L(t)V_n(t), \tag{4.19}$$

where $L(t)$ is the length of the slip face at time t, and $V_n(t)$ is its normal velocity (see Figure 4.6). If $\theta > 0$ is the angle of repose, then the length is

$$L(t) = \frac{s(a(t), t) - s(b(t), t)}{\sin\theta} = \frac{b(t) - a(t)}{\cos\theta}. \tag{4.20}$$

We now consider the forward velocity of the slip face. A curve defined by

$$f(x, y, t) = 0 \tag{4.21}$$

satisfies

$$\frac{\mathrm{d}f}{\mathrm{d}t} = \dot{\boldsymbol{r}} \cdot \nabla f + \frac{\partial f}{\partial t} = 0, \tag{4.22}$$

and since ∇f is perpendicular to a line $f =$ constant, it is parallel to the normal to the curve $f = 0$ and we have

$$V_n = \dot{\boldsymbol{r}} \cdot \frac{\nabla f}{|\nabla f|} = -\frac{f_t}{|\nabla f|}. \tag{4.23}$$

Here the outward pointing normal corresponds to an increasing f in that direction; we therefore take

$$f(x, y, t) = y - s(a(t), t) + (x - a(t)) \tan\theta = 0, \tag{4.24}$$

so that its normal velocity is

$$V_n(t) = \left[\left(\frac{\partial s}{\partial x} + \tan\theta\right)\dot{a} + \frac{\partial s}{\partial t}\right]\Bigg|_{x=a(t)} \cos\theta. \tag{4.25}$$

Substituting this into (4.19) and solving for $\dot{a}$, we obtain an ODE for the position of the brink of the slip face

$$\frac{\mathrm{d}}{\mathrm{d}t}a(t) = \frac{\frac{q(a(t),t)}{b(t)-a(t)} - \frac{\partial s}{\partial t}(a(t), t)}{\frac{\partial s}{\partial x}(a(t), t) + \tan\theta}. \tag{4.26}$$

We may also obtain an expression for the change in the bed height s at a, since

$$\frac{\mathrm{d}}{\mathrm{d}t}s(a(t), t) = \frac{\mathrm{d}}{\mathrm{d}t}a(t)\frac{\partial s}{\partial x}(a(t), t) + \frac{\partial s}{\partial t}(a(t), t) = \frac{\mathrm{d}}{\mathrm{d}t}a(t)\frac{\partial s}{\partial x}(a(t), t) - \frac{\partial q}{\partial x}(a(t), t). \tag{4.27}$$

4.5 Numerical implementation

We now describe our method of solution of an evolution system incorporating a mixing length model for shear stress, a polynomial flow separation model, a non-saturated flux equation, and a propagating slip face. We first recapitulate the system that we are solving, before detailing the numerical schemes used.

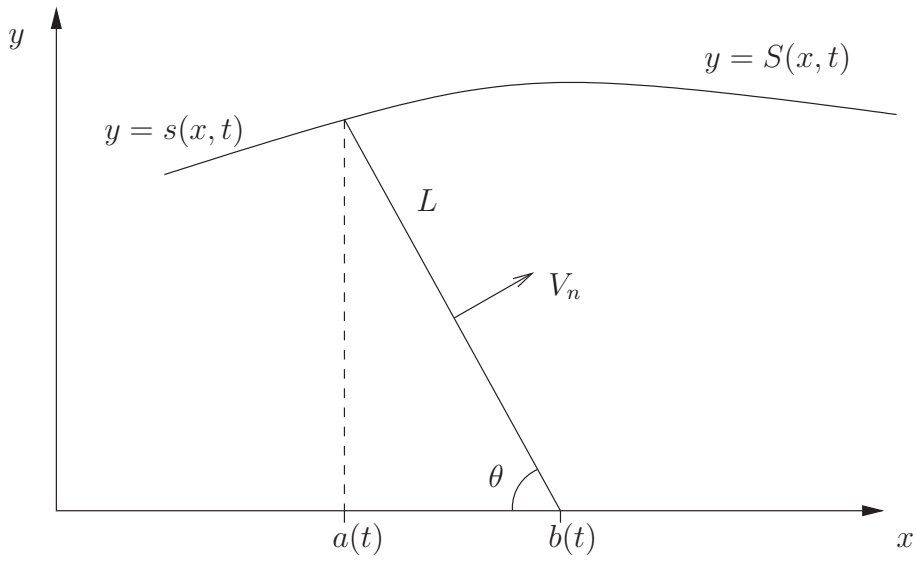


Figure 4.6: Geometry for a propagating slip face

4.5.1 Evolution system

The non-saturated flux equation is

$$\gamma q_x = Q - q, \tag{4.28}$$

with saturated flux

$$Q = \tau^{3/2}. \tag{4.29}$$

In combining the shear stress model with flow separation, we use the wake profile to calculate the non-local contribution to the shear stress outside the separated region, while inside this region the stress is taken to be zero. Hence we write

$$\tau = \begin{cases} 0, & x \in [a,c], \\ 1 - \alpha\mathcal{H}(S_x) + \beta S_x, & x \notin [a,c], \end{cases} \tag{4.30}$$

where a and c are the endpoints of the separated region (and may be considered as functions of time t), and $S(x,t)$ is the combination of the bed profile outside the separated region, and the wake region where this exists. Hence for polynomial separation

$$S(x,t) = \begin{cases} s(a) + s'(a)(x-a) + A_2(x-a)^2 + A_3(x-a)^3, & x \in [a,c], \\ s(x,t), & x \notin [a,c] \end{cases} \tag{4.31}$$

with the coefficients

$$A_2 = \frac{1}{(c-a)^2}\left(3(s(c)-s(a)) - (c-a)(2s'(a)+s'(c))\right), \tag{4.32}$$

$$A_3 = \frac{1}{(c-a)^3}\left((c-a)(s'(a)+s'(c)) - 2(s(c)-s(a))\right). \tag{4.33}$$

The reattachment point c is given by the algebraic equation

$$\begin{aligned} &\left[(c-a)(2s'(a)+s'(c)) - 3(s(c)-s(a))\right]^2 \\ &\quad = 3(c-a)(s'(a)+\mu_c)\left[(c-a)(s'(a)+s'(c)) - 2(s(c)-s(a))\right], \end{aligned} \tag{4.34}$$

while the separation point a is given by the differential equation

$$\frac{\mathrm{d}a}{\mathrm{d}t} = \left.\frac{\frac{q}{b-a} + q_x}{s_x + \tan\theta}\right|_{x=a}. \tag{4.35}$$

The evolution of the bed profile outside the separated region is described by

$$s_t + q_x = 0 \tag{4.36}$$

as usual. Inside the wake we have a slip face described by

$$s(x,t) = s(a,t) - \mu_s(x-a), \quad x \in [a,b] \tag{4.37}$$

where μ_s is the (constant) slope of the slip face, and b is the horizontal position of the bottom of the slip face, obtained from

$$s(b,t) = s(a,t) - (b-a)\tan\theta. \tag{4.38}$$

Throughout the region downwind of the slip face and upwind of the reattachment point the bed remains constant.

The above system may be considered as an evolution system for s consisting of 8 relations between 8 unknown functions $q(x,t)$, $Q(x,t)$, $\tau(x,t)$, $s(x,t)$, $S(x,t)$, $a(t)$, $b(t)$, and $c(t)$. Here we take (4.36) and (4.37), along with the condition that s is constant in t in the interval $[b,c]$, to be one relationship between s, q, a, b, and c.

We have assumed here that a slip face is present and that flow separation occurs. In the absence of these we would solve the reduced system

$$\gamma q_x = \tau^{3/2} - q, \tag{4.39}$$

$$\tau = 1 - \alpha\mathcal{H}(s_x) + \beta s_x, \tag{4.40}$$

$$s_t + q_x = 0. \tag{4.41}$$

We discuss later a mechanism for transition between the two systems, but for now we assume that a slip face is always present and separation occurs.

4.5.2 Numerical schemes

In order to solve the system (4.28) to (4.38), we use a Fourier spectral method for the spatial derivatives, and a simple forward Euler scheme for the time derivatives. The spectral method used has the advantage that the Hilbert transform term may easily be calculated without use of quadrature, since the Fourier transform of $\mathcal{H}(S_x)$ is $-|k|\widehat{S}$, where $\widehat{S}$ denotes the Fourier transform of S.

When solving the system (4.28) to (4.38), we therefore carry out the following procedure:

1. Start with a dune profile s, and the brink position a.
2. Calculate S, the wake profile, using (4.31) and (4.34).
3. Use S to get τ (4.30) and therefore Q (4.29).

4. Solve (4.28) to give q.

5. Use (4.35) to update the value of a at the next time step.

6. Evolve the dune profile over the same time step using (4.36), (4.37), and (4.38)

7. Return to 1.

4.6 Results of simulation

The system described above enables a fairly general study of dune evolution. We are now able to study a number of different situations.

4.6.1 A 2d barchan dune

We first consider the situation analogous to a barchan dune in 3d, with a finite volume of sand moving over an unerodible bed. This bed is dealt with by simply taking the shear stress τ to be zero whenever the bed elevation s reaches zero. Hence s may never become less than zero.

The Fourier spectral method forces the use of periodic boundary conditions, but we may still model the evolution of a single isolated dune. This is because upwind of the dune, where $s = 0$, the sediment transport rate q will be zero, and similarly downwind of the dune, since all sediment is deposited onto the slip face, the sediment flux will again be zero. We may therefore take our periodic domain to be as long as we wish, and the boundary conditions will be $s = q = 0$. This is also analogous to the dune system studied in Section 2.7.1.1.

We start the simulation with a sinusoidal bed profile

$$s(x, 0) = \sin^2 x, \tag{4.42}$$

with a slipface starting at an arbitrary point on the dune. The profile rapidly settles down to a shape which appears to be a steady-state travelling wave. The brink of the slipface occurs slightly upwind of where the top of the dune would be if the slip face were not present (i. e. the slope of the dune at the brink is small and positive). In Figure 4.7 we show a sequence of dune and wake profiles indicating the evolution of the profiles with increasing time. A close-up of the shape that the dune settles down to is shown in Figure 4.8, while Figure 4.9 is a plot of the flux q against bed elevation s for the profile in Figure 4.8. The linear relationship between q and s confirms that the dune is indeed a steady state travelling wave.

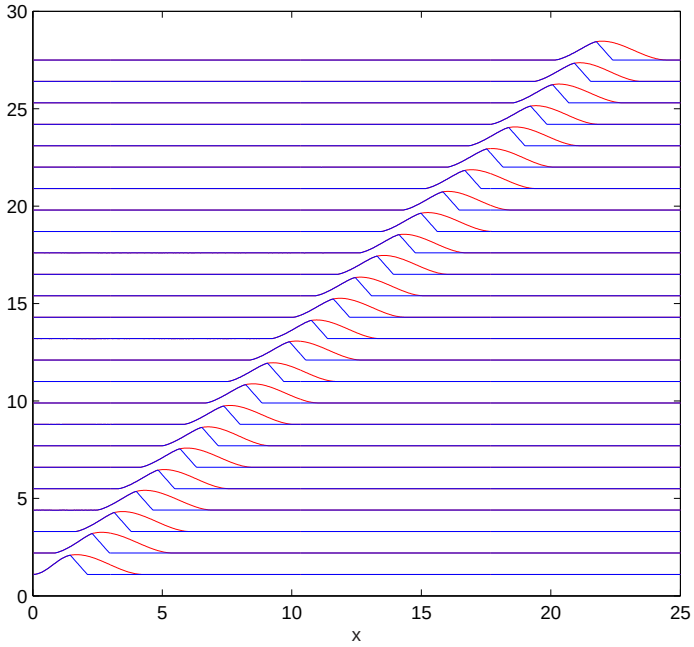


Figure 4.7: Series of plots of solution at regular time intervals to dune system with polynomial flow separation. The profile quickly settles down into a steady configuration.

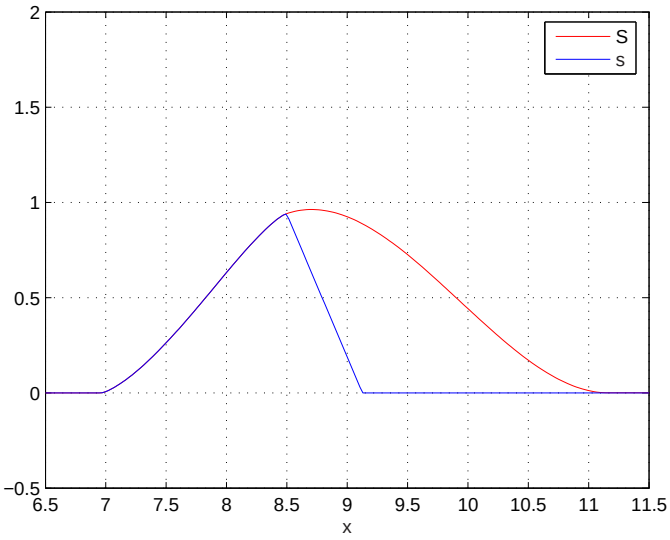


Figure 4.8: Close up of the dune profile and its associated wake profile for the steady state travelling wave that the solutions in Figure 4.7 settle down to.

4.6.1.1 Slipface disappears

We notice, while adjusting the various parameters in our model, that we may control the speed that the dune propagates downstream through the value of α. This is a result of the expression (3.223) for the wavespeed of perturbations, which increases linearly with α. Hence reducing the value of α results in a dune which propagates more slowly downstream. We note further that when this happens, any slipface propagates forward quicker than the bulk of the dune, spreading the dune out, and ultimately disappearing when its height reaches zero.

In order to study the evolution of a dune in this situation, we must adjust our numerical implementation to account for the possibility that the slipface (and thus any separation) disappears due to its size reaching zero. We do this by adding an extra step between steps 2 and 3 in the procedure in Section 4.5.2 which, if the length of the wake region is found to be zero, switches over to the non-separated evolution model of Chapter 3.

A sequence of dune and wake profiles arising from this implementation is shown in Figure 4.10. We observe that the slipface moves to the downstream end of the dune before disappearing, and then the dune continues to propagate downstream without a slipface in a steady state configuration. A close-up of this dune is shown in Figure 4.11, and the linear relationship between q and s in Figure 4.12 confirms that the profile is again a steady state travelling wave.

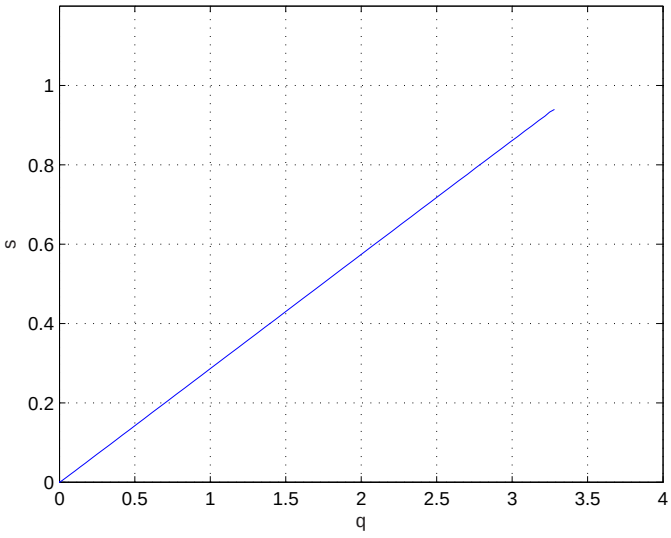


Figure 4.9: Plot of flux q against bed height s for the dune in Figure 4.8. The linear relationship confirms the existence of a steady state travelling wave.

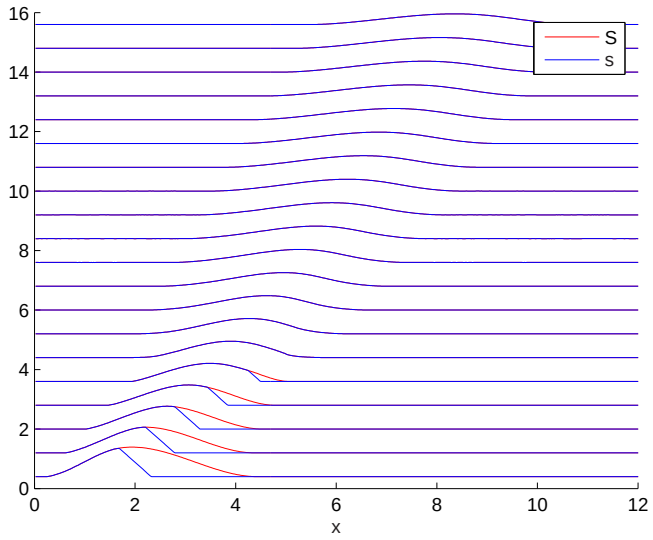


Figure 4.10: Series of plots of solution at regular time intervals to dune system with polynomial flow separation and parameters adjusted so that the slipface does not persist. The slipface moves forward and disappears, and the profile settles down into a steady configuration without separation.

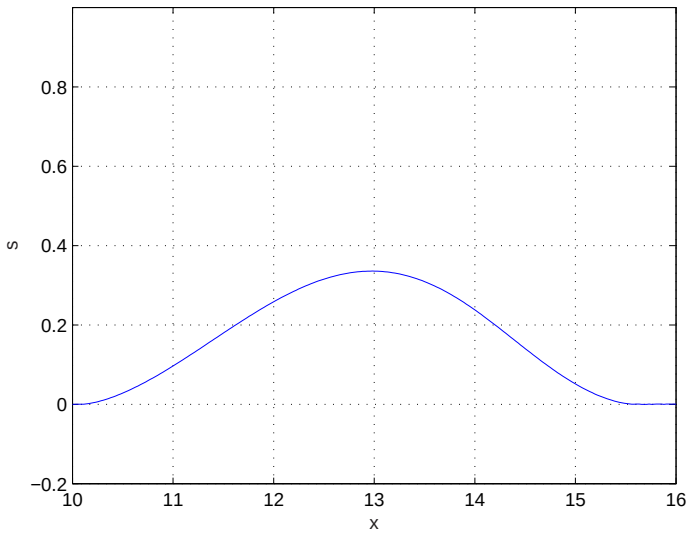


Figure 4.11: Close up of the dune profile without separation for the steady state travelling wave that the solutions in Figure 4.10 settle down to.

4.6.1.2 Slipface appears

We may now study the converse of the previous Section, that is, a dune without a slipface that subsequently gains one. We know that a slipface occurs when the slope of the dune exceeds the critical slope μ_c; if we start with a dune whose slope is everywhere less than μ_c and find that the dune steepens as it evolves, we must find a method of implementing the formation of a slipface.

The simplest way to initiate a slipface is to find the point at which the slope first reaches the critical slope, put a slipface there and then find the wake region. However, this approach does not work because there is no slope discontinuity at the brink of the slipface when it forms, so that there is no solution for the wake profile. Instead we must allow the slipface to propagate downstream, without separation, until the slope at the brink is sufficiently discontinuous for there to be a solution to the separation problem. We therefore have three different configurations that our system can be in: no slipface and no separation, slipface without separation, and slipface with separation. In the first case, we simply use the Exner equation (4.36) to evolve the profile everywhere. In the second case, we use the slipface equations (4.35) and (4.38) to propagate the slipface downstream, and use (4.36) to evolve the profile everywhere else. Finally, in the third case, we use (4.35) and (4.38) to propagate the slipface, leave the profile unchanged in the rest of the wake region, and use (4.36) everywhere else.

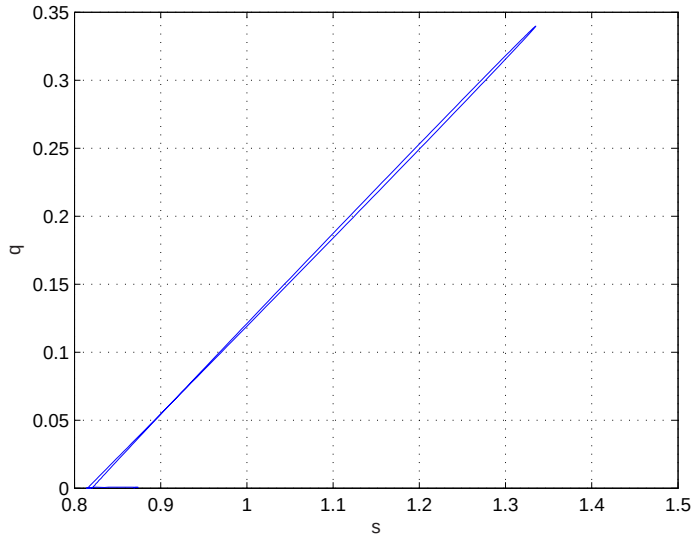


Figure 4.12: Plot of flux q against bed height s for the dune in Figure 4.11. The linear relationship confirms the existence of a steady state travelling wave.

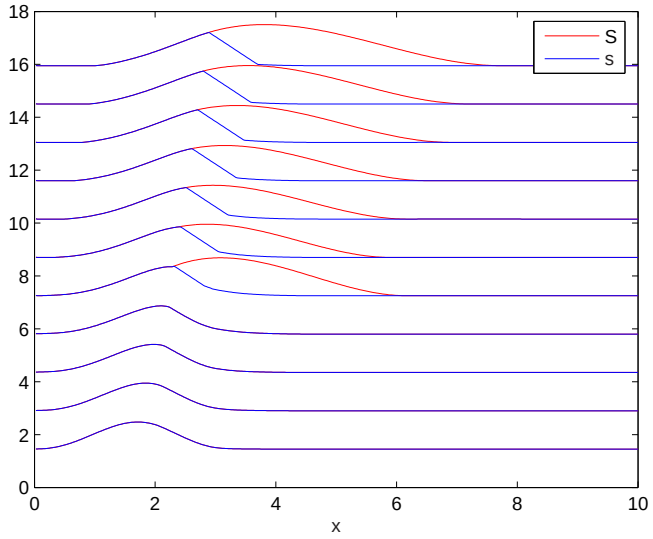


Figure 4.13: A sequence of solutions to the evolution system (4.28) to (4.38). We start with a profile without a slipface; this profile steepens and a slipfaces forms, before a wake region later appears and the dune approaches a steady state.

A sequence of solutions for this case is shown in Figure 4.13. We start with a Gaussian profile whose slope is everywhere less than the critical slope μ_c (in this case $\mu_c = 1.5$). As the profile evolves, the slope steepens on the downstream side of the dune. When the slope reaches the critical value μ_c, a slipface forms and grows in length. After a short time, there is a sufficient discontinuity in slope at the brink for a wake region to exist. After the slipface moves over what is left of the original dune, we are left with a steady state dune propagating downstream as in Section 4.6.1.

4.6.2 A dune moving over an inerodible obstacle

So far each of our simulations has been of a dune consisting of a finite volume of sand moving over a flat bed. This means that $s(b,t)$, the elevation of the bed at the bottom of the slipface, is always constant (and, without loss of generality, this constant can be zero). Hence the term $\frac{q}{b-a}$ in (4.35) may be written (using (4.38)) as $\frac{q\tan\theta}{s(a,t)}$ and so (4.35) and (4.38) decouple and may be solved independently. However, when $s(b,t)$ is not constant, the two equations (4.35) and (4.38) must be solved simultaneously. The simple forward Euler scheme for (4.35) that we used previously now fails, since it does not take into account the changing height of $s(b,t)$ when calculating the new position of the slipface. When $s(b,t)$ is increasing, the forward speed of the slipface is underestimated and the dune loses volume; conversely when $s(b,t)$ is decreasing,

the slipface propagates too quickly and the dune gains volume.

Instead we may use a *predictor-corrector* approach when solving (4.35) and (4.38): we use a forward Euler method for (4.35) to *predict* a new value of a, then use this predicted value to predict b from (4.38). We then use these predicted values in (4.35) to *correct* the value of a, and then use the corrected value of a to find a corrected value of b. We now write this method down more precisely. Let us write (4.35) and (4.38) as

$$\dot{a} = f(a,b), \tag{4.43}$$
$$b = g(a), \tag{4.44}$$

where we have assumed that (4.38) has a unique solution. The forward Euler scheme used previously may be written

$$a_{n+1} := a((n+1)\delta t) = a_n + \delta t f(a_n, b_n), \tag{4.45}$$
$$b_{n+1} := b((n+1)\delta t) = g(a_{n+1}), \tag{4.46}$$

where δt is the timestep used. Our improved predictor-corrector method is thus

$$a'_{n+1} = a_n + \delta t f(a_n, b_n), \tag{4.47}$$
$$b'_{n+1} = g(a'_{n+1}), \tag{4.48}$$
$$a_{n+1} = a_n + \delta t f(a'_{n+1}, b'_{n+1}), \tag{4.49}$$
$$b_{n+1} = g(a_{n+1}), \tag{4.50}$$

or more simply,

$$a_{n+1} = a_n + \delta t f\left(a_n + \delta t f(a_n, b_n), g(a_n + \delta t f(a_n, b_n))\right), \tag{4.51}$$
$$b_{n+1} = g(a_{n+1}). \tag{4.52}$$

In order to test this implementation, we introduce an inerodible obstacle for a dune to move over. In our example the obstacle is the piecewise linear profile

$$B = \begin{cases} \frac{1}{2}\left(1 - \frac{1}{\pi}|x - 4\pi|\right), & |x - 4\pi| < \pi, \\ 0, & |x - 4\pi| \geqslant \pi. \end{cases} \tag{4.53}$$

The obstacle is implemented in the same way to the inerodible bed: the shear stress τ is set to zero whenever $s \leqslant B$.

Results of the simulation are shown in Figures 4.14 to 4.17. We note that as the dune climbs the upwind slope, the slipface moves forward with respect to the dune, while on the downwind slope it retreats. This is consistent with the $\frac{q}{b-a}$ term in

(4.35) that was discussed above. We also note that the wake region becomes very small when the slipface moves forward, while on the downwind slope when the slipface retreats, the wake region becomes very large, both because of the retreating slipface as well as the fact that the dune is higher up due to the obstacle. Further, the dune has a lower height after passing the obstacle than before (and is thus more spread out horizontally); this is corrected as the dune moves downstream away from the obstacle and reapproaches the steady state. Finally, a plot of dune volume (which may easily be assessed qualitatively by summing the values of s at each grid point) shows that the volume remains constant throughout the simulation and therefore the predictor-corrector approach is successful.

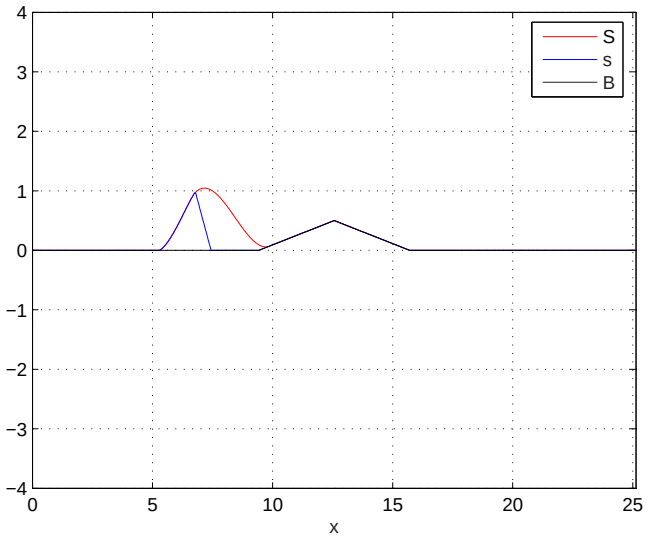


Figure 4.14: The first in a sequence of solutions to the system (4.28) to (4.38) in the case of an inerodible obstacle ($t = 1$).

4.6.3 A pair of 2d barchan dunes

Having successfully modelled the movement of a dune over an *inerodible* obstacle in the previous Section, the logical next step is to simulate the movement of a dune over an *erodible* obstacle, i. e. another dune. We may do this by taking our initial conditions to be a pair of dunes, sufficiently close together that the wake region of the first dune overlaps the second dune. Since there are (at least initially) two dunes, we must keep track of two slipfaces and two wake regions, letting each evolve independently.

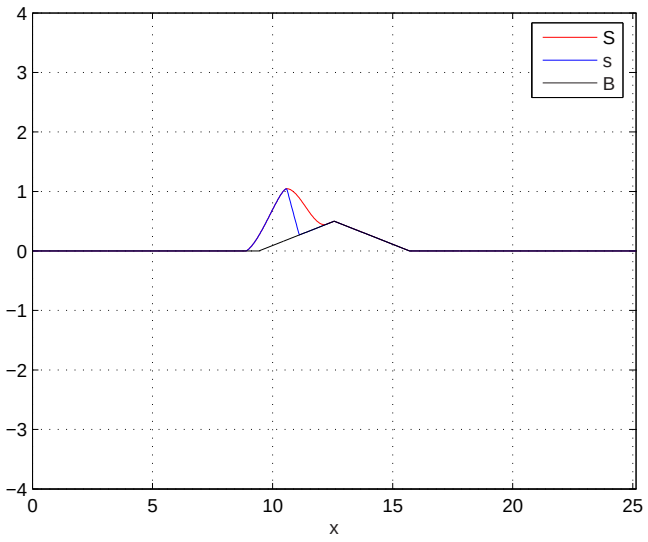


Figure 4.15: The second in a sequence of solutions to the system (4.28) to (4.38) in the case of an inerodible obstacle ($t = 1.5$).

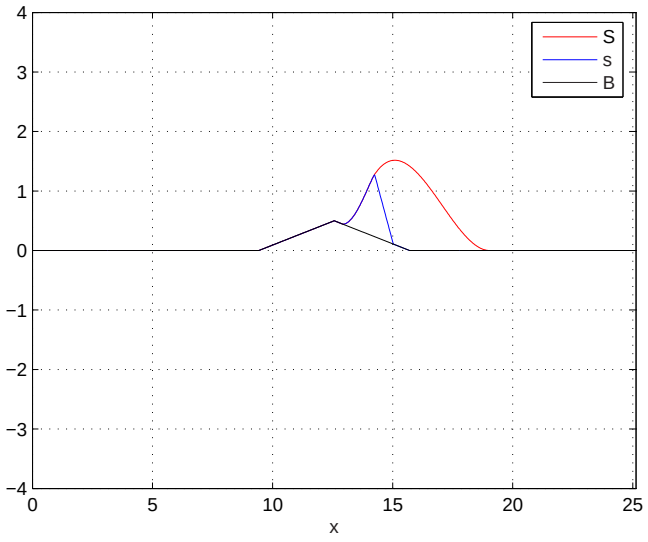


Figure 4.16: The third in a sequence of solutions to the system (4.28) to (4.38) in the case of an inerodible obstacle ($t = 2$).

One complication that arises in this situation is due to our method of solution of the non-saturated flux equation (4.28). In the case of one dune we could be sure that $q = 0$ at the foot of the dune because of the boundary conditions at $x = 0$. In this case, we require $q = 0$ both at the foot of the first dune and at the first reattachment point c_1 (since all sediment transported over the first dune is absorbed by its slipface). However, the spectral method used to solve (4.28) returns a continuous solution for q which does not satisfy $q = 0$ at c_1 (see Figure 4.18).

In order to overcome this difficulty, we may solve (4.28) in two parts. We first solve it as if only the second (right-hand) dune is present[1]. This ensures that $q = 0$ upwind of the dune and gives us a solution for q in $x > c_1$. We then solve (4.28) with only the first dune present, and this gives us a solution for q in $x < c_1$. On combining the two solutions, we have a solution q to (4.28) which satisfies $q(0) = q(c_1) = 0$.

While we keep track of two slipfaces and two wake regions, we must also allow for the possibility that the two dunes may start to overlap, and thus that their slipfaces and/or wake regions will overlap also. The first important thing that will happen after two dunes start to overlap is that the brink of the slipface of the second dune will fall inside the wake region of the first dune. At this time the brink will cease to be a separation point since it will lie inside the wake region of the first dune; there

[1]In fact we calculate the shear stress τ with both dunes present, so that both dunes contribute to the global Hilbert integral. We then calculate Q and set it to be zero over the extent of the first dune

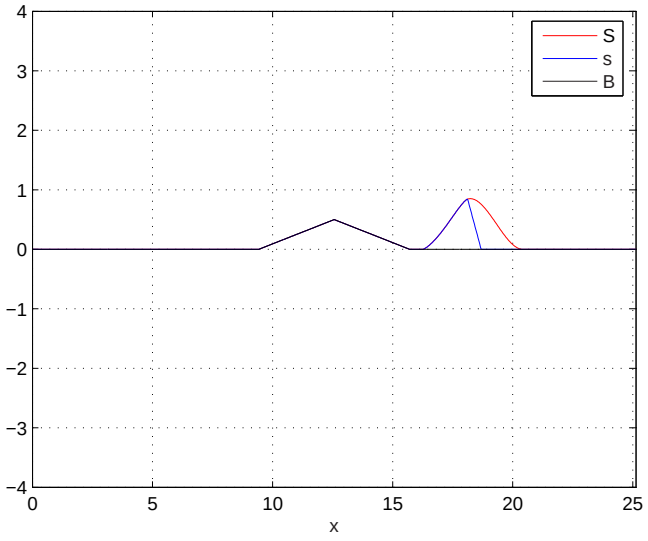


Figure 4.17: The fourth in a sequence of solutions to the system (4.28) to (4.38) in the case of an inerodible obstacle ($t = 2.5$)..

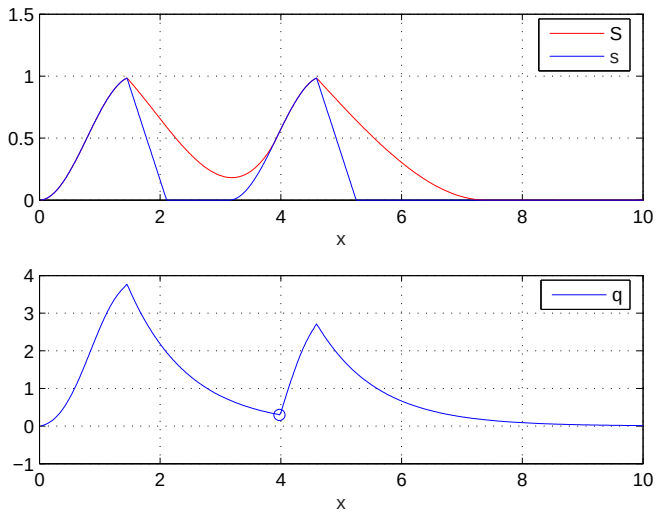


Figure 4.18: Standard continuous solution to (4.28) for q that does not satisfy $q = 0$ at the reattachment point c_1 (signified by a blue dot).

will be no flow to separate. Also, because the slipface of the second dune will be inside the wake region, it will no longer propagate forward. The first dune's slipface will then continue downstream until it reaches the second slipface. The two slipfaces will then become one, and the two dunes will propagate downstream as one single dune.

To demonstrate an example of how this situation happens, we may start with two sinusoidal profiles with slipfaces, placed sufficiently close together that the flow reattaches after the first wake region on the upwind slope of the second dune (see Figure 4.19). A sequence of solutions to the subsequent evolution is shown in Figures 4.20 to 4.23. The second dune immediately gets caught in the wake region of the first and spreads out. The first dune starts to climb up on the second, then the second dune gets completely enveloped by the first wake region, and finally the two slipfaces merge and the two dunes become one. We are then left with one large dune propagating downstream in a steady state configuration, as in Section 4.6.1.

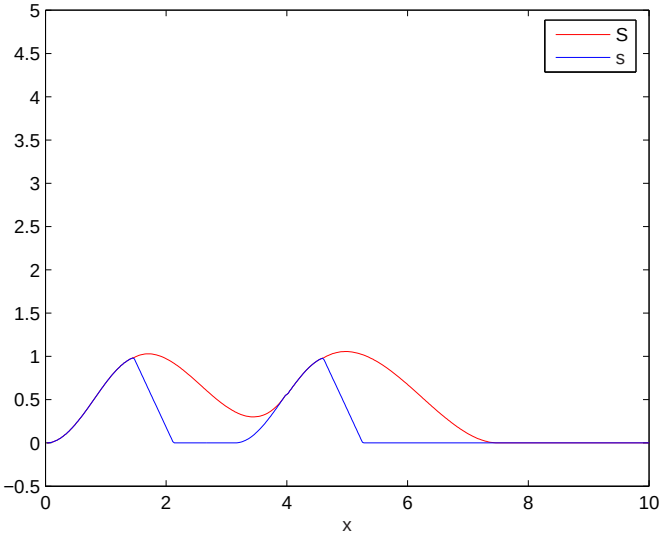


Figure 4.19: Initial conditions for the simulation of the interaction of two dunes. Note that the second dune is partly inside the wake region of the first.

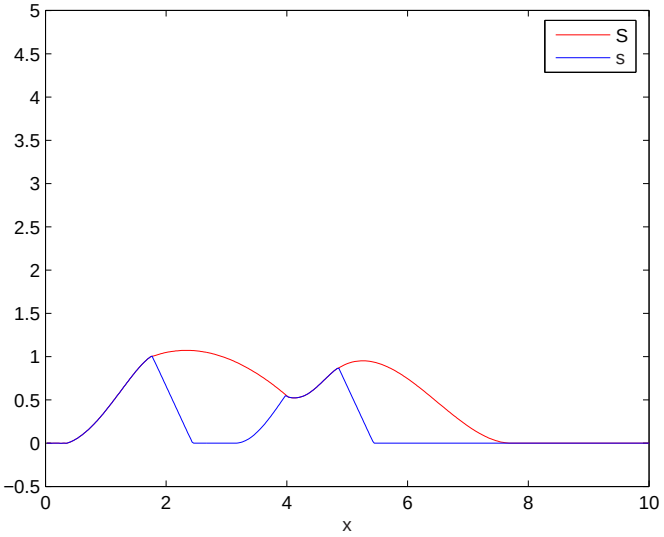


Figure 4.20: First in a sequence of solutions to (4.28) to (4.38) in the case of two interacting dunes ($t = 1$). The top of the second dune is being eroded and is causing the slipface to move downstream.

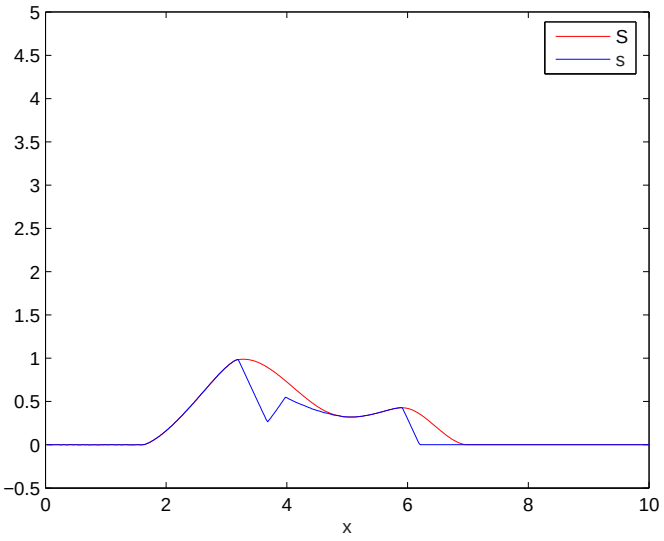


Figure 4.21: Second in a sequence of solutions to (4.28) to (4.38) in the case of two interacting dunes ($t = 2$). The second dune has spread out significantly due to being caught in the wake region of the first dune, and the first dune has started to move over the second dune.

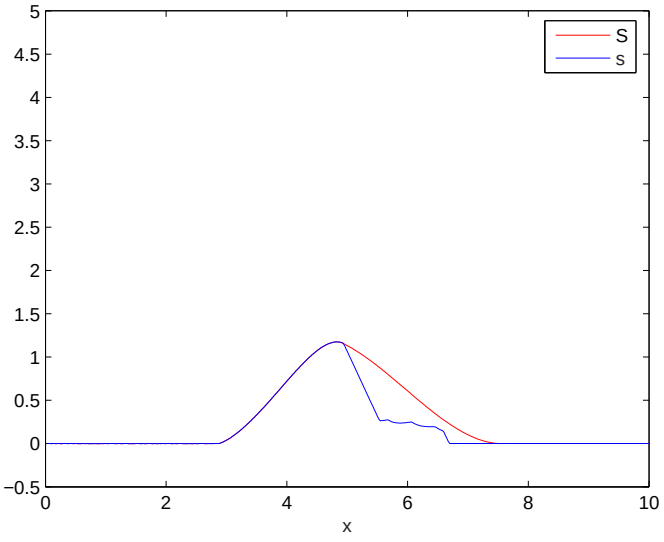


Figure 4.22: Third in a sequence of solutions to (4.28) to (4.38) in the case of two interacting dunes ($t = 3$). The wake region of the first dune now contains both dunes, as the first dune moves over what is left of the second dune.

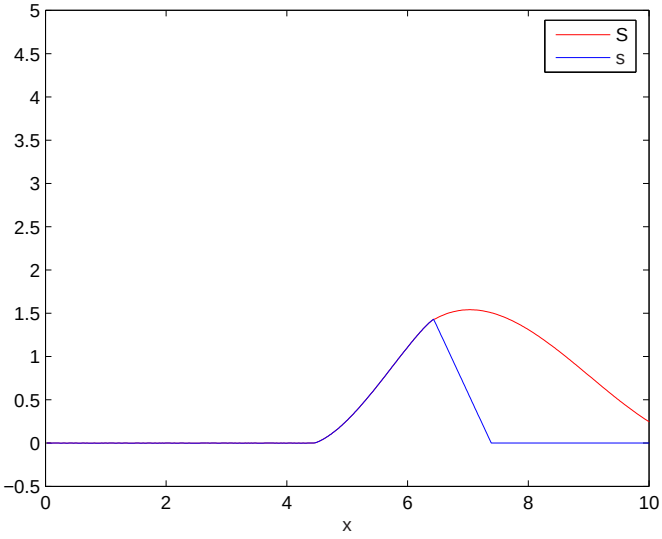


Figure 4.23: Fourth in a sequence of solutions to (4.28) to (4.38) in the case of two interacting dunes ($t = 4$). The two dunes have now become one large dune which moves downstream in a steady state configuration.

Chapter 5

Flow separation in the lee of a dune

The asymptotic theory for the flow of wind over a small hill presented in Chapter 3, and applied to dune evolution in Chapter 4, does not allow for the key mechanism of flow separation; the theory is based on the assumption that the flow remains attached everywhere. In this Chapter, we present a model for separated flow based on the asymptotic theory of Chapter 3. Our aim is to find the shape of the wake region (Figure 5.1).

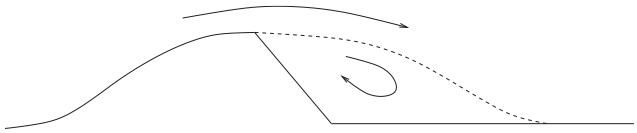


Figure 5.1: Recirculating wake in the lee of a dune. We hope to find the shape of the dotted line.

There is a considerably-sized literature on *triple deck theory* (for reviews see Smith [61]), which describes the structure of separated flow in a variety of circumstances. In the case of flow past a wall separating behind a disturbance (see e. g. [62]), a qualitative description of the flow is that the flow downstream of the disturbance consists of a recirculating region nearest the wall (the wake region), an undisturbed outer region, and an intermediate shear layer between the two. This is shown in Figure 5.2. The nature of this shear layer is that it increases in thickness further from the separation point, until it meets the wall again and the flow reattaches. In addition, if the disturbance has an aspect ratio ε, then the shear layer will have a typical thickness ε relative to its length.

We now describe and justify the assumptions that we make about the nature of the flow in the different regions. In the non-separated region, we saw in Chapter 3 that

there is a boundary layer of thickness ε (actually there are two layers — the roughness layer with thickness $e^{-1/\varepsilon}$, and the shear layer with thickness ε). We also know that there is a shear layer in the separated part of the flow which acts as a transition layer between the flow in the recirculating wake region below and the undisturbed flow above. If we assume that the magnitude of the flow in the wake region is small and may be neglected, then the shear layer above the wake region is identical to the boundary layer in the non-separated region, and thus the boundary conditions in the outer region are the same throughout the flow.

The triple-deck literature suggests that if the outer flow is $O(1)$, then the flow in the wake region will be $O(\varepsilon)$ (see e. g. [60]). It is therefore sensible to make the above assumption. While by doing this we have a boundary condition which applies everywhere, the position of the boundary on which the condition applies is unknown in the separated region. We therefore require a further condition for the flow in the wake region which will fix the position of the boundary.

Since we assume that the flow speed is an order of magnitude smaller in the wake region than in the outer flow, we may further assume that the pressure variation is of order ε in this region,

$$p = p_0 + \varepsilon p_1, \tag{5.1}$$

so that to a first approximation it is constant. This is analogous to previous studies which used a Helmholtz-Kirchhoff flow with constant pressure. Other studies also use the Prandtl-Batchelor Theorem [1], which states that a region of flow inside closed streamlines will have constant vorticity, or a combined approach (e. g. [48]).

To leading order in ε we have, from (3.15) to (3.17),

$$u_x + v_y = 0, \tag{5.2}$$

$$u_x + p_x = 0, \tag{5.3}$$

$$v_x + p_y = 0 \tag{5.4}$$

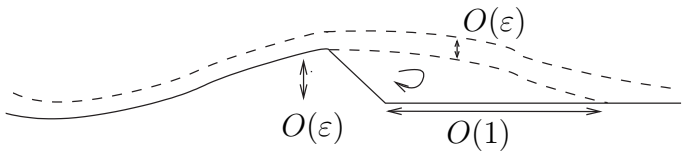


Figure 5.2: A schematic layout of separated flow

for u, v, and p. We may immediately eliminate u to obtain

$$p_x = v_y, \tag{5.5}$$

$$p_y = -v_x \tag{5.6}$$

which are the Cauchy-Riemann equations of complex analysis [50] for p and v, and imply, under suitable assumptions about the first derivatives of p and v, that $p+iv$ is a holomorphic function of $z = x + iy$. Alternatively we may further eliminate v from the system, which leaves Laplace's equation for p,

$$\nabla^2 p = 0. \tag{5.7}$$

These two approaches are related due to the well-known fact that the real part of a holomorphic function is harmonic.

We now denote the position of the bed as $y = s_0(x)$, and the position of the boundary layer as $y = s_1(x)$. Hence in the separated region, s_1 is the upper limit of the wake region, while outside the separated region, $s_0 = s_1$.

The boundary condition, from (3.82), is therefore

$$v = s_1'(x) \quad \text{on} \quad y = s_1(x), \tag{5.8}$$

which may be differentiated and written in terms of p to obtain

$$p_y = -s_1''(x) \quad \text{on} \quad y = s_1(x). \tag{5.9}$$

Since s_1 is assumed to be small, we may linearize this boundary condition and evaluate it on $y = 0$.

We further have the condition

$$p \to 0 \quad \text{as} \quad y \to \infty. \tag{5.10}$$

Our assumption that p was constant in the wake region means that we are able to state the entire problem in terms of two unknowns, p and s_1:

$$\nabla^2 p = 0, \quad y > 0, \tag{5.11}$$

$$p_y = -s_1'', \quad y = 0, \tag{5.12}$$

$$s_1(x) = s_0(x) \quad \text{outside separated region}, \tag{5.13}$$

$$p = \text{constant inside separated region}, \tag{5.14}$$

$$p \to 0 \quad \text{as} \quad y \to \infty. \tag{5.15}$$

As mentioned above, we may equivalently look for an analytic function

$$\theta(z) = p(x, y) + iv(x, y) \tag{5.16}$$

whose real part p satisfies the boundary conditions above. Now if θ is analytic then so is

$$\theta' = \frac{\mathrm{d}\theta}{\mathrm{d}z}; \tag{5.17}$$

hence if we recast the problem in terms of θ', the condition

$$p = \text{constant} \tag{5.18}$$

becomes

$$p_x = 0, \tag{5.19}$$

which is easier to deal with.

We now extend θ' to a function which is analytic everywhere in $\mathbb{C}$, except on the real axis. We do this by defining

$$\Omega(z) = \begin{cases} \theta'(z), & \operatorname{Im} z > 0, \\ -\overline{\theta'(\overline{z})}, & \operatorname{Im} z < 0. \end{cases} \tag{5.20}$$

Using

$$\frac{\partial}{\partial x} = \frac{\partial}{\partial z} + \frac{\partial}{\partial \overline{z}} \tag{5.21}$$

and

$$\frac{\partial}{\partial y} = i\left(\frac{\partial}{\partial z} - \frac{\partial}{\partial \overline{z}}\right), \tag{5.22}$$

the boundary condition that p is constant becomes

$$\begin{aligned} 0 &= p_x|_{y=0} \\ &= \frac{1}{2}\left(\lim_{y\to 0+} \theta'(z) + \lim_{y\to 0-} \overline{\theta'(\overline{z})}\right) \\ &= \frac{1}{2}(\Omega^+ - \Omega^-), \end{aligned} \tag{5.23}$$

where

$$\Omega^+ = \lim_{y\to 0+} \Omega(z) \tag{5.24}$$

and

$$\Omega^- = \lim_{y\to 0-} \Omega(z). \tag{5.25}$$

Hence

$$\Omega^+ = \Omega^-, \tag{5.26}$$

and so Ω is continuous over the part of the real axis corresponding to the separated region.

The boundary condition

$$p_y = -s_1''(x) \tag{5.27}$$

becomes

$$\Omega^+ + \Omega^- = 2is_1''(x). \tag{5.28}$$

Denoting the part of the real axis corresponding to the separated region by $B := [a, b] \subset \mathbb{R}$, and the remaining part by $B' = \mathbb{R} \setminus B$, we see from (5.26) and (5.28) that Ω is analytic everywhere in $\mathbb{C} \setminus B'$. B' may therefore be considered as a branch cut for Ω.

In order to progress further with this problem, it is necessary to make additional assumptions about the bed profile $s_0(x)$. We make the assumption that the bed consists of a periodic train of dunes. For convenience, we may scale x so that the period is 2π, ensuring for simplicity that $[a, b] \in [0, 2\pi]$.

Having made this assumption, we may now apply a conformal mapping to the complex plane so that the real axis is mapped to the unit circle centred at the origin. The transformation is

$$\zeta = e^{iz}. \tag{5.29}$$

We denote the images of B and B' by Γ and Γ', i. e.

$$\Gamma = \left\{ e^{ix} : x \in B \right\} \tag{5.30}$$

and

$$\Gamma' = \left\{ e^{ix} : x \in B' \right\}. \tag{5.31}$$

We also write

$$\xi = e^{ix}, \tag{5.32}$$

$$w(\zeta) = \Omega(z), \tag{5.33}$$

$$\sigma_0(\xi) = s_0''(x), \tag{5.34}$$

and

$$\sigma_1(\xi) = s_1''(x). \tag{5.35}$$

The problem is now to find a function $w(\zeta)$, which is analytic in $\mathbb{C} \setminus (\Gamma \cup \Gamma') = \{\zeta \in \mathbb{C} : |\zeta| \neq 1\}$, and a function $\sigma_1(\xi)$, defined on $\Gamma \cup \Gamma'$, satisfying

$$\begin{aligned} w^+(\xi) + w^-(\xi) &= 2i\sigma_1(\xi), \qquad \xi \in \Gamma \cup \Gamma', && (5.36)\\ w^+(\xi) &= w^-(\xi), \qquad \xi \in \Gamma, && (5.37)\\ \sigma_0(\xi) &= \sigma_1(\xi), \qquad \xi \in \Gamma', && (5.38)\\ w(0) &= 0, && (5.39)\\ w(\zeta) &= -w^*(\zeta), && (5.40) \end{aligned}$$

where

$$w^*(\zeta) := \overline{w\left(1/\overline{\zeta}\right)}. \tag{5.41}$$

Since $w^+(\zeta) = \Omega^+(z)$, and the upper half plane maps under (5.29) to the interior of the unit circle, w^+ is taken on the interior of the unit circle, and w^- on the exterior.

This problem is a Hilbert problem, see e. g. [16] or [46], with the added complication that the location of Γ is unknown, i. e. the end points $\xi_a = e^{ia}$ and $\xi_b = e^{ib}$ must be found. The geometry of the problem is shown in Figure 5.3.

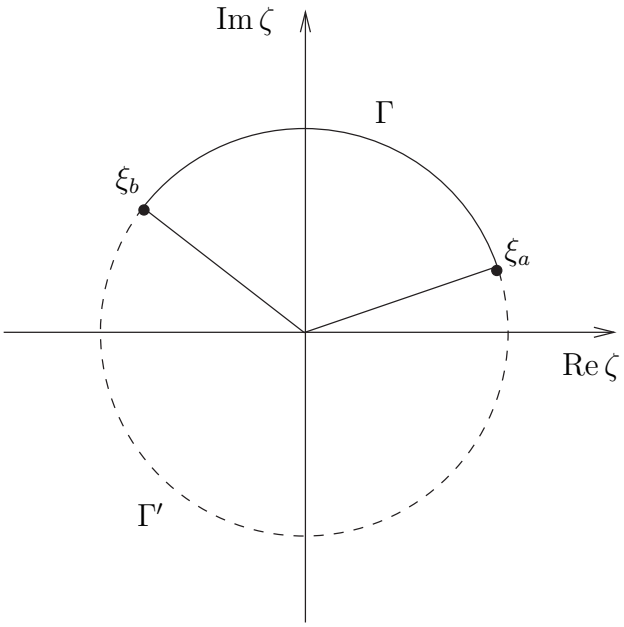


Figure 5.3: Geometry for mixed Hilbert problem

Once we have solved the Hilbert problem for w (along with the endpoints a and b), we may use (5.28) to obtain s'' on Γ, where it is unknown. Integrating twice, and using the two arbitrary constants to preserve continuity, will give us s, the upper profile of the wake region. We return to this in Section 5.3.

5.1 Solution of Hilbert problem

We first find an expression for $w(\zeta)$, ignoring the fact that the endpoints of Γ' are unknown. If we can find a function $\chi(\zeta)$ satisfying

$$\chi^+ + \chi^- = 0 \tag{5.42}$$

on Γ', with χ continuous on Γ and analytic everywhere else, then equation (5.36) may be written

$$w^+ - \frac{\chi^+}{\chi^-} w^- = 2i\sigma_1, \tag{5.43}$$

or

$$\frac{w^+}{\chi^+} - \frac{w^-}{\chi^-} = \frac{2i\sigma_1}{\chi^+}. \tag{5.44}$$

By Cauchy's integral formula,

$$\int_{|z|=1} \frac{f(z)}{z-a}\,\mathrm{d}z = \begin{cases} 2\pi i f(a), & |a|<1, \\ 0, & |a|>1. \end{cases} \tag{5.45}$$

Let

$$\begin{aligned} \phi(\zeta) &= \frac{1}{\pi}\int_{\Gamma'} \frac{\sigma_1(\xi)}{\chi^+(\xi)(\xi-\zeta)}\,\mathrm{d}\xi, \\ &= \frac{1}{\pi}\left(\int_{|\xi|=1} \frac{\sigma_1}{(\xi-\zeta)\chi^+}\,\mathrm{d}\xi - \int_{\Gamma} \frac{\sigma_1}{\chi^+(\xi-\zeta)}\,\mathrm{d}\xi\right), \end{aligned} \tag{5.46}$$

where we have continued the function $\sigma_1(\xi)$ onto Γ. Now take ζ to be on the inside of the unit circle, then since σ_1/χ^+ is analytic, the first term is equal to $i\sigma_1(\xi)/\chi^+(\xi)$ by (5.45). Taking ζ on the outside of the circle, the first term disappears from (5.46). Hence

$$\phi^+(\xi) = \frac{2i\sigma_1(\xi)}{\chi^+(\xi)} - \frac{1}{\pi}\int_{\Gamma} \frac{\sigma_1(\widehat{\xi})}{(\widehat{\xi}-\xi)\chi^+(\widehat{\xi})}\,\mathrm{d}\widehat{\xi} \tag{5.47}$$

and

$$\phi^-(\xi) = -\frac{1}{\pi}\int_{\Gamma} \frac{\sigma_1(\widehat{\xi})}{(\widehat{\xi}-\xi)\chi^+(\widehat{\xi})}\,\mathrm{d}\widehat{\xi} \tag{5.48}$$

so that ϕ satisfies

$$\phi^+(\xi) - \phi^-(\xi) = \frac{2i\sigma_1(\xi)}{\chi^+(\xi)} \quad \text{on } \Gamma'. \tag{5.49}$$

Here we need σ_1/χ^+ to be *Hölder continuous* [46] for the integral in the definition of ϕ (5.46) to exist. Substituting (5.49) into (5.44) gives

$$\frac{w^+}{\chi^+} - \phi^+ = \frac{w^-}{\chi^-} - \phi^- \tag{5.50}$$

on Γ', so that $w/\chi - \phi$ is analytic everywhere. Therefore it may be written as an analytic function $f(\zeta)$. We may therefore write

$$w(\zeta) = \chi(\zeta)\left[\phi(\zeta) + f(\zeta)\right]. \tag{5.51}$$

It remains to find χ satisfying (5.42). Taking logs gives

$$\log \chi^+ - \log \chi^- = \pi i. \tag{5.52}$$

Replacing σ_1/χ^+ with π in (5.46), we see that a solution is

$$\log \chi(\zeta) = \frac{1}{2}\int_{\Gamma'} \frac{1}{\xi - \zeta}\,\mathrm{d}\xi, \tag{5.53}$$

and integration and exponentiation leads to

$$\chi(\zeta) = \left[\frac{\zeta - \xi_b}{\zeta - \xi_a}\right]^{\frac{1}{2}}. \tag{5.54}$$

A more general form for χ may be found by multiplying by integer powers of $\zeta - \xi_a$ and $\zeta - \xi_b$. Let

$$\widetilde{\chi}(\zeta) = \chi(\zeta)(\zeta - \xi_a)^m(\zeta - \xi_b)^{n+1}, \tag{5.55}$$

where m and n are integers. Then $\widetilde{\chi}(\zeta)$ is a multi-function,

$$\widetilde{\chi}(\zeta) = \pm\,|\zeta - \xi_a|^{m+\frac{1}{2}}\,|\zeta - \xi_b|^{n+\frac{1}{2}}\,e^{(m+\frac{1}{2})i\alpha}e^{(n+\frac{1}{2})i\beta}, \tag{5.56}$$

where

$$\alpha = \arg(\zeta - \xi_a) \tag{5.57}$$

and

$$\beta = \arg(\zeta - \xi_b), \tag{5.58}$$

with $\alpha, \beta \in [0, 2\pi)$. Going from $\widetilde{\chi}^+$ to $\widetilde{\chi}^-$ corresponds to a change in α or β of 2π, so (5.56) shows that this change will cause a sign change in $\widetilde{\chi}$, whatever the values of the integers m and n, and hence $\widetilde{\chi}$ satisfies (5.42). We therefore replace χ with the more general form $\widetilde{\chi}$.

We must also choose the value (i. e. the branch) of the multi-function (5.56). We do this by requiring that $\chi \sim \zeta^{m+n+1}$ as $\zeta \to \infty$, and that Γ' is a branch cut, so that χ is continuous on $\mathbb{C}\setminus\Gamma'$. We detail this procedure further when we come to solve the problem numerically, when we require an expression for χ in terms of real variables.

We can see that χ is finite at $\zeta = 0$, and since w and ϕ are both finite at zero, $f = w/\chi - \phi$ will be also. We may therefore write f in the form of a power series expansion about zero,

$$f(\zeta) = \sum_{k=0}^{\infty} f_k \zeta^k. \tag{5.59}$$

We now have a function

$$w(\zeta) = (\zeta - \xi_a)^{m+\frac{1}{2}} (\zeta - \xi_b)^{n+\frac{1}{2}} \left(\frac{1}{\pi} \int_{\Gamma'} \frac{\sigma_1(\xi)}{\chi^+(\xi)(\xi - \zeta)} \, \mathrm{d}\xi + \sum_{k=0}^{\infty} f_k \zeta^k \right) \tag{5.60}$$

which satisfies

$$w^+ + w^- = i\sigma_1 \tag{5.61}$$

on Γ', with w analytic in $\mathbb{C} \setminus \Gamma'$, for any $m, n \in \mathbb{Z}$ and $f_k \in \mathbb{R}$. We also require $w(0) = 0$, which implies, since $\chi(0) \neq 0$, that

$$f_0 + \frac{1}{\pi} \int_{\Gamma'} \frac{\sigma_1}{\xi \chi^+} \, \mathrm{d}\xi = 0. \tag{5.62}$$

We now consider possible values for m and n. If $m > 0$ or $n > 0$ then the function ϕ will not exist because $1/\chi^+$ will have a non-integrable singularity at the corresponding endpoint of the range of integration. Hence we require $m \leqslant 0$ and $n \leqslant 0$.

If $m < 0$, then ϕ has a finite limit as $\zeta \to \xi_a$, and $\chi \sim (\zeta - \xi_a)^{m+1/2}$. If $m = 0$, then $\phi \sim (\zeta - \xi_a)^{-1/2}$, and χ has a finite limit. Hence for all $m \leqslant 0$, $\chi\phi \sim (\zeta - \xi_a)^{m+1/2}$ as $\zeta \to \xi_a$. Similarly for $n \leqslant 0$, $\chi\phi \sim (\zeta - \xi_b)^{n+1/2}$ as $\zeta \to \xi_b$.

Since

$$s_1''(x) = \sigma_1(\xi) = -\frac{i}{2} \left(w^+(\xi) + w^-(\xi) \right), \tag{5.63}$$

s_1'' has the same singularities at a and b as w has at ξ_a and ξ_b, and therefore the same singularities as $\chi\phi$. This further restricts the possible values of m and n; in order for s_1'' to be twice integrable (so that we may find s_1), we must have $m \geqslant -2$ and $n \geqslant -2$. However, we may immediately reject the cases $m = -2$ and $n = -2$ since in these cases, $s_1'' \sim (x-a)^{-3/2}$ or $(x-b)^{-3/2}$, and so $s_1' \sim (x-a)^{-1/2}$ or $(x-b)^{-1/2}$, so that the slope of s_1 is infinite and thus unphysical.

We are left with two possible values for each of m and n. The choice of m and n will specify the type of singularity at each of the endpoints a and b. For now, we delay choosing m and n, and continue to consider each of the four possible cases.

Our final condition on w is that for all ζ, $w(\zeta) = -w^*(\zeta)$. Since

$$w^*(\zeta) = \chi^*(\zeta)(\phi^*(\zeta) + f^*(\zeta)), \tag{5.64}$$

we consider each of the three functions χ, ϕ, f in turn. Firstly

$$\chi^*(\zeta)^2 = \overline{\left(1/\overline{\zeta} - \xi_a\right)^{2m+1}\left(1/\overline{\zeta} - \xi_b\right)^{2n+1}} = \frac{\chi(\zeta)^2}{\chi(0)^2}\zeta^{-2(m+n+1)}, \tag{5.65}$$

and then using $\chi \sim \zeta^{m+n+1}$ as $\zeta \to \infty$, the correct branch to take is

$$\chi^*(\zeta) = \frac{\chi(\zeta)}{\chi(0)}\zeta^{-(m+n+1)}. \tag{5.66}$$

Then using

$$\overline{\chi^+(\xi)} = \chi^{-*}(\xi) = -\frac{\chi^+(\xi)\xi^{-(m+n+1)}}{\chi(0)} \text{ on } \Gamma' \tag{5.67}$$

and

$$\overline{\mathrm{d}\xi} = -\xi^{-2}\mathrm{d}\xi, \tag{5.68}$$

we see that

$$\phi^*(\zeta) = \frac{\chi(0)}{\pi}\int_{\Gamma'} \frac{\sigma_1(\xi)\xi^{m+n}\zeta}{(\zeta-\xi)\chi^+(\xi)}\,\mathrm{d}\xi. \tag{5.69}$$

Finally

$$f^*(\zeta) = \sum_{j=0}^{\infty} \overline{f_j}\zeta^{-j}. \tag{5.70}$$

Taking the limit $\zeta \to 0$ in

$$\chi(\zeta)\left(\phi(\zeta) + f(\zeta)\right) = -\chi^*(\zeta)\left(\phi^*(\zeta) + f^*(\zeta)\right) \tag{5.71}$$

gives

$$w(0) = 0 = -\chi^*(0)f^*(0) \tag{5.72}$$

since $\phi^*(0) = 0$. Hence we need

$$\lim_{\zeta\to 0}\frac{\chi(\zeta)}{\chi(0)}\sum_{j=0}^{\infty}\overline{f_j}\zeta^{-(j+m+n+1)} = 0, \tag{5.73}$$

so that

$$f_j = 0 \quad \forall j \geqslant -(m+n+1). \tag{5.74}$$

Therefore $f \equiv 0$ unless $m = n = -1$, which is the most singular of our possible solutions. Since we have previously found

$$f_0 = -\frac{1}{\pi}\int_{\Gamma'}\frac{\sigma_1}{\xi\chi^+}\,\mathrm{d}\xi, \tag{5.75}$$

this integral must be zero unless $m = n = -1$.

Now substituting for χ, ϕ, and f in (5.71), we obtain

$$\int_{\Gamma'} \frac{2\sigma_1}{(\xi-\zeta)\chi^+}\,\mathrm{d}\xi + 2\pi f_0 = \zeta^{-(m+n)} \int_{\Gamma'} \frac{2\xi^{m+n}\sigma_1}{(\xi-\zeta)\chi^+}\,\mathrm{d}\xi - \frac{2\pi\overline{f_0}\zeta^{-(m+n+1)}}{\chi(0)}, \tag{5.76}$$

and then using the expression (5.75) and its complex conjugate

$$\overline{f_0} = -\frac{\chi(0)}{\pi}\int_{\Gamma'} \frac{\xi^{m+n}\sigma_1}{\chi^+}\,\mathrm{d}\xi, \tag{5.77}$$

this condition is equivalent to

$$I := \int_{\Gamma'} \frac{2(\zeta^{m+n+2} - \xi^{m+n+2})\sigma_1(\xi)}{\xi(\xi-\zeta)\chi^+(\xi)}\,\mathrm{d}\xi = 0. \tag{5.78}$$

When $m+n=-2$, the numerator of the integrand vanishes and so $I=0$. When $m+n=-1$, $I = 2\pi f_0 = 0$. Finally when $m+n=0$,

$$I = -\int_{\Gamma'} \frac{2(\zeta+\xi)\sigma_1}{\xi\chi^+}\,\mathrm{d}\xi = 2\pi\zeta f_0 - \frac{2\pi}{\chi(0)}\overline{f_0} = 0. \tag{5.79}$$

Hence the condition $w = -w^*$ is satisfied for each of the four possible combinations of m and n.

We therefore have four possible solutions, with four pairs of values for the exponents m and n. In the cases (i) $m=n=0$, (ii) $m=0$, $n=-1$, and (iii) $m=-1$, $n=0$, we have

$$w(\zeta) = \frac{1}{\pi}(\zeta-\xi_a)^{m+\frac{1}{2}}(\zeta-\xi_b)^{n+\frac{1}{2}}\int_{\Gamma'} \frac{\sigma_1(\xi)}{(\xi-\zeta)\chi^+(\xi)}\,\mathrm{d}\xi. \tag{5.80}$$

The condition

$$f_0 = \int_{\Gamma'} \frac{2\sigma_1(\xi)}{\xi\chi^+(\xi)}\,\mathrm{d}\xi = 0 \tag{5.81}$$

must also be satisfied.

In case (iv) $m=n=-1$, we have

$$w(\zeta) = \frac{\zeta}{\pi}(\zeta-\xi_a)^{m+\frac{1}{2}}(\zeta-\xi_b)^{n+\frac{1}{2}}\int_{\Gamma'} \frac{\sigma_1(\xi)}{\xi(\xi-\zeta)\chi^+(\xi)}\,\mathrm{d}\xi, \tag{5.82}$$

but we do not have the condition (5.81).

5.2 Choice of singularities

Condition (5.81) (in cases (i), (ii), and (iii) above) may be thought of as an equation for the unknown endpoints a and b. Since (5.81) involves complex variables, it is

effectively two real equations for the real variables a and b. However, in cases (ii) and (iii), when $m+n=-1$, we may see from (5.77) that

$$f_0 = -\chi(0)\overline{f_0}, \tag{5.83}$$

and hence if the real part of f_0 is zero, then so is the imaginary part, since $\chi(0) \neq 0$. The complex condition (5.81) is therefore one real condition relating a and b.

Further conditions relating a and b may be found by considering the behaviour of $s_1(x)$ at the endpoints a and b. We know from (5.36) that

$$s_1''(x) = -iw(e^{ix}) \tag{5.84}$$

which is a second order ODE for s_1; when integrating this to find s_1 we have the freedom to specify two constants of integration. There are however four conditions which we would expect s_1 to satisfy in order for our solution to be physically realistic: firstly, we require s_1 to be continuous at a and b, so that

$$s_0(a) = s_1(a) \tag{5.85}$$

and

$$s_0(b) = s_1(b), \tag{5.86}$$

and secondly it is reasonable to require that s_1 joins smoothly to s_0 at a and b, so that

$$s_0'(a) = s_1'(a) \tag{5.87}$$

and

$$s_0'(b) = s_1'(b). \tag{5.88}$$

We may satisfy two of these conditions by choosing constants of integration, which leaves two conditions for a and b. In fact, we show below that two of these conditions are equivalent, so that we actually have only one extra condition for a and b.

We consider the integral

$$I = \int_{\Gamma\cup\Gamma'} \frac{w^+ + w^-}{\xi}\,\mathrm{d}\xi \tag{5.89}$$

by splitting it in two different ways. Firstly by Cauchy's theorem,

$$\int_{\Gamma\cup\Gamma'} \frac{w^+}{\xi}\,\mathrm{d}\xi = 2\pi i w(0) = 0, \tag{5.90}$$

and secondly by an extension to Cauchy's theorem for exterior regions [46],

$$\int_{\Gamma\cup\Gamma'} \frac{w^-}{\xi}\,\mathrm{d}\xi = 2\pi i w(\infty), \tag{5.91}$$

which is equal to zero since $w(\infty) = \overline{w^*(0)} = -\overline{w(0)} = 0$. Hence $I = 0$. We now consider I by splitting the range of integration and changing the variable of integration, so that

$$\int_\Gamma \frac{w^+ + w^-}{\xi}\,\mathrm{d}\xi = -\int_a^b 2s_1''(x)\,\mathrm{d}x = 2(s_1'(a) - s_1'(b)), \tag{5.92}$$

and

$$\int_{\Gamma'} \frac{w^+ + w^-}{\xi}\,\mathrm{d}\xi = -\int_b^{a+2\pi} 2s_0''(x)\,\mathrm{d}x = 2(s_0'(b) - s_0'(a)). \tag{5.93}$$

Therefore

$$s_1'(a) - s_0'(a) = s_1'(b) - s_0'(b). \tag{5.94}$$

Hence if we impose the condition that s_1 joins smoothly at $x = a$, it is automatic that it joins smoothly at $x = b$.

We therefore choose the constants of integration arising from (5.84) to satisfy (5.85) and (5.87); as demonstrated above this means that (5.88) is also satisfied, and hence we have one further condition (5.86) relating a and b. It is convenient to write this in the form

$$\int_a^b x\left(s_0''(x) + iw(e^{ix})\right)\,\mathrm{d}x = 0, \tag{5.95}$$

since the integrand is $x(s_0''(x) - s_1''(x))$.

We are now in a position to reject three of the four possible combinations of pairs of values of m and n.

In case (i), $m = n = 0$, condition (5.81) is a complex one, and so provides two real conditions for a and b. Along with (5.95), we therefore have three conditions for two unknowns, and we cannot hope to satisfy all three.

In the two cases (ii) and (iii), where $m + n = -1$, (5.81) and (5.95) provide two conditions for a and b, so we may hope to be able to solve this pair of equations for a and b. However, an initial search for solutions provides only the trivial solution $a = b$. If we compare our pair of equations with Fowler's similar work on cavities beneath sliding glaciers (see [22] and [58]), we note that Fowler's system (which is derived from a fourth-order PDE for the pressure) is identical to ours in the case when the glacier sliding velocity tends to zero. In this limit, the cavity length tends to zero (see for example the sequence of cavity profiles in Figure 4 of [22]), which is consistent both with our findings of only trivial solutions, as well as with physical considerations of glacier sliding. We therefore reject these two pairs of values of m and n, which leaves us with only the final case (iv) $m = n = -1$.

In this case the condition (5.81) does not apply, and we therefore have only the condition (5.95) relating a and b. This corresponds to introducing singularities in s_1'' at both endpoints, which, since we know from (5.9) that the first derivative of p is related to the second derivative of s_1, is equivalent to saying that p is continuous, but not smooth, at the two endpoints. This choice of m and n means that the singularities are symmetric in the x-direction; in other words, the solution is unaffected by the direction of the flow. At first sight this is surprising, as one would expect the shape of the wake region to be strongly dependent upon the direction of the flow. However, the linearized system (5.11) to (5.15) that we are solving is also invariant under a change of direction of flow (it is an elliptic problem; replacing x with $-x$ leads to the same problem) so there is no reason for the solution not to be invariant also. While for a given bed profile s_0 the solution s_1 is independent of flow direction, an asymmetric bed profile will lead to an asymmetric wake profile. We expect the bed profile to be asymmetric due to the directionality of the wind flow, and therefore the wake profile will be asymmetric also. Hence the wind direction affects the wake profile not through the solution of the Hilbert problem derived from (5.11) to (5.15), but indirectly through the bed profile s_0 which influences the solution for the wake profile.

5.3 Finding endpoints

We are thus looking for a and b which satisfy the equation

$$\int_a^b x\left(s_0''(x) + iw(e^{ix})\right)\,\mathrm{d}x = 0, \tag{5.96}$$

where

$$w(\zeta) = \frac{\zeta\chi(\zeta)}{\pi}\int_{\Gamma'}\frac{\sigma_1(\xi)}{(\xi-\zeta)\xi\chi^+(\xi)}\,\mathrm{d}\xi, \tag{5.97}$$

$$\chi(\zeta) = \frac{1}{\sqrt{(\zeta-\xi_a)(\zeta-\xi_b)}}, \tag{5.98}$$

and

$$\chi \sim \frac{1}{\zeta} \quad \text{as} \quad \zeta \to \infty. \tag{5.99}$$

For purposes of computation, we wish to write these equations in terms of real variables. We require values of χ on the unit circle only, so we may use elementary circle geometry along with the condition that $\chi \sim 1/\zeta$ as $\zeta \to \infty$ to find an explicit real form for χ.

By the continuity of χ, the sign in (5.56) can only change when crossing Γ' or one of the lines $\alpha = 0$ or $\beta = 0$. Since $\chi \sim 1/\zeta$ at ∞, we must therefore take the negative root in (5.56) when considering χ^+ which is the value of χ on the inside of Γ'.

We suppose that the line through ξ_a and ξ_b makes an angle γ with the real axis. We may then see from Figure 5.4 that

$$\gamma + (2\pi - b) + (\pi - \frac{1}{2}(\pi - b + a)) = \pi, \tag{5.100}$$

so that

$$\gamma = \frac{1}{2}(a + b - 3\pi). \tag{5.101}$$

We now let

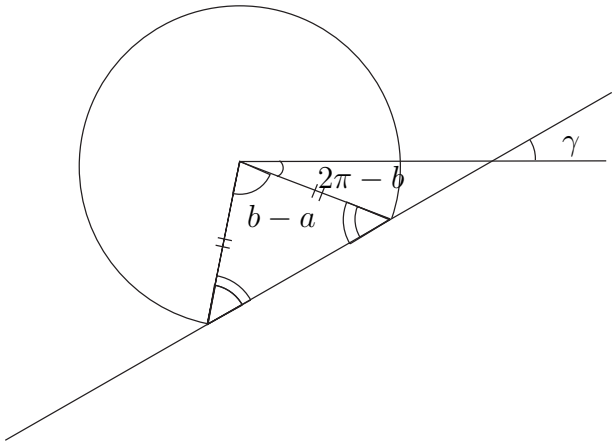


Figure 5.4: Circle geometry showing derivation of γ.

$$\xi = e^{ix}, \tag{5.102}$$

$$\alpha' = \alpha - \gamma, \tag{5.103}$$

$$\beta' = \beta - \gamma, \tag{5.104}$$

and consider Figure 5.5. Since the angle between two chords of a circle is equal to half the angle at the centre, we see from Figure 5.5 that on Γ',

$$\alpha' - \beta' = \frac{1}{2}(a - b). \tag{5.105}$$

We may see further from Figure 5.6 that

$$\alpha' = \frac{1}{2}(x - b), \tag{5.106}$$

so that using (5.105), we have

$$\beta' = \alpha' - \frac{1}{2}(a - b) = \frac{1}{2}(x - a). \tag{5.107}$$

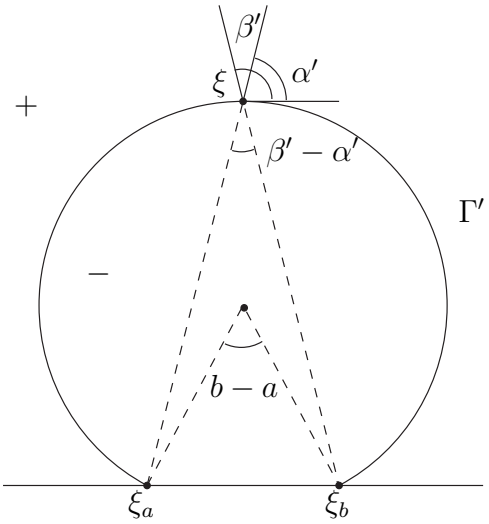


Figure 5.5: Circle geometry showing derivation of $\alpha' - \beta'$.

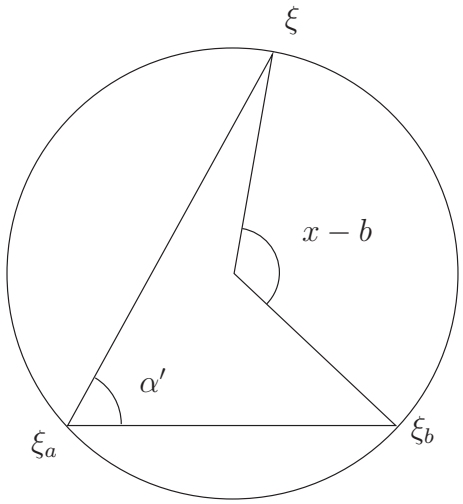


Figure 5.6: Circle geometry showing derivation of α'.

Hence

$$\begin{aligned}\alpha+\beta &= \alpha'+\beta'+2\gamma \\ &= x-\frac{1}{2}(a+b)+a+b-3\pi \\ &= x+\frac{1}{2}(a+b)-3\pi. \end{aligned} \tag{5.108}$$

We may also appeal to the cosine rule to see that

$$|\xi-\xi_a| = \sqrt{2(1-\cos(x-a))} = 2\left|\sin\frac{x-a}{2}\right| \tag{5.109}$$

and similarly

$$|\xi-\xi_b| = 2\left|\sin\frac{x-b}{2}\right|, \tag{5.110}$$

so that

$$\begin{aligned}\chi^+(e^{ix}) &= -\frac{1}{2}\left|\sin\frac{x-a}{2}\right|^{-\frac{1}{2}}\left|\sin\frac{x-b}{2}\right|^{-\frac{1}{2}} e^{-\frac{i}{2}(x+\frac{1}{2}(a+b)-3\pi)} \\ &= \frac{i}{2}\left|\sin\frac{x-a}{2}\right|^{-\frac{1}{2}}\left|\sin\frac{x-b}{2}\right|^{-\frac{1}{2}} e^{-\frac{i}{4}(a+b)}e^{-\frac{ix}{2}} \end{aligned} \tag{5.111}$$

on Γ'.

We may use a similar geometric argument (swapping a and b) to see that on Γ,

$$\alpha+\beta = x+\frac{1}{2}(a+b), \tag{5.112}$$

so that

$$\chi(e^{ix}) = \frac{1}{2}\left|\sin\frac{x-a}{2}\right|^{-\frac{1}{2}}\left|\sin\frac{x-b}{2}\right|^{-\frac{1}{2}} e^{-\frac{i}{4}(a+b)}e^{-\frac{ix}{2}}. \tag{5.113}$$

We are now in a position to write (5.96) in terms of real variables. It becomes

$$\int_a^b x\left(s_0''(x)-\frac{1}{\pi f(x)}\int_b^{a+2\pi}\frac{s_0''(y)f(y)\sin\frac{1}{2}(x-y)}{1-\cos(x-y)}\,\mathrm{d}y\right)\mathrm{d}x = 0, \tag{5.114}$$

where

$$f(x) := \sqrt{\left|\sin\frac{x-a}{2}\sin\frac{x-b}{2}\right|}. \tag{5.115}$$

Having found endpoints a and b, we may obtain the wake profile using

$$s_1(x) = s_0(a)+(x-a)s_0'(a)+\int_a^x (x-y)s_1''(y)\,\mathrm{d}y, \tag{5.116}$$

where

$$s_1''(x) = \frac{1}{\pi f(x)}\int_b^{a+2\pi}\frac{s_0''(y)f(y)\sin\frac{1}{2}(x-y)}{1-\cos(x-y)}\,\mathrm{d}y. \tag{5.117}$$

Since we have only one equation (5.114) for a and b, we are forced to make a further assumption about the nature of the separation region. The most obvious assumption to make here, at least for the case of flow over a sand dune, is that the flow separates at the brink of a downwind-facing slip face, due to the discontinuity in slope that exists. When there is no slip face present, it is less clear where the flow should separate; one might assume either that separation does not occur, that the separation point coincides with the point of maximum (downwind) slope, or that separation occurs where the pressure gradient is most adverse, as in classical studies of boundary layer separation.

For now, we assume that a slip face is always present, and solve (5.114) for various bed profiles.

5.4 Numerical solution

We are solving (5.114) for a given profile $s_0(x)$ and separation point a, in order to find the reattachment point b. The difficulty in evaluating the integrals in this equation caused by the presence of singularities at the end-points of the outermost integral (where the integrand $\sim 1/f(x) \sim 1/\sqrt{\sin(x)}$) may be overcome by using Gauss-Chebyshev quadrature [31]. This method is used for integrals of the form

$$I = \int_{-1}^{1} w(x)g(x)\,\mathrm{d}x, \tag{5.118}$$

where the weight function w is of the form

$$w(x) = \frac{1}{\sqrt{1-x^2}}. \tag{5.119}$$

While our integrand is not exactly of this form, if we scale x such that its limits are -1 and 1, and take a factor of w out of the integrand, then the 'g' of (5.118) is well-behaved at $x = \pm 1$ and we may use this method.

The integral is then estimated using

$$I \approx \frac{\pi}{N} \sum_{i=1}^{N} g(x_i), \tag{5.120}$$

where the abscissae x_i are the roots of Chebyshev polynomials,

$$x_i = \cos\frac{(2i-1)\pi}{2N}, \quad i = 1, \ldots, N. \tag{5.121}$$

This may then be implemented in MATLAB; we use only vector arithmetic and avoid completely the use of loops so that the double integral in (5.114) may be efficiently

calculated. It is then possible to use a non-linear optimization routine to find a zero of the equation; with a solution b we may then go on to calculate (using a similar method) the wake region profile $s_1(x)$.

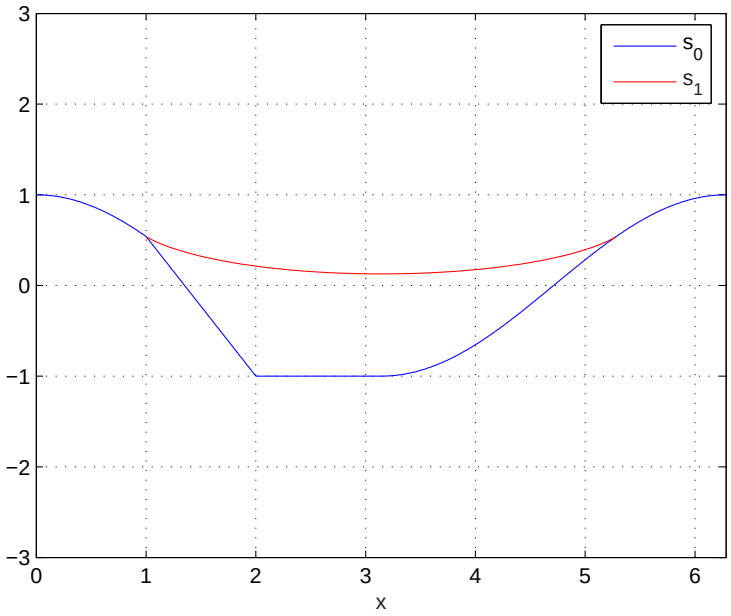


Figure 5.7: Wake profile (red) calculated from the sinusoidal bed profile (blue) with a slip face between $x = 1$ and $x = 2$, and with the separation point $a = 1$.

Figure 5.7 shows the calculated wake profile for a dune profile which is sinusoidal and contains a slip face. As can be seen from the Figure, the reattachment point appears to be at the same level as the separation point (i. e. $s_0(a) = s_0(b)$) and the two points are symmetric about the point $x = \pi$. This suggests a certain symmetry for this simple case that permits further analysis; we return to this below. Since the wake profile depends only on the bed profile in the region of attached flow (as can be seen from the integral (5.117)), and the calculated wake profile remains above the curve $y = \cos x$, we would have obtained the same wake profile s_1 without having to introduce a slip face. Some experimentation shows that this is true for any choice of $a \in [0, \pi]$, corresponding to the separation point being on the part of the dune with negative slope, as shown in Figure 5.8. If instead the separation point is on the part with positive slope, we would expect the wake profile to lie below the curve $y = \cos x$, making it necessary to consider the slip face position.

As discussed above in the section dealing with the choice of singularities for the solution to the separation problem, in general we would not expect the wake profile

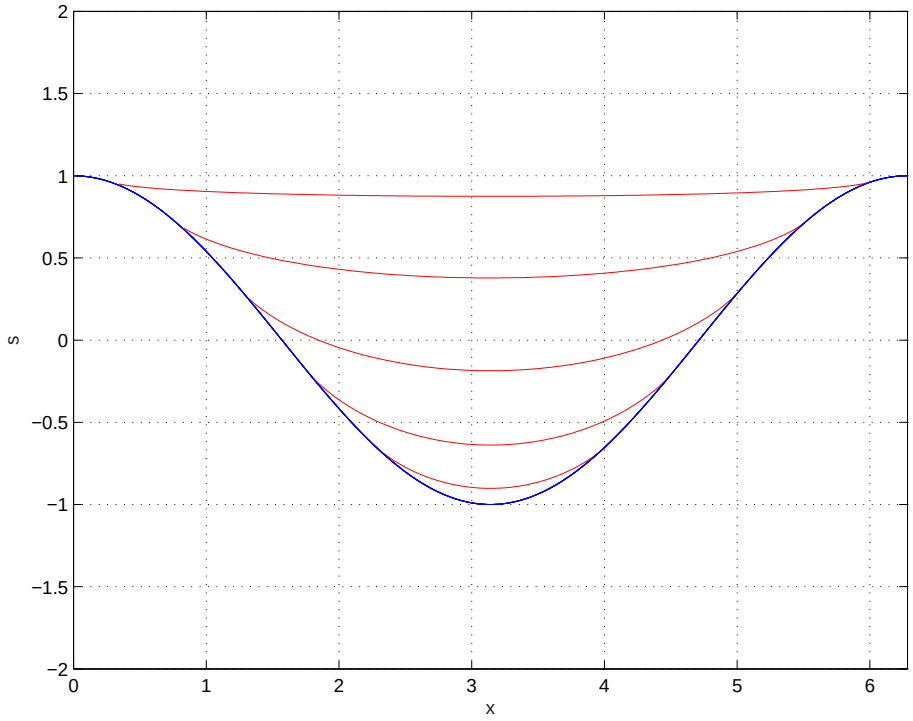


Figure 5.8: A series of wake profiles (red) calculated from the sinusoidal bed profile (blue) with varying positions of the separation point a. Slip faces were not introduced as they would not affect the solutions.

to be symmetric in the x-direction, even though it was in the previous example. We claimed that the asymmetry in the wake profile arises due to the asymmetry in the dune profile. We would therefore now like to calculate the wake profile for a more realistic, asymmetric, dune profile. Figure 5.9 shows the wake profile calculated from the dune profile obtained from the steady state travelling wave solution to the evolution equation (2.197). As is to be expected, the wake profile is asymmetric.

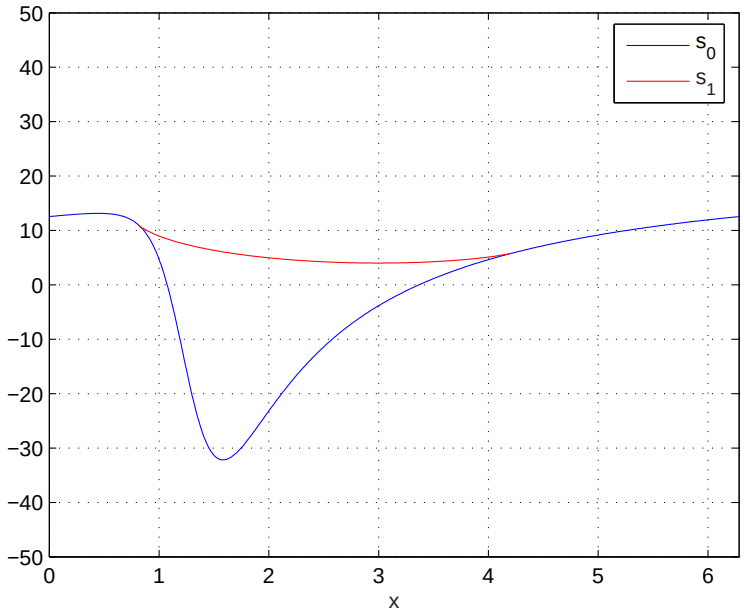


Figure 5.9: Wake profile (red) calculated from the bed profile (blue) which was the steady state travelling wave solution to (2.197), with a separation point $a = 0.8$. No slip face was introduced in this case.

The next wake profile that we calculate is for a Gaussian dune profile (Figure 5.10). We note that in this example the reattachment occurs on the horizontal part of s_0 downwind of the slip face, and not on the upwind part of the next dune downwind, as in the previous examples.

5.5 Further analysis for a sinusoidal bed

We now consider the solution to (5.114) in the case when

$$s_0(x) = \cos x. \tag{5.122}$$

Then

$$s_0''(x) = -\cos x = -\frac{1}{2}(e^{ix} + e^{-ix}), \tag{5.123}$$

so that

$$\sigma_0(\xi) = -\frac{1}{2}\left(\xi + \frac{1}{\xi}\right). \tag{5.124}$$

Since the shape of the wake region and the position of the reattachment point do not depend on the bed profile inside the wake region (as discussed in Section 5.4), we may avoid introducing a slipface into our bed profile, and simply choose our separation point a to be where it would be, if a slipface were present.

We define the function

$$g_n(\zeta) = \int_{\Gamma'} \frac{\xi^n}{(\xi - \zeta)\chi^+(\xi)}\,\mathrm{d}\xi, \tag{5.125}$$

so that we may write

$$\begin{aligned} s_1''(x) = -iw(e^{ix}) &= -\frac{ie^{ix}\chi(e^{ix})}{\pi}\int_{\Gamma'} \frac{-\frac{1}{2}\left(\xi + \frac{1}{\xi}\right)}{\xi(\xi - e^{ix})\chi^+(\xi)}\,\mathrm{d}\xi \\ &= \frac{ie^{ix}\chi(e^{ix})}{2\pi}\left(g_0(e^{ix}) + g_{-2}(e^{ix})\right). \end{aligned} \tag{5.126}$$

By the Plemelj formulae [46], we know that we may write the integral (5.125) as

$$g_n(\zeta) = h_n(\zeta) - F_n(\zeta), \tag{5.127}$$

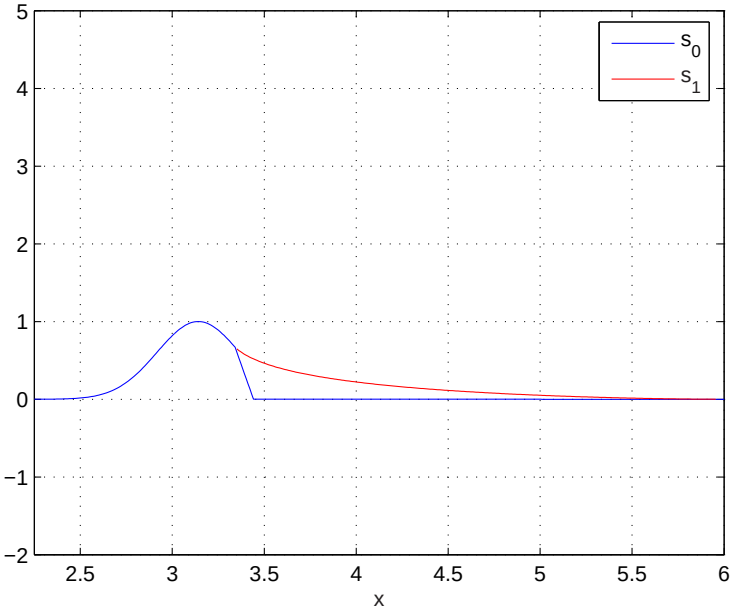


Figure 5.10: Wake profile (red) calculated from the Gaussian bed profile (blue) with a slip face between $x = \pi + 0.2$ and $x = \pi + 0.3$, and with the separation point $a = \pi + 0.2$.

where h_n is a function, holomorphic on $\mathbb{C} \setminus \Gamma'$, satisfying

$$h_n^+(\xi) - h_n^-(\xi) = \frac{2\pi i \xi^n}{\chi^+(\xi)} \quad \text{on} \quad \Gamma', \tag{5.128}$$

and F_n is a polynomial function which satisfies

$$h_n \sim F_n \quad \text{as} \quad \zeta \to \infty. \tag{5.129}$$

In order for h_n to be holomorphic on $\mathbb{C} \setminus \Gamma'$, we clearly require $n \geqslant 0$ to avoid a pole at $\zeta = 0$. Using $\chi^+ = -\chi^-$ on Γ', we may rearrange (5.128) to obtain

$$h_n^+(\xi) - \frac{\pi i \xi^n}{\chi^+(\xi)} = h_n^-(\xi) - \frac{\pi i \xi^n}{\chi^-(\xi)}, \tag{5.130}$$

so that a solution to (5.128) is given by

$$h_n(\zeta) = \frac{\pi i \zeta^n}{\chi(\zeta)}. \tag{5.131}$$

Since $\chi \sim 1/\zeta$ as $\zeta \to \infty$, F_n must be a polynomial of degree $n+1$. Hence

$$g_n(\zeta) = \frac{\pi i \zeta^n}{\chi(\zeta)} - F_n(\zeta) \tag{5.132}$$

for $n \geqslant 0$.

In order to find an expression for g_n for negative n, we may take the complex conjugate of (5.125) to obtain

$$\overline{g_n(\zeta)} = \int_{\Gamma'} \frac{\xi^{-(n+2)} \chi(0)}{(1 - \xi\bar{\zeta})\chi^+(\xi)} \, \mathrm{d}\xi, \tag{5.133}$$

where we have used (5.67) and (5.68). As we require g_n on Γ only, we may consider the case $\zeta = e^{ix} \in \Gamma$, where we obtain

$$\begin{aligned} \overline{g_n(e^{ix})} &= -e^{ix}\chi(0) \int_{\Gamma'} \frac{\xi^{-(n+2)}}{(\xi - e^{ix})\chi^+(\xi)} \, \mathrm{d}\xi \\ &= -e^{ix}\chi(0) g_{-(n+2)}(e^{ix}), \end{aligned} \tag{5.134}$$

and we therefore have an expression for g_n for all $n \neq 1$.

In the specific case we are considering, we have

$$s_1''(x) = \frac{ie^{ix}\chi(e^{ix})}{2\pi} \left(g_0(e^{ix}) - \frac{1}{e^{ix}\chi(0)} \overline{g_0(e^{ix})} \right). \tag{5.135}$$

Since

$$\begin{aligned}\overline{\chi(e^{ix})} &= \left(\frac{1}{e^{ix}}-\frac{1}{e^{ia}}\right)^{-\frac{1}{2}}\left(\frac{1}{e^{ix}}-\frac{1}{e^{ib}}\right)^{-\frac{1}{2}} \\ &= \frac{e^{ix}\chi(e^{ix})}{\chi(0)},\end{aligned} \tag{5.136}$$

we may write this as

$$\begin{aligned}s_1''(x) &= \frac{i}{2\pi}\left(e^{ix}\chi(e^{ix})g_0(e^{ix})-e^{-ix}\frac{e^{ix}\chi(e^{ix})}{\chi(0)}\overline{g_0(e^{ix})}\right) \\ &= -\frac{1}{\pi}\operatorname{Im}\left\{e^{ix}\chi(e^{ix})g_0(e^{ix})\right\}.\end{aligned} \tag{5.137}$$

Finally, we know

$$g_0(e^{ix}) = \frac{\pi i}{\chi(e^{ix})} - F_0(e^{ix}), \tag{5.138}$$

and we may find the linear function F_0 by expanding, as $\zeta \to \infty$,

$$\begin{aligned}\frac{\pi i}{\chi(\zeta)} &= \pi i(\zeta-e^{ia})^{\frac{1}{2}}(\zeta-e^{ib})^{\frac{1}{2}} \\ &= \pi i\left(\zeta-\frac{1}{2}(e^{ia}+e^{ib})+\cdots\right),\end{aligned} \tag{5.139}$$

so that

$$F_0(e^{ix}) = \pi i\left(e^{ix}-\frac{1}{2}(e^{ia}+e^{ib})\right). \tag{5.140}$$

Finally using (5.113),

$$\begin{aligned}e^{ix}\chi(e^{ix})g_0(e^{ix}) &= \pi i e^{ix}-\pi i e^{ix}\chi(e^{ix})\left(e^{ix}-\frac{1}{2}(e^{ia}+e^{ib})\right) \qquad (5.141)\\ &= \pi i\left[e^{ix}-\frac{1}{2f(x)}\left(e^{\frac{3ix}{2}-\frac{i}{4}(a+b)}-\frac{1}{2}e^{\frac{ix}{2}-\frac{i}{4}(b-3a)}-\frac{1}{2}e^{\frac{ix}{2}-\frac{i}{4}(a-3b)}\right)\right],\end{aligned}$$

so that

$$\begin{aligned}s_1''(x) &= -\cos x+\frac{1}{2f(x)}\left[\cos\left(\frac{3x}{2}-\frac{a+b}{4}\right)-\frac{1}{2}\cos\left(\frac{x}{2}+\frac{3a-b}{4}\right)\right. \\ &\quad \left.-\frac{1}{2}\cos\left(\frac{x}{2}+\frac{3b-a}{4}\right)\right].\end{aligned} \tag{5.142}$$

Given a, we must solve

$$\int_a^b x(s_0''(x)-s_1''(x))\,\mathrm{d}x = 0 \tag{5.143}$$

for b. In this case, where $s_0(x) = \cos x$, this is equivalent to

$$\int_a^b \frac{x}{f(x)} \left[\cos\left(\frac{3x}{2} - \frac{a+b}{4}\right) - \frac{1}{2}\cos\left(\frac{x}{2} + \frac{3a-b}{4}\right) - \frac{1}{2}\cos\left(\frac{x}{2} + \frac{3b-a}{4}\right) \right] \mathrm{d}x = 0. \tag{5.144}$$

We solve this numerically, using techniques similar to those described in Section 5.4 though now simpler, for various values of a; results are shown in Figure 5.11. The

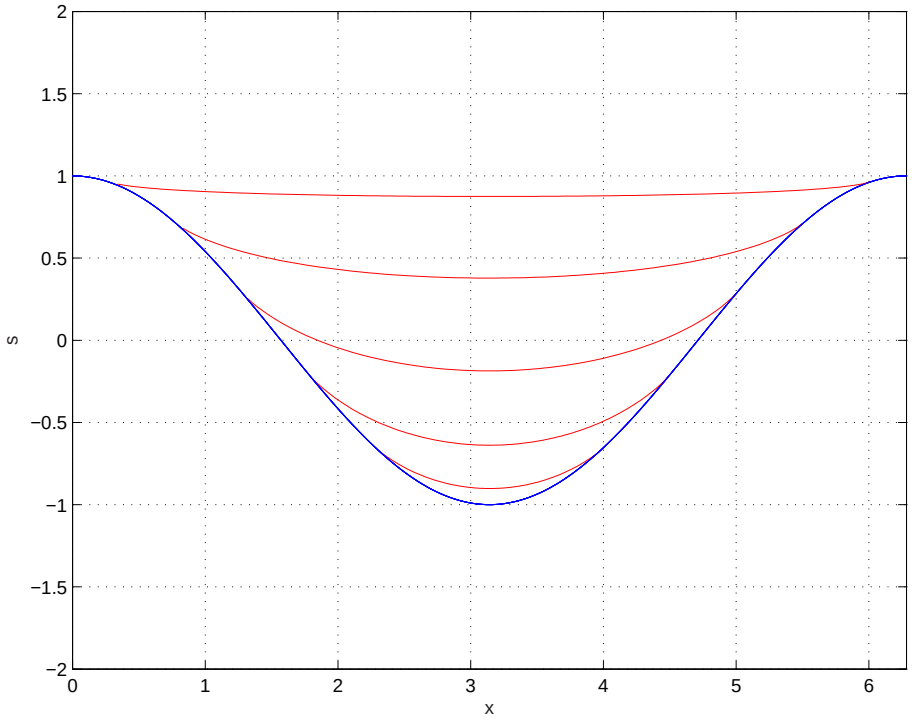


Figure 5.11: A series of solutions (varying a) of (5.144)

results agree exactly with those of Figure 5.8 which is to be expected and validates our earlier numerical work. It is evident from Figure 5.11 that the solutions are symmetric about $x = \pi$, i. e. that $a + b = 2\pi$; we prove this below.

Let $b = 2\pi - a$, then

$$\begin{aligned} f(x) &= \sqrt{\left|\sin\frac{x-a}{2}\sin\frac{x+a-2\pi}{2}\right|} \\ &= \sqrt{\frac{1}{2}\left|\cos a - \cos x\right|}, \end{aligned} \tag{5.145}$$

so that the integrand in (5.144) is

$$\begin{aligned}
&\frac{x}{\sqrt{\frac{1}{2}|\cos a - \cos x|}}\left[\sin\frac{3x}{2} - \frac{1}{2}\sin\left(\frac{x}{2}+a\right) - \frac{1}{2}\sin\left(\frac{x}{2}-a\right)\right] \\
= \;& \frac{\sqrt{2}x\left(\sin x\cos\frac{x}{2} + \sin\frac{x}{2}(\cos x - \cos a)\right)}{\sqrt{\cos a - \cos x}} \\
= \;& 2\sqrt{2}x\frac{\mathrm{d}}{\mathrm{d}x}\left(\cos\frac{x}{2}\sqrt{\cos a - \cos x}\right), \qquad (5.146)
\end{aligned}$$

and hence the condition (5.144) is, after integrating by parts,

$$I := \int_a^{2\pi-a} \cos\frac{x}{2}\sqrt{\cos a - \cos x}\,\mathrm{d}x = 0. \qquad (5.147)$$

Now substituting

$$y = 2\pi - x, \qquad (5.148)$$

we see that

$$I = \int_{2\pi-a}^{a} \cos\left(\pi - \frac{y}{2}\right)\sqrt{\cos a - \cos(2\pi - y)}(-\,\mathrm{d}y) = -I, \qquad (5.149)$$

so that $I = 0$ and (5.144) is satisfied for all (a, b) such that $a + b = 2\pi$.

We may go further and find an explicit form for $s_1(x)$. From above, we know

$$\begin{aligned}
s_1'(x) &= \int_a^x -\cos y + \sqrt{2}\frac{\mathrm{d}}{\mathrm{d}x}\left(\cos\frac{y}{2}\sqrt{\cos a - \cos y}\right)\,\mathrm{d}y \\
&= -\sin x + \sqrt{2}\cos\frac{x}{2}\sqrt{\cos a - \cos x}, \qquad (5.150)
\end{aligned}$$

and so

$$s_1(x) = \cos x + \sqrt{2}\int_a^x \cos\frac{y}{2}\sqrt{\cos a - \cos y}\,\mathrm{d}y. \qquad (5.151)$$

This integral may be found explicitly by making the substitution

$$\sin\frac{a}{2}\cosh Y = \sin\frac{y}{2} \qquad (5.152)$$

for $a \neq 0$. Then

$$\sin\frac{a}{2}\sinh Y = \sqrt{\cos a - \cos y} \qquad (5.153)$$

and

$$s_1(x) = \cos x + 2\left[\sqrt{\cos a - \cos x}\sin\frac{x}{2} - \sin^2\frac{a}{2}\cosh^{-1}\left(\frac{\sin\frac{x}{2}}{\sin\frac{a}{2}}\right)\right]. \qquad (5.154)$$

In the case $a = 0$, we have

$$\begin{aligned} s_1(x) &= \cos x + \sqrt{2} \int_0^x \cos \frac{y}{2} \sqrt{1 - \cos y} \, \mathrm{d}y \\ &= \cos x + \int_0^x \sin y \, \mathrm{d}y \\ &= 1, \end{aligned} \tag{5.155}$$

which is indeed the limit as $a \to 0$ of (5.154). Again, these exact solutions agree closely with previous numerical approximations, thereby providing validation of our numerical scheme.

Chapter 6

Evolution systems with flow separation

We may now use the new model for flow separation derived in Chapter 5 in conjunction with our earlier evolution equations to simulate more accurately the evolution of an aeolian dune. We start by describing and justifying our method of calculating the surface shear stress due to the wind when separation is present, before going on to state the system we are solving, describe our method of implementation, and finally discuss our results.

6.1 Shear stress calculation

In Chapter 3 we described a method for calculating the perturbation to the shear stress on the surface of a dune caused by the shape of the dune (which perturbs the flow). The expression obtained for the stress τ was

$$\tau = 1 - \alpha s_x + \beta \mathcal{H}(s_x). \tag{6.1}$$

The derivation of this expression used the assumption that there was no separation present; now that we have a model for the mechanism of separation behind a dune, we may consider how the presence of separation affects the shear stress exerted on the dune.

As discussed in Chapter 5, the structure of the flow in the presence of separation consists of a wake region behind the dune, with a shear layer between this wake region and the outer undisturbed flow. In Chapter 5, we used the fact that this shear layer had a thickness of order ε to justify our assumption that the boundary conditions for the outer flow are the same in both the separated region and in the region where the

flow remains attached. Under this assumption, we were able in Chapter 5 to find the shape of the upper limit s_1 of the wake region.



Figure 6.1: Two flows past dunes; the first with separation, the second with a dune profile the same shape as the wake profile in the first. The two outer flows are identical.

Consider the two flow régimes in Figure 6.1: the first is the separated flow over a dune profile s_0, leading to a wake profile s_1, and the second is the flow over a new dune which is the shape of the combination of the first dune and its wake profile. Since the boundary conditions for the outer flow in the separated case are the same in both separated and non-separated parts of the flow (i. e. for all x), the outer flows in the two cases are identical. It is this fact that enables us to proceed.

In order to find the shear stress exerted by the separated flow, we may therefore replace the separated flow with the non-separated flow that leads to the same outer flow. For the non-separated flow, we may calculate the shear stress using (6.1). Of course, this shear stress only applies to the separated flow where it remains attached, i. e. for $x \in \mathbb{R} \setminus [a, b]$ (in the notation of Chapter 5). Inside the separated region, the shear stress exerted will depend on the nature of the recirculating flow, which we have not considered in detail; we do however know that this flow velocity is small compared to the outer flow. A reasonable first assumption to make is that this velocity is an order of magnitude in ε smaller than the outer flow velocity, so that we may approximate the stress with zero.[1]

Given a dune profile $s_0(x, t)$, with a slip face brink at $x = a$, we may therefore use (5.96) and (5.117), remembering that s_0 is now time dependent, to find the reattachment point b and the wake profile s_1, and then the shear stress τ is given by

$$\tau = \begin{cases} 1 + \alpha \frac{\partial s_0}{\partial x} + \beta \mathcal{H}\left(\frac{\partial s_1}{\partial x}\right), & x \notin [a, b], \\ 0, & x \in [a, b]. \end{cases} \tag{6.2}$$

[1]Even if we take the stress to be small but non-zero, as long as it is less than the critical stress τ_c then the effective stress will still be zero due to (2.3).

6.2 Separation problem: a spectral approach

The method of solution of the separation problem outlined in Chapter 5 works well when calculating the wake profile of a single dune. However, when calculating a rapid succession of dunes, as we will need to do as part of our evolution system, the method suffers from being too computationally intensive, and we would hope to be able to find a method which is less so.

This inefficiency arises due to the outermost integral in (5.114), which for each guess of the value of b requires an evaluation of the integral on a new grid. In addition, there is a conflict between the uniform grid of the spectral method and the non-uniform grid used to accurately evaluate the integral, which would require us to interpolate s_0 in some way[2].

Instead we wish to use a method which relies on the fact that we have a spectral representation of s_0, i. e. that we may write s_0 in terms of a truncated Fourier series. We present this method below.

We have, from (5.84),

$$s_1''(x) = \sigma_1(\xi) = -iw(\xi) = -\frac{i\xi\chi(\xi)}{\pi}\int_{\Gamma'}\frac{\sigma_0(\widehat{\xi})}{\widehat{\xi}(\widehat{\xi}-\xi)\chi^+(\widehat{\xi})}\,\mathrm{d}\widehat{\xi}, \tag{6.3}$$

where

$$\xi = e^{ix}. \tag{6.4}$$

Suppose that we may write s_0 in terms of a Fourier series, so that

$$s_0(x) = \sum_{n=-\infty}^{\infty} a_n e^{inx}. \tag{6.5}$$

Since s_0 is real, we know further that $\overline{a_n} = a_{-n}$. Then

$$\sigma_0(\xi) = s_0''(x) = -\sum_{n=-\infty}^{\infty} n^2 a_n \xi^n, \tag{6.6}$$

and so

$$\begin{aligned}\sigma_1(\xi) &= \frac{i\xi\chi(\xi)}{\pi}\int_{\Gamma'}\frac{\sum_{n=-\infty}^{\infty} n^2 a_n \widehat{\xi}^n}{\widehat{\xi}(\widehat{\xi}-\xi)\chi^+(\widehat{\xi})}\,\mathrm{d}\widehat{\xi} \\ &= \frac{i\xi\chi(\xi)}{\pi}\sum_{n=-\infty}^{\infty} n^2 a_n g_{n-1}(\xi),\end{aligned} \tag{6.7}$$

[2]The obvious way would be to interpolate using its Fourier series expansion since we are assuming that s_0 is periodic.

where we are justified in changing the order of summation and integration because of the uniform convergence of the Fourier series.

We know from Chapter 5 that

$$g_n(\xi) = \frac{\pi i \xi^n}{\chi(\xi)} - F_n(\xi) \tag{6.8}$$

and

$$g_{-(n+2)}(\xi) = -\frac{\overline{g_n(\xi)}}{\xi\chi(0)} \tag{6.9}$$

for $n \geqslant 0$, where F_n is a polynomial of degree $n+1$ satisfying

$$\frac{\pi i \zeta^n}{\chi(\xi)} \sim F_n(\zeta) \tag{6.10}$$

as $\zeta \to \infty$.

If we write

$$\frac{1}{\chi(\zeta)} = \sum_{n=-\infty}^{1} b_n \zeta^n \tag{6.11}$$

as the Laurent expansion of $1/\chi$ at ∞, which we know terminates at $n = 1$ since $\chi \sim 1/\zeta$ as $\zeta \to \infty$ by definition, then

$$\begin{aligned} g_n(\xi) &= \pi i \xi^n \sum_{m=-\infty}^{1} b_m \xi^m - F_n(\xi) \\ &= \pi i \sum_{m=-\infty}^{-(n+1)} b_m \xi^{m+n} \end{aligned} \tag{6.12}$$

for $n \geqslant 0$, and

$$g_n(\xi) = \frac{\pi i}{\xi\chi(0)} \sum_{m=-\infty}^{n+1} \overline{b_m} \xi^{-(m-n-2)} \tag{6.13}$$

for $n \leqslant -2$. Hence (6.7) becomes

$$\begin{aligned} \sigma_1(\xi) &= -\xi\chi(\xi) \left(\sum_{n=1}^{\infty} n^2 a_n \sum_{m=-\infty}^{-n} b_m \xi^{m+n-1} + \sum_{n=-\infty}^{-1} \frac{1}{\xi\chi(0)} n^2 a_n \sum_{m=-\infty}^{n} \overline{b_m} \xi^{-m+n+1} \right) \\ &= -\sum_{n=1}^{\infty} \sum_{m=-\infty}^{-n} n^2 \chi(\xi) \left(a_n b_m \xi^{m+n} + \frac{\xi}{\chi(0)} a_{-n} \overline{b_m} \xi^{-m-n} \right), \end{aligned} \tag{6.14}$$

which, since

$$\overline{\chi(\xi)} = \frac{\xi\chi(\xi)}{\chi(0)} \tag{6.15}$$

and

$$a_{-n} = \overline{a_n}, \tag{6.16}$$

may be written as

$$\sigma_1(\xi) = -2\,\mathrm{Re}\left\{\chi(\xi)\sum_{n=1}^{\infty} n^2 a_n \sum_{m=-\infty}^{-n} b_m \xi^{m+n}\right\}. \tag{6.17}$$

Then

$$\sum_{m=-\infty}^{-n} b_m \xi^{m+n} = \xi^n \left(\frac{1}{\chi(\xi)} - \sum_{m=-n+1}^{1} b_m \xi^m\right), \tag{6.18}$$

so that

$$\begin{aligned}\sigma_1(\xi) &= -2\,\mathrm{Re}\left\{\sum_{n=1}^{\infty} n^2 a_n \xi^n - \chi(\xi)\sum_{n=1}^{\infty} n^2 a_n \sum_{m=-n+1}^{1} b_m \xi^{m+n}\right\} \\ &= \sigma_0(\xi) + 2\,\mathrm{Re}\left\{\chi(\xi)\sum_{n=1}^{\infty}\sum_{m=-n+1}^{1} n^2 a_n b_m \xi^{m+n}\right\}. \end{aligned} \tag{6.19}$$

Finally we may rearrange the order of summation and write

$$c_n = \sum_{m=0}^{\infty} (m+n)^2 a_{m+n} b_{1-m} \tag{6.20}$$

to obtain

$$s_1''(x) = s_0''(x) + 2\,\mathrm{Re}\left\{e^{ix}\chi(e^{ix})\sum_{n=0}^{\infty} c_n e^{inx}\right\}. \tag{6.21}$$

This expression for $s_1''(x)$ may then be integrated twice to find $s_1(x)$. The advantage of this expression over our previous expression (5.117) for s_1'' is that this expression does not contain any integrals involving $s_0''(x)$, so that we do not require s_0'' to be evaluated at arbitrary grid points, as was the case before. We may simply use the Fourier coefficients a_n of s_0'', which we already have from our use of a spectral method. We approximate the infinite sums in (6.21) by truncating them; again this is consistent with our spectral approach where functions are approximated by truncating their Fourier series.

The condition (5.114) which, given a, fixes b may therefore be written

$$\mathrm{Re}\int_a^b x e^{ix}\chi(e^{ix})\sum_{n=0}^{\infty} c_n e^{inx}\,\mathrm{d}x = 0; \tag{6.22}$$

once we have found b, the wake profile is given by

$$s_1(x) = s_0(x) + 2\,\mathrm{Re}\int_a^x (x-y)e^{iy}\chi(e^{iy})\sum_{n=0}^{\infty} c_n e^{iny}\,\mathrm{d}y, \tag{6.23}$$

which is the updated version of (5.116).

In order to calculate the coefficients b_n of the Laurent series expansion (6.11) of $1/\chi(\zeta)$, we write

$$F\left(\frac{1}{\zeta}\right) = \frac{1}{\zeta\chi(\zeta)}; \tag{6.24}$$

then the coefficients are

$$b_n = \frac{1}{(1-n)!}F^{(1-n)}(0). \tag{6.25}$$

The derivatives of F may be found by noting that the Laurent expansion of F^2 is simply

$$F^2(z) = 1 - (\xi_a + \xi_b)z + \xi_a\xi_b z^2, \tag{6.26}$$

and that by the product rule,

$$\left(\frac{\mathrm{d}}{\mathrm{d}z}\right)^n [F^2(z)] = 2F^{(n)}(z) + \sum_{i=1}^{n-1} \frac{n!}{i!(n-i)!}F^{(i)}(z)F^{(n-1)}(z). \tag{6.27}$$

Combining (6.25), (6.26), and (6.27), we therefore obtain a recurrence relationship for b_n:

$$b_n = -\frac{1}{2}\sum_{i=1}^{-n} b_{1-i}b_{n+i}, \qquad n \leqslant -2, \tag{6.28}$$

with

$$b_1 = 1, \tag{6.29}$$

$$b_0 = -\frac{1}{2}(\xi_a + \xi_b), \tag{6.30}$$

and

$$b_{-1} = -\frac{1}{8}(\xi_a - \xi_b)^2, \tag{6.31}$$

from which we may calculate the coefficients b_n iteratively.

Finally we wish to compute the Fourier coefficients a_n of $s_0(x)$. In our numerical simulation, we have values of s_0 on a uniform grid. We write

$$\boldsymbol{s} = (s_1, s_2, \ldots, s_N), \tag{6.32}$$

where

$$s_j = s_0(jh), \tag{6.33}$$

and $h = 2\pi/N$ is the grid size.

The discrete Fourier transform of $\boldsymbol{s}$ (as computed by MATLAB's `fft` routine) is

$$\widehat{\boldsymbol{s}} = (\widehat{s}_1, \widehat{s}_2, \ldots, \widehat{s}_N), \tag{6.34}$$

where

$$\widehat{s}_j = \sum_{n=1}^{N} s_n e^{-ih(j-1)(n-1)}. \tag{6.35}$$

The Fourier coefficients of $s_0(x)$ are given by

$$a_n = \frac{1}{2\pi} \int_0^{2\pi} s_0(x) e^{-inx} \, \mathrm{d}x, \tag{6.36}$$

and given our knowledge of s_0 on a uniform grid, it is natural to approximate the integral with the trapezium rule, so that

$$a_n \approx \frac{1}{N} \sum_{j=1}^{N} s_j e^{-ihjn}. \tag{6.37}$$

Hence we may write an approximation to the Fourier coefficients of s_0 in terms of the discrete Fourier transform of $\boldsymbol{s}$,

$$a_n \approx \frac{1}{N} e^{-ihn} \widehat{s}_{n+1}. \tag{6.38}$$

Using the above expressions, we may implement a numerical approximation of $\frac{\partial^2 s_1}{\partial x^2}$ by simply truncating the infinite series. Having found $\frac{\partial^2 s_1}{\partial x^2}$, we may then integrate it using the same Gauss-Chebyshev quadrature as in Chapter 5 in order to solve the constraint (6.22) for b and then to find the wake profile s_1.

In Figures 6.2 to 6.5 we show the results of repeating the calculations of wake profiles from Chapter 5. These compare favourably on a qualitative level with the results of Chapter 5. More detailed comparison shows that in the case of a sinusoidal dune (Figure 6.2) the profiles are indistinguishable, but in the case of the dune profile from Chapter 2, there is a clear difference between the calculated wake profiles (Figure 6.4)[3]. This can be explained due to the fact that in the case of a sinusoidal dune, the Fourier series terminates after one term and so there is no error caused by truncating (6.20).

6.3 Implementation into evolution system

We now describe how we include this method of calculating the wake profile into a dune evolution system. We proceed as in Section 4.5.1, the major difference being the replacement of the polynomial wake profile with one derived using our new method.

[3]In particular, the reattachment point here is calculated to be $b \approx 4.7$ using the spectral method, compared to $b \approx 4.1$ using the method of Chapter 5.

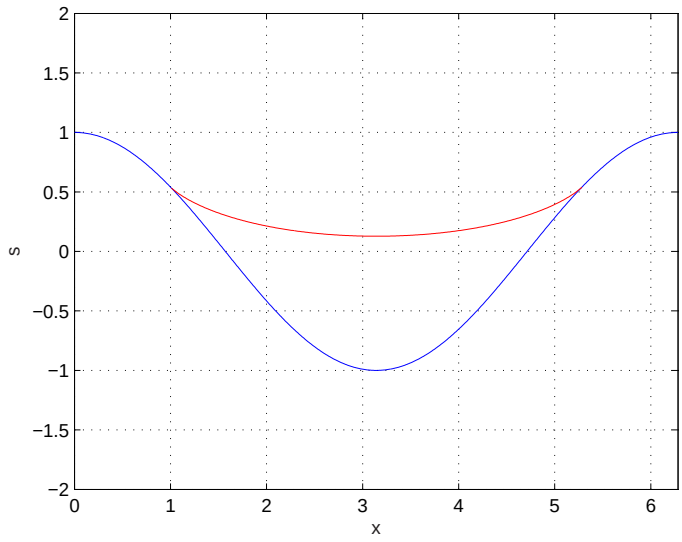


Figure 6.2: Wake region (red) calculated for a sinusoidal dune profile (blue) using the spectrally-based method of Section 6.2.

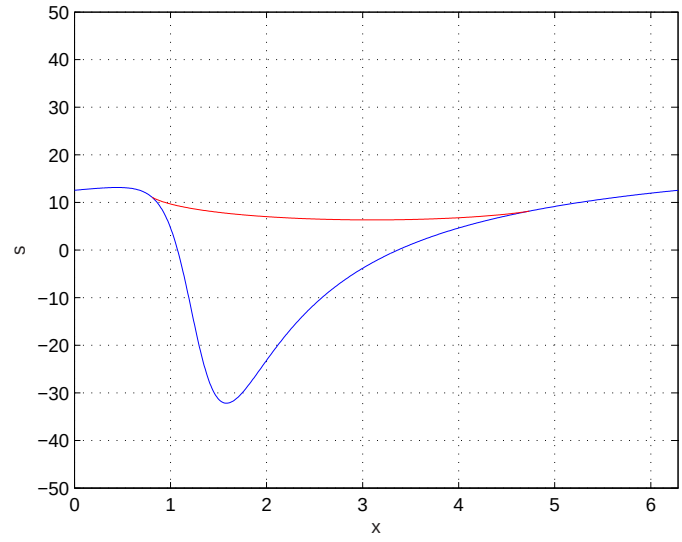


Figure 6.3: Wake profile (red) calculated for the constant eddy viscosity solution dune profile of Chapter 2 (blue) using the spectrally-based method of Section 6.2.

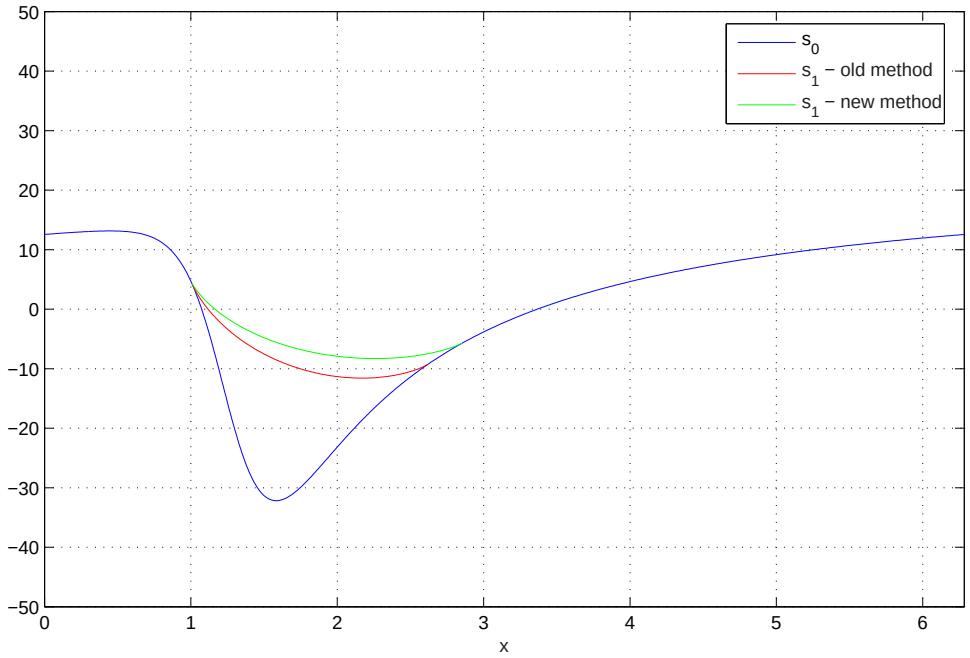


Figure 6.4: Comparison between spectral method (green) and the method of Chapter 5 (red) for calculating wake profiles for the constant eddy viscosity profile (blue).

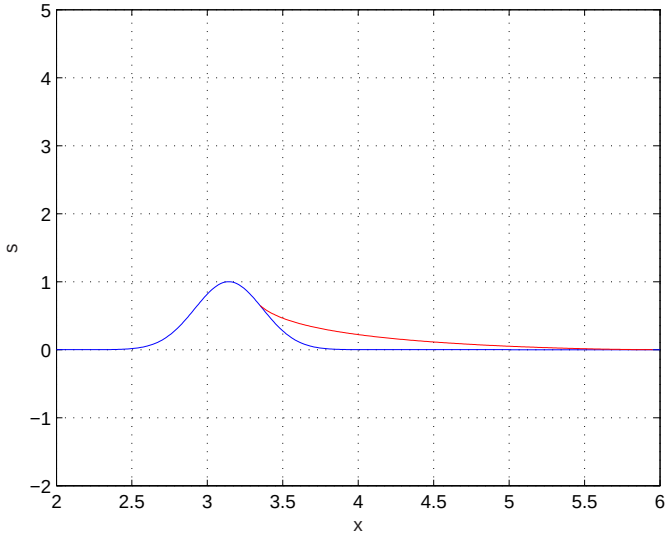


Figure 6.5: Wake profile (red) calculated for a Gaussian dune profile (blue) using the spectrally-based method of Section 6.2.

The Exner equation for conservation of mass of bed sediment is

$$\frac{\partial s_0}{\partial t} + \frac{\partial q}{\partial x} = 0 \tag{6.39}$$

as usual. We use the non-saturated flux relation

$$\gamma \frac{\partial q}{\partial x} = Q - q \tag{6.40}$$

with the Meyer-Peter & Müller relation

$$Q = \tau^{\frac{3}{2}}. \tag{6.41}$$

The stress is calculated using the mixing-length based model of Chapter 3; we evaluate it only outside the wake region $[a, b]$, so that

$$\tau = \begin{cases} 0, & x \in [a, b], \\ 1 - \alpha \mathcal{H}\left(\frac{\partial s_1}{\partial x}\right) + \beta \frac{\partial s_0}{\partial x}, & x \notin [a, b]. \end{cases} \tag{6.42}$$

Here the function $s_1(x, t)$ which describes the wake profile within the separated region must also be defined outside this region; we take it to be the same as the bed profile s_0, so that

$$s_1(x, t) = s_0(x, t), \quad x \notin [a, b]. \tag{6.43}$$

Within the wake region, we have the expression obtained above for s_1, which is

$$s_1(x) = s_0(x) + 2 \operatorname{Re} \int_x^a (x - y) \chi(e^{iy}) \sum_{n=0}^{\infty} C_n e^{iny} \, \mathrm{d}y, \tag{6.44}$$

where

$$\chi(e^{ix}) = \frac{e^{-\frac{i}{4}(a+b)} e^{-\frac{ix}{2}}}{2\sqrt{\left|\sin \frac{x-a}{2} \sin \frac{x-b}{2}\right|}}, \tag{6.45}$$

$$C_n(a(t), b(t)) = \sum_{m=0}^{\infty} (m + n)^2 A_{m+n} B_{1-m}, \tag{6.46}$$

$A_n(t)$ are the Fourier coefficients of $s_0(x, t)$, and $B_n(a(t), b(t))$ are the Laurent coefficients of $1/\chi(\zeta)$.

The reattachment point $b(t)$ is the solution to

$$\operatorname{Re} \int_a^b x \chi(e^{ix}) \sum_{n=0}^{\infty} C_n e^{inx} \, \mathrm{d}x = 0. \tag{6.47}$$

The position of the separation point $a(t)$ (which is also the brink of the slip face) is given by the evolution equation

$$\frac{\mathrm{d}a}{\mathrm{d}t} = \left. \frac{\frac{q}{b-a} + \frac{\partial q}{\partial x}}{\frac{\partial s_0}{\partial x} + \tan \theta} \right|_{x=a}, \tag{6.48}$$

where θ is the angle of repose (i. e. the angle of slope of the slip face, typically about 35°).

The height of the dune on the slip face is given by

$$s_0(x,t) = s_0(a,t) - (x-a)\tan\theta, \quad x \in [a,c], \tag{6.49}$$

where $c(t)$ is the horizontal position of the bottom of the slip face, obtained from

$$s_0(c,t) = s_0(a,t) - (c-a)\tan\theta. \tag{6.50}$$

Finally the bed profile remains constant (in time) between the bottom of the slip face and the reattachment point:

$$\frac{\partial s_0}{\partial t} = 0, \quad x \in [c,b]. \tag{6.51}$$

Again we have an evolution system for $s_0(x,t)$ consisting of 11 relations between 8 unknown functions $s_0(x,t)$, $q(x,t)$, $Q(x,t)$, $\tau(x,t)$, $s_1(x,t)$, $a(t)$, $b(t)$, and $c(t)$, along with the three sets of coefficients $A_n(t)$, $B_n(t)$, and $C_n(t)$. Here we have taken (6.39), (6.49), and (6.51) to be one condition relating s_0, q, a, b, and c, since between them they describe the evolution of s_0 throughout the range of x, and we take (6.43) and (6.44) to be one condition relating s_0, s_1, a, b, and C_n, since between them they define s_1 throughout the range of x.

The above system applies whenever a slip face is present, and hence the flow is separated. When a slip face is not present, it is unclear whether or not flow separation occurs; it is certainly a possibility. As before, we are forced to simply assume that flow separation does not occur. In this case, we revert to the reduced system

$$\gamma\frac{\partial q}{\partial x} = \tau^{\frac{3}{2}} - q, \tag{6.52}$$

$$\tau = 1 - \alpha\mathcal{H}\left(\frac{\partial s_0}{\partial x}\right) + \beta\frac{\partial s_0}{\partial x}, \tag{6.53}$$

$$\frac{\partial s_0}{\partial t} + \frac{\partial q}{\partial x} = 0, \tag{6.54}$$

and we may implement a mechanism for transition between these two situations as in Chapter 4.

6.4 Numerical implementation

In solving the system (6.39) to (6.51), we again use a Fourier spectral method for the spatial derivatives, along with a forward Euler scheme for the time derivatives.

The Fourier coefficients A_n are estimated using (6.38), the Laurent coefficients B_n are calculated iteratively using (6.28) to (6.31), and the infinite sum in (6.44) and (6.47) is approximated using

$$\begin{aligned}\sum_{n=0}^{\infty} C_n e^{inx} &= \sum_{n=0}^{\infty}\sum_{m=0}^{\infty}(m+n)^2 A_{m+n}B_{1-m}e^{inx} \\ &\approx \sum_{m=0}^{N-1}\sum_{n=0}^{N-1}(m+n)^2 A_{m+n}B_{1-m}e^{inx}, \end{aligned} \tag{6.55}$$

with $A_n = 0$ for $n > N$.

The integrals in (6.44) and (6.47) are then evaluated using Gauss-Chebyshev quadrature as described in Chapter 5, and the `fzero` routine in MATLAB is used to find the root b of (6.47).

When solving the system (6.39) to (6.50), we therefore carry out the following procedure:

1. Start with a dune profile s_0 and separation point a.
2. Find b, the root of (6.47).
3. Given a and b, calculate the wake profile s_1 from (6.44).
4. Use s_0 and s_1 to calculate τ (6.42), and from that Q (6.41).
5. Solve (6.40) to find q.
6. Use (6.48) to find the position of a at the next time step.
7. Use (6.50) with the updated value of a to find the new value of c.
8. Evolve the dune profile s_0 over the same time step using (6.39), (6.49), and (6.51).
9. Return to 1.

6.5 Remarks

On implementing the evolution system as described above, we may run simulations in various configurations as in Chapter 4, and obtain qualitatively similar results. At this point, we may make a number of remarks regarding this process.

Firstly we note that while the spectral method of calculating the wake profile is computationally much more efficient than the previous method using double integrals

(for the reasons described above), we still need to calculate the set of coefficients b_n, $n = 1, \ldots, N$ for each guess for the endpoint c. This means that a computational inefficiency remains, especially when compared to the polynomial separation method of Chapter 4.

The second observation that we make here concerns the domain of definition of the wake profile s_1, that is, the region of the dune profile s_0 that defines s_1. From the expression (6.3) for $s_1''(x)$, we see that s_1 depends only on the shape of s_0 in the non-separated region, i. e. when $x \in [0, a] \cup [c, 2\pi]$ (or $x \in [c, a]$ if $c < a$, remembering that we are working with a periodic domain). However, the spectral method of this Chapter uses the Fourier coefficients a_n which in turn depend on the shape of the dune profile throughout the periodic domain. While our expression for s_1'' in terms of a_n is exact and hence does not depend on s_0 in the separated part of the domain, as soon as we approximate the expression (as we must do in order to solve numerically), we immediately pick up some influence on s_1 from s_0 inside this separated region. This can become a problem when the dune profile contains discontinuities in shape or in slope, which is almost certainly the case when a slipface is present, due to the presence of Gibbs phenomena adversely affecting the accuracy of the Fourier coefficients and thus the solution for the wake profile s_1.

This error may be reduced in two ways: first, we may reduce the grid size for increased accuracy, but this further exacerbates the problem of computational inefficiency mentioned above; second, we may seek to smooth out slope discontinuities in some way[4], since this should not affect the exact solution if changes are made within the separated part of the domain.

[4]One possible method would be to calculate a wake profile using the polynomial method of Chapter 4 and use that as the dune profile from which we calculate the wake profile using the method of this Chapter. Of course we would have to be careful to ensure that the polynomial reattachment point lies upstream of the actual reattachment point.

Chapter 7

Three-dimensional dune systems

The models for wind flow and dune motion in the previous Chapters have all assumed a symmetry that meant that all analysis and simulation could be done in only two spatial dimensions. The assumptions were firstly that the wind flow is uni-directional, and secondly that the movement of the sand is uni-directional, thus ensuring a symmetry in the dune profile in a direction transverse to the wind flow.

In the case of transverse dunes these assumptions were reasonable ones to make, and the resulting dune systems were successful in predicting transverse dunes. In the case of a limited sand supply, however, the isolated dune which was predicted was not very realistic because it had an unlimited sand supply in a direction transverse to the wind, but a limited supply in the direction of the wind. Further, in order to predict any other variety of dune we must relax one or both assumptions and consider a dune system in three dimensions, since only a transverse dune is truly two-dimensional.

In this Chapter we consider a series of three-dimensional dune models, in which we relax the above assumptions. We start by relaxing the assumption that the sand motion is uni-directional and consider both of the shear stress models of Chapter 2 and Chapter 3. We then go on to consider the effect of flow separation in three dimensions, as well as discussing possible methods for modelling three-dimensional flow separation. Finally we consider ways to relax our other assumption of uni-directional wind flow.

7.1 Constant eddy viscosity shear stress model with uni-directional wind flow and down-slope term

We begin by revisiting the shear stress model derived in Chapter 2 and based on a constant eddy viscosity assumption for turbulent flow. We take our two independent

spatial variables to be x and y; the surface of the sand is at

$$z = s(x, y, t). \tag{7.1}$$

We assume the wind flow to be in the direction of a unit vector $\boldsymbol{w}$ in the (x, y)-plane, and for now at least we may assume $\boldsymbol{w}$ to be constant.

The three-dimensional versions of equations (2.164) to (2.168) are then

$$\begin{aligned} h &= 1 - s, && (7.2)\\ \frac{\partial s}{\partial t} + \nabla \cdot \boldsymbol{q} &= 0, && (7.3)\\ hu &= 1, && (7.4)\\ \boldsymbol{q} &= \sqrt{|\boldsymbol{\tau}|}\boldsymbol{\tau}, && (7.5)\\ \boldsymbol{\tau} &= u^2 \left(1 - s + K * (\boldsymbol{w} \cdot \nabla s)\right) \boldsymbol{w}. && (7.6) \end{aligned}$$

At this point the model is effectively the same model as the two-dimensional one in parallel slices, since there is nothing to induce a three dimensional effect. To do this, we may introduce a term analogous to the one introduced in Section 2.6.4, corresponding to a buoyancy-induced stress modification.

This term modelled the tendency of sand particles to roll down a slope. The three-dimensional analogue is to write

$$\boldsymbol{\tau}' = \boldsymbol{\tau} - \beta \nabla s. \tag{7.7}$$

This has the effect of both stabilising the system (in the same way as in Chapter 2) and introducing a three-dimensional effect, since the effective stress $\boldsymbol{\tau}'$ is no longer in the same direction as the wind flow.

Without loss of generality we may take $\boldsymbol{w}$ to be parallel to the x-axis, so that $\boldsymbol{w} = (1, 0)$. Then the system may be written

$$\begin{aligned} \frac{\partial s}{\partial t} + \nabla \cdot \boldsymbol{q} &= 0, && (7.8)\\ \boldsymbol{q} &= \sqrt{|\boldsymbol{\tau}|}\boldsymbol{\tau}, && (7.9)\\ \boldsymbol{\tau} &= \left(\frac{1}{1-s} + \frac{1}{(1-s)^2} K * \frac{\partial s}{\partial x} - \beta \frac{\partial s}{\partial x}, -\beta \frac{\partial s}{\partial y} \right), && (7.10) \end{aligned}$$

and this may be linearized and scaled as before to obtain the canonical evolution equation

$$\frac{\partial s}{\partial t} + s\frac{\partial s}{\partial x} - \frac{\partial^2 s}{\partial x^2} - \frac{\partial^2 s}{\partial y^2} + \int_0^\infty \xi^{-\frac{1}{3}} \frac{\partial^2 s}{\partial x^2}(x - \xi, y, t)\, \mathrm{d}\xi = 0. \tag{7.11}$$

This is of course the same equation obtained in (2.196) but with an extra term, which is a diffusive term in the y-direction. A linear stability analysis in the manner of Section 2.5 confirms that this is the case, the growth rate being given by

$$\operatorname{Re}\sigma = \frac{3k^{\frac{4}{3}}}{4\Gamma(2/3)} - \beta k^2 - \beta l^2 \tag{7.12}$$

for a perturbation of the form

$$s = s_0 e^{\sigma t + ikx + ily}. \tag{7.13}$$

Hence the system remains unstable to perturbations in the x-direction (parallel to the wind), with a stabilisation provided by the buoyancy term, but is stable with regards to perturbations in the y-direction (transverse to the wind). Hence we expect solutions to (7.11) to behave similarly to solutions to (2.196) in the downwind direction, with a spreading-out in the crosswind direction caused by the diffusion term. Hence three-dimensional dunes will have a tendency to become two-dimensional, approaching solutions to (2.196) (which are of course also solutions to (7.11)).

It is simple to extend the method of solution of (2.196) to (7.11); we may simply take Fourier transforms in the y-direction as well as the x-direction and treat the two diffusive terms identically. Again we may adjust the spatial scalings in order to have either periodic boundary conditions or zero boundary conditions in each direction independently.

Figures 7.1 to 7.4 show the downstream evolution from the initial conditions of a single Gaussian heap. As in Figures 2.12 to 2.16, the dune propagates downstream while growing (though it initially loses height as it spreads in the y-direction), before a depression grows downstream of the dune, and then another dune grows downstream of this depression. This pattern then repeats for as long as we run the simulation.

Figures 7.6 to 7.9 show the three-dimensional equivalent of the original system studied in Section 2.7.1, i. e. that shown in Figures 2.7 to 2.10. As before, we start with a random bed perturbation (shown in Figure 7.5). The perturbation grows into one large dune filling the whole domain, and propagates downstream across the periodic boundaries in the same manner as in Section 2.7.1.

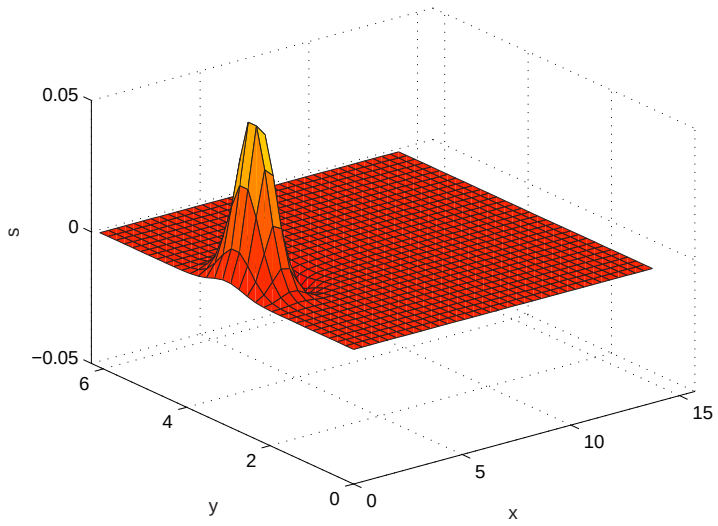


Figure 7.1: The first in a sequence of solutions to (7.11) with a long domain in the x-direction (c. f. Figure 2.16), most of which is not shown ($t = 0$).

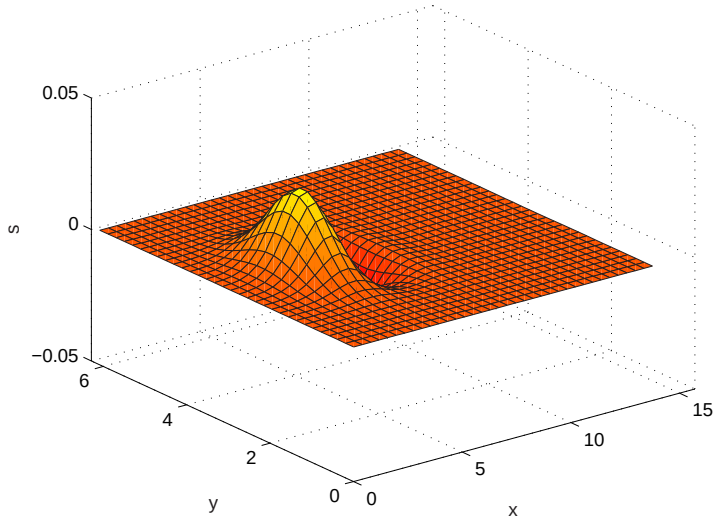


Figure 7.2: The second in a sequence of solutions to (7.11). A depression has started to form downstream of the dune ($t = 1$).

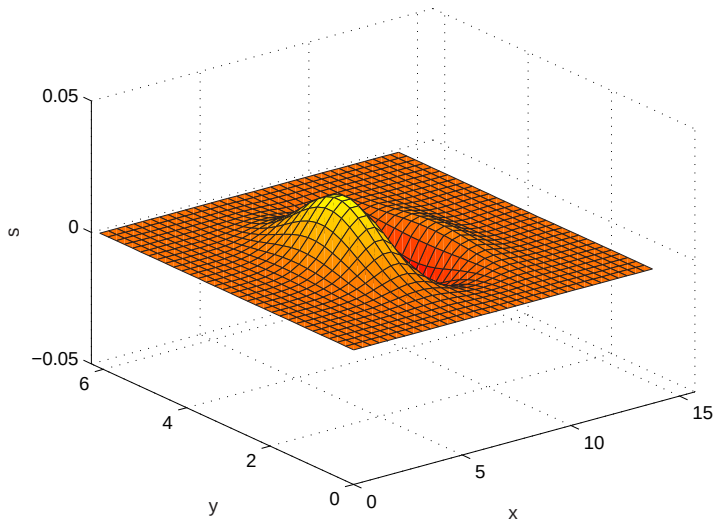


Figure 7.3: The third in a sequence of solutions to (7.11). Another dune has started to form downstream of the depression ($t = 2$).

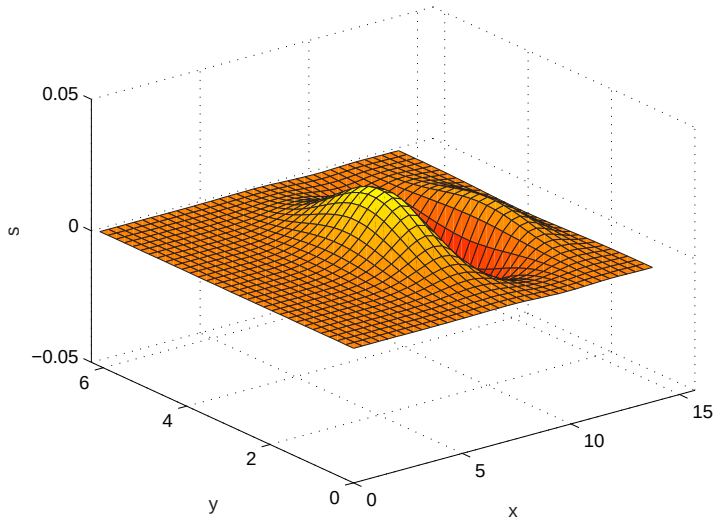


Figure 7.4: The fourth in a sequence of solutions to (7.11) ($t = 3$). The pattern of new depressions and dunes repeats for as long as we run the simulation.

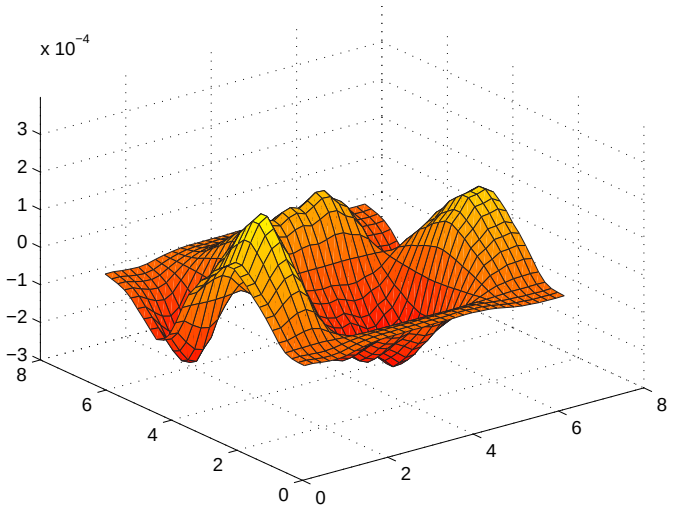


Figure 7.5: Typical random bed perturbation used as initial conditions for the simulation shown in Figures 7.6 to 7.9.

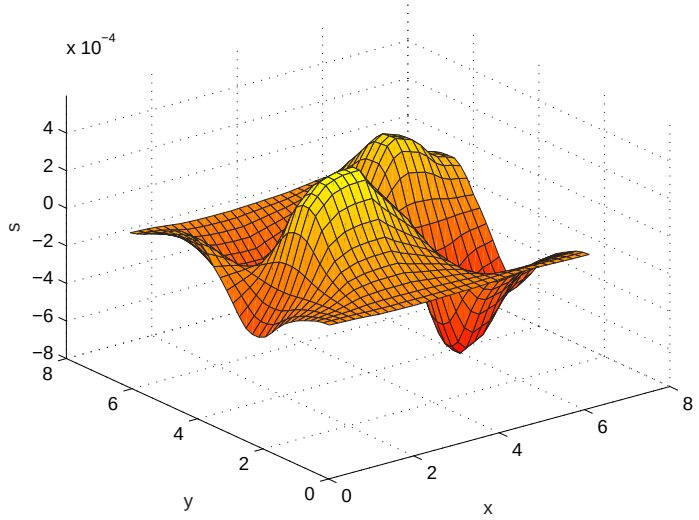


Figure 7.6: First in a sequence of solutions to 7.11 growing from an initial random perturbation ($t = 1$).

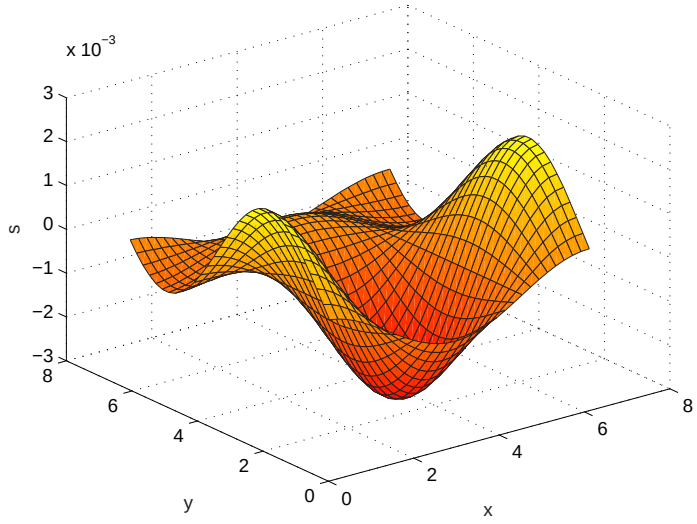


Figure 7.7: Second in a sequence of solutions to 7.11 growing from an initial random perturbation ($t = 2$). The dunes begin to fill the periodic domain

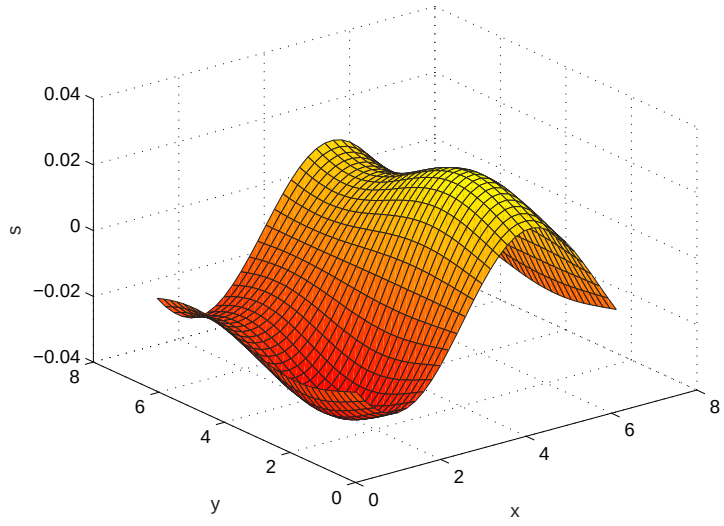


Figure 7.8: Third in a sequence of solutions to 7.11 growing from an initial random perturbation ($t = 3$). The dunes begin to arrange themselves transversely to the wind direction.

7.2 Mixing length shear stress model with non-separated uni-directional wind flow and down-slope term

We now consider a three-dimensional dune model similar to that described in the previous Section, but now based on the shear stress form derived in Chapter 3, based on an assumption of a mixing length theory for turbulent flow. The shear stress in three-dimensional form is thus

$$\boldsymbol{\tau} = (1 - \alpha\mathcal{H}(\boldsymbol{w}\cdot\nabla s) + \beta\boldsymbol{w}\cdot\nabla s)\,\boldsymbol{w}, \tag{7.14}$$

where as before $\boldsymbol{w}$ is the unit vector in the (x, y)-plane giving the wind direction, and we use this along with the equations

$$\begin{aligned}
\frac{\partial s}{\partial t} + \nabla\cdot\boldsymbol{q} &= 0, && (7.15)\\
\boldsymbol{q} &= q\widehat{\boldsymbol{\tau}}, && (7.16)\\
\gamma\widehat{\boldsymbol{\tau}}\cdot\nabla q &= Q - q, && (7.17)\\
Q &= |\boldsymbol{\tau}|^{\frac{3}{2}}, && (7.18)\\
\widehat{\boldsymbol{\tau}} &= \frac{\boldsymbol{\tau}}{|\boldsymbol{\tau}|}, && (7.19)
\end{aligned}$$

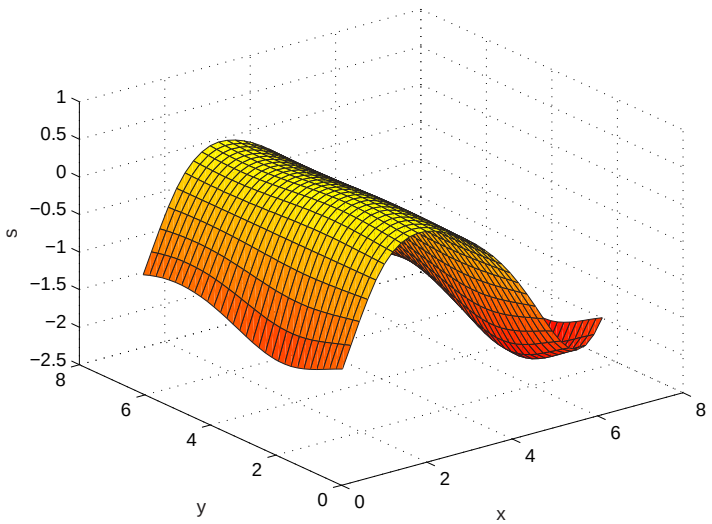


Figure 7.9: Fourth in a sequence of solutions to 7.11 growing from an initial random perturbation ($t = 4$). The solution has become symmetric in the y-direction and is the equivalent of the two-dimensional solutions found in Chapter 2.

which are the generalisations of the model equations into three dimensions.

Again we must modify this system in order to induce a three-dimensional effect; we do this by introducing an effective stress $\boldsymbol{\tau}'$ so that

$$\boldsymbol{\tau}' = \boldsymbol{\tau} - \delta \nabla s \tag{7.20}$$

as before, where δ is the coefficient of buoyancy previously denoted by β.

We may study the linear stability of this system by considering a perturbation of the form

$$\begin{aligned} s &= \widehat{s} e^{\sigma t + i(kx+ly)}, && (7.21)\\ \boldsymbol{q} &= (1 + \widehat{q}_1 s, \widehat{q}_2 s), && (7.22)\\ q &= 1 + \widehat{q} s, && (7.23)\\ Q &= 1 + \widehat{Q} s, && (7.24)\\ \boldsymbol{\tau} &= (1 + \widehat{\tau}_1 s, \widehat{\tau}_2 s), && (7.25) \end{aligned}$$

which leads to

$$\sigma = \frac{3}{2} k^2 \frac{1 - i\gamma k}{1 + \gamma^2 k^2} \left(\beta - \delta - i\alpha \operatorname{sgn} k\right) - \delta l^2, \tag{7.26}$$

and hence

$$\operatorname{Re} \sigma = \frac{3}{2} \frac{k^2}{1 + \gamma^2 k^2} \left(\beta - \delta - \alpha\gamma |k|\right) - \delta l^2, \tag{7.27}$$

so that provided $\delta < \beta$, the system preserves the instability in the downwind direction found in the two-dimensional model, along with the stabilising effect at high wavenumber due to the non-saturated flux equation. The extra term introduced by the three-dimensional modification has the same effect as in the previous Section, causing a diffusion in the direction perpendicular to the wind flow. We note further that since the instability in the downwind direction arises from a backward diffusion term, it is possible for this term to be cancelled out by the forward diffusive effect of the buoyancy term. As noted above, this occurs when $\delta > \beta$.

We may again use spectral methods in a manner similar to Chapter 3 to solve the system (7.14) to (7.19). Figures 7.10 to 7.13 show the results of such numerical simulation.

7.2.1 Limited sand supply

At this point it is natural to consider a simulation involving a limited sand supply moving over a hard bed, as an extension into three dimensions of the methods of Chapter 4, at this point without separation. However, we note that due to the

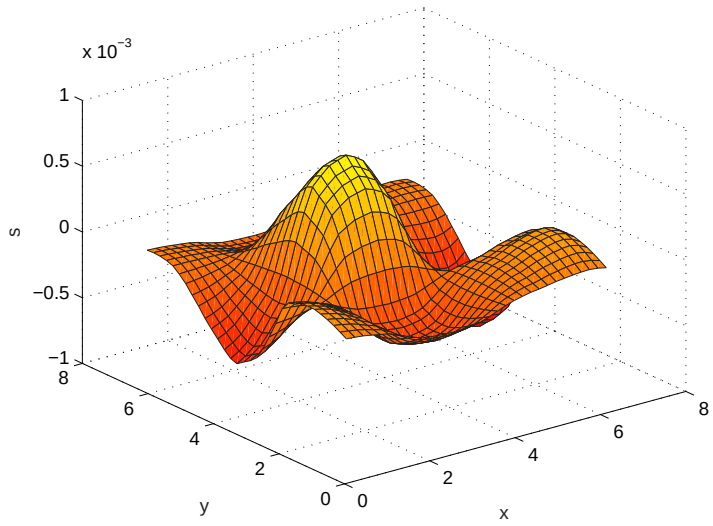


Figure 7.10: First in a sequence of solutions to (7.14) to (7.19) growing from an initial random perturbation ($t = 1$).

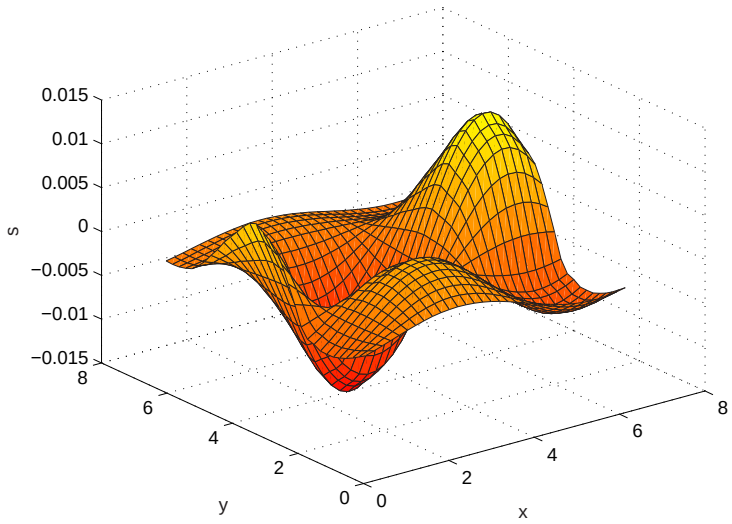


Figure 7.11: Second in a sequence of solutions to (7.14) to (7.19) growing from an initial random perturbation ($t = 2$).

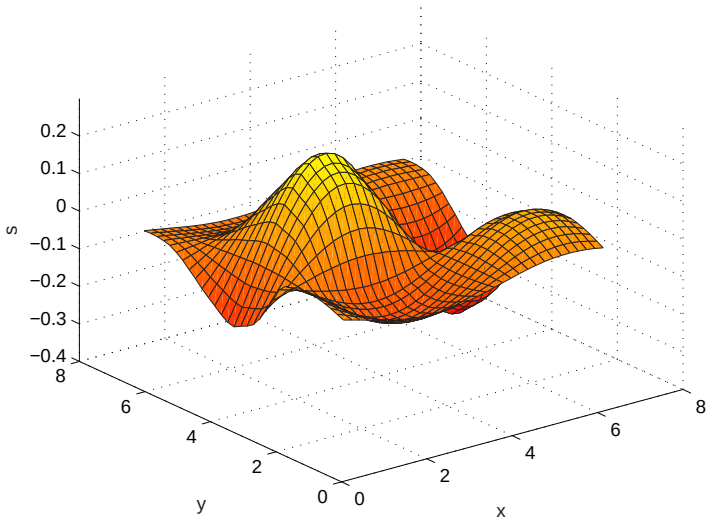


Figure 7.12: Third in a sequence of solutions to (7.14) to (7.19) growing from an initial random perturbation ($t = 3$).

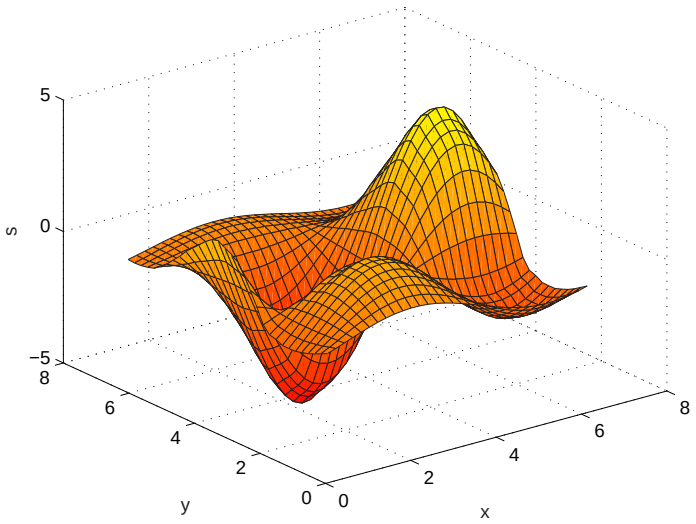


Figure 7.13: Fourth in a sequence of solutions to (7.14) to (7.19) growing from an initial random perturbation ($t = 4$).

diffusive nature of our three-dimensional term in the above systems, any finite sand pile will ultimately diffuse away in the transverse direction and thus is stable in this model. We must therefore consider alternative stress models in three dimensions in order to predict such finite dunes.

7.3 Improved mixing length shear stress model for three-dimensional flow

According to Weng et al [69], the Fourier transform of the three-dimensional surface shear stress over a dune $s(x, y)$ is given, under assumptions of a mixing-length theory with slowly varying topography and a uni-directional mean wind flow in the x-direction, by

$$\mathcal{F}_{xy}[\boldsymbol{\tau}](k_x, k_y) = \left(\frac{k_x^2}{\sqrt{k_x^2 + k_y^2}} \left(a \log |k_x| + b + ic \right), d \frac{k_x k_y}{\sqrt{k_x^2 + k_y^2}} \right) \mathcal{F}_{xy}[s], \qquad (7.28)$$

where a, b, c, and d are constants, $\mathcal{F}_{xy}[]$ denotes the double Fourier transform in the x- and y-directions, and k_x and k_y are the corresponding wavenumbers. On setting $k_y = 0$, we recover the two-dimensional form for the stress used in Chapter 3.

We may easily implement the above shear stress form into our simulations, since the fact that we are using a spectral method means that we do not have to invert the above Fourier transforms. Figures 7.14 to 7.17 show the results of such a simulation, and we observe that a three-dimensional dune grows from a random perturbation, and that the dune does not tend towards a two-dimensional dune as was previously the case.

7.4 Three-dimensional separated wind flow

7.4.1 The slipface in three dimensions

We now consider a method for describing the form of a slipface on a three-dimensional dune. In our previous studies in two dimensions we simply modelled the slipface as a straight line descending at the angle of repose $\theta \approx 34^\circ$ from its brink (which was known) down to the base of the dune. In the three-dimensional case, however, while we know that the slope of the slipface is at the angle of repose, we do not know in which direction this slope is, and in general it will not be in the downwind direction. Finding the profile of the slipface therefore requires more detailed analysis which we present below.

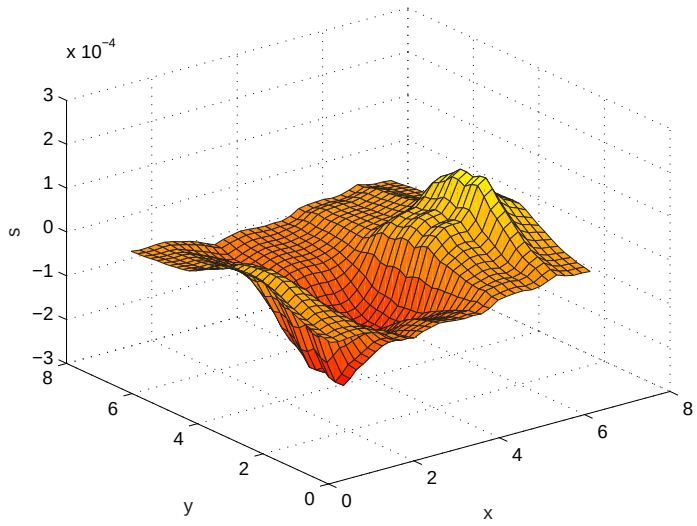


Figure 7.14: First in a sequence of solutions growing from an initial random perturbation and using (7.28) for the three-dimensional surface shear stress ($t = 1$).

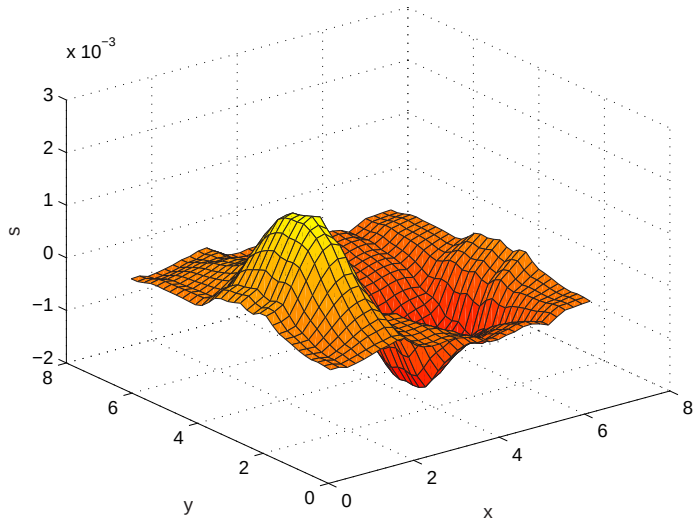


Figure 7.15: Second in a sequence of solutions growing from an initial random perturbation and using (7.28) for the three-dimensional surface shear stress ($t = 2$).

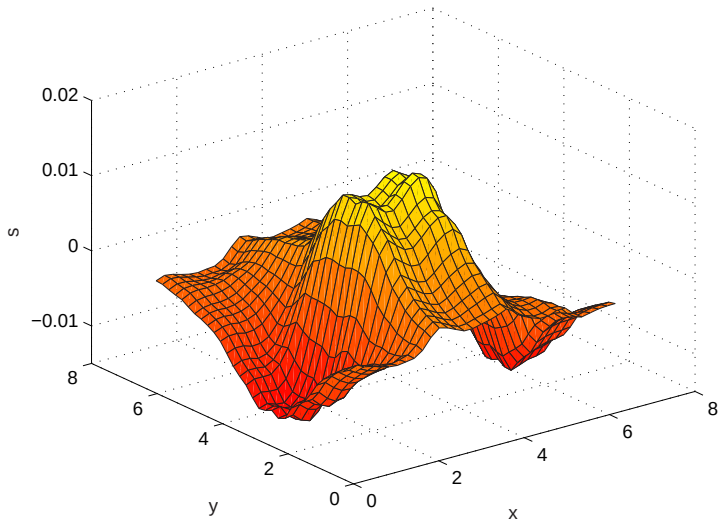


Figure 7.16: Third in a sequence of solutions growing from an initial random perturbation and using (7.28) for the three-dimensional surface shear stress ($t = 3$).

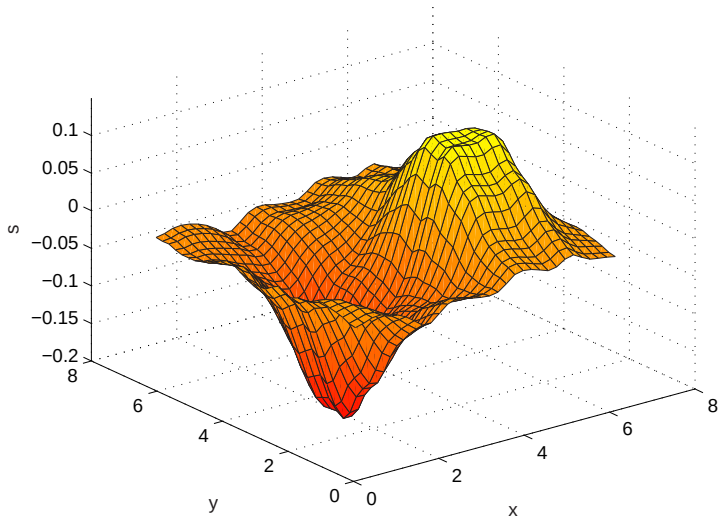


Figure 7.17: Fourth in a sequence of solutions growing from an initial random perturbation and using (7.28) for the three-dimensional surface shear stress ($t = 4$).

We know that the maximum slope attainable on the dune is that which is at the angle of repose; we assume further that at every point on the slipface, this maximum gradient is attained in some direction. We therefore have

$$|\nabla s| = \mu := \tan\theta \quad \text{for} \quad (x, y) \in D, \tag{7.29}$$

where $s(x, y)$ is the height of the dune, and $D \subset \mathbb{R}^2$ is the (unknown) region occupied by the slipface. This is the well-known *eikonal equation* for sandpiles [47]. We assume as before that the elevation of the brink of the slipface is known; this may be written as

$$s(x_1(\sigma), y_1(\sigma)) = s_1(\sigma) \tag{7.30}$$

on some given open curve $C_1 = \{(x_1(\sigma), y_1(\sigma)) : \sigma \in \mathbb{R}\}$ which forms part of the boundary of D (see Figure 7.18). The remaining part C_2 of the boundary of D is

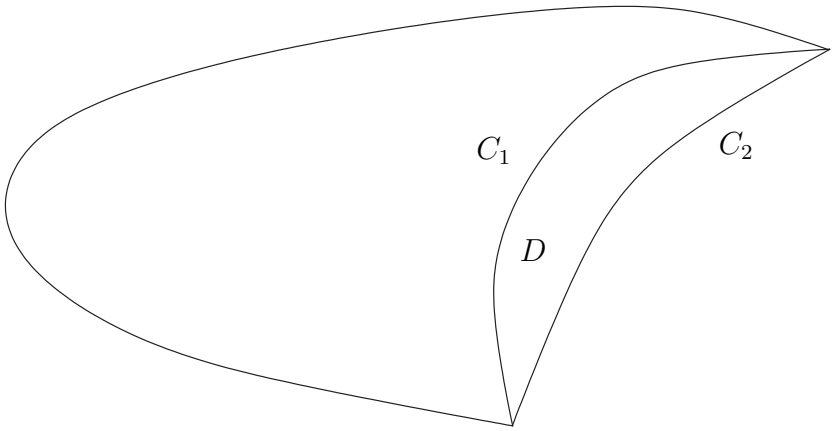


Figure 7.18: A barchan dune with a slipface showing the slipface region D, the brink curve C_1, and the base curve C_2.

then given by requiring that the slipface ends when it meets the underlying bed profile (given by $s_0(x, y)$), i. e.

$$s(x_2(\sigma), y_2(\sigma)) = s_0(x_2(\sigma), y_2(\sigma)) \tag{7.31}$$

on the curve $C_2 = \{(x_2(\sigma), y_2(\sigma)) : \sigma \in \mathbb{R}\}$. The eikonal equation (7.29) may be solved using Charpit's method; we obtain the parametric solution

$$s(\sigma, t) = 2\mu^2 t + s_1(\sigma), \tag{7.32}$$

$$x(\sigma, t) = 2p_1(\sigma)t + x_1(\sigma), \tag{7.33}$$

$$y(\sigma, t) = 2q_1(\sigma)t + y_1(\sigma), \tag{7.34}$$

where the functions $p_1(\sigma)$ and $q_1(\sigma)$ are given by

$$s_1'(\sigma) = p_1(\sigma)x_1'(\sigma) + q_1(\sigma)y_1'(\sigma) \tag{7.35}$$

and

$$p_1(\sigma)^2 + q_1(\sigma)^2 = \mu^2, \tag{7.36}$$

so that

$$p_1(\sigma) = \frac{x_1'(\sigma)s_1'(\sigma) \pm y_1'(\sigma)\sqrt{\mu^2(x_1'(\sigma)^2 + y_1'(\sigma)^2) - s_1'(\sigma)^2}}{x_1'(\sigma)^2 + y_1'(\sigma)^2} \tag{7.37}$$

and

$$q_1(\sigma) = \frac{y_1'(\sigma)s_1'(\sigma) \mp x_1'(\sigma)\sqrt{\mu^2(x_1'(\sigma)^2 + y_1'(\sigma)^2) - s_1'(\sigma)^2}}{x_1'(\sigma)^2 + y_1'(\sigma)^2}. \tag{7.38}$$

In particular, when the dune is moving over a horizontal bed at $z = 0$, (7.32) tells us that

$$t = -\frac{s_1(\sigma)}{2\mu^2} \tag{7.39}$$

where the slipface meets the bed, and hence from (7.33) and (7.34) we have the parametrization of the base curve C_2 given by

$$x_2(\sigma) = -\frac{p_1(\sigma)s_1(\sigma)}{\mu^2} + x_1(\sigma) \tag{7.40}$$

and

$$y_2(\sigma) = -\frac{q_1(\sigma)s_1(\sigma)}{\mu^2} + y_1(\sigma). \tag{7.41}$$

Of course the above analysis assumes that there is a unique mapping between (x, y) and (σ, t). When this is not the case, or equivalently when

$$J = \begin{vmatrix} x_\sigma & x_t \\ y_\sigma & y_t \end{vmatrix} = 0 \text{ or } \infty, \tag{7.42}$$

we have non-unique solutions for s and hence our analysis breaks down. Physically this corresponds to a slope discontinuity on the surface; since we know that the height s must be continuous here, we may take the continuity as the condition telling us the curve along which there is a jump in slope. More simply, we may just find all solutions and at each point take the maximum value of s obtained for the true physical solution.

7.4.2 Implementation of separation

Having found the location of the slipface, we are now in a position to find the separation region downwind of the dune. Since our previous methods for finding the shape of the wake region were inherently two-dimensional, we must find a suitable way to adapt them for use in the three-dimensional case. The most obvious way to do this is to simply assume that we have a two-dimensional wind flow and calculate the two-dimensional wake region separating at each point on the brink curve. The envelope of all of the two-dimensional wake regions is thus the three-dimensional wake bubble. We may do this with either of the two methods of flow separation (from Chapters 4 or 5).

There is no obvious way to modify either of these methods for a more accurate model of three-dimensional flow separation. The polynomial method of Chapter 4 appears to be extendable by use of a three-dimensional polynomial surface like

$$s_1(x,y) = Ax^3 + Bx^2y + Cxy^2 + Dy^3 + Ex^2 + Fxy + Gy^2 + Hx + Iy + J, \quad (7.43)$$

but of course this has only ten degrees of freedom and in general cannot be made to coincide with s_0 at all points of the brink curve. The method of Chapter 5 is certainly not generalizable to three dimensions due to its heavy reliance upon complex analysis.

Having calculated the surface of the wake region by either method, we may then proceed as in the two-dimensional case by calculating the surface shear stress using the combination of the dune surface and the wake surface. We may then use the stress to calculate the sand transport rate and subsequently evolve the sand surface in the usual way. We may also use a three-dimensional analogue of (4.26) to evolve the brink curve using principles of conservation of mass. This procedure is then repeated in order to simulate the evolution of the dune.

Chapter 8

Conclusions

In this thesis we have successfully explored the use of a number of deterministic models to simulate the formation and evolution of fluvial and Aeolian dunes. We now review the thesis and discuss some opportunities for further study.

We began the thesis by describing various aspects of the physical geography of dunes which acted as motivation for our models. In Chapter 2 we described a theory of turbulent fluid flow over an uneven boundary based on a constant eddy viscosity model for turbulence. By use of an asymptotic analysis of the Reynolds equations based on a large Reynolds number, we obtained an expression for the surface shear stress in terms of a convolution integral. We carried out a linear stability analysis of the system and found that it was unstable at high wavenumber; we therefore found two different methods of stabilising the system to avoid this ill-posedness. We then obtained a canonical, parameterless evolution equation and were able to obtain solutions to this equation which exhibited clear dune-like behaviour. We then went on to consider a modification involving a non-saturated flux relation from which we derived an alternative evolution equation which had the advantage of containing a length scale.

While the theory of Chapter 2 was based on work carried out in the context of river flow, we continued in Chapter 3 by considering a different shear stress form based on work on wind flow. We used a turbulence model based on mixing-length theory, and carried out an asymptotic analysis of the Reynolds equations using a small parameter based on the ratio of the large depth of the atmospheric boundary layer and the very small surface roughness length. We obtained an expression for the shear stress in terms of a Hilbert integral, and again found that the resulting system was unstable at high wavenumber. The methods used in Chapter 2 to stabilise the system were not applicable here, but we found that use of the non-saturated flux relation had the

desired effect and we were able to obtain qualitatively similar solutions to those in Chapter 2.

The next part of the thesis was concerned with the vital phenomenon of flow separation. We started in Chapter 4 by exploring the use of an existing method based heuristically on the use of a polynomial curve to model the upper surface of the separated region, and then using this curve as if it were part of the dune in order to calculate the shear stress. We used this method to calculate the shape of the wake region for various dune shapes, and we discussed some of the limitations of this method. We then described a method for modelling the propagation of a slipface, and combined this method with the polynomial flow separation model in order to obtain an evolution model for a dune with a slipface and flow separation. We simulated a number of different dune configurations, including a dune moving over an obstacle, and two dunes interacting with each other and merging into one dune.

Chapter 5 was concerned with the derivation of a new model for flow separation based on the mixing-length theory started in Chapter 3. We formulated a Riemann-Hilbert problem for the shape of the wake region, and used techniques of contour integration to solve the problem and obtain an explicit expression for the second derivative of the wake profile, which we could then integrate to find the shape of the wake region. We used this method to calculate the wake profiles for a number of dune shapes, and compared the results to the method of Chapter 4. We also were able to carry out some further analysis in the case of a sinusoidal dune and obtain an exact expression for the wake profile and for the position of the reconnection point; this enabled us to verify the accuracy of our numerical solution techniques.

At this point we were finally able to justify the method used in Chapter 4 of calculating the surface shear stress by replacing the dune profile in the separated region with the wake profile. Also in Chapter 6 we derived a different expression for the second derivative of the wake profile motivated by our use of a spectral method for the evolution systems. Finally we discussed the use of the new method in evolution systems, as well as its disadvantages in terms of computational inefficiency. Further work on this Chapter would concentrate on increased computational efficiency without sacrificing accuracy; this may be possible by further analysis of the results of Chapter 5.

In the final part of the thesis, in Chapter 7, we discussed the use of the two-dimensional methods so far derived in a three-dimensional context. We implemented three-dimensional versions of the shear stress forms used in Chapters 3 and 4 and found that we could induce a three-dimensional effect by adding a diffusion term in

the cross-wind direction. We also considered a fully three-dimensional version of the mixing-length shear stress model from which we obtained solutions that do not exhibit the symmetry in the third dimension that the other models did. We then found an expression for the shape of a slipface given the brink curve, which is necessary for the study of flow separation in three dimensions, and concluded by discussing the problem of finding the shape of a three-dimensional wake region using our existing, two-dimensional, methods.

The work in Chapter 7 provides the most scope for extension. We would hope to be able to further explore the use of separation in three dimensions to obtain simulations of, for example, barchan dunes, which should be possible using the two-dimensional techniques we describe. Further, while we exclude the possibility of extending our flow separation model to three dimensions, it may be possible to use the constant eddy viscosity model of Chapter 2 to obtain a different flow separation model which would not be based on complex analysis and would therefore be extendable to three dimensions. As before, we would also have to bear in mind concerns of computational efficiency. Finally, in order to simulate dune types other than transverse dunes or barchans, we would need to simulate multi-directional wind flow. The obvious way to do this is by simply switching direction at arbitrary point in time; it may be possible however to do this instead by simulating a simultaneous distribution of wind directions.

Appendix A

Turbulent flow modelling

It is well known that turbulent solutions of the Navier-Stokes equations

$$\frac{\partial u_i}{\partial x_i} = 0, \tag{A.1}$$

$$\rho\left(\frac{\partial u_j}{\partial t} + u_i\frac{\partial u_j}{\partial x_i}\right) = -\frac{\partial p}{\partial x_j} + \mu\frac{\partial^2 u_j}{\partial x_i \partial x_i} \tag{A.2}$$

(where we use the summation convention for notational simplicity later) may be found at some sufficiently large length scale for any non-zero value of the viscosity μ.

In order to model the effect of such turbulence, we may assume that the flow u_j may be expressed in two parts: a time-independent mean flow $\overline{u_j}$, relative to which there are turbulence-induced fluctuations u'_j; we thus follow Schlichting [57] and write

$$u_j = \overline{u_j} + u'_j. \tag{A.3}$$

We assume also that the effects of the viscosity μ on the mean flow are unimportant, i. e. the main effect of viscosity is to induce turbulence. This is appropriate for the small values of the viscosity that are relevant to this thesis. We therefore take $\mu = 0$ in (A.2)

We define the mean flow $\overline{u_j}$ to be the time average of u_j, taken over a sufficiently long time interval to ensure that the mean is independent of time. Therefore we may see straight away that $\overline{u'_j} = 0$.

A.1 Reynolds equations

Substituting (A.3) into (A.1), we obtain

$$\frac{\partial \overline{u_i}}{\partial x_i} + \frac{\partial u'_i}{\partial x_i} = 0, \tag{A.4}$$

and taking the time average gives

$$\frac{\partial \overline{u_i}}{\partial x_i} = 0, \tag{A.5}$$

from which we immediately obtain

$$\frac{\partial u_i'}{\partial x_i} = 0. \tag{A.6}$$

Hence both $\overline{u_j}$ and u_j' satisfy the equation of conservation of mass.

Taking the time average of (A.2) and substituting (A.3) leads us to

$$\rho \overline{u_i} \frac{\partial \overline{u_j}}{\partial x_i} = -\frac{\partial \overline{p}}{\partial x_j} - \rho \overline{u_i' \frac{\partial u_j'}{\partial x_i}}, \tag{A.7}$$

using

$$\frac{\partial \overline{u_j}}{\partial t} = 0 \text{ and } \overline{u_i \overline{u_j}} = \overline{u_i}\,\overline{u_j}. \tag{A.8}$$

Noting also that

$$u_i \frac{\partial u_j}{\partial x_i} = \frac{\partial}{\partial x_i}(u_i u_j) - u_j \frac{\partial u_i}{\partial x_i}, \tag{A.9}$$

we may use this with (A.6) to write (A.7) as

$$\rho \overline{u_i} \frac{\partial \overline{u_j}}{\partial x_i} = -\frac{\partial \overline{p}}{\partial x_j} - \frac{\partial}{\partial x_i}\left(\rho \overline{u_i' u_j'}\right). \tag{A.10}$$

We may think of (A.10) as being a momentum equation for $\overline{u_j}$, with the final term corresponding to the viscous effect of the turbulent eddies on the mean flow.

The standard sress tensor τ_{ij} in the Navier-Stokes equations may be written

$$\tau_{ij} = \mu\left(\frac{\partial u_i}{\partial x_j} + \frac{\partial u_j}{\partial x_i}\right); \tag{A.11}$$

hence by analogy we write the Reynolds stress tensor as

$$\tau_{ij} = -\rho \overline{u_i' u_j'} = \mu_T\left(\frac{\partial \overline{u_i}}{\partial x_j} + \frac{\partial \overline{u_j}}{\partial x_i}\right), \tag{A.12}$$

where μ_T is an eddy viscosity reflecting the viscous effect that turbulent eddies have on the mean flow, and which in general will vary with the flow.

Dropping overbars, we have the Reynolds equations

$$\frac{\partial u_i}{\partial x_i} = 0, \tag{A.13}$$

$$\rho u_i \frac{\partial u_j}{\partial x_i} = -\frac{\partial p}{\partial x_j} + \frac{\partial}{\partial x_i}\left\{\mu_T\left(\frac{\partial u_i}{\partial x_j} + \frac{\partial u_j}{\partial x_i}\right)\right\}, \tag{A.14}$$

where we must further specify the eddy viscosity μ_T.

A.2 Mixing length theory

In the context of turbulent shear flow past a wall (which is applicable to the problems under consideration in this thesis), Prandtl [49] suggested an expression for the eddy viscosity which was

$$\mu_T = \rho l^2 \left| \frac{\partial u}{\partial z} \right| \tag{A.15}$$

where the mixing length l is some function of the flow and/or position. The mixing length may be interpreted [57] as being a length, in a direction transverse to the flow, that an eddy must travel for its velocity to adjust to that of the mean flow.

Prandtl further suggested that the mixing length was proportional to the distance from the wall,

$$l = \kappa z, \tag{A.16}$$

where $\kappa \approx 0.4$ is the *von Kármán constant*. Under the further assumption that the shear stress

$$\tau = \rho \kappa^2 z^2 \left| \frac{\partial u}{\partial z} \right| \frac{\partial u}{\partial z} \tag{A.17}$$

is constant and equal to the wall stress τ_0, one may solve (A.17) for u to obtain

$$u = \frac{1}{\kappa} \sqrt{\frac{\tau_0}{\rho}} \log \frac{z}{z_0}, \tag{A.18}$$

where z_0 is a *roughness length*, a small length above the wall at which the velocity is zero (since otherwise $u \to -\infty$ at $z = 0$). Hence the mean velocity profile is logarithmic with distance from the wall, which is consistent with observations.

The results of the previous paragraph may be seen in a different way if we use von Kármán's similarity hypothesis [37] for the mixing length

$$l = \kappa \left| \frac{\partial u / \partial z}{\partial^2 u / \partial z^2} \right|, \tag{A.19}$$

and assume the logarithmic mean velocity profile in (A.18). From these we obtain

$$l = \kappa z \tag{A.20}$$

and

$$\tau = \tau_0, \tag{A.21}$$

so that the two expressions for the mixing length (A.16) and (A.19) are consistent in this case.

A simpler, though cruder, way to model the eddy viscosity is to assume that it is constant. This may be thought of as taking an average of the mixing-length eddy viscosity.

Bibliography

[1] D. J. Acheson, *Elementary Fluid Dynamics* (Oxford, 1990).

[2] J. R. Allen, *Current Ripples* (North-Holland, 1968).

[3] J. R. L. Allen, *Principles of Physical Sedimentology* (Chapman & Hall, London, 1985).

[4] R. S. Anderson, "Eolian ripples as examples of self-organization in geomorphological systems," *Earth-Sci. Rev.*, **29**:77 (1990).

[5] B. Andreotti, "A two species model of aeolian sand transport," Submitted to J. Fluid Mech.

[6] B. Andreotti, P. Claudin, and S. Douady, "Selection of dune shapes and velocities. Part 1: Dynamics of sand, wind and barchans," *Eur. Phys. J. B*, **28**:321–339 (2002).

[7] B. Andreotti, P. Claudin, and S. Douady, "Selection of dune shapes and velocities. Part 2: A two-dimensional modelling," *Eur. Phys. J. B*, **28**:341–352 (2002).

[8] R. A. Bagnold, *The Physics of Blown Sand and Desert Dunes* (Chapman & Hall, 1971).

[9] N. Balmforth and A. Provenzale (Editors), *Geomorphological Fluid Dynamics* (Springer-Verlag, 2002).

[10] B. O. Bauer and R. G. D. Davidson-Arnott, "A general framework for modeling sediment supply to coastal dunes including wind angle, beach geometry, and fetch effects," *Geomorphology* (2002).

[11] S. E. Belcher and J. C. R. Hunt, "Turbulent flow over hills and waves," *Ann. Rev. Fluid Mech.*, **30**:507–538 (1998).

[12] S. E. Belcher, T. M. J. Newley, and J. C. R. Hunt, "The drag on an undulating surface induced by the flow of a turbulent boundary-layer," *J. Fluid Mech.*, **249**:557–596 (1993).

[13] S. E. Belcher and N. Wood, "Form and wave drag due to stably stratified turbulent flow over low ridges," *Q. J. R. Meteorol. Soc.*, **122**:863–902 (1996).

[14] T. B. Benjamin, "Shearing flow over a wavy boundary," *J. Fluid Mech.*, **6**:161–205 (1959).

[15] J.-P. Bouchaud, M. E. Cates, J. Ravi Prakash, and S. F. Edwards, "Hysteresis and metastability in a continuum sandpile model," *Phys. Rev. Lett.*, **74**(11):1982–1985 (1995).

[16] G. F. Carrier, M. Krook, and C. E. Pearson, *Functions of a Complex Variable* (McGraw-Hill, 1966).

[17] V. Cornish, "On the formation of sand dunes," *Geographical Journal*, **9**(3):278–308 (1897).

[18] V. Cornish, *Waves of Sand and Snow and the Eddies Which Make Them Up* (Open Court Publishing Co., Chicago, 1914).

[19] P. G. Drazin and W. H. Reid, *Hydrodynamic Stability* (Cambridge University Press, 1981).

[20] F. Engelund, "Instability of erodible beds," *J. Fluid Mech.*, **42**(2):225–244 (1970).

[21] F. M. Exner, "Über die Wechselwirkung zwischen Wasser und Geschiebe in Flüssen," *Sitzungsberichte der Akademie der Wissenschaften in Wien, Teil 2a*, **134**:165–203 (1925).

[22] A. C. Fowler, "A sliding law for glaciers of constant viscosity in the presence of subglacial cavitation," *Proc. R. Soc. Lond. A*, **407**:147–170 (1986).

[23] A. C. Fowler, *Mathematics and the Environment*, Lecture Notes (Mathematical Institute, Oxford, 2001).

[24] A. C. Fowler, "Dunes and drumlins," in Balmforth and Provenzale [9].

[25] H. Frank, K. Heldt, S. Emeis, and F. Fiedler, "Flow over an embankment: Speed-up and pressure perturbation," *Boundary-Layer Meteorol.*, **63**:163–182 (1993).

[26] A. Goudie, *The Nature of the Environment* (Blackwell, Oxford, 1993).

[27] E. Guyon and H. J. Herrmann, "Granular community goes to the desert," *Europhysics News*, **32**(5) (2001).

[28] D. S. Henn and R. I. Sykes, "Large-eddy simulation of flow over wavy surfaces," *J. Fluid Mech.*, **383**:75–112 (1999).

[29] H. J. Herrmann, "Evolution and shapes of dunes," *Comptes Rendus Physique*, **3**:197–206 (2002).

[30] H. J. Herrmann and G. Sauermann, "The shape of dunes," *Physica A*, **283**:24–30 (2000).

[31] F. B. Hildebrand, *Introduction to Numerical Analysis*, International Series in Pure and Applied Mathematics (McGraw-Hill, 1956).

[32] J. Houghton, *The Physics of Atmospheres*, 3rd edition (Cambridge University Press, 2002).

[33] R. B. Hoyle and A. Mehta, "Two-species continuum model for aeolian sand ripples," *Phys. Rev. Lett.*, **83**(24):5170–5173 (1999).

[34] R. B. Hoyle and A. W. Woods, "Analytical model of propagating sand ripples," *Phys. Rev. E*, **56**:6861–6868 (1997).

[35] J. C. R. Hunt, S. Leibovich, and K. J. Richards, "Turbulent shear flows over low hills," *Q. J. R. Meteorol. Soc.*, **114**:1435–1470 (1988).

[36] P. S. Jackson and J. C. R. Hunt, "Turbulent wind flow over a low hill," *Q. J. R. Meteorol. Soc.*, **101**:929–955 (1975).

[37] T. von Kármán, "Mechanische Ähnlichkeit und Turbulenz," *Collected Works*, **2**:337–346 (1948).

[38] J. F. Kennedy, "The mechanics of dunes and anti-dunes in erodible-bed channels," *J. Fluid Mech.*, **16**:521–544 (1963).

[39] K. Kroy, G. Sauermann, and H. J. Herrmann, "A minimal model for sand dunes," *Phys. Rev. Lett.*, **88**:054301 (2002).

[40] N. Lancaster, W. G. Nickling, C. K. McKenna Neuman, and V. E. Wyatt, "Sediment flux and airflow on the stoss slope of a barchan dune," *Geomorphology*, **17**:55–62 (1996).

[41] S. Leliavsky, *An Introduction to Fluvial Hydraulics* (Constable, 1955).

[42] K. Lettau and H. Lettau, "Experimental and micrometeorological field studies of dune migration," in H. Lettau and K. Lettau (editors), *Exploring the world's driest climate* (Center for Climatic Research, University of Wisconsin, Madison, 1978).

[43] M. C. Malin, K. S. Edgett, M. H. Carr, G. E. Danielson, M. E. Davies, W. K. Hartmann, A. P. Ingersoll, P. B. James, H. Masursky, A. S. McEwen, L. A. Soderblom, P. Thomas, J. Veverka, M. A. Caplinger, M. A. Ravine, T. A. Soulanille, and J. L. Warren, "Sand Dunes in Kaiser Crater," NASA's Planetary Photojournal (`http://photojournal.jpl.nasa.gov/`), MOC2-306, 18 April 2002.

[44] E. Meyer-Peter and R. Müller, "Formulas for bed-load transport," *Proc. Int. Assoc. Hydraul. Res., 3rd annual conference, Stockholm*, pages 39–64 (1948).

[45] T.-D. Miao, Q.-S. Mu, and S.-Z. Wu, "Computer simulation of aeolian sand ripples and dunes," *Phys. Lett. A*, **288**:16–22 (2001).

[46] N. I. Muskhelishvili, *Singular Integral Equations* (Noordhoff, 1953).

[47] J. R. Ockendon, S. D. Howison, A. A. Lacey, and A. B. Movchan, *Applied Partial Differential Equations*, 2nd edition (Oxford, 2003).

[48] K. O'Malley, A. D. Fitt, T. V. Jones, J. R. Ockendon, and P. Wilmott, "Models for high-Reynolds-number flow down a step," *J. Fluid Mech.*, **222**:139–155 (1991).

[49] L. Prandtl, "Bericht über Untersuchungen zur ausgebildeten Turbulenz," *Zeitschrift für Angewandte Mathematik und Mechanik*, **5**:136–139 (1925).

[50] H. A. Priestley, *Introduction to Complex Analysis* (Oxford, 1990).

[51] L. Prigozhin, "Nonlinear dynamics of aeolian sand ripples," *Phys. Rev. E*, **60**(1):729–733 (1999).

[52] A. J. Raudkivi, "Bed forms in alluvial channels," *J. Fluid Mech.*, **26**:507 (1966).

[53] A. J. Reynolds, "Waves on the erodible bed of an open channel," *J. Fluid Mech.*, **22**(1):113–133 (1965).

[54] G. Sauermann, J. S. Andrade Jr., L. P. Maia, U. M. S. Costa, A. D. Araújo, and H. J. Herrmann, "Wind velocity and sand transport on a barchan dune," *Geomorphology*, **1325**:1–11 (2003).

[55] G. Sauermann, K. Kroy, and H. J. Herrmann, "Continuum saltation model for sand dunes," *Phys. Rev. E*, **64** (2001).

[56] G. Sauermann, K. Kroy, and H. J. Herrmann, "Saturation transients in saltation and their implications on dune shapes," Contribution to the 2iem Atelier International "Formation et Migration des Dunes", Nouakchott, 7-13 February 2001, available at `http://www.ica1.uni-stuttgart.de/~hans/nouakchott.pdf` (2001).

[57] H. Schlichting, *Boundary-Layer Theory* (McGraw-Hill, 1979).

[58] C. Schoof, *Mathematical models of glacier sliding and drumlin formation*, D.Phil. thesis, University of Oxford (2002).

[59] F. T. Smith, "Laminar flow over a small hump on a flat plate," *J. Fluid Mech.*, **57**:803–824 (1973).

[60] F. T. Smith, "On the high Reynolds number theory of laminar flows," *IMA J. Appl. Math.*, **28**:207–281 (1982).

[61] F. T. Smith, "On physical mechanisms in two- and three-dimensional separations," *Phil. Trans. R. Soc. Lond. A*, **358**:3091–3111 (2000).

[62] F. T. Smith and P. G. Daniels, "Removal of Goldstein's singularity at separation, in flow past obstacles in wall layers," *J. Fluid Mech.*, **110**:1–37 (1981).

[63] J. D. Smith, "Stability of a sand bed subjected to a shear flow of low Froude number," *J. Geophys. Res.*, **75**(30):5928–5940 (1970).

[64] M. Sørensen, "An analytic model of wind-blown sand transport," *Acta Mech. Suppl.*, **1**:67–81 (1991).

[65] R. I. Sykes, "An asymptotic theory of incompressible turbulent boundary-layer flow over a small hump," *J. Fluid Mech.*, **101**(3):647–670 (1980).

[66] L. N. Trefethen, *Spectral Methods in* Matlab (SIAM, 2000).

[67] H. Tsoar, "Types of aeolian sand dunes and their formation," in Balmforth and Provenzale [9].

[68] N. Vandewalle and S. Galam, "Ripples versus giant dunes in a saltation-avalanche model," *Int. J. Mod. Phys. C*, **10**(6):1071–1076 (1999).

[69] W. S. Weng, J. C. R. Hunt, D. J. Carruthers, A. Warren, G. F. S. Wiggs, I. Livingstone, and I. Castro, "Air flow and sand transport over sand-dunes," *Acta Mech. Suppl.*, **2**:1–22 (1991).

[70] F. K. Wippermann and G. Gross, "The wind-induced shaping and migration of an isolated dune: A numerical experiment," *Boundary Layer Meteorol.*, **36**:319–334 (1985).

[71] N. Wood, "Wind flow over complex terrain: A historical perspective and the prospect for large-eddy modelling," *Boundary-Layer Meteorol.*, **96**:11–32 (2000).

[72] X.-Y. Zou, Z.-L. Wang, Q.-Z. Hao, C.-L. Zhang, Y.-Z. Liu, and G.-R. Dong, "The distribution of velocity and energy of saltating sand grains in a wind tunnel," *Geomorphology*, **36**:155–165 (2001).